MODELING AND SIMULATIONS FOR SOLID-STATE DEWETTING PROBLEMS IN TWO DIMENSIONS

WANG YAN

NATIONAL UNIVERSITY OF SINGAPORE

2016

MODELING AND SIMULATIONS FOR SOLID-STATE DEWETTING PROBLEMS IN TWO DIMENSIONS

WANG YAN

(B.Sc., Beijing Normal University)

A THESIS SUBMITTED
FOR THE DEGREE OF DOCTOR OF PHILOSOPHY
DEPARTMENT OF MATHEMATICS
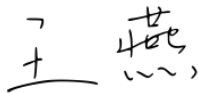## NATIONAL UNIVERSITY OF SINGAPORE
2016

DECLARATION

I hereby declare that this thesis is my original work and it has

been written by me in its entirety.

I have duly acknowledged all the sources of information which

have been used in the thesis.

This thesis has also not been submitted for any degree in any

university previously.

Wang Yan

30 December 2015

Acknowledgements

It is my great honor here to thank those who made this thesis possible.

First and foremost, I would very much like to thank my supervisor Prof. Weizhu Bao, who helped me overcome all the problems that I encountered and shaped me to be a professional person. His generous support, patient guidance, constructive suggestion and encouragement enabled me to conduct such an interesting research project.

I would like to express my appreciation to my collaborators Prof. David J. Srolovitz, Dr. Wei Jiang and Mr. Quan Zhao for their contribution to the work. Many thanks to Dr. Wei Jiang and Mr. Quan Zhao for fruitful discussions and suggestions on this topic, as well as for reading the draft.

I sincerely thank all the former colleagues and fellow graduates in our group. I heartfeltly thank my friends, especially Ying Cui, Yufei Zhao, Hengfei Lu, Lei Qiao, Ran Wei, Chen Yang, Liuqin Yang and Jinjiong Yu, for all the encouragement, emotional support, comradeship and entertainment they offered.

I would also like to thank NUS for awarding me the Research Scholarship during my Ph.D candidature, and for the financial assistance during the conference leaves.

Last but not least, thank my family and my boy friend for their encouragement and unconditional support. My life has always been brighter and happier with your presence.

Yan Wang

December 2015

Contents

Summary

Dewetting of solid thin films is a spontaneous physical phenomenon similar to wetting/dewetting of liquid films, describing the rupture of large continuous thin films and the formation of small agglomerates. It is a process which occurs well below the melting temperature of the metallic film and is driven by the total interfacial energy reduction. Therefore, solid-state dewetting is usually modeled as a surface-tracking problem driven by surface diffusion, combined with moving contact lines where the film, vapor, substrate phases meet.

The aim of this thesis is to propose mathematical models and numerical methods for simulating solid-state dewetting problems in two dimensions. The models and the corresponding boundary conditions are derived rigorously via a thermodynamic variational approach. We implement the models by either a "marker particle" method based on an explicit finite difference scheme or a semi-implicit parametric finite element method. Extensive numerical results are presented in this work. Although simulations are performed in two dimensions, they capture many of the complexities associated with real solid-state dewetting experiments.

This thesis mainly discusses modeling and simulations for solid-state dewetting problems progressively in the following three parts.

The first part focuses on the dewetting problems with weakly anisotropic surface

energies on a flat substrate. In this part, we first present the rigorous derivation of the sharp interface model based on an energy variational approach, considering a small perturbation of the film/vapor interface, as well as proofs of the mass conservation and energy dissipation. In the model, the movement of the contact line can be explicitly described by a relaxed contact angle boundary condition, which gives rise to an anisotropic Young equation for determining the static contact angle in the equilibrium morphology. Then, we introduce two methods for implementing the proposed model, which are a revised "marker particle" method and a semi-implicit parametric finite element method. At last, simulations are performed for small and large thin film islands, semi-infinite films and films with holes.

The second part is to understand the strongly anisotropy effects on morphologies of thin films on a flat substrate. The model proposed in the first part becomes ill-posed when the film/vapor interfacial energy density increases to the strongly anisotropic case. Therefore, we revise the total free energy by adding a Willmore energy and re-derive the governing equation and boundary conditions analogously. We note that the equation deduced from the new relaxed contact angle boundary condition converges to the anisotropic Young equation (in the first part) which may have multiple roots in the strongly anisotropic case. So, the roots to the anisotropic Young equation and the effects of strong anisotropy on the equilibrium construction are discussed later. Simulation results perfectly coincide with our deduction.

The last part is to investigate the dewetting on curved substrates based on the ideas in the first two parts on a flat substrate. In particular, instead of the unary anisotropic Young equation, we obtained a binary generalized Young equation for the static contact angle. According to this equation, asymmetric topography of the substrate may result in multiple contact angles in the final morphology even in the weakly anisotropic case. Moreover, our numerical simulations show the migration of small islands from the convex to concave sites and the formation of ordered structures by template-assisted dewetting on inverted pyramidal pits, which confirm the observation in the experiments.

List of Tables

List of Figures

List of Symbols and Abbreviations

MPM	marker particle method
PFEM	parametric finite element method
Ω_0	atomic volume
D_s	surface diffusivity
ν	the number of diffusing atoms per unit area
$k_B T_e$	thermal energy
γ_0	unit scale of film/vapor interfacial energy density
γ_{FS}	film/substrate interfacial energy density
γ_{VS}	vapor/substrate interfacial energy density
σ	a dimensionless parameter equals to $\frac{\gamma_{VS} - \gamma_{FS}}{\gamma_0}$
β	degree of the anisotropy
m	order of the rotational symmetry
ϕ	phase shift angle
ϵ	small perturbation parameter
ε	small regularization parameter
θ_i	isotropic Young angle
θ_a	anisotropic Young angle
θ_c	static contact angle

θ_d	dynamic contact angle
t	time
s	arc length of the film/vapor interface
p	a variable for parameterizing the film/vapor interface
τ	arc length of the curved substrate
θ	tangent/normal angle of the film/vapor interface
$\gamma(\theta),\ \gamma_{FV}$	film/vapor interfacial energy density
γ^*	generalized film/vapor interfacial energy density
$\widetilde{\gamma}$	surface stiffness
$x,\ y$	x, y-coordinates of the film/vapor interface
$x_{\text{sub}},\ y_{\text{sub}}$	x, y-coordinates of the curved substrate
κ	curvature in 2D
H	mean curvature in 3D
H_γ	weighted mean curvature in 3D
μ	chemical potential
V_n	normal velocity of the film/vapor interface
Γ	film/vapor interface, $\Gamma = \Gamma(t)$
$\mathbf{X}$	film/vapor interface, $\mathbf{X} = \mathbf{X}(s,t) = \mathbf{X}(p,t) = (x,\ y)$
$\Gamma^\epsilon(t)$	film/vapor interface after perturbation
Γ_{sub}	curved substrate
$\mathbf{X}_{\text{sub}}$	film/vapor interface, $\mathbf{X}_{\text{sub}} = \mathbf{X}_{\text{sub}}(\tau) = (x_{\text{sub}},\ y_{\text{sub}})$
$\mathcal{T}$	unit tangent vector of film/vapor interface
$\mathcal{N}$	unit normal vector of film/vapor interface
$\mathcal{T}_{\text{sub}}$	unit tangent vector of the (curved) substrate
$\mathcal{N}_{\text{sub}}$	unit normal vector of the (curved) substrate
W	total interfacial (surface) energy
W_{FV}	film/vapor interfacial energy
W_{FS}	film/substrate interfacial energy
W_{VS}	vapor/substrate interfacial energy

W_{w}	Willmore energy
∇_s	surface gradient operator

Chapter 1

Introduction

1.1 Solid-state dewetting and applications

Wetting/dewetting of liquid is a ubiquitous phenomenon in our daily life. It usually occurs on solid substrates, such as the formation of water drops on glass. Similar to the dewetting of liquid, a solid thin film resting on a foreign solid substrate will break up and agglomerate to form isolated islands (see Fig. 1.1) when heated to sufficiently high temperature, which is well below the melting point of the solid film [125]. This process is called solid-state dewetting since the thin film dewets when it still remains in the solid state.
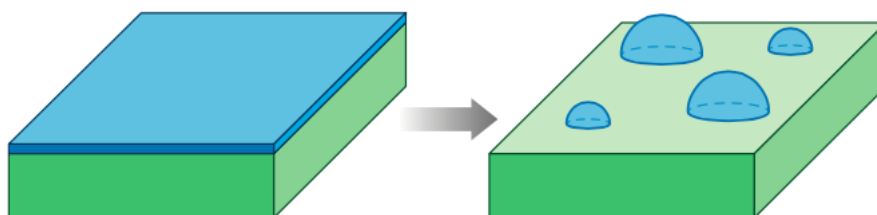
Figure 1.1: Schematic illustration of solid-state dewetting. Both the substrate (green) and the thin film (blue) are in the solid state. The image is reproduced from Thompson [125].

Many microelectronic and optoelectronic devices use solid thin films as basic

components [23, 89], the surface-area-to-volume ratios of these thin films are very large due to the small size of the devices. These solid thin films are especially unstable, that is, they are easy to dewet when the devices are heated. This kind of solid-state dewetting limits the reliability of the devices, so that solid-state dewetting has been a problem plagued makers of integrated circuits and other micro-systems for a long time. Therefore, many studies [2, 35, 37, 41, 64, 65, 68, 69, 94, 97] have been carried out to characterize and prevent dewetting, especially for metal silicides and silicon-on-insulator structures. It has been shown that many approaches, including using thick films, controlling the residual stress in films and so on, can be used to suppress the solid-state dewetting.
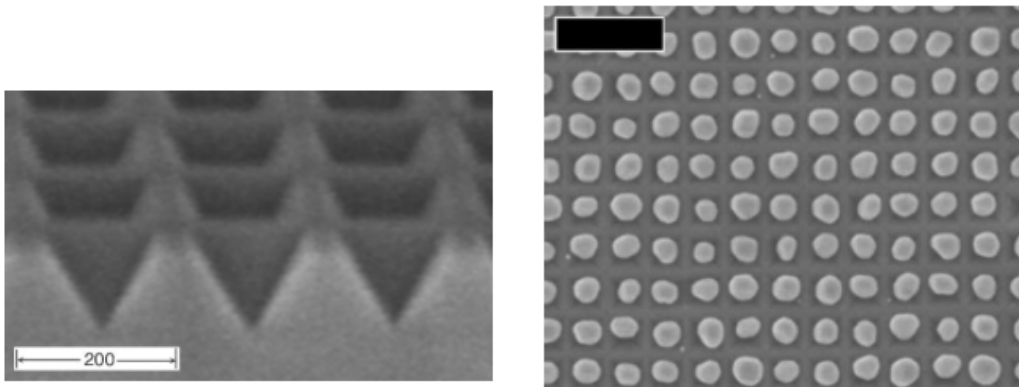
Figure 1.2: Template-assisted solid-state dewetting of gold films on oxidized silicon surfaces patterned with arrays of inverted pyramid shaped pits. The left figure is the substrate, the right one shows the ordered arrays forming via dewetting. The image is reproduced from Giermann & Thompson [55].

In recent years, it has been found that template-assisted dewetting [55, 56] can lead to periodic square arrays of particles with very narrow size distributions (an experimental example is shown in Fig. 1.2). It has also been shown that the single-crystal films [94, 95] has regular dewetting morphologies (an experimental example is shown in Fig. 1.3). Due to the recent understanding on solid-state dewetting, it has been purposely induced in engineering applications: making particle arrays in
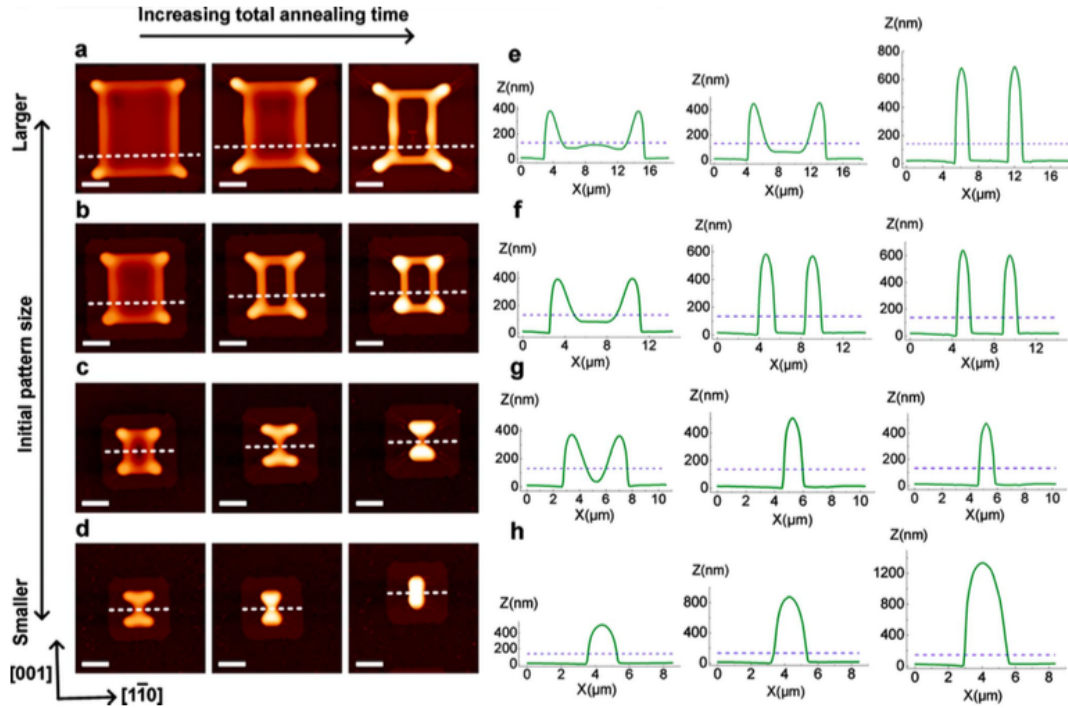
Figure 1.3: Dewetting of single-crystal films with different sizes. The image is reproduced from Ye & Thompson [137].

sensors [4,88], optical and magnetic devices [4,107], producing catalysts for growth of carbon nanotubes [31,93,106,141] and semiconductor nanowires [32,34,113], forming elements in electrical memory devices [30] and complex electrode structures [20].

In addition, in a recent set of experiments, Ye and Thompson [136–139] demonstrated the geometric complexity and importance of crystalline anisotropy in dewetting (an experimental example is shown in Fig. 1.4). These, and related, recent experiments have led to renewed interest in understanding solid-state dewetting and the influence of anisotropy on dewetting phenomena [44,66,75,76,82,99,100,104,144]. In the next several sections of this chapter, we will introduce the physical background, mathematical modeling and numerical results of solid-state dewetting problems.
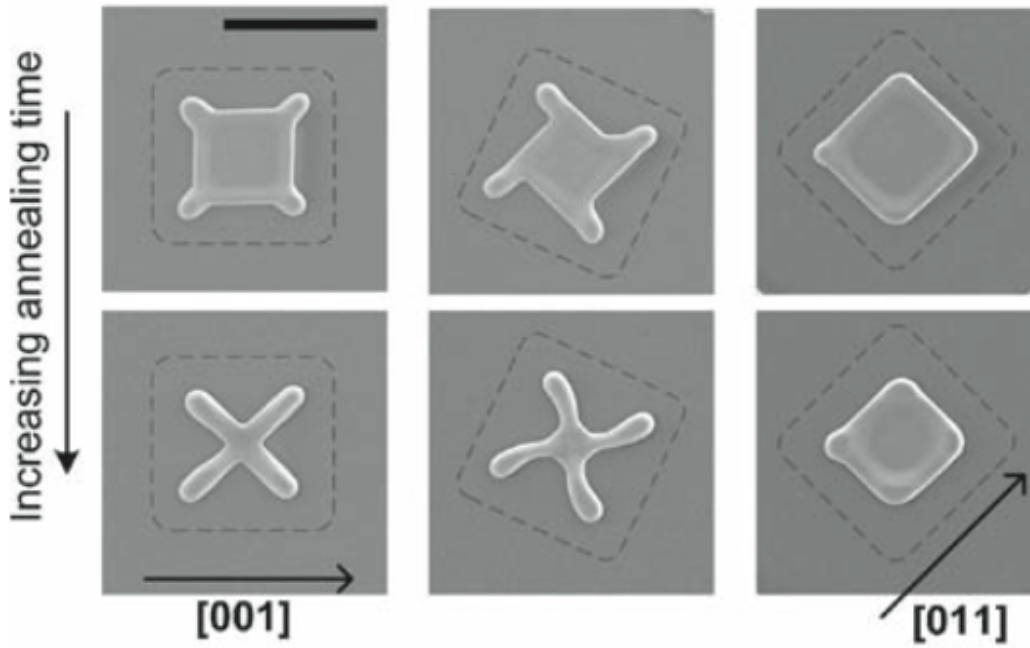
Figure 1.4: Dewetting of square patches with three different in-plane orientations. The image is reproduced from Ye & Thompson [137].

1.2 Physical background

1.2.1 Interfacial energy densities and their classifications

Considering a solid thin film lying on a rigid solid substrate in two dimensions (2D) (as illustrated in Fig. 1.5). $\gamma_{FV}, \gamma_{FS}, \gamma_{VS}$ represent film/vapor, film/substrate and vapor/substrate interfacial energy densities, respectively. γ_{FS} and γ_{VS} are always viewed as constants, and γ_{FV} depends on the orientation of the film/vapor interface. Usually, γ_{FV} is defined as a function of the tangent (normal) angle θ of the film/vapor surface, i.e., $\gamma_{FV} := \gamma(\theta)$. γ_{FV} can also be written as a function of the normal vector $\mathcal{N}$ of the film/vapor surface, which is consistent with the expression in three dimensions (3D). In this thesis, we use the notation $\gamma(\theta)$ as the film/vapor interfacial energy density unless otherwise specified.

In the real world of crystals, $\gamma(\theta)$ is always not differentiable (almost everywhere) [59]. While in order to make the solid-state dewetting and some related
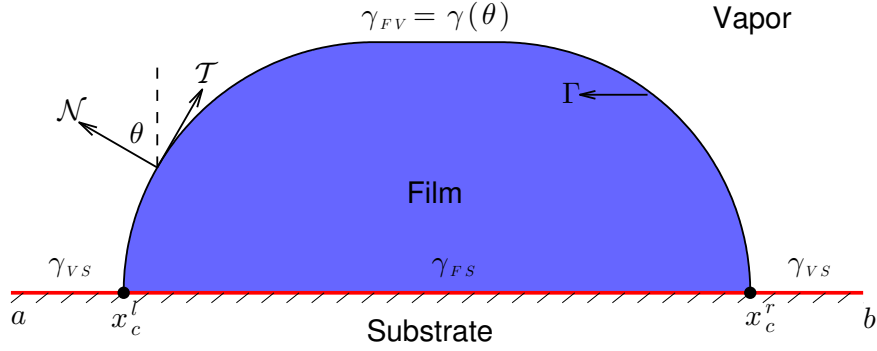
Figure 1.5: A schematic illustration of a solid thin film lying on a rigid solid substrate.

problems feasible, the researchers usually simplify $\gamma(\theta)$ to either the "smooth" case [41, 43, 48, 66, 98, 118, 134] or the finite cusped case [14, 16, 17, 28, 41, 75, 143, 144] in modeling.

By saying "smooth", we actually mean that $\gamma(\theta) \in C^2([-\pi, \pi])$, and it can be classified into the following three types:

1. *Isotropic case* [43, 66, 117, 118, 134]. In this case, $\gamma(\theta)$ is a constant function, and the equilibrium shape of the solid thin film must be a circle arc.

2. *Weakly anisotropic case* [41, 98]. In this case, $\gamma(\theta)$ is a C^2 function and it satisfies

$$\widetilde{\gamma}(\theta) := \gamma(\theta) + \gamma''(\theta) > 0, \qquad \forall\, \theta \in [-\pi, \pi], \tag{1.2.1}$$

where $\widetilde{\gamma}(\theta)$ is called the surface stiffness. An example of this kind of $\gamma(\theta)$ can be found in Fig. 1.9(a).

3. *Strongly anisotropic case* [48, 98, 122]. In this case, $\gamma(\theta)$ is also a C^2 function, but it does not satisfy Eq. (1.2.1). That is, $\widetilde{\gamma}(\theta) \leq 0$ for θ in some regions. An example of this kind of $\gamma(\theta)$ can be found in Fig. 1.9(c).

A widely used smooth $\gamma(\theta)$ is of the following (dimensionless) form (shown in Fig. 1.9a,c)

$$\gamma(\theta) = 1 + \beta \cos[m(\theta + \phi)], \qquad \theta \in [-\pi, \pi], \tag{1.2.2}$$

where β is the degree of anisotropy, m is the order of the rotational symmetry and ϕ represents a phase shift angle describing a rotation of the crystallographic axes from a reference orientation (the substrate plane). The isotropic, weakly anisotropic and strongly anisotropic cases correspond to $\beta = 0$, $0 < \beta < \frac{1}{m^2-1}$ and $\beta \geq \frac{1}{m^2-1}$, respectively.

The finite cusped $\gamma(\theta)$ means that $\gamma(\theta)$ is piecewise smooth (C^2) and not differentiable at finite points. Thus, the polar plot has finite (several) cusps. An example of this kind of $\gamma(\theta)$ can be found in Fig. 1.8. A commonly used cusped $\gamma(\theta)$ (shown in Fig. 1.11(a)) is

$$\gamma(\theta) = \sum_{i=1}^{n} |\sin(\theta - \alpha_i)|, \qquad \theta \in [-\pi, \pi], \tag{1.2.3}$$

where $\alpha_i \in [0, \pi], i = 1, ..., n$ are given constants. In computation, the regularization may be necessary due to the requirement of the method [14, 16, 17]. Here is a kind of regularization (shown in Fig. 1.11(c)):

$$\gamma(\theta) = \sum_{i=1}^{n} \sqrt{\varepsilon + (1 - \varepsilon) \sin^2(\theta - \alpha_i)}, \qquad \theta \in [-\pi, \pi], \tag{1.2.4}$$

where $\varepsilon > 0$ is a small regularization parameter. After the regularization, we have

$$\widetilde{\gamma}(\theta) = \sum_{i=1}^{n} \frac{\varepsilon}{\left(1 - (1 - \varepsilon) \cos^2(\theta - \alpha_i)\right)^{3/2}} > 0, \qquad \forall\, \theta \in [-\pi, \pi].$$

It can be seen that the cusped $\gamma(\theta)$ is regularized to the weakly anisotropic case.

1.2.2 Surface energy and diffusion

Solid thin films are usually at metastable or unstable states as deposited. When heated to a sufficiently high temperature (below the melting point), the thin film

will dewet and alter its morphology in an effort to reach the equilibrium. It is generally suggested that the surface diffusion is the dominant process compared to other transport processes of matter [57, 66, 90, 91, 134], such as viscous flow, evaporation/condensation, and volume diffusion, when the temperature is $\frac{1}{2}$ to $\frac{2}{3}$ of the melting point of a crystalline material, at which dewetting is observed [65]. Therefore, unlike dewetting of liquids on substrates, solid-state dewetting problems are viewed as capillarity-driven surface diffusion-controlled mass transport problems, where the surface energy reduction is the only driving force for surface motion. The kinetics of the capillarity-driven surface diffusion can be explained as follows.

The total interfacial energy of the (bounded) system (refer to Fig. 1.5) is the summation of the film/vapor, film/substrate and vapor/substrate interfacial energies

$$
\begin{aligned}
W & = W_{FV} + W_{FS} + W_{VS} \\
& = \int_{\Gamma} \gamma_{FV}\, d\Gamma + (x_c^r - x_c^l)\gamma_{FS} + (b - x_c^r + x_c^l - a)\gamma_{VS} \\
& = \int_{\Gamma} \gamma(\theta)\, d\Gamma + (x_c^r - x_c^l)(\gamma_{FS} - \gamma_{VS}) + (b - a)\gamma_{VS},
\end{aligned}
$$

where x_c^l, x_c^r denote the left and right contact points and $[a, b]$ is an arbitrary bounded region with $a < x_c^l < x_c^r < b$. Since $(b - a)\gamma_{VS}$ in the above identity is a constant term during the dewetting process, it is always omitted in the energy for simplicity. That is, the total interfacial energy is defined as

$$
W = \int_{\Gamma} \gamma(\theta)\, d\Gamma + (x_c^r - x_c^l)(\gamma_{FS} - \gamma_{VS}). \tag{1.2.5}
$$

With the given total interfacial energy, the chemical potential μ of the film/vapor surface, which describes the surface diffusion, can be defined as [58]

$$
\mu = \Omega_0 \frac{\delta W}{\delta \Gamma}, \tag{1.2.6}
$$

where Ω_0 represents the atomic volume (area in 2D). In 2D, it has been shown in [41, 58] that the chemical potential can be written as

$$
\mu = \Omega_0 \big(\gamma(\theta) + \gamma''(\theta)\big)\kappa = \Omega_0 \tilde{\gamma}(\theta)\kappa.
$$

Here, κ is the curvature of the film/vapor interface (curve). In 3D, the chemical potential becomes

$$\mu = \Omega_0 H_\gamma,$$

where H_γ is the weighted mean curvature [122]. If the surface energy density is isotropic, i.e., $\gamma(\theta) = \gamma_0$ is a constant, then H_γ is proportional to the mean curvature of the surface, i.e., $H_\gamma = \gamma_0 H$. However, both expressions are only valid for low curvature (isotropic and weakly anisotropic cases) interfaces without facets. When it turns to the strongly anisotropic case, it is necessary to add a regularization term in μ [96, 126].

The gradients of chemical potential along the surface will produce a drift of surface atoms with an average velocity given by the Nernst-Einstein relation [41, 70, 90],

$$V = -\frac{D_s}{k_B T_e} \nabla_s \mu,$$

where D_s is the surface diffusivity, $k_B T_e$ is the thermal energy, ∇_s (∂_s in 2D with s the arc length of the film/vapor interface) is the surface gradient operator. This gives the flux of the surface atoms

$$J = -\frac{D_s \nu}{k_B T_e} \nabla_s \mu$$

with ν the number of diffusing atoms per unit area.

Taking the surface divergence of $-J$, we can obtain the increment of the number of atoms per unit area per unit time. Then, the normal velocity V_n of the surface is defined by Fick's law [5] as:

$$V_n = \frac{D_s \nu \Omega_0}{k_B T_e} \nabla_s^2 \mu. \tag{1.2.7}$$

For example, assuming that the surface energy density is isotropic, where the chemical potential is proportional to the curvature $\mu = \Omega_0 \gamma_0 H$, and considering a semi-infinite long film with a sharp corner. Then in order to reduce the total energy, the surface atoms transport from the corner (with high curvature) to the flat region
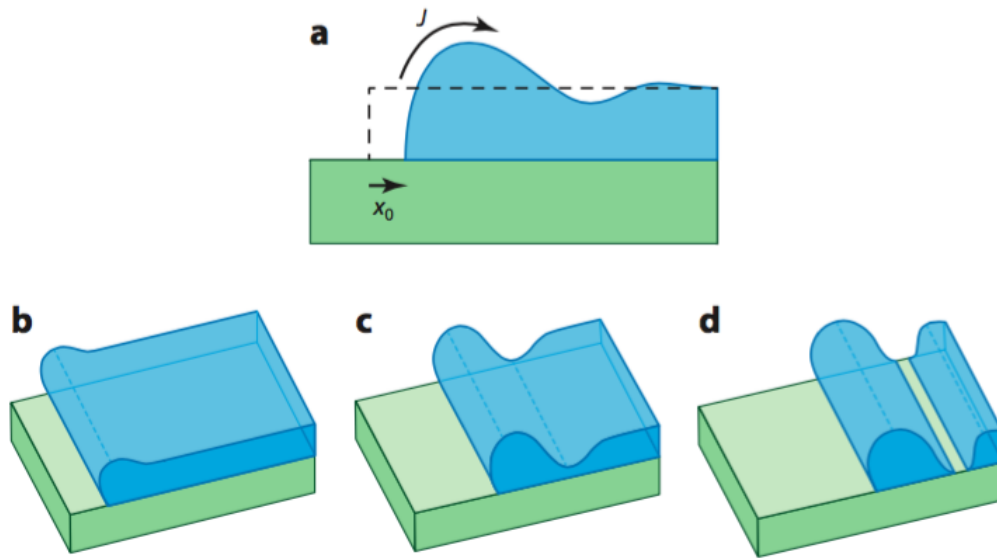
Figure 1.6: A schematic illustration of the edge retraction and pinch-off of a semi-infinite step film (shown as the dash line in 'a'). The image is reproduced from Thompson [125].

(with low curvature) as illustrate in Fig. 1.6. Finally, this will lead to pinch-off of the thin film.

Mullins [90] first proposed the governing equation (evolution law) for the motion by surface diffusion, assuming an isotropic surface energy density. From then on, this surface diffusion type geometric evolution equations has been extensively studied for closed surfaces (or curves). Davi and Gurtin [38] provided a derivation based on some balance laws, where they also included the anisotropy. In [49–51], the authors provided the existence, uniqueness and stability results. Also, many computational methods and efficient schemes, such as the crystalline method [3, 28, 111, 123], the level set method [33, 42, 73, 115, 116, 120], the phase field method [10, 48, 126], the parametric finite element method [6, 11–17, 46] and the $\theta - L$ formulation [62], have been proposed for closed interfaces.

1.2.3 Contact line migration

In addition to being a surface diffusion type of surface-tracking problem, solid-state dewetting has the additional feature of a moving contact line. The moving contact line problem is also a classical problem in fluid mechanics. In two-phase immiscible flows, extensive studies have been carried out on the moving contact line problem [7,29,39,45,54,63,79,80,101–103,108–110,124,129]. However, different with the moving contact line in fluid mechanics, where the fluid-fluid phases interface intersects the solid wall, it is the intersection of the solid-vapor interface and the solid substrate in solid-state dewetting.

We first review the situation of static contact line, the contact line at the steady/equilibrium state, in solid-state dewetting. Assuming isotropic (film/vapor) surface energy, i.e., $\gamma_{FV} = \gamma_0$ is a constant, the configuration of the static contact line is the same as that in fluid mechanics [39,140]. As illustrated in Fig. 1.7, by the force balance in the horizontal direction or minimizing the total surface energy, one can obtain the well known isotropic Young equation [140]

$$\gamma_{VS} = \gamma_{FS} + \gamma_0 \cos\theta_c, \tag{1.2.8}$$

where θ_c is the static contact angle (tangent/normal angle at the contact point in the equilibrium state). That is, the static contact angle θ_c should be equal to the isotropic Young angle

$$\theta_i = \arccos(\sigma) = \arccos\frac{\gamma_{VS} - \gamma_{FS}}{\gamma_0}.$$

Here we introduce a dimensionless coefficient σ to denote the ratio $\sigma := (\gamma_{VS} - \gamma_{FS})/\gamma_{FV}$.

As to the boundary conditions for the moving contact line in solid-state dewetting, there are several possible treatments.

- A widely used approach is to directly adopt the static contact line condition (i.e., Eq. (1.2.8)) in isotropic problems [43,118,134]. That is, it is assumed that the force balance condition is aways attained at the moving contact line. This
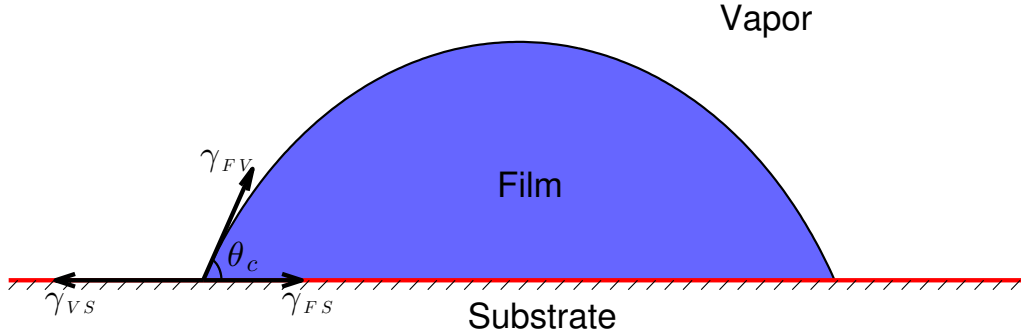
Figure 1.7: Schematic illustration of the equilibrium shape of a solid thin film on a flat substrate.

assumption is reasonable when the thin film approaches its equilibrium state. However, it is not consistent with the experimental and atomistic simulation observations during the entire process [35, 108, 109, 127]. In addition, this condition no longer holds when considering anisotropic film/vapor interface energy densities [41, 133](also shown in Fig. 1.13).

- Dornel *et al.* [41] proposed a numerical treatment for the movement of the contact line in a discrete form. However, neither rigorous derivation nor proof of the energy dissipation is provided for this condition.

- Recently, Klinger *et al.* [77, 78] demonstrated another numerical treatment for the movement of the contact line, considering both the film/vapor surface diffusion and the film/substrate interface diffusion. This is also in a discrete form, and the equations seem to be quite complicated by introducing the film/substrate interface diffusion.

Therefore, it remains challenging to propose a proper boundary condition for the moving contact line in solid-state dewetting.

1.3 Equilibrium shapes

Many researchers have attempted to study the steady state and dynamics of it via optimization theories and numerical simulations. In this section, we review the studies on the steady state (or equilibrium configuration) problem, and the studies on the dynamics are reviewed in next section.

1.3.1 Minimization problems

As stated in section 1.2, the total surface free energy of the dewetting system is minimized at its equilibrium, so determining the equilibrium shape of the thin film can be described as the following energy minimization problem

$$\min_{\Omega} \left(\int_{\Gamma_{FV}} \gamma_{FV} d\Gamma_{FV} + \int_{\Gamma_{FS}} \gamma_{FS} d\Gamma_{FS} + \int_{\Gamma_{VS}} \gamma_{VS} d\Gamma_{VS} \right) \quad \text{s.t.} \quad |\Omega| = \text{const.} \quad (1.3.1)$$

Here, Ω denotes the region occupied by the thin film, $|\Omega|$ is the volume of the film, $\Gamma_{FV}, \Gamma_{FS}, \Gamma_{VS}$ are the film/vapor, film/substrate and vapor/substrate interfaces.

The studies on the above minimization problem are based on a simplified minimization problem,

$$\min_{\Omega} \int_{\Gamma_{FV}} \gamma_{FV} d\Gamma_{FV} \qquad \text{s.t.} \quad |\Omega| = \text{const}, \tag{1.3.2}$$

which assumes that the film is of free standing geometries (i.e., without a substrate).

The above two problems are applicable for both 2D and 3D. When restricting to 2D (refer to Fig. 1.5), the problems become

$$\min_{\Omega} \left(\int_{\Gamma} \gamma_{FV} \, d\Gamma + (x_c^r - x_c^l)(\gamma_{FS} - \gamma_{VS}) \right) \quad \text{s.t.} \quad |\Omega| = \text{const}, \tag{1.3.3}$$

and

$$\min_{\Omega} \int_{\Gamma} \gamma_{FV} d\Gamma \qquad \text{s.t.} \quad |\Omega| = \text{const}, \tag{1.3.4}$$

respectively. Here, $|\Omega|$ is the area of the film.

Problem (1.3.2) was first solved by Wulff in 1901 [135] without proof. Wulff states that in a crystal at equilibrium, the distances of the faces from the center of

the crystal are proportional to their surface energy densities per area. This is known as the Gibbs-Wulff theorem (or Gibbs-Wulff construction, or Wulff construction). Later, various proofs of the theorem are given by many researchers, for example, in [40, 52, 59, 83, 86, 121]. According to the theorem, the equilibrium shape of a free standing particle (Wulff shape) can be geometrically constructed based on the γ-plot. In 1970s, Cahn and Hoffman introduced the ξ-vector to describe the Wulff shape in a mathematical way [26, 53, 60, 61, 98, 132].

Although Wulff did not give a proof of the theorem at that time, this theorem is highly significant in that not only does it provide a way for determining the equilibrium of a free standing particle, but also it is the cornerstone of the studies on equilibrium configuration with a substrate. It also establishes a comparison standard for the numerical simulations.

Based on the Wulff construction, Problem (1.3.1) is solved by Kaischew [72], Bauer [19] and Witterbottom [133], which is known as the Wulff Kaischew theorem or the Winterbottom construction. The Winterbottom construction is a major milestone in the development of studies on solid-state dewetting problems due to its powerfulness in the equilibrium configuration. It also has been used as a comparison standard for the numerical simulations. Numerically, Korzec *et al.* [81] developed a discrete minimization formulation for the 2D problems (1.3.3, 1.3.4). Also, some softwares are developed for the construction of the equilibrium shapes [21, 22, 112, 114, 143].

In the next two subsections, we review some details related to the Wulff and Winterbottom constructions.

1.3.2 Wulff construction

The Wulff construction can be explained visually as follows and a schematic illustration in 2D can be seen in Fig. 1.8. Assuming that γ_{FV} is expressed as a function of the film/vapor interface unit outer normal vector $\mathcal{N}$. First, plot γ_{FV} radially (shown as the heavy blue curve) as a function $\mathcal{N}$. Then, for each point at

the interface, we can draw a plane (shown as the black solid lines) perpendicular to the radius line (shown as the dash lines). The equilibrium shape (Wulff shape) is given by the inner envelope (red solid line) of the planes (black solid lines).
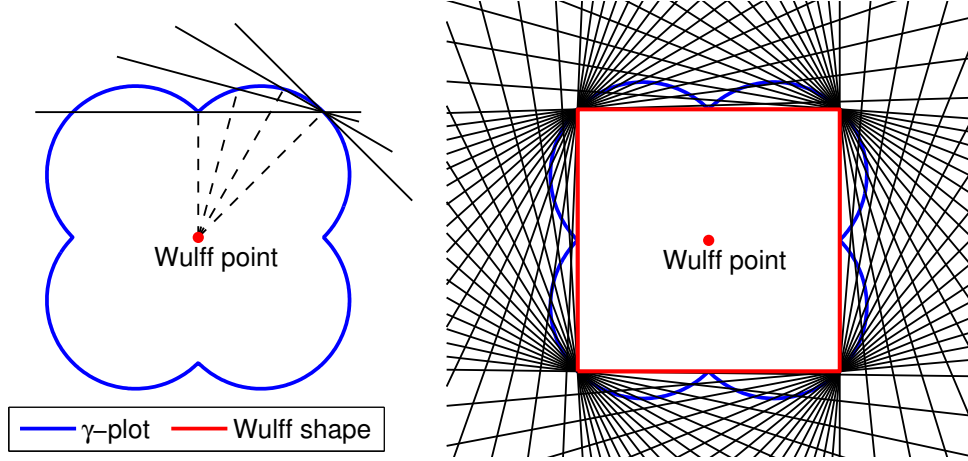
Figure 1.8: The polar plot of γ_{FV} (heavy blue solid curve) with the Wulff construction (red solid line). The black solid lines are perpendicular to the dash lines.

In 2D, assuming a "smooth" $\gamma_{FV} = \gamma(\theta)$, the expression of the Wulff envelope (ξ-vector) can be explicitly written as

$$\begin{cases} x(\theta) = -\gamma(\theta)\sin\theta - \gamma'(\theta)\cos\theta, \\ y(\theta) = \gamma(\theta)\cos\theta - \gamma'(\theta)\sin\theta, \end{cases} \qquad \theta \in [-\pi, \pi]. \qquad (1.3.5)$$

Compared to the one written in [24, 48, 98], we here changed the expression a little so that the θ is exactly the tangent angle of the equilibrium curve or just of the opposite sign.

It can be verified that the tangent vector of the curve given by Eq. (1.3.5) is

$$\big(x'(\theta),\ y'(\theta)\big) = -(\gamma(\theta) + \gamma''(\theta))(\cos\theta,\ \sin\theta).$$

Therefore,

- the corresponding Wulff envelope does not contain flat segments, that is, no faceting;

- if $\tilde{\gamma}(\theta) > 0$, i.e., the film/vapor surface energy density belongs to the isotropic or weakly anisotropic cases, the resulting Wulff envelope is convex and it is exactly the Wulff shape. An example is shown in Fig. 1.9(a, b);

- if $\tilde{\gamma}(\theta)$ does not change sign and reaches 0 at some points, the Wulff envelope, which is the Wulff shape, is convex but with kinks at points where $\tilde{\gamma}(\theta) = 0$;

- when the degree of the anisotropy becomes large enough, i.e., $\tilde{\gamma}(\theta)$ changes sign, unphysical ears appear in the Wulff envelope (as shown in Fig. 1.9(c, d)), whereas the Wulff shape is given by the inner convex shape (inner envelope) removing the ears [92].

For the $\gamma_{FV} = \gamma(\theta)$ with cusps, the Wulff shape may contain flat segments or even be a polygon (fully faceted). Based on the study by Herring [59], it can be summarized and concluded that:

- If $\gamma(\theta)$ satisfies the following conditions, the Wulff shape is a polygon:

  1. $\gamma(\theta)$ contains N cusps with $N \geq 3$, the corresponding θ are denoted as $0 \leq \theta_1 < ... < \theta_N < 2\pi$. For simplicity, we additionally define $\theta_{N+1} = \theta_1 + 2\pi$;

  2. $\theta_{j+1} - \theta_j < \pi, \quad j = 1, 2, ..., N$;

  3. $\gamma(\theta) \geq \gamma_j(\theta)$, for $\theta \in (\theta_j, \theta_{j+1}), \quad j = 1, 2, ..., N$. The $\gamma_j(\theta)$ is defined as

  $$\gamma_j(\theta) = d\cos\left(\theta - \theta_j - \arccos(\frac{\gamma(\theta_j)}{d})\right),$$

  where $d = \dfrac{\sqrt{\gamma^2(\theta_j) + \gamma^2(\theta_{j+1}) - 2\gamma(\theta_j)\gamma(\theta_{j+1})\cos(\theta_{j+1} - \theta_j)}}{\sin(\theta_{j+1} - \theta_j)}$.

  It's easy to see that conditions 1 and 2 are necessary for forming a polygon equilibrium. Assuming that O is the Wulff point, A and B are two adjacent cusps in the γ-plot with $BC \perp OB, AC \perp OA$ (as shown in Fig. 1.10(a)). We can see that the four points O, A, C, B are on a circle with diameter OC. Condition 3 means that $\gamma(\theta)$ is outside the circumcircle of OACB. According to
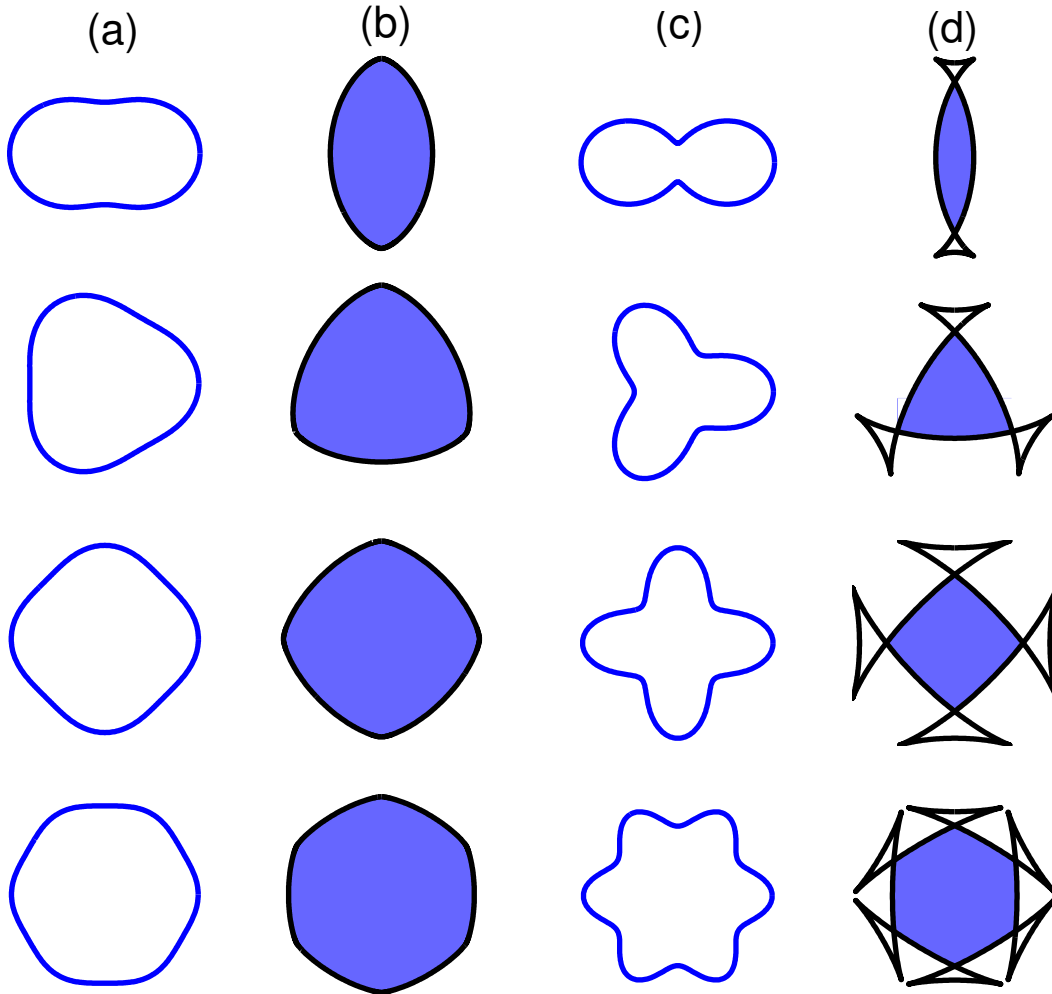
Figure 1.9: Columns (a) and (c) show polar plots of weakly and strongly anisotropic $\gamma(\theta)$, respectively. Columns (b) and (d) show the corresponding Wulff envelope (black solid curve) and Wulff shape (shaded area) for the $\gamma(\theta)$ in Column (a) and (c), respectively. $\gamma(\theta)$ is of form $\gamma(\theta) = 1 + \beta \cos(m\theta)$. The four rows are, in turn, for $m = 2, 3, 4, 6$.

the Wulff construction, we draw a line EF which is perpendicular to the radius line OE (E is an arbitrary point on $\widehat{AB}$) to form the envelope. If $OE > OD$ where D is the intersection of line OE and the circle OACB, line EF will be parallel to CD and outside the polygon OABC Since $OD \perp CD$. Therefore, AC and BC will be segments of the Wulff shape.

- If $\gamma(\theta)$ satisfies the following condition, the Wulff shape contains flat segments: There exists a cusp, denoted as $\gamma(\theta_j)$, such that

$$A \cap B = \left\{\Big(\gamma(\theta_j)\cos(\theta_j),\ \gamma(\theta_j)\sin(\theta_j)\Big)\right\},$$

where

$$A = \{(x,y)|\ x = \gamma(\theta)\cos\theta,\ y = \gamma(\theta)\sin\theta,\ \theta \in [-\pi,\pi]\},$$
$$B = \{(x,y)|\ x = \frac{\gamma(\theta_j)}{2}\Big(\cos\theta + \cos(\theta_j)\Big),$$
$$y = \frac{\gamma(\theta_j)}{2}\Big(\sin\theta + \sin(\theta_j)\Big),\ \theta \in [-\pi,\pi]\}.$$

The geometric explanation is shown in Fig. 1.10(b). Assuming that C is a cusped point. If the $\gamma(\theta)$ is outside the circle with diameter OC, the line EF which is normal to radius vector OE (E is an arbitrary point on γ-plot) will be parallel to CD where D is the intersection of line OE and the circle with diameter OC, then there exists at least a flat segment near the point C in the Wulff shape.
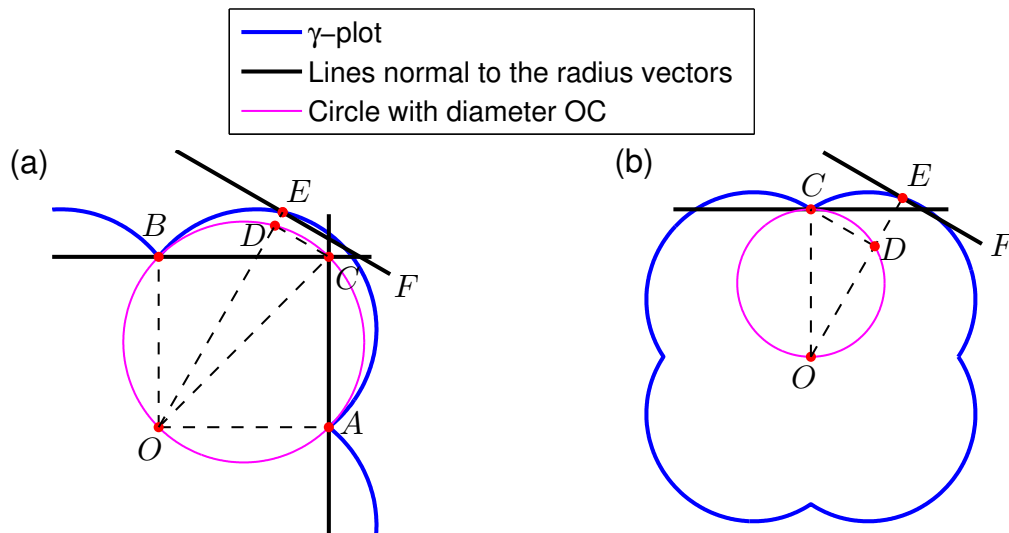
Figure 1.10: Geometric explanations for predicting properties of the Wulff shapes.

For the cusped $\gamma(\theta)$ of form as written in Eq. (1.2.3), Fig. 1.11 shows the polar plots of $\gamma(\theta)$, the regularized $\gamma(\theta)$ and the corresponding Wulff shapes. It can be clearly seen that the Wulff shapes are polygons without regularization.
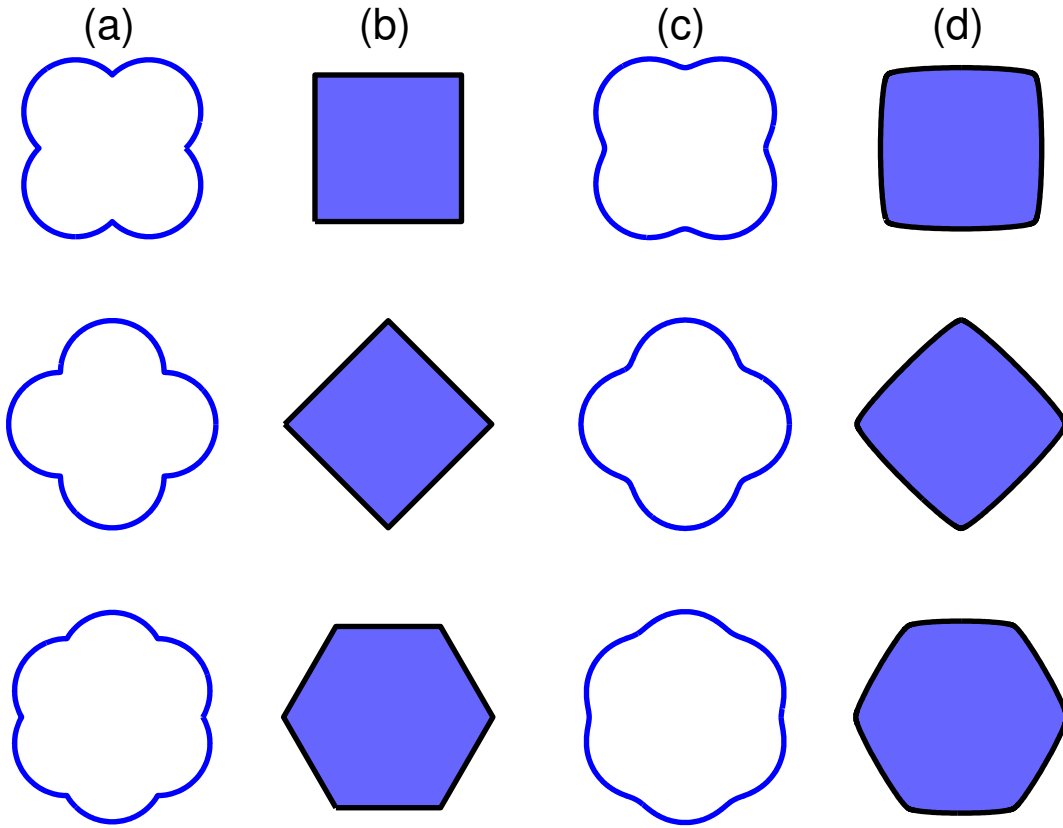
Figure 1.11: Column (a) shows polar plots of cusped $\gamma(\theta)$ of form as in Eq. (1.2.3), and column (c) shows the plots of the regularized form as in Eq. (1.2.4) with $\varepsilon = 0.01$. Columns (b) and (d) show the corresponding Wulff envelope (black solid curve) and Wulff shape (shaded area) for the $\gamma(\theta)$ in Column (a) and (c), respectively. The first row is for $n = 2, \alpha_{1,2} = 0, \pi/2$, the second row is for $n = 2, \alpha_{1,2} = \pi/4, 3\pi/4$, and the last row is for $n = 3, \alpha_{1,2,3} = 0, \pi/3, 2\pi/3$.

1.3.3 Winterbottom construction

The idea of Winterbottom construction [133] is using a new generalized surface energy density $\gamma^*(\theta)$ instead of the original film/vapor surface energy density $\gamma(\theta)$ (taking 2D as example):

$$\gamma^*(\theta) = \begin{cases} \gamma(\theta), & \theta \text{ corresponds to the film/vapor interface,} \\ \gamma_{FS} - \gamma_{VS}, & \text{otherwise.} \end{cases}$$

With this new $\gamma^*(\theta)$, problems (1.3.3, 1.3.1) can be simplified to problems (1.3.4, 1.3.2). A schematic illustration of the Winterbottom construction is shown in Fig. 1.12.
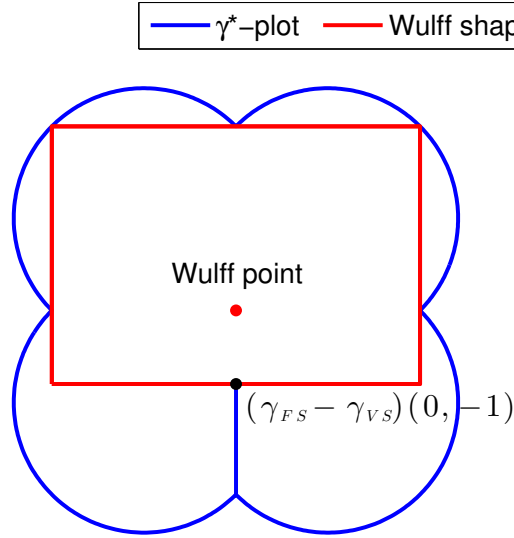
Figure 1.12: A schematic illustration of Winterbottom construction.

Therefore, in 2D, combining the Winterbottom construction and Eq. (1.3.5) , given an arbitrary weakly anisotropic $\gamma(\theta)$, the equilibrium shape (without scaling) for an island on a flat, rigid substrate has the following expression:

$$\begin{cases} x(\theta) = -\gamma(\theta)\sin\theta - \gamma'(\theta)\cos\theta, \\ y(\theta) = \gamma(\theta)\cos\theta - \gamma'(\theta)\sin\theta + \gamma_{FS} - \gamma_{VS}, \end{cases} \quad y \geq 0,$$

Similarly, this expression with strongly anisotropic $\gamma(\theta)$ contains unstable or metastable ears. The shape by clipping off the ears gives the Winterbottom construction.

Based on this construction, Winterbottom classify the possible shape of a particle in contact with a foreign substrate into four types 1.13: (a) non-wetting, (b) partial wetting with $\gamma_{FS} - \gamma_{VS} > 0$, (c) partial wetting with $\gamma_{FS} - \gamma_{VS} < 0$, (d) complete wetting. It is important to note from Fig. 1.13 that the isotropic Young equation (1.2.8) is not true for anisotropic surface energy.

1.4 Models and methods for dynamical evolution

Based on the physical understanding, many models and methods have been proposed to study the dynamics of solid-state dewetting problems. In this section, we will review some of these in detail, together with some interesting numerical results.

1.4.1 Sharp interface models for isotropic case

The sharp interface model is the earliest model for solid-state dewetting problems. In general, it is a type of front tracking method, and it explicitly describes the evolution of the moving film front (FV interface).

In 1986, Srolovitz and Safran [118] first proposed the sharp interface model for solid-state dewetting problems, assuming isotropic surface energy. The model is based on the physical background that the film/vapor interface has normal velocity V_n given by Eq. (1.2.7). Assuming that the film is of cylindrical symmetry and the slope at the contact line is small as illustrated in Fig. 1.14, Eq. (1.2.7) can be further simplified and the corresponding sharp interface model, a partial differential equation for the profile of the film $h(r,\ t)$ with respect to time t and the radius r as follows:

$$\frac{\partial h}{\partial t} = -\frac{B}{r}\frac{\partial}{\partial r}\left\{r\frac{\partial}{\partial r}\left[\frac{1}{r}\frac{\partial}{\partial r}\left(r\frac{\partial h}{\partial r}\right)\right]\right\}, \qquad r > \rho,\ t > 0, \tag{1.4.1}$$
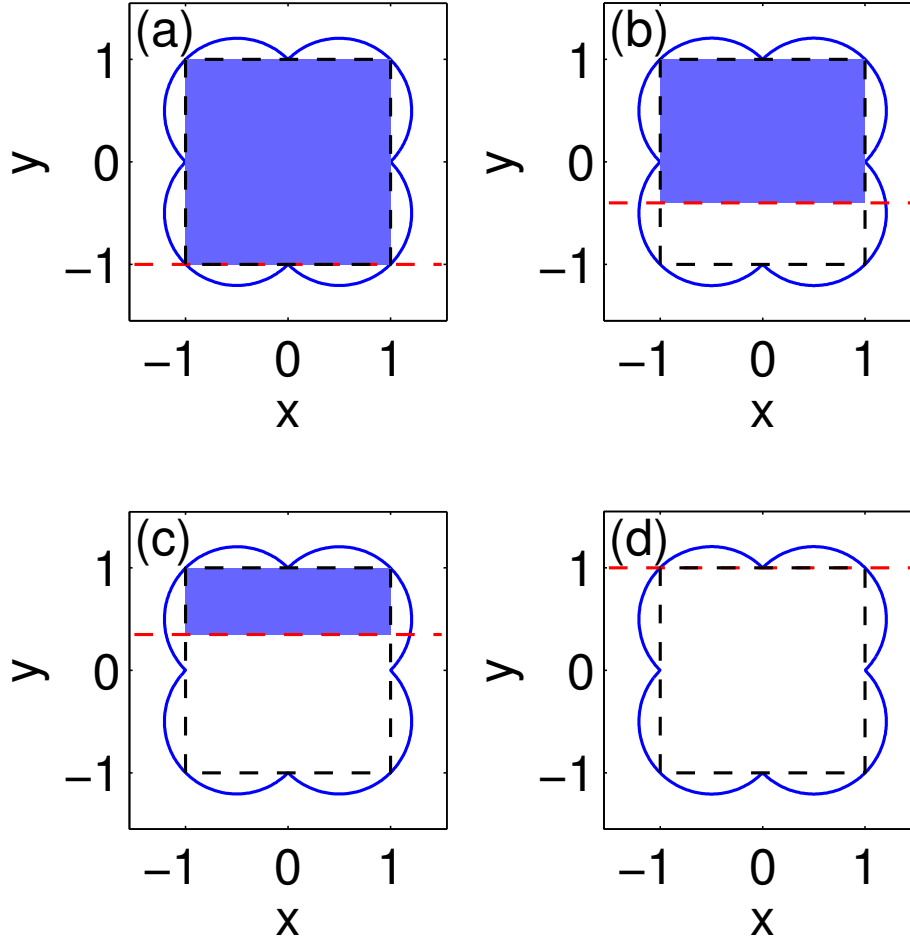
Figure 1.13: γ^*-plot and the corresponding equilibrium shapes. In each figure, the blue solid line is the γ^*-plot, the black dash line is the Wulff construction, the red dash line is the substrate and the shadow part is the equilibrium shape. (d) means that the film wets the whole substrate.

where $B = D_s \nu \gamma_{FV} \Omega_0^2 / (k_B T_e)$ is a material constant (notations are the same as those in section 1.2.2), and ρ is the radius of the hole.

For the governing equation (1.4.1), the authors also proposed the following
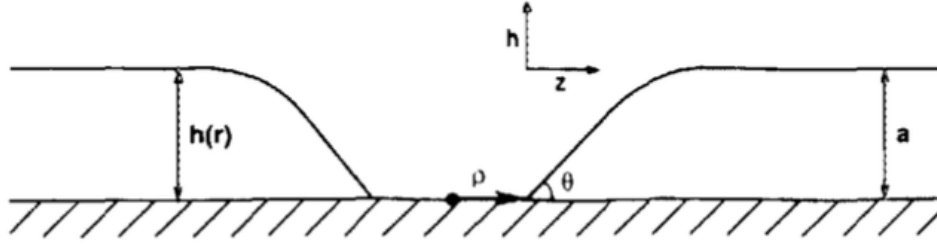
Figure 1.14: A schematic illustration of a cylindrically symmetric thin film on a rigid substrate, with a hole of radius ρ inside. The image is reproduced from Srolovitz & Safran [118].

boundary conditions:

$$h(\rho, t) = -a, \tag{1.4.2a}$$

$$\frac{\partial h}{\partial r}(\rho, t) = \tan \theta_i, \tag{1.4.2b}$$

$$\frac{\partial^3 h}{\partial r^3}(\rho, t) + \frac{1}{\rho}\frac{\partial^2 h}{\partial r^2}(\rho, t) - \frac{1}{\rho^2}\frac{\partial h}{\partial r}(\rho, t) = 0, \tag{1.4.2c}$$

$$h(r, 0) = 0 \quad \text{as} \quad r \to \infty. \tag{1.4.2d}$$

Condition (1.4.2a) ensures that the contact point always moves along the substrate, and condition (1.4.2d) ensures that the film is not disturbed at far field. Eq. (1.4.2b) is the boundary condition for the moving contact line, which is in fact the static contact line condition (1.2.8), and θ_i stands for the isotropic Young angle which satisfies the Young equation. Eq. (1.4.2c) ensures that there is no transport processes of matter at the contact point. This model with moving contact line was further converted to a problem with fixed boundaries to study the hole growth rate during the dewetting process. Their numerical results suggest that the moving distance (retraction distance) of the contact line can be scaled by $t^{1/4}$.

This is the first (mathematical) model and it makes numerical simulations possible for studying the solid-state dewetting. Although it is a simplified model which is only valid for the cylindrically symmetric problems in the small slope limit, it can be easily extended to a 2D or 3D model in Lagrangian representation. It has shed

considerable light on the numerical simulations for solid-state dewetting problems.
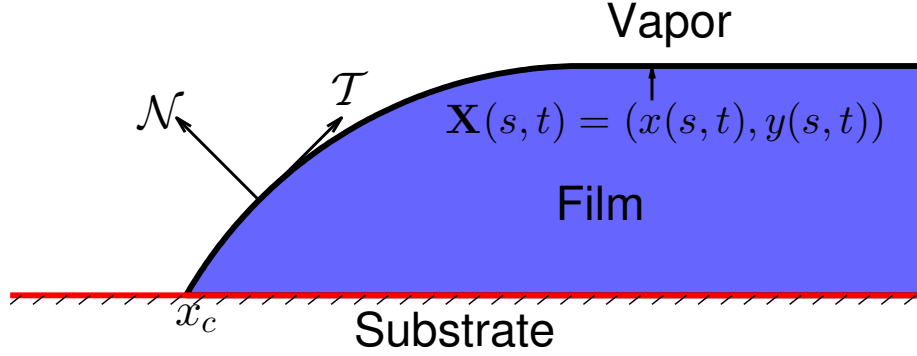
Figure 1.15: A schematic view of a semi-infinite film on a rigid substrate.

Based on the above model, a series of studies on solid-state dewetting has been launched. Wong, *et al.* [134] proposed a dimensionless sharp interface model in Lagrangian representation for solid-state dewetting problems with isotropic surface energy in 2D. The dimensionless model can be written as follows (see a schematic illustration in Fig. 1.15):

$$
\begin{cases}
\dfrac{\partial \mathbf{X}}{\partial t} = V_n \mathcal{N}, \\
V_n = \dfrac{\partial^2 \kappa}{\partial s^2},
\end{cases}
\tag{1.4.3}
$$

where $\mathbf{X}(s,t) = \big(x(s,t), y(s,t)\big)$ represents the film/vapor interface with arc length s and time t, V_n stands for the moving velocity of the interface in the direction of its outward normal, $\mathcal{N}$ is the interface outer unit normal direction, and the interface curvature κ is simplified to $\kappa = \partial_{ss}x \, \partial_s y - \partial_{ss}y \, \partial_s x$. The corresponding boundary conditions are

$$
y(x_c, t) = 0,
\tag{1.4.4a}
$$

$$
\frac{\partial y/\partial s}{\partial x/\partial s}(x_c, t) = \tan \theta_i,
\tag{1.4.4b}
$$

$$
\frac{\partial \kappa}{\partial s}(x_c, t) = 0,
\tag{1.4.4c}
$$

$$
\frac{\partial x}{\partial s} = 1, \; y \to 1 \quad \text{as} \quad s \to \infty,
\tag{1.4.4d}
$$

where x_c represents the moving contact point where the film, substrate and vapor meet and θ_i is the isotropic Young angle. The four conditions are similar to that for Eq. (1.4.1): Conditions (1.4.4a, 1.4.4d) describe the profile of the film at the contact line and far from the edge, respectively. Condition (1.4.4b) is equivalent to the isotropic Young equation, and condition (1.4.4c) ensures that the total mass of the thin film is conserved, implying that there is no mass flux at the contact point.

Wong, *et al.* [134] also designed a "marker particle" numerical scheme for the above model to study the dynamics of solid-state dewetting in 2D. The numerical scheme can be summarized as two steps: i) update the evenly distributed marker points on the interface, as well as the contact point(s), according to the governing equation and boundary conditions; ii) evenly redistribute the new marker points. Their numerical experiments indicated that: i) the retracting film edge forms a thickened ridge followed by a valley; ii)with increasing time, the ridge grows in height and the valley sinks, eventually touching the substrate and leading to pinch-off events; iii) the remaining semi-infinite film restarts this retraction and pinch-off cycle; iv) the retraction distance $x_0(t) \sim t^{2/5}$ at late time, which is consistent with the small-slope late-time analytic solution given by their asymptotic analysis.

After that, the model and scheme were extended to three dimensions in Cartesian coordinates to study the evolution of a perturbed cylindrical film with the cross-sectional shape of a part-circle (as illustrated in Fig. 1.16) by Du, *et al.* [43]. The dimensionless model reads

$$
\begin{cases}
\dfrac{\partial \mathbf{X}}{\partial t} = V_n \mathbf{n}, \\
V_n = \nabla_s^2 H,
\end{cases}
\tag{1.4.5}
$$

where $X(t) = \big(x(t), y(t), z(t)\big)$ stands for the film/vapor surface, $\mathbf{n}$ is the unit outer normal vector. In Cartesian coordinates, the surface Laplacian and mean curvature are

$$
\nabla_s^2 = \frac{1}{a}\Big[a_{22}\frac{\partial^2}{\partial x^2} - 2a_{12}\frac{\partial}{\partial x}\frac{\partial}{\partial y} + a_{11}\frac{\partial^2}{\partial y^2} + H a^{1/2}\Big(h_x\frac{\partial}{\partial x} + h_y\frac{\partial}{\partial y}\Big)\Big],
\tag{1.4.6}
$$
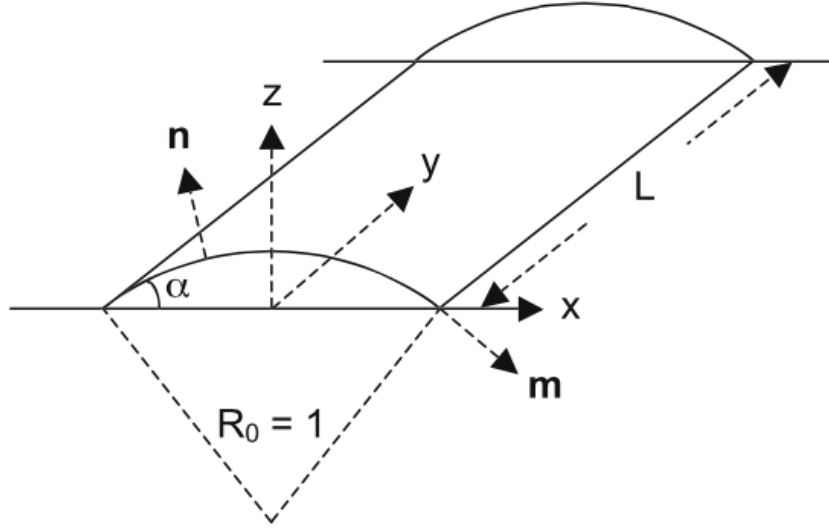
Figure 1.16: A schematic view of a cylindrical film on a rigid substrate. The image is reproduced from Du *et al.* [43].

$$H = -\frac{a_{22}h_{xx} - 2a_{12}h_{xy} + a_{11}h_{yy}}{a^{3/2}}, \tag{1.4.7}$$

where

$$a = 1 + h_x^2 + h_y^2, \quad a_{11} = 1 + h_x^2, \quad a_{22} = 1 + h_y^2, \quad a_{12} = h_x h_y. \tag{1.4.8}$$

The corresponding boundary conditions, which are similar to Eqs. (1.4.2, 1.4.4), at the contact line $x = x_c(y)$ are

$$z = 0, \tag{1.4.9a}$$

$$\mathbf{n} \cdot (0, 0, 1) = \cos\alpha, \tag{1.4.9b}$$

$$\mathbf{m} \cdot \nabla_s H = 0. \tag{1.4.9c}$$

Since the governing equation (1.4.5) was calculated for $y \in [0, L]$, it was imposed a symmetry condition

$$\frac{\partial F}{\partial y} = 0$$

at $y = 0$ and $y = L$, with F any quantity that cross the symmetry boundaries. Their numerical results also show a thickened ridge followed by a valley and pinch-off events.

As revealed by the numerical results, the sharp interface model is able to capture and predict some experimental results. Also, it is easy to solve by the "marker particle" scheme in two dimensions. However, its extension to three dimensions is awkward as obtaining the quantities in the governing equation are tedious and complicated (shown in Eqs. (1.4.6 - 1.4.8)). Another shortcoming is that the constraint for time step in the "marker particle" scheme is too strong due to its explicitness.

1.4.2 Phase field models

In order to avoid the shortcomings of explicitly tracking the interface, Jiang, *et al.* [66] first proposed a phase field model for the solid-state dewetting problems with isotropic surface energy. They considered the total energy functional of the dewetting system (as illustrated in Fig. 1.17) using the phase field function $\phi(\mathbf{x}$, where the sets $\{\mathbf{x} : \phi(\mathbf{x}) = 0\}, \{\mathbf{x} : \phi(\mathbf{x}) > 0\}, \{\mathbf{x} : \phi(\mathbf{x}) < 0\}$ represent the film/vapor interface, film phase and vapor phase, respectively. By minimizing the total energy, they obtained the following governing equations of the phase field model

$$\begin{cases} \dfrac{\partial \phi}{\partial t} &= \nabla \cdot (M\nabla\mu), \\ \mu &= \phi^3 - \phi - \varepsilon^2 \Delta\phi, \end{cases} \tag{1.4.10}$$

where the mobility M is defined as: $M = 1 - \phi^2$, μ is the chemical potential of the system, and ε is a small parameter that represents the interface width. To close the model, the governing equations are subject to the following boundary conditions:

- on the substrate:

$$\begin{cases} \varepsilon\dfrac{\partial \phi}{\partial n} + \dfrac{\sqrt{2}}{2}(\phi^2 - 1)\cos\theta_i = 0, \\ \dfrac{\partial \mu}{\partial n} = 0, \end{cases} \tag{1.4.11}$$

where θ_i is the isotropic Young angle.
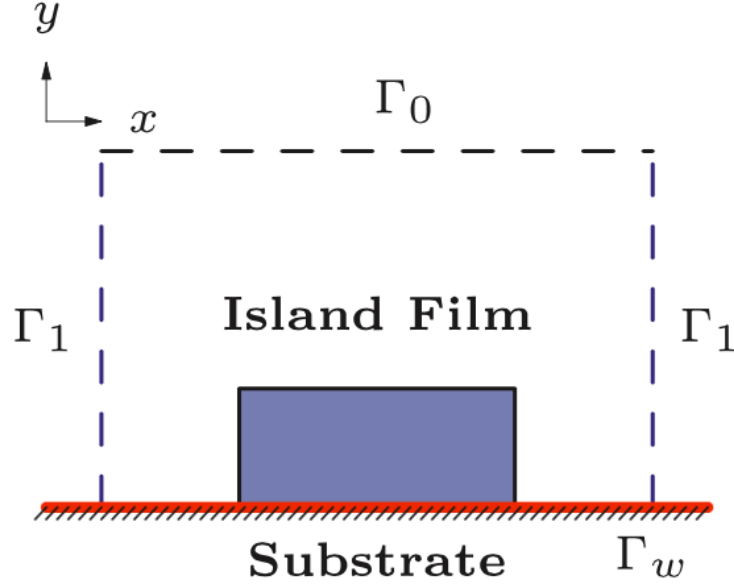
Figure 1.17: A schematic illustration of dewetting system. The image is reproduced from Jiang *et al.* [66].

- on the other boundaries:

$$\frac{\partial \phi}{\partial n} = 0, \qquad \frac{\partial \mu}{\partial n} = 0. \tag{1.4.12}$$

For solving the equations, they designed a stabilized semi-implicit finite difference scheme based on discrete cosine transforms.

Their numerical simulations in 2D showed that: i) the retraction distance of the contact point of a semi-infinite film obeys a power law $x_0(t) \sim t^{2/5}$, which coincides with the result of Wong, *et al.* [134]; ii) a thin film with a hole inside can lead to hole growth or wetting with different θ_i; iii) pinch-off event occurs when the film is long enough. In addition, the simulations for rectangular and square thin films in 3D demonstrate some interesting morphological evolutions, among which some are similar as that in 2D: a) for a rectangular film, the edges retract followed by valleys, pinch-off occurs when the valley touches the substrate; b) for a small square thin film, it agglomerates to form an isolated island and the edges retract faster in the x, y-direction than that in the diagonal direction; c) for a large square thin film, a hole forms in the center.

From the numerical results presented by Jiang *et al.*, we can see that the phase field model naturally captures the topological evolution during solid-state dewetting, and it can be easily extended to three dimensions. Moreover, the numerical scheme is semi- implicit, which leads to an efficient algorithm. However, the small parameter ε in the model is unphysical, and the computational cost in two dimensions is much higher than that of the sharp interface model. This is because the phase field model is based on a two dimensional phase field function. In order to represent the function, the number of nodes that need to be used is nearly square of that in the sharp interface model.

The above phase field model is only valid for the isotropic case, the extension to weakly anisotropic case has recently been proposed by Dziwnik *et. al.* in [47]. The authors have also derived the corresponding sharp interface limit via matched asymptotic analysis involving multiple inner layers. The resulting limit is consistent with the pure sharp interface model. However, the extension to the strongly anisotropic case has not been mentioned yet.

1.4.3 Other models

As the importance of crystalline anisotropy has been noted in the recent experiments [136–139], some other models have been proposed to efficiently simulate the weakly anisotropic case and the cusped case.

In 2006, Dornel *et. al.* [41] developed a method, calculating and using the discrete surface chemical potential, to deal with the large curvature regime for anisotropic (including isotropic) surface energy densities. The authors studied the influence of two main parameters in this problem: the film aspect ratio (half-length/height) and the adhesion energy between the film and substrate (related to the isotropic Young angle), and quantified the retraction rate, breaking time and the number of islands formed. Their numerical results suggests that the fragmentation of a thin film with a given isotropic Young angle can be predicted (See Fig. 1.18(left) for the isotropic surface energy, and Fig. 1.18(right) for a anisotropic surface energy). As can be seen

in Fig. 1.18(right), the fragmentation of thin films with a fixed θ_i requires a larger aspect ratio in the anisotropic case than that in the isotropic case, which implies that this kind of anisotropy delays the pinch-off event.
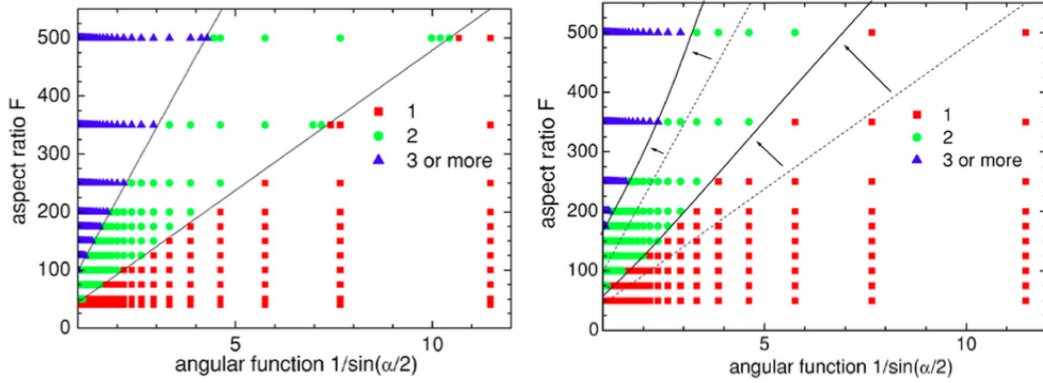
Figure 1.18: Number of agglomerates in the (left) isotropic and (right) anisotropic cases for different isotropic Young angles (θ_i in our notation, α in the figure) and different aspect ratios. Left: The lower straight line is $F = 48.3/\sin(\alpha/2) - 4.33$, the upper line is $F = 123.4/\sin(\alpha/2) - 24.6$. Right: The anisotropic surface energy density is chosen as $\gamma(\theta) = 1 - 0.01332 \cos(8\theta)$. The dash lines are from the left figure. This image is reproduced from Dornel *et al.* [41].

Later, the kinetic Monte Carlo approach has been used to study the dewetting of ultra-thin solid films by Pierre-Louis *et al.* [44, 99, 100] since 2009. They also found a power law of the motion of the dewetting front and the instability is suppressed along faceted orientations.

More recently, Zucker *et al.* [75, 144] developed a crystalline formulation method, using the crystalline formulation in which the interfaces are assumed to be completely faceted and restricted on the facets appeared in the Wulff construction, to study the morphological evolution during edge retraction. Based on the crystalline method developed by Roosen *et al.* [25, 28, 111] dealt with free standing structures in 2D, they introduced a film/substrate interface according to the Winterbottom construction and added some restrictions, including mass conservation and no formulation of new facets. Their simulations also predicts that the retraction distance

can be scaled by $t^{2/5}$. However, unlike in the isotropic case, valleys do not form ahead of the retracting ridge.

The work by Dornel *et al.* is highly commendable for providing the valuable information (the quantities), which provides guidelines for later studies on solid-state dewetting problems. The simulation using the crystalline formulation method provide a valuable tool for forming specific complex patterns with templated solid-state dewetting. The power law obtained by all these simulations is quantitatively consistent with the experimental results. However, they all did not provide any explicit governing equations or boundary conditions for the problem, neither did they consider strongly anisotropic surface energy densities.

1.5 Purpose and scope of this thesis

As shown in the previous section, several models have been developed to study the dynamics of solid-state dewetting problems, and the numerical results are able to capture the topological evolution, quantitatively or qualitatively consistent with the experiments. However, there are still some limitations:

- There is no rigorous mathematical derivation of the sharp interface models. Moreover, the studies on the sharp interface model are based upon the assumption that all interface energies were isotropic. Anisotropy of the film/vapor interface was not included in the modeling.

- The other methods, such as the discrete scheme proposed by Dornel *et al.*, the crystalline method and the kinetic Monte Carlo method, did not provide explicit governing equations or boundary conditions.

- There is no efficient numerical method for the sharp interface model. The "marker particle" method developed by Wong *et al.* is an explicit finite difference method, so the time step has to be very small and the computation cost is high.

- Even though the phase field model has been employed to study the solid-state dewetting problem, it can only provide qualitative description from the present point of view. This is because its sharp interface limits is unclear. On the other hand, the small parameter introduced in the phase field model increases the burden on the computational cost.

- Most of these models assume that the rigid substrate is flat, however, it might be curved or rough in the experiments, such as the migration of a small metal particle from the convex to concave sites on a rigid curved substrate [1, 74], the templated solid-state dewetting [18,55,56,128] (also shown in Fig. 1.2) and the burrowing of rigid particles into a deformable substrate [142].

Hence, the purposes of this study were to:

- propose sharp interface models for solid-state dewetting problems in a rigorous mathematical framework, i.e., based on an energy variational approach;

- propose an efficient numerical method for the sharp interface models to simulate the dewetting problems;

- take all types of anisotropic surface energies into consideration, including the weakly and strongly anisotropic cases, and the case that $\gamma(\theta)$ has cusp points.

- extend the sharp interface model to curved substrates.

The anisotropy included model proposed in this study should open up new avenues for studies on anisotropic solid-state dewetting with explicit governing equations. The numerical results presented in the thesis may contribute to a better understanding of the anisotropy effect in solid-state dewetting.

In this study, we derived the sharp interface models for solid-state dewetting problems with both flat and curved substrates only in 2D. We believe that our approach and numerical algorithm can be generalized to 3D cases. But this topic is beyond the scope of this thesis, and this is our future work.

The thesis is organized as follows. Chapters 2 will focus on the sharp interface model for the weakly anisotropic solid-state dewetting with a flat substrate. Chapter 3 and 4 are extensions to the strongly anisotropic case and curved substrate case, respectively. At last, we will state our conclusion and future work in Chapter 5. The main works in Chapters 2, 3, 4 are based on the papers [8, 9, 67, 130, 131].

Chapter 2

A Sharp Interface Model for Weakly Anisotropic Case

Based on an energy variational approach, we first propose a sharp interface model for simulating solid-state dewetting of thin films with (weakly) anisotropic surface energies on a flat rigid substrate. The morphology evolution of thin films is governed by surface diffusion and contact line migration. For the contact line migration, we introduce a relaxation kinetics with a finite contact line mobility by energy gradient flow method. Then, we show the mass conservation and energy dissipation properties of the proposed mathematical model. Next, we introduce two methods, which are the revised "marker particle" method (MPM) with cubic spline interpolation and the parametric finite element method (PFEM), for the proposed model. At last, following validation of the mathematical and numerical approaches, we simulate the morphology evolution of small and large islands, the retraction and pinch-off of semi-infinite films, and the evolution of films with holes.

2.1   The model

Consider the case of a thin solid island on a flat, rigid substrate in two dimensions, as illustrated in Fig. 2.1. The total free energy of the system for solid-state dewetting

problems with weakly anisotropic surface energies can be written as:

$$W = \int_{\Gamma} \gamma(\theta) \, d\Gamma + \left(\gamma_{FS} - \gamma_{VS}\right)(x_c^r - x_c^l), \tag{2.1.1}$$

where $\Gamma := \Gamma(t)$ represents the moving film front (film/vapor interface) which intersects with the vapor and substrate phases at the two contact points (x_c^r and x_c^l), and γ_{FV}, γ_{FS} and γ_{VS} are, respectively, the surface energy densities of the film/vapor, film/substrate and vapor/substrate interfaces. Here, we describe the film/vapor interface energy (density) γ_{FV} as a function only of the interface outer normal (tangent) angle, i.e. $\gamma_{FV} = \gamma(\theta)$.
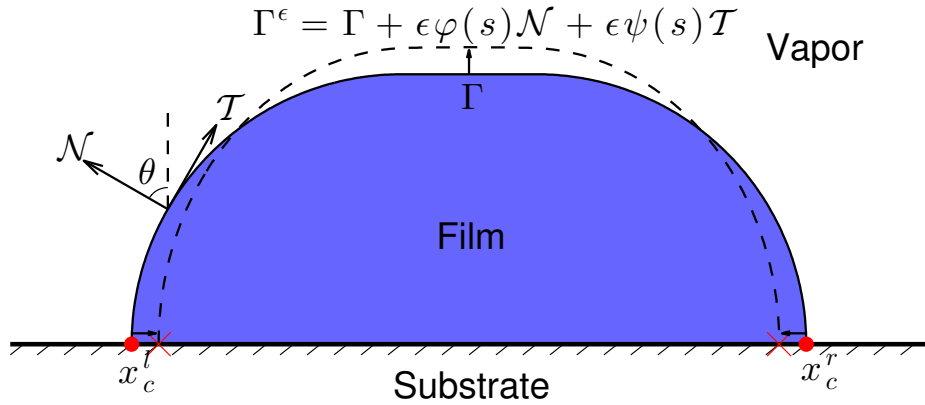
Figure 2.1: A schematic illustration of a discontinuous solid thin film on a flat, rigid substrate in 2D and an infinitesimal perturbation of the curve Γ along its normal and tangent direction. As the film morphology evolves, the contact points x_c^l and x_c^r move.

Denote $\Gamma(t) := \mathbf{X}(s, t) = (x(s, t), y(s, t)), s \in [0, L(t)]$ with arc length s and time t, and $L(t)$ represents the length of the moving curve at the time t. Then the outer unit normal vector $\mathcal{N}$ and unit tangent vector $\mathcal{T}$ can be expressed as: $\mathcal{N} = (-y_s, x_s)$ and $\mathcal{T} = (x_s, y_s)$. Assume that x_c^l and x_c^r are respectively x-axis coordinates of the left and right contact points at the time t, i.e. $x(0, t) = x_c^l(t)$ and $x(L, t) = x_c^r(t)$.

Consider an infinitesimal deformation of the curve $\Gamma(t)$ along its normal and tangent directions, as illustrated in Fig. 2.1:

$$\Gamma^{\epsilon}(t) \;=\; \Gamma(t) + \epsilon\varphi(s)\mathcal{N} + \epsilon\psi(s)\mathcal{T}, \tag{2.1.2}$$

where ϵ is an infinitesimal number, and $\varphi(s), \psi(s)$ are arbitrary smooth functions with respect to arc length s. Then the two components of the new curve $\Gamma^{\epsilon}(t)$ can be expressed as follows:

$$
\begin{aligned}
\Gamma^{\epsilon}(t) \;&=\; (x^{\epsilon}(s,t), y^{\epsilon}(s,t)) \\
&=\; (x(s,t) + \epsilon u(s,t), y(s,t) + \epsilon v(s,t)),
\end{aligned} \tag{2.1.3}
$$

where the two component increments along the $x-$aixs and $y-$axis are defined as

$$
\begin{cases}
u(s,t) = x_s(s,t)\psi(s) - y_s(s,t)\varphi(s), \\
v(s,t) = x_s(s,t)\varphi(s) + y_s(s,t)\psi(s).
\end{cases} \tag{2.1.4}
$$

Equivalently, the function $\varphi(s)$ and $\psi(s)$ can be expressed by

$$
\begin{cases}
\varphi(s) = x_s(s,t)v(s,t) - y_s(s,t)u(s,t), \\
\psi(s) = x_s(s,t)u(s,t) + y_s(s,t)v(s,t).
\end{cases} \tag{2.1.5}
$$

As illustrated in Fig. 2.1 that the contact points move along the substrate, so the increments along the $y-$axis at the two contact points must be zero, i.e.,

$$v(0,t) = v(L,t) = 0. \tag{2.1.6}$$

We can calculate the total free energy W^{ϵ} of the new curve $\Gamma^{\epsilon}(t)$ as follows:

$$
\begin{aligned}
W^{\epsilon} \;&=\; \int_{\Gamma^{\epsilon}} \gamma(\theta^{\epsilon})\, d\Gamma^{\epsilon} + \big(\gamma_{FS} - \gamma_{VS}\big)\Big[\big(x_c^r + \epsilon u(L,t)\big) - \big(x_c^l + \epsilon u(0,t)\big)\Big] \\
&=\; \int_0^L \gamma\Big(\arctan2\big(\frac{y_s + \epsilon v_s}{x_s + \epsilon u_s}\big)\Big)\sqrt{(x_s + \epsilon u_s)^2 + (y_s + \epsilon v_s)^2}\, ds \\
&\quad + \big(\gamma_{FS} - \gamma_{VS}\big)\Big[\big(x_c^r + \epsilon u(L,t)\big) - \big(x_c^l + \epsilon u(0,t)\big)\Big].
\end{aligned} \tag{2.1.7}
$$

where

$$\theta^\epsilon := \arctan2\Big(\frac{y_s + \epsilon v_s}{x_s + \epsilon u_s}\Big) = \begin{cases} \arctan\dfrac{y_s + \epsilon v_s}{x_s + \epsilon u_s}, & x_s^\epsilon > 0, \\[2mm] \arctan\dfrac{y_s + \epsilon v_s}{x_s + \epsilon u_s} + \pi, & x_s^\epsilon < 0, y_s^\epsilon \geq 0, \\[2mm] \arctan\dfrac{y_s + \epsilon v_s}{x_s + \epsilon u_s} - \pi, & x_s^\epsilon < 0, y_s^\epsilon < 0, \\[2mm] \dfrac{\pi}{2}, & x_s^\epsilon = 0, y_s^\epsilon > 0, \\[2mm] -\dfrac{\pi}{2}, & x_s^\epsilon = 0, y_s^\epsilon < 0, \\[2mm] 0, & x_s^\epsilon = 0, y_s^\epsilon = 0. \end{cases} \qquad (2.1.8)$$

Then we can calculate the change rate of total free energy about the curve $\Gamma(t)$ because of this infinitesimal deformation with respect to ϵ at the time t:

$$\begin{aligned} \frac{dW^\epsilon}{d\epsilon}\Big|_{\epsilon=0} &= \lim_{\epsilon\to 0} \frac{W^\epsilon - W}{\epsilon} \\ &= \lim_{\epsilon\to 0} \frac{1}{\epsilon}\Big\{ \int_0^L \gamma\Big(\arctan2\big(\frac{y_s + \epsilon v_s}{x_s + \epsilon u_s}\big)\Big)\sqrt{(x_s + \epsilon u_s)^2 + (y_s + \epsilon v_s)^2}\, ds \\ &\quad - \int_0^L \gamma\Big(\arctan2\big(\frac{y_s}{x_s}\big)\Big)\, ds \Big\} + \big(\gamma_{FS} - \gamma_{VS}\big)\Big[u(L,t) - u(0,t)\Big] \\ &= \int_0^L \Big\{ \lim_{\epsilon\to 0}\frac{1}{\epsilon}\Big[\gamma\Big(\arctan2\big(\frac{y_s + \epsilon v_s}{x_s + \epsilon u_s}\big)\Big)\sqrt{(x_s + \epsilon u_s)^2 + (y_s + \epsilon v_s)^2} \\ &\quad - \gamma\Big(\arctan2\big(\frac{y_s}{x_s}\big)\Big)\Big]\Big\}\, ds + \big(\gamma_{FS} - \gamma_{VS}\big)\Big[u(L,t) - u(0,t)\Big] \\ &= \int_0^L \Big[\gamma'(\theta)(\varphi_s - \kappa\psi) + \gamma(\theta)\kappa\varphi + \gamma(\theta)\psi_s\Big]\, ds \\ &\quad + \big(\gamma_{FS} - \gamma_{VS}\big)\Big[u(L,t) - u(0,t)\Big] \\ &= \Big(\gamma'(\theta)\varphi\Big)\Big|_{s=0}^{s=L} + \int_0^L \gamma''(\theta)\kappa\varphi\, ds - \int_0^L \gamma'(\theta)\kappa\psi\, ds + \int_0^L \gamma(\theta)\kappa\varphi\, ds \\ &\quad + \Big(\gamma(\theta)\psi\Big)\Big|_{s=0}^{s=L} + \int_0^L \gamma'(\theta)\kappa\psi\, ds + \big(\gamma_{FS} - \gamma_{VS}\big)\Big[u(L,t) - u(0,t)\Big] \\ &= \int_0^L \Big(\gamma''(\theta) + \gamma(\theta)\Big)\kappa\varphi\, ds \\ &\quad + \Big[\big(\gamma'(\theta)\varphi\big)\Big|_{s=L} + \big(\gamma(\theta)\psi\big)\Big|_{s=L} + \big(\gamma_{FS} - \gamma_{VS}\big)u(L,t)\Big] \\ &\quad - \Big[\big(\gamma'(\theta)\varphi\big)\Big|_{s=0} + \big(\gamma(\theta)\psi\big)\Big|_{s=0} + \big(\gamma_{FS} - \gamma_{VS}\big)u(0,t)\Big], \qquad (2.1.9) \end{aligned}$$

where the curvature of the curve is defined as $\kappa = -y_{ss}x_s + x_{ss}y_s = -\theta_s$. Assume that θ_d^l and θ_d^r are the (dynamical) contact angle at the left and right contact points,

respectively. Then we have the following expressions:

$$x_s(0,t) = \cos\theta_d^l, \qquad y_s(0,t) = \sin\theta_d^l, \tag{2.1.10}$$

$$x_s(L,t) = \cos\theta_d^r, \qquad y_s(L,t) = \sin\theta_d^r. \tag{2.1.11}$$

By making use of Eq. (2.1.5) and Eq. (2.1.6), we have:

$$\begin{cases} \psi(0) = u(0,t)\cos\theta_d^l, & \varphi(0) = -u(0,t)\sin\theta_d^l, \\ \psi(L) = u(L,t)\cos\theta_d^r, & \varphi(L) = -u(L,t)\sin\theta_d^r. \end{cases} \tag{2.1.12}$$

Therefore, we can rewrite the expression for the left and right contact points x_c^l, x_c^r (i.e. $s=0, s=L$) in Eq. (2.1.9) as follows:

$$\left(\gamma'(\theta)\varphi\right)\Big|_{s=0} + \left(\gamma(\theta)\psi\right)\Big|_{s=0} + \left(\gamma_{FS} - \gamma_{VS}\right)u(0,t)$$

$$= \left[\gamma(\theta_d^l)\cos\theta_d^l - \gamma'(\theta_d^l)\sin\theta_d^l + \left(\gamma_{FS} - \gamma_{VS}\right)\right]u(0,t). \tag{2.1.13}$$

$$\left(\gamma'(\theta)\varphi\right)\Big|_{s=L} + \left(\gamma(\theta)\psi\right)\Big|_{s=L} + \left(\gamma_{FS} - \gamma_{VS}\right)u(L,t)$$

$$= \left[\gamma(\theta_d^r)\cos\theta_d^r - \gamma'(\theta_d^r)\sin\theta_d^r + \left(\gamma_{FS} - \gamma_{VS}\right)\right]u(L,t). \tag{2.1.14}$$

Combining Eqs. (2.1.9) (2.1.13) and (2.1.14), we can define the first variation of the total free energy W with respect to the moving curve Γ and the right contact point x_c^r and left contact point x_c^l as follows :

$$\frac{\delta W}{\delta\Gamma} = \left(\gamma(\theta) + \gamma''(\theta)\right)\kappa, \tag{2.1.15}$$

$$\frac{\delta W}{\delta x_c^l} = -\left[\gamma(\theta_d^l)\cos\theta_d^l - \gamma'(\theta_d^l)\sin\theta_d^l + \left(\gamma_{FS} - \gamma_{VS}\right)\right], \tag{2.1.16}$$

$$\frac{\delta W}{\delta x_c^r} = \gamma(\theta_d^r)\cos\theta_d^r - \gamma'(\theta_d^r)\sin\theta_d^r + \left(\gamma_{FS} - \gamma_{VS}\right). \tag{2.1.17}$$

According to Eq. (1.2.6), the chemical potential of the system can be defined as

$$\mu = \Omega_0\frac{\delta W}{\delta\Gamma} = \Omega_0\left(\gamma(\theta) + \gamma''(\theta)\right)\kappa, \tag{2.1.18}$$

which is the anisotropic Gibbs-Thomson relation [119]. Note that the term $\tilde{\gamma}(\theta) = \gamma(\theta) + \gamma''(\theta)$ in Eq. (2.1.18), called as the surface stiffness, plays an important role

in capillarity-driven morphology evolution. As pointed out in the references [48, 92], spontaneous faceting can occur when $\tilde{\gamma}(\theta)$ becomes negative. According to Eq. (1.2.7), the normal velocity V_n of the moving interface is defined as:

$$V_n = \frac{D_s \nu \Omega_0^2}{k_B T_e} \frac{\partial^2}{\partial s^2} \left[\left(\gamma(\theta) + \gamma''(\theta) \right) \kappa \right]. \tag{2.1.19}$$

Analogous to the isotropic case, the above equation can be called as the anisotropic surface diffusion, which governs the motions of "the particles" on the interface away from the contact points.

However, we still need the boundary conditions which govern the movements of the contact points. These can be obtained by calculating the first variation of the total energy functional with respect to the contact points, i.e. Eqs. (2.1.16) and (2.1.17). We assume that the moving process of the contact points can be taken as the energy gradient flow, which gives the time-dependent Ginzburg-Landau kinetic equations to minimization process of the total free energy:

$$\frac{dx_c^l(t)}{dt} = -\eta \frac{\delta W}{\delta x_c^l}, \quad \text{at} \quad x = x_c^l, \tag{2.1.20}$$

$$\frac{dx_c^r(t)}{dt} = -\eta \frac{\delta W}{\delta x_c^r}, \quad \text{at} \quad x = x_c^r, \tag{2.1.21}$$

where $\delta W/\delta x_c^r$ and $\delta W/\delta x_c^l$ are given by Eqs. (2.1.16) and (2.1.17), respectively, and the constant η, $0 < \eta < \infty$, represents contact line mobility, which is a reciprocal of a constant friction coefficient. If $\eta \to \infty$, then $\frac{\delta W}{\delta x_c^l}$ and $\frac{\delta W}{\delta x_c^r}$ go to zero because the moving velocity of contact points must be finite. In this case, Eqs. (2.1.20) and (2.1.21) collapse to the equation as follows [87]:

$$\gamma(\theta) \cos \theta - \gamma'(\theta) \sin \theta + \gamma_{FS} - \gamma_{VS} = 0. \tag{2.1.22}$$

It can be seen that if the film/vapor interfacial energy is isotropic (i.e. γ is independent of θ), then Eq. (2.1.22) reduces to the well-known isotropic Young equation (1.2.8). If the interfacial energy is anisotropic (i.e. $\gamma = \gamma(\theta)$), a bending term $\gamma'(\theta)$ appears which acts perpendicular to the film surface. We refer to Eq. (2.1.22) as the anisotropic Young equation, which is also the static boundary

condition for the contact line. If we adopt Eq. (2.1.22) as the boundary condition for the moving contact line, similar to the conditions (1.4.2b) and (1.4.4b) in the isotropic case we reviewed in Chapter 1, this amounts to assume that the contact angle must keep fixed as a value θ_a which satisfies Eq. (2.1.22) during the evolution. However, this approach of fixing the contact angle becomes subtle and unpractical in the anisotropic case, because when the surface energy anisotropy increases, Eq. (2.1.22) may have multiple solutions, which will be discussed in next chapter. Therefore, we think that it is more reasonable that we adopt Eqs. (2.1.16) and (2.1.17) as the boundary conditions for the moving contact line.

In addition, the introduction of relaxation kinetics for the contact point position, Eqs. (2.1.20) and (2.1.21), has its origin in the complex atomic structure of the contact point, where typically atoms are not all exactly on perfect crystal sites. This variation in the atomic structure in the vicinity of the contact point can be associated with elastic deformation, slipping between film and substrate, dislocations at the film/substrate interface, reconstruction of the interfaces, and other forms of non-elastic deformation. The local distortion of the atomic lattice at the contact point must be propagated along with the moving contact point and because its structure is distinct from that of the remaining film or film/substrate interface it has its own distinct kinetics. Hence, we can think of this contact point as having a unique mobility $M_c = \eta$. A similar concept was introduced to describe the effect of grain boundary triple junctions (where three grain boundaries meet) on the motion of grain boundaries [36,127] and contact lines in liquid film wetting of substrates [39, 103, 105, 108].

Assume that the length and surface energies are scaled by the two constants R_0 and γ_0, respectively. By choosing the time scale to be $R_0^4/(B\gamma_0)$, where $B = D_s \nu \gamma_{FV} \Omega_0^2/(k_B T_e)$ is a material constant defined the same as in section 1.4, and the contact line mobility scale to be B/R_0^3, the two-dimensional solid-state dewetting of a thin film on a solid substrate can be described in the following dimensionless form

by the sharp-interface model:

$$\frac{\partial \mathbf{X}}{\partial t} = V_n \mathcal{N} = \frac{\partial^2 \mu}{\partial s^2} \mathcal{N} = \frac{\partial^2}{\partial s^2} \left[\left(\gamma(\theta) + \gamma''(\theta) \right) \kappa \right] \mathcal{N}. \tag{2.1.23}$$

Note that $\mathbf{X}, t, V_n, s, \mu, \gamma$ and η are dimensionless variables, and we still use the same notations for brevity.

The governing equation (2.1.23) for the solid-state dewetting problem is subject to the following dimensionless conditions:

(i) Contact point condition (**BC1**)

$$y(x_c^l, t) = 0, \qquad y(x_c^r, t) = 0, \tag{2.1.24}$$

and this condition ensures that the contact points move along the flat substrate.

(ii) Relaxed (or dissipative) contact angle condition (**BC2**)

$$\frac{dx_c^l}{dt} = \eta f(\theta_d^l), \qquad \frac{dx_c^r}{dt} = -\eta f(\theta_d^r) \tag{2.1.25}$$

where η represents the contact line mobility. $f(\theta)$ is defined as the dimensionless expression of the left side of the anisotropic Young equation (2.1.22):

$$f(\theta) := \gamma(\theta) \cos \theta - \gamma'(\theta) \sin \theta - \sigma, \quad \text{with} \quad \sigma := \frac{\gamma_{VS} - \gamma_{FS}}{\gamma_0}. \tag{2.1.26}$$

It can be seen that $\sigma = \cos \theta_i$ for $\sigma \in [-1, 1]$ with θ_i the isotropic Young contact angle. In this chapter, we still use the notation θ_i since the discussions are all for $\sigma \in [-1, 1]$.

(iii) Zero-mass flux condition (**BC3**)

$$\frac{\partial \mu}{\partial s}(x_c^l, t) = 0, \qquad \frac{\partial \mu}{\partial s}(x_c^r, t) = 0, \tag{2.1.27}$$

and this condition ensures that the total mass (denoted as $A(t)$) of the thin film is conserved, implying that there is no mass flux at the contact points. (See more details in section 2.2).

Under the above equations (2.1.23)-(2.1.27), we can rigorously prove that the total free energy of the system always decreases during the evolution (please refer to section 2.2). On the other hand, it should be noted that the (smooth) surface energy anisotropies have been divided into the following two categories according to the value of surface stiffness $\tilde{\gamma}$ in section 1.2.1: the weakly anisotropic case and the strongly anisotropic case. The governing equation (2.1.23) is mathematically well-posed for the weakly anisotropic case. However, for the strongly anisotropic case, some high energy surface orientations do not occur, and such surfaces undergo spontaneous faceting, and Eq. (2.1.23) becomes an anti-diffusion type equation and so it is ill-posed. In this chapter, we mainly focus on the weakly anisotropic case, and Chapter 3 is devoted to the strongly anisotropic case.

2.2 Mass conservation and energy dissipation

In this section, we mainly prove two properties of the proposed model: mass conservation and energy dissipation. To begin the proof, we first introduce a new variable $p \in [0, 1]$, which is independent of time t, to parameterize the moving film/vapor interface. Therefore, $p = 0$ and $p = 1$ can be used to represent the left and right contact points, respectively. The arc length s is a function of p and t, i.e., $s = s(p, t)$.

Proof of mass conservation. The mass(area) of the thin film is defined as

$$A(t) = \int_0^1 y x_p \, dp. \tag{2.2.1}$$

Then the change rate of the area can be calculated as

$$
\begin{aligned}
\frac{dA}{dt} &= \int_0^1 (y_t x_p + y x_{pt}) \, dp \\
&= \int_0^1 (y_t x_p - y_p x_t) \, dp + y x_t \Big|_{p=0}^{p=1} \qquad (2.2.2) \\
&= \int_0^1 (x_t, y_t) \cdot (-y_p, x_p) \, dp \\
&= \int_0^{L(t)} \mathbf{X}_t \cdot \mathcal{N} \, ds \\
&= \int_0^{L(t)} \mu_{ss} \, ds \\
&= \mu_s\big(L(t), t\big) - \mu_s\big(0, t\big) = 0. \qquad (2.2.3)
\end{aligned}
$$

Note that in step $(2.2.2)$ we have used integration by parts and the condition that the contact points move along the substrate, i.e. $y(p = 0, t) = y(p = 1, t) = 0$. From the above formulations, we can see that the zero-mass flux condition $(2.1.27)$ or $(1.4.4c)$ ensures that the equation $(2.2.3)$ is valid.

Hence, the total area (or mass) of the thin film is conserved during the evolution.

$\square$

Proof of energy dissipation. The total free energy of the system can be written as

$$
W(t) = \int_0^1 \gamma(\theta) s_p \, dp + (\gamma_{FS} - \gamma_{VS})(x_c^r - x_c^l), \qquad (2.2.4)
$$

where

$$
s_p = \frac{\partial s}{\partial p} = (x_p^2 + y_p^2)^{1/2} = (\mathbf{X}_p \cdot \mathbf{X}_p)^{1/2}.
$$

Note that the following equations hold:

$$
s_{pt} = \frac{x_p x_{pt} + y_p y_{pt}}{(x_p^2 + y_p^2)^{1/2}} = \frac{1}{s_p} \mathbf{X}_{pt} \cdot \mathbf{X}_p = \mathbf{X}_{pt} \cdot \mathcal{T},
$$

$$
\theta = \arctan2\Big(\frac{y_p}{x_p}\Big), \quad \theta_p = -\kappa s_p,
$$

$$
\theta_t s_p = \mathbf{X}_{pt} \cdot \mathcal{N}.
$$

We can calculate the changing rate of the total free energy as follows:

$$
\begin{aligned}
\frac{dW}{dt} &= \int_0^1 \big(\gamma'(\theta)\theta_t s_p + \gamma(\theta)s_{pt}\big)\,dp + (\gamma_{FS} - \gamma_{VS})\Big(\frac{dx_c^r}{dt} - \frac{dx_c^l}{dt}\Big) \\
&= \int_0^1 \mathbf{X}_{pt} \cdot \big(\gamma'(\theta)\,\mathcal{N} + \gamma(\theta)\,\mathcal{T}\big)\,dp \qquad\qquad (2.2.5) \\
&\quad + (\gamma_{FS} - \gamma_{VS})\Big(\frac{dx_c^r}{dt} - \frac{dx_c^l}{dt}\Big) \\
&= -\int_0^1 \mathbf{X}_t \cdot \Big(\big(\gamma''(\theta)\theta_p\mathcal{N} + \gamma'(\theta)\kappa s_p\mathcal{T}\big) \\
&\qquad\qquad + \big(\gamma'(\theta)\theta_p\mathcal{T} - \gamma(\theta)\kappa s_p\mathcal{N}\big)\Big)\,dp \qquad (2.2.6) \\
&\quad + \Big[\mathbf{X}_t \cdot \big(\gamma'(\theta)\,\mathcal{N} + \gamma(\theta)\,\mathcal{T}\big)\Big]_{p=0}^{p=1} + (\gamma_{FS} - \gamma_{VS})\Big(\frac{dx_c^r}{dt} - \frac{dx_c^l}{dt}\Big) \\
&= \int_0^{L(t)} \kappa\big(\gamma(\theta) + \gamma''(\theta)\big)\,\mathbf{X}_t \cdot \mathcal{N}\,ds \\
&\quad + \frac{dx_c^r}{dt}\Big(\gamma(\theta)\cos\theta - \gamma'(\theta)\sin\theta + \gamma_{FS} - \gamma_{VS}\Big)_{\theta=\theta_d^r} \\
&\quad - \frac{dx_c^l}{dt}\Big(\gamma(\theta)\cos\theta - \gamma'(\theta)\sin\theta + \gamma_{FS} - \gamma_{VS}\Big)_{\theta=\theta_d^l} \\
&= \int_0^{L(t)} \mu\mu_{ss}\,ds - C\Big[\Big(\frac{dx_c^r}{dt}\Big)^2 + \Big(\frac{dx_c^l}{dt}\Big)^2\Big] \qquad (2.2.7) \\
&= \mu\mu_s\Big|_{s=0}^{s=L(t)} - \int_0^{L(t)} \mu_s^2\,ds - C\Big[\Big(\frac{dx_c^r}{dt}\Big)^2 + \Big(\frac{dx_c^l}{dt}\Big)^2\Big] \qquad (2.2.8) \\
&= -\int_0^{L(t)} \mu_s^2\,ds - C\Big[\Big(\frac{dx_c^r}{dt}\Big)^2 + \Big(\frac{dx_c^l}{dt}\Big)^2\Big] \le 0.
\end{aligned}
$$

In the above calculations, we have used integration by parts from step (2.2.5) to step (2.2.6); step (2.2.7) is obtained by making use of the contact angle boundary conditions: $C = \gamma_0/\eta > 0$, $0 < \eta < \infty$ when choosing the relaxed contact angle boundary conditions (2.1.25), and $C = 0$ when applying the anisotropic Young equation (2.1.22); step (2.2.8) is obtained by integration by parts and the zero-mass flux condition (2.1.27).

Hence, we have proved that the total free energy of the system is dissipative during the evolution. □

2.3   A marker particle method (MPM)

In this section, we present a revised "marker particle" method(MPM) for simulating the proposed model, based on the one developed by Wong *et. al.* [134]. It rests on two steps:

Step 1. Refer to Fig. 2.2(a). Update the evenly distributed marker points (blue stars) on the given curve (blue solid line) to the new marker points (red dots) according to the governing equation (2.1.23), and update the given contact points (green squares) to the intermediate ones (magenta stars)according to the boundary conditions (2.1.24, 2.1.25).

Step 2. Refer to Fig. 2.2(b). Fit a curve (red solid line), which is piecewise cubic polynomial, for the intermediate marker points (red dots) with cubic spline interpolation and redistribute those marker points (red dots) evenly to be the new ones (blue stars).

The detailed algorithm at the nth time step is as follows.

Initially, given $N + 1$ marker points uniformly distributed on the film/vapor interface (curve) with respect to the arc length at the time step n. We denote the total arc length of the curve as L^n, the mesh size as $h^n := L^n/N$, the time step as k^n, and the uniformly distributed marker points as $(x_j^n, y_j^n), j = 0, 1, \ldots, N$. Evolving the $N + 1$ marker points according to Eqs. (2.1.23)-(2.1.27) based on the following explicit finite difference method, we obtain the positions of the $N+1$ marker points at the time step $n + 1$, denoted as $(\tilde{x}_j^{n+1}, \tilde{y}_j^{n+1}), j = 0, 1, \ldots, N$. In addition, we denote κ_j^n and μ_j^n to be approximations to the curvature and the chemical potential, respectively, on the jth marker point at the nth time step. Next, we introduce the following finite difference discretization operators:

$$\delta_t^+ x_j^n = \frac{\tilde{x}_j^{n+1} - x_j^n}{k^n}, \quad \delta_s x_j^n = \frac{x_{j+1}^n - x_{j-1}^n}{2h^n}, \quad \delta_s^2 x_j^n = \frac{x_{j+1}^n - 2x_j^n + x_{j-1}^n}{(h^n)^2}.$$
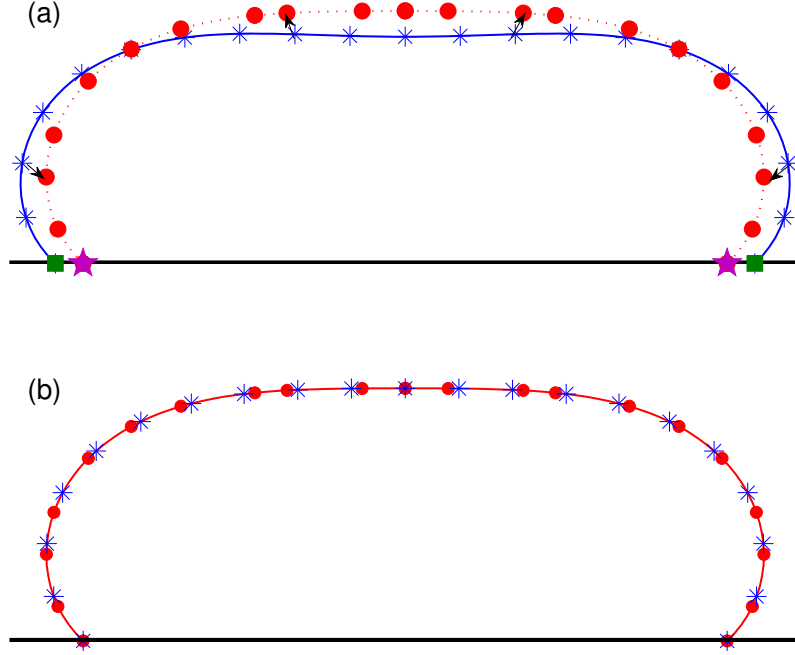
Figure 2.2: A schematic illustration of the "marker particle" method.

Using a central finite difference scheme for discretizing the spatial derivatives and a forward Euler scheme for discretizing the temporal derivatives, the governing equations (2.1.23) become

$$
\begin{cases}
\delta_t^+ x_j^n = -\left(\delta_s^2 \mu_j^n\right)\left(\delta_s y_j^n\right), \\
\delta_t^+ y_j^n = \left(\delta_s^2 \mu_j^n\right)\left(\delta_s x_j^n\right), \\
\mu_j^n = \kappa_j^n\,\widetilde{\gamma}(\theta_j^n), & j = 1, \ldots, N-1, \\
\kappa_j^n = \left(\delta_s y_j^n\right)\left(\delta_s^2 x_j^n\right) - \left(\delta_s x_j^n\right)\left(\delta_s^2 y_j^n\right),
\end{cases}
\tag{2.3.1}
$$

and the boundary conditions (2.1.24)-(2.1.27) become

$$
\tilde{y}_0^{n+1} = \tilde{y}_N^{n+1} = 0,
$$

$$
\delta_t^+ x_0^n = \eta\big[\gamma(\theta_0^n)\cos(\theta_0^n) - \gamma'(\theta_0^n)\sin(\theta_0^n) - \cos\theta_i\big],
$$

$$
\delta_t^+ x_N^n = -\eta\big[\gamma(\theta_N^n)\cos(\theta_N^n) - \gamma'(\theta_N^n)\sin(\theta_N^n) - \cos\theta_i\big],
$$

$$
\mu_0^n = \frac{4}{3}\mu_1^n - \frac{1}{3}\mu_2^n, \quad \mu_N^n = \frac{4}{3}\mu_{N-1}^n - \frac{1}{3}\mu_{N-2}^n.
$$

Based on this numerical scheme, we immediately obtain the positions of the marker points $(\tilde{x}_j^{n+1}, \tilde{y}_j^{n+1}), j = 0, 1, \ldots, N$. Note that these marker points may not be uniformly distributed along the curve with respect to the arc length. Thus, we redistribute these marker points via a cubic spine interpolation such that they are uniformly distributed as follows. First, making use of these new marker points $(\tilde{x}_j^{n+1}, \tilde{y}_j^{n+1}), j = 0, 1, \ldots, N$, we construct a piecewise curve $\{(X_j^{n+1}(p), Y_j^{n+1}(p)), \ p \in [(j-1)h^n, jh^n]\}_{j=1,2,\ldots,N}$ by using a cubic spline interpolation. Here, $X_j^{n+1}(p)$ and $Y_j^{n+1}(p)$ are cubic polynomials obtained from a cubic spline interpolation for the points $\{(jh^n, \tilde{x}_j^{n+1}), j = 0, 1, \ldots, N\}$ and $\{(jh^n, \tilde{y}_j^{n+1}), j = 0, 1, \ldots, N\}$, respectively. By using these cubic polynomials, we directly compute the arc length of each piecewise cubic polynomial curve, denoted as $L_j^{n+1}, j = 1, 2, \ldots, N$. Then, we obtain the total arc length $L^{n+1} = \sum_{j=1}^{N} L_j^{n+1}$ and determine the uniform mesh size at the $(n+1)^{\text{th}}$ time step as $h^{n+1} = L^{n+1}/N$. In order to redistribute the $N+1$ points uniformly according to the arc length for the $(n+1)^{\text{th}}$ time step computation, we set $x_0^{n+1} = \tilde{x}_0^{n+1}, y_0^{n+1} = \tilde{y}_0^{n+1} = 0, x_N^{n+1} = \tilde{x}_N^{n+1}, y_N^{n+1} = \tilde{y}_N^{n+1} = 0$. For each fixed $j = 1, 2, \ldots, N-1$, we first locate to which unique piecewise cubic polynomial curve the new j^{th} point (x_j^{n+1}, y_j^{n+1}) belongs, i.e. finding a unique $1 \le i \le N$ such that $\sum_{l=1}^{i-1} L_l^{n+1} \le jh^{n+1} < \sum_{l=1}^{i} L_l^{n+1}$, then numerically solve the following equation

$$
\begin{aligned}
g(q) &= \int_{(i-1)h^n}^{(i-1)h^n+q} \sqrt{\left(\frac{dX_i^{n+1}(p)}{dp}\right)^2 + \left(\frac{dY_i^{n+1}(p)}{dp}\right)^2} \, dp \\
&= jh^{n+1} - \sum_{l=1}^{i-1} L_l^{n+1}, \quad 0 \le q < h^n,
\end{aligned}
$$

to obtain its unique root $q = q^*$, and finally the position of the jth uniformly distributed marker point at the $(n+1)^{\text{th}}$ time step is obtained as $x_j^{n+1} = X_i^{n+1}((i-1)h^n + q^*)$ and $y_j^{n+1} = Y_i^{n+1}((i-1)h^n + q^*)$.

2.4 A parametric finite element method (PFEM)

The proposed MPM made use of cubic spline interpolation which reduces the computation cost in redistribution, compared to the traditional MPM which uses

local circle arcs for interpolation. Moreover, due to its explicitness, MPM is easy to implement. However, the explicitness makes this method suffer from a severe stability constraint, that is, the time steps should be of $\mathcal{O}((h^k)^4)$ since the equation is a fourth order equation. This time step is intolerable when the aspect ratio (length/height) of the film is large (the dewetting process will last for a long time). Therefore, we propose an efficient method (for implementation we use P^1 elements), the parametric finite element method (PFEM), based on [11–13, 15–17] in this section.

2.4.1 Weak formulation

Before defining the weak formulation, we first introduce some notations. In addition to the arc length s, we introduce a new parameter $p \in I = [0, 1]$. It also parameterizes the moving film/vapor interface $\Gamma(t)$:

$$\Gamma(t) = \mathbf{X}(p, t) : I \times [0, T] \to \mathbb{R}^2$$

where $\mathbf{X}(0, t)$ and $\mathbf{X}(1, t)$ are the left and right contact points $x_c^l(t), x_c^r(t)$, respectively. The relation between s and p is

$$s_p := \frac{\partial s}{\partial p} = |\mathbf{X}_p|.$$

Let

$$H_{a,b}^1 = \{\phi \mid \phi \in H^1(I, \mathbb{R}), \ \phi(0) = a, \ \phi(1) = b\}.$$

When $a = b = 0$, it collapses to H_0^1. We also define the following inner product for scalar and vector valued function $u, v \in H^1(I, Z)$ with $Z = \mathbb{R}$ or $\mathbb{R}^2$:

$$(u, \ v)_\Gamma = \int_{\Gamma(t)} u(p) \cdot v(p) \, ds = \int_I u(p) \cdot v(p) s_p \, dp, \tag{2.4.1a}$$

$$a_\Gamma(u, \ v) = \int_{\Gamma(t)} u_s(p) \cdot v_s(p) \, ds = \int_I u_p(p) \cdot v_p(p) \frac{1}{s_p} \, dp, \tag{2.4.1b}$$

where "$\cdot$" stands for scaler multiplication if u, v are scaler valued functions, and it means inner product if u, v are vectors.

We can rewrite the governing equation (2.1.23) as

$$\mathbf{X}_t \cdot \mathcal{N} = \mu_{ss}, \tag{2.4.2a}$$

$$\mu = \widetilde{\gamma}(\theta)\kappa, \tag{2.4.2b}$$

$$\kappa\mathcal{N} = -\mathbf{X}_{ss}. \tag{2.4.2c}$$

Eq. (2.1.24) sets boundary values of the y-coordinate to be 0, and Eq. (2.1.25) can be used to calculate the boundary values of the x-coordinate. Therefore, we define the weak solution of the problem by the following weak formulation: Given $\Gamma(0) = \mathbf{X}(I,0)$, for all $t \in (0,T]$ find $\Gamma(t) = \mathbf{X}(I,t)$ with $\mathbf{X}(t) \in H^1_{l,r} \times H^1_0$ (l and r stand for x^l_c, x^r_c, respectively), $\mu(t), \kappa(t) \in H^1$ such that

$$(\mathbf{X}_t \cdot \mathcal{N}, \ \varphi)_\Gamma + a_\Gamma(\mu, \ \varphi) = 0, \qquad \forall \varphi \in H^1, \tag{2.4.3a}$$

$$(\mu, \ \phi)_\Gamma - (\widetilde{\gamma}(\theta)\kappa, \ \phi)_\Gamma = 0, \qquad \forall \phi \in H^1, \tag{2.4.3b}$$

$$(\kappa\mathcal{N}, \ \mathbf{w})_\Gamma - a_\Gamma(\mathbf{X}, \ \mathbf{w}) = 0, \qquad \forall \mathbf{w} \in H^1_0 \times H^1_0. \tag{2.4.3c}$$

Note that in order to get Eq. (2.4.3a), Eq. (2.1.27) is used when using integration by parts.

For the proposed weak formulation (2.4.3a) - (2.4.3c), we have the following two propositions.

Proposition 2.4.1 (Mass conservation for weak solutions)**.** *Assume that* $\Gamma(t) = \mathbf{X}(p,t)$, $\mu(p,t)$ *and* $\kappa(p,t)$ *are the weak solution to the variational formulation* (2.4.3a)-(2.4.3c), *then the total mass of the thin film for the weak solution is always conserved during the evolution.*

Proof. By directly calculating the time derivative with respect to $A(t)$, defined in Eq. (2.2.1), we can obtain the following expressions:

$$\begin{aligned}
\frac{d}{dt}A(t) &= \frac{d}{dt}\int_{\Gamma(t)} yx_s \, ds = \frac{d}{dt}\int_0^1 yx_p \, dp \\
&= \int_0^1 (y_t x_p + yx_{pt}) \, dp = \int_0^1 (y_t x_p - y_p x_t) \, dp + \left. \big(yx_t\big)\right|_{p=0}^{p=1} \\
&= \int_0^1 (x_t, y_t) \cdot (-y_p, x_p) \, dp = \int_{\Gamma(t)} \mathbf{X}_t \cdot \mathcal{N} \, ds.
\end{aligned}$$

By choosing the test function in Eq. (2.4.3a) as $\varphi = 1$, we can obtain that:

$$
\begin{aligned}
\frac{d}{dt}A(t) &= \int_{\Gamma(t)} \mathbf{X}_t \cdot \mathcal{N} \, ds \\
&= -\int_{\Gamma(t)} \mu_s \, \varphi_s \, ds \\
&= 0.
\end{aligned}
$$

Hence, the weak solution to the variational formulation satisfies the mass conservation during the evolution of solid-state dewetting. $\qquad\square$

Proposition 2.4.2 (Energy dissipation for weak solutions). *Assume that $\Gamma(t) = \mathbf{X}(p, t)$, $\mu(p, t)$ and $\kappa(p, t)$ are the weak solution to the variational formulation (2.4.3a)-(2.4.3c), and furthermore, if we assume that the solution of the moving interface has higher regularity, i.e., $\mathbf{X}(p, t) \in C^1\big(C^2(I); [0, T]\big) \times C^1\big(C^2(I); [0, T]\big)$, then the total energy of the system for the weak solution is always dissipative during the evolution.*

Proof. First, we can calculate energy dissipation rate about the total free energy $W(t)$ (defined in Eq. (2.2.4)) as follows:

$$
\begin{aligned}
\frac{d}{dt}W(t) &= \frac{d}{dt}\int_{\Gamma(t)} \gamma(\theta) \, ds - \Big(\frac{dx_c^r}{dt} - \frac{dx_c^l}{dt}\Big)\sigma \\
&= \frac{d}{dt}\int_0^1 \gamma(\theta)s_p \, dp - \Big(\frac{dx_c^r}{dt} - \frac{dx_c^l}{dt}\Big)\sigma \\
&= \int_0^1 \gamma'(\theta)\theta_t s_p \, dp + \int_0^1 \gamma(\theta)s_{pt} \, dp - \Big(\frac{dx_c^r}{dt} - \frac{dx_c^l}{dt}\Big)\sigma \\
&:\triangleq\ I + II + III. \qquad\qquad (2.4.4)
\end{aligned}
$$

Therefore, we can divide the above formulation about energy dissipation rate into the three parts. Before deriving the exact expressions for the three parts, we note that the following expressions hold:

$$
\theta_s = -\mathbf{X}_s^\perp \cdot \mathbf{X}_{ss}, \qquad \theta_t = -\frac{\mathbf{X}_p^\perp \cdot \mathbf{X}_{pt}}{|\mathbf{X}_p|^2}, \qquad s_{pt} = \frac{x_p x_{p,t} + y_p y_{pt}}{(x_p^2 + y_p^2)^{1/2}} = \frac{1}{s_p}\mathbf{X}_{pt} \cdot \mathbf{X}_p,
$$

$$
\mathbf{X}_{ss} \parallel \mathcal{N}, \qquad \mathbf{X}_s = \mathcal{N}^\perp,
$$

where the notation "$\perp$" denotes clockwise rotation by 90 degrees.

By making use of integration by parts, contact point boundary condition (i.e., Eq. (2.1.24)) and the above expressions, we can obtain the following expressions for the above defined three parts, respectively:

$$
\begin{aligned}
I &\triangleq \int_0^1 \gamma'(\theta)\theta_t s_p \, dp = \int_0^1 \gamma'(\theta)\frac{-\mathbf{X}_p^\perp \cdot \mathbf{X}_{pt}}{s_p} \, dp \\
&= \left(\gamma'(\theta)\frac{-\mathbf{X}_p^\perp \cdot \mathbf{X}_t}{s_p}\right)\Big|_{p=0}^{p=1} + \int_0^1 \left(\gamma'(\theta)\frac{\mathbf{X}_p^\perp}{s_p}\right)_p \cdot \mathbf{X}_t \, dp \\
&= \left(\gamma'(\theta)\vec{n} \cdot \mathbf{X}_t\right)\Big|_{s=0}^{s=L(t)} + \int_\Gamma \left(\gamma'(\theta)\mathbf{X}_s^\perp\right)_s \cdot \mathbf{X}_t \, ds \\
&= \left(\gamma'(\theta)\vec{n} \cdot \mathbf{X}_t\right)\Big|_{s=0}^{s=L(t)} + \int_\Gamma \gamma''(\theta)(-\mathbf{X}_s^\perp \cdot \mathbf{X}_{ss})(\mathbf{X}_s^\perp \cdot \mathbf{X}_t) \, ds + \int_\Gamma \gamma'(\theta)\mathbf{X}_{ss}^\perp \cdot \mathbf{X}_t \, ds \\
&= \left(\gamma'(\theta)\vec{n} \cdot \mathbf{X}_t\right)\Big|_{s=0}^{s=L(t)} - \int_\Gamma \gamma''(\theta)(\vec{n} \cdot \mathbf{X}_{ss})(\vec{n} \cdot \mathbf{X}_t) \, ds + \int_\Gamma \gamma'(\theta)\mathbf{X}_{ss}^\perp \cdot \mathbf{X}_t \, ds \\
&= \left(\gamma'(\theta)\vec{n} \cdot \mathbf{X}_t\right)\Big|_{s=0}^{s=L(t)} - \int_\Gamma \gamma''(\theta)\mathbf{X}_{ss} \cdot \mathbf{X}_t \, ds + \int_\Gamma \gamma'(\theta)\mathbf{X}_{ss}^\perp \cdot \mathbf{X}_t \, ds,
\end{aligned}
$$

$$
\begin{aligned}
II &\triangleq \int_0^1 \gamma(\theta)s_{pt} \, dp = \int_0^1 \gamma(\theta)\frac{\mathbf{X}_{pt} \cdot \mathbf{X}_p}{|\mathbf{X}_p|} \, ds \\
&= \left(\gamma(\theta)\frac{\mathbf{X}_p \cdot \mathbf{X}_t}{|\mathbf{X}_p|}\right)\Big|_{p=0}^{p=1} - \int_0^1 \left(\gamma(\theta)\frac{\mathbf{X}_p}{|\mathbf{X}_p|}\right)_p \cdot \mathbf{X}_t \, dp \\
&= \left(\gamma(\theta)\mathbf{X}_s \cdot \mathbf{X}_t\right)\Big|_{s=0}^{s=L(t)} - \int_\Gamma \left(\gamma(\theta)\mathbf{X}_s\right)_s \cdot \mathbf{X}_t \, ds \\
&= = \left(\gamma(\theta)\mathbf{X}_s \cdot \mathbf{X}_t\right)\Big|_{s=0}^{s=L(t)} - \int_\Gamma \gamma(\theta)\mathbf{X}_{ss} \cdot \mathbf{X}_t \, ds - \int_\Gamma \gamma'(\theta)(-\mathbf{X}_s^\perp \cdot \mathbf{X}_{ss})(\mathbf{X}_s \cdot \mathbf{X}_t) \\
&= = \left(\gamma(\theta)\mathbf{X}_s \cdot \mathbf{X}_t\right)\Big|_{s=0}^{s=L(t)} - \int_\Gamma \gamma(\theta)\mathbf{X}_{ss} \cdot \mathbf{X}_t \, ds - \int_\Gamma \gamma'(\theta)\mathbf{X}_{ss} \cdot \mathbf{X}_t \, ds,
\end{aligned}
$$

$$
III \triangleq -\left(\frac{dx_c^r}{dt} - \frac{dx_c^l}{dt}\right)\sigma.
$$

At the two contact points, we have the following expressions:

$$
\mathbf{X}_s\Big|_{s=0} = (\cos\theta_d^l, \sin\theta_d^l), \quad \mathcal{N}\Big|_{s=0} = (-\sin\theta_d^l, \cos\theta_d^l), \quad \mathbf{X}_t\Big|_{s=0} = \left(\frac{dx_c^l}{dt}, 0\right),
$$

$$
\mathbf{X}_s\Big|_{s=L} = (\cos\theta_d^r, \sin\theta_d^r), \quad \mathcal{N}\Big|_{s=L} = (-\sin\theta_d^r, \cos\theta_d^r), \quad \mathbf{X}_t\Big|_{s=L} = \left(\frac{dx_c^r}{dt}, 0\right).
$$

By substituting the expressions for the three parts of energy dissipation rate into Eq. (2.4.4) and making use of the relaxed contact angle boundary condition, i.e.

Eq. (2.1.25), we can obtain the energy dissipation rate as follows:

$$
\begin{aligned}
\frac{d}{dt}W(t) &= I + II + III \\
&= \left(\gamma'(\theta)\mathbf{X}_t \cdot \mathcal{N} + \gamma(\theta)\mathbf{X}_t \cdot \mathbf{X}_s \right)\Big|_{s=0}^{s=L(t)} - \left(\frac{dx_c^r}{dt} - \frac{dx_c^l}{dt} \right)\sigma \\
&\quad - \int_{\Gamma(t)} \left[\gamma(\theta) + \gamma''(\theta) \right] \left(\mathbf{X}_t \cdot \mathbf{X}_{ss} \right) ds, \\
&= \frac{dx_c^r}{dt} \left[\gamma(\theta_d^r) \cos\theta_d^r - \gamma'(\theta_d^r) \sin\theta_d^r - \sigma \right] \\
&\quad - \frac{dx_c^l}{dt} \left[\gamma(\theta_d^l) \cos\theta_d^l - \gamma'(\theta_d^l) \sin\theta_d^l - \sigma \right] - \int_{\Gamma(t)} \left[\gamma(\theta) + \gamma''(\theta) \right]\left(\mathbf{X}_t \cdot \mathbf{X}_{ss} \right) \\
&= -\frac{1}{\eta}\left[\left(\frac{dx_c^r}{dt} \right)^2 + \left(\frac{dx_c^l}{dt} \right)^2 \right] - \int_{\Gamma(t)} \left[\gamma(\theta) + \gamma''(\theta) \right]\left(\mathbf{X}_t \cdot \mathbf{X}_{ss} \right) ds. \quad (2.4.5)
\end{aligned}
$$

In the following steps, by making use of Eq. (2.4.5), we will show that the weak solution to the variational formulation (2.4.3a)-(2.4.3c) satisfies the energy dissipation property. In order to prove the proposition, we choose the test functions $\varphi, \psi, \mathbf{w}$ in the variational formulation (2.4.3a)-(2.4.3c) as follows:

$$
\varphi = \mu, \qquad \psi = \mathbf{X}_t \cdot \mathcal{N}, \qquad \mathbf{w} = \left[\gamma(\theta) + \gamma''(\theta) \right] \vec{X}_t - c_1 \frac{dx_c^l}{dt} \boldsymbol{\zeta}_1 - c_2 \frac{dx_c^r}{dt} \boldsymbol{\zeta}_2, \quad (2.4.6)
$$

where in order to ensure the test function $\mathbf{w} \in H_0^1(I) \times H_0^1(I)$ in Eq.(2.4.3c), the two parameters c_1 and c_2 are defined as: $c_1 = \gamma(\theta_d^l) + \gamma''(\theta_d^l)$ and $c_2 = \gamma(\theta_d^r) + \gamma''(\theta_d^r)$, and the two vector functions $\boldsymbol{\zeta}_1$ and $\boldsymbol{\zeta}_2$ belong to the following defined vector function spaces:

$$
\boldsymbol{\zeta}_1(p) \in \{ (\zeta_1(p), 0) : \quad \zeta_1 \in H^1(I), \ \zeta_1(0) = 1, \ \zeta_1(1) = 0 \}, \quad (2.4.7)
$$

$$
\boldsymbol{\zeta}_2(p) \in \{ (\zeta_2(p), 0) : \quad \zeta_2 \in H^1(I), \ \zeta_2(0) = 0, \ \zeta_2(1) = 1 \}. \quad (2.4.8)
$$

Inserting the expressions of the test functions defined above into the variational formulation (2.4.3a)-(2.4.3c), and making use of Eq. (2.4.5), we can obtain that the energy dissipation rate with respect to the weak solution satisfies the following

expression:

$$
\begin{aligned}
\frac{d}{dt}W(t) \;=\; & -\frac{1}{\eta}\left[\left(\frac{dx_c^l}{dt}\right)^2 + \left(\frac{dx_c^r}{dt}\right)^2\right] - \int_{\Gamma(t)} \left(\mu_s\right)^2 ds \\
& - c_1 \frac{dx_c^l}{dt} \int_{\Gamma(t)} \boldsymbol{\zeta}_1 \cdot (\kappa\mathcal{N} + \vec{X}_{ss})\, ds \\
& - c_2 \frac{dx_c^r}{dt} \int_{\Gamma(t)} \boldsymbol{\zeta}_2 \cdot (\kappa\mathcal{N} + \mathbf{X}_{ss})\, ds.
\end{aligned}
\tag{2.4.9}
$$

For the above expression, we can clearly see that the first two terms are always less than zero. For the other two terms defined in Eq. (2.4.9), because the vector function $(\kappa\mathcal{N} + \mathbf{X}_{ss}) \in L^2(I) \times L^2(I)$, ζ_1 and ζ_2 are any functions defined in the spaces (2.4.7)-(2.4.8), and at any time t the two constants $c_1\frac{dx_c^l}{dt}$ and $c_2\frac{dx_c^r}{dt}$ are finite, then the two integral terms in Eq. (2.4.9) can be shown arbitrary small as we want, by choosing proper functions ζ_1 and ζ_2.

Then, $\frac{d}{dt}W(t) \leq 0$. The proof is completed. $\qquad\square$

2.4.2 Finite element approximation

Firstly, we decompose the spatial domain as

$$
I = \bigcup_{j=1}^{J} I_j, \qquad I_j = [q_{j-1}, q_j], \quad \text{with } q_j = jh,\ h := \frac{1}{J}.
$$

The temporal domain is decomposed as $0 = t_0 < t_1 < \dots t_M = T$. Let $\Gamma^m = \mathbf{X}^m$ denote a sequence of polygonal curves (approximation to $\Gamma(t_m)$), $m = 0, \dots, M$. We define the following two finite element spaces:

$$
V^h = \{\chi \mid \chi \in C(I, \mathbb{R}),\ \chi \text{ is linear in } I_j, \forall j = 1\dots M\},
$$

$$
V_{a,b}^h = \{\chi \mid \chi \in V^h,\ \chi(0) = a,\ \chi(1) = b\}.
$$

$$
V_0^h = \{\chi \mid \chi \in V^h,\ \chi(0) = 0,\ \chi(1) = 0\}.
$$

The normal vector of Γ^m, which is a step function with discontinuities at point $q_j, j = 1 \dots M$, can be computed as

$$
\mathcal{N}^m = -[\mathbf{X}_s^m]^{\perp} = -\frac{[\mathbf{X}_p^m]^{\perp}}{|\mathbf{X}_p^m|}.
$$

Based on the definition of inner products defined in Eq. (2.4.1), we define the following discrete forms for continuous, piecewise linear functions u and v on Γ^m:

$$(u,\ v)_{\Gamma^m} = \frac{h}{2} \sum_{j=1}^{J} |\mathbf{X}_p^m(q_{j-\frac{1}{2}})| \left((u \cdot v)(q_j^-) + (u \cdot v)(q_{j-1}^+) \right), \qquad (2.4.10a)$$

$$a_{\Gamma^m}(u,\ v) = \int_0^1 u_s \cdot v_s \, |\mathbf{X}_p^m| \, ds = \int_0^1 u_p \cdot v_p \frac{1}{|\mathbf{X}_p^m|} \, dp, \qquad (2.4.10b)$$

where $u(q_j^+)$ and $u(q_j^-)$ are the right hand and left hand limits, respectively.

Therefore, the finite element approximation to Eq. (2.4.3) can be written as follows. For $m \geq 0$, given $\Gamma^m = \mathbf{X}^m \in V_{l,r}^h \times V_0^h$ with $l = x_c^l(t_m), r = x_c^r(t_m)$, $\mu^m, \kappa^m \in V^h$, find $\Gamma^{m+1} = \mathbf{X}^{m+1} \in V_{l,r}^h \times V_0^h$ with $l = x_c^l(t_{m+1}), r = x_c^r(t_{m+1})$, and $\mu^{m+1}, \kappa^{m+1} \in V^h$ such that

$$(\frac{\mathbf{X}^{m+1} - \mathbf{X}^m}{t_{m+1} - t_m} \cdot \mathcal{N}^m, \ \varphi)_{\Gamma^m} + a_{\Gamma^m}(\mu^{m+1}, \ \varphi) = 0, \qquad \forall \varphi \in V^h, \qquad (2.4.11a)$$

$$(\mu^{m+1}, \ \phi)_{\Gamma^m} - (\widetilde{\gamma}(\theta^m)\kappa^{m+1}, \ \phi)_{\Gamma^m} = 0, \qquad \forall \phi \in V^h, \qquad (2.4.11b)$$

$$(\kappa^{m+1}\mathcal{N}^m, \ \mathbf{w})_{\Gamma^m} - a_{\Gamma^m}(\mathbf{X}^{m+1}, \ \mathbf{w}) = 0, \qquad \forall \mathbf{w} \in V_0^h \times V_0^h. \qquad (2.4.11c)$$

Note that $x_c^l(t_{m+1})$ and $x_c^r(t_{m+1})$ are computed previously by discretizing boundary condition (2.1.25), which is similar to that in MPM.

2.5 Numerical tests

Based on the mathematical model and numerical methods, we now present the results from several simulations to determine the effect of the contact line mobility η. We then simulate solid-state dewetting in several different thin film geometries with weakly anisotropic surface energy in two dimensions. For simplicity, we set the initial film thickness to unity and assume a dimensionless anisotropic surface energy of the form (Eq. (1.2.2)) introduced in Chapter 1:

$$\gamma(\theta) = 1 + \beta \cos[m(\theta + \phi)], \qquad \theta \in [-\pi, \pi]. \qquad (2.5.1)$$

In this thesis, ϕ is set to 0, except where noted.

2.5.1 Contact line mobility

The contact line mobility η determines the rate of relaxation of the dynamic contact angle θ_d to the equilibrium contact angle θ_a which satisfies the anisotropic Young equation (2.1.22). In general, for small η, the relaxation is very slow and the contact points move very slowly. On the other hand, if η is very large, the relaxation process occurs very quickly such that the dynamic contact angle θ_d quickly converges to θ_a. In this case, the time steps for numerically integrating Eq. (2.1.25) must be chosen very small in order to maintain numerical stability. From the point of view of numerics, the choice of η must represent a balance between these factors. On the other hand, in any physical system, η is a material parameter and must be determined either from experiments or microscopic (e.g., molecular dynamics) simulations.

Figure 2.3a shows the evolution of the dynamic contact angle θ_d as a function of time for seven different mobilities ($\eta = 1.25, 2.5, 5, 10, 20, 100, 200$) for a case of an initially short, thin rectangular island (length $L = 5$, thickness $h = 1$) with $\beta = 0$ and $\theta_i = 3\pi/4$, compared to the anisotropic Young angle $\theta_a = 3\pi/4$ (note that $\theta_a = \theta_i$ in the isotropic case). The contact angle, initially grows very quickly from its initial value of $\pi/2$ to a near steady-state dynamical value (see the inset to Fig. 2.3a). Then, as the island approaches its equilibrium shape the contact point slows and $\theta_d \to \theta_a$. The near steady-state dynamical angle, seen in the inset for large η, is always smaller than the equilibrium value θ_a and θ_d increases with increasing contact line mobility η (see Fig. 2.3b). This is consistent with experimental and atomistic simulation observations of the effect triple junction drag on dynamic triple junction angles in grain boundaries [36,127] and in contact lines of fluids on substrates [108, 109].

In order to further clarify the effects of the choice of the mobility η, we performed a series of numerical simulations of the evolution of an initially rectangular, thin film island ($\beta = 0, \theta_i = 3\pi/4$) of three different initial lengths $L = 5, 100$ and semi-infinite, for several values of η and different coefficients. When $L = 5$, the island
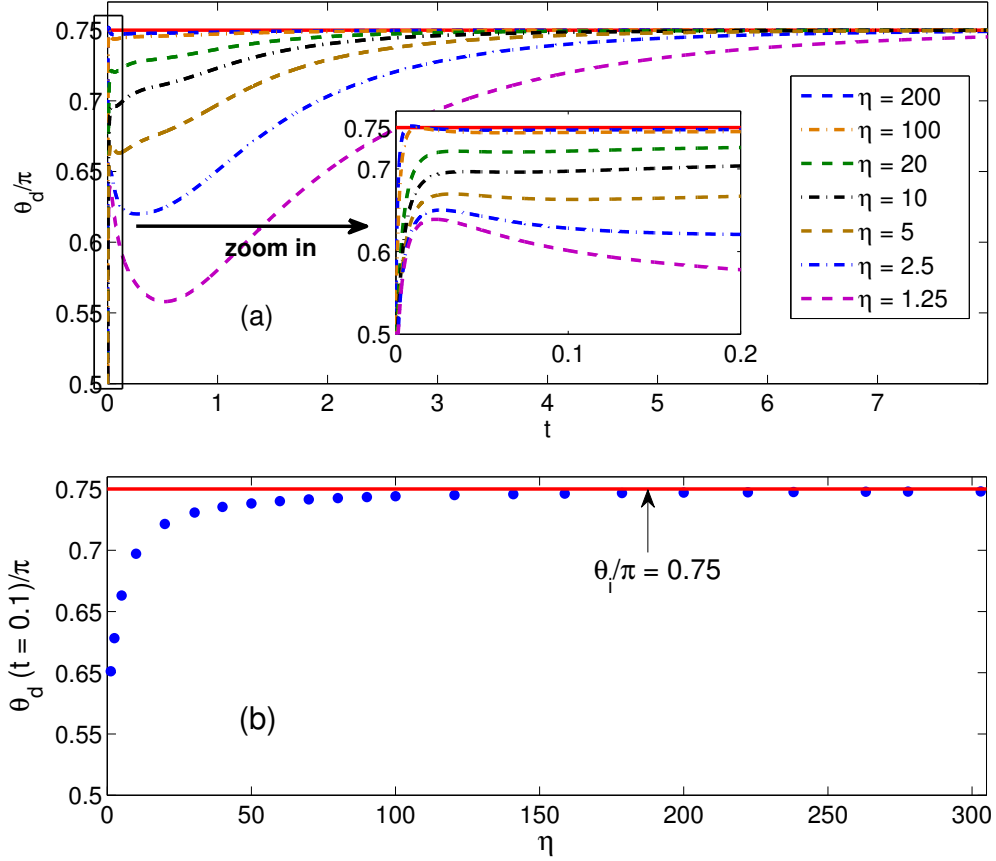
Figure 2.3: (a) The dynamic contact angle θ_d as a function of time for several different contact line mobilities and simulation parameters $\beta = 0$, $\theta_a = \theta_i = 3\pi/4$ (upper panel). The initial island is rectangular with length $L = 5$, thickness $h = 1$ and $\theta_d(t = 0) = \pi/2$. (b) The dynamic angle θ_d measured at $t = 0.1$ as a function of the contact line mobility η. In the both figures, the red solid lines represent $\theta_a = 3\pi/4$.

η	200	100	20	10
$L = 5$	1.34×10^1	1.35×10^1	1.38×10^1	1.4309×10^1
$L = 100$	1.41×10^3	1.41×10^3	1.41×10^3	1.4094×10^3
semi-infinite	1.64×10^4	1.64×10^4	1.64×10^4	1.6392×10^4

Table 2.1: Equilibration times for rectangular islands of thickness $h = 1$ and several initial lengths for different contact line mobilities η (see the text for more details).

evolves to an arc of a circle (equilibrium state) and the simulations are terminated when the maximum error in the adjacent time level of marker point separation is smaller than a threshold value. For the $L = 100$ and semi-infinite cases, the simulations are terminated when the first pinch-off event (the film thins to zero thickness creating new contact points) occurs. We compared the results for three different values of $\eta = 10, 20, 100$ and found that η has no discernible effect on the equilibrium island shapes (not shown). η also has very little effect on the simulation termination/island equilibration times (see Table 2.1). For the semi-infinite thin film case, we numerically computed the contact point position as a function of time and found that it is well described by a power law with the value 0.42, regardless of the contact line mobility η [75, 125]. Unless otherwise noted, the simulations reported below were all performed with $\eta = 100$.

2.5.2 Convergence test of MPM

We now investigate the convergence of MPM by performing simulations for a rectangular island of length $L = 5$ and thickness $h = 1$. In this case, the equilibrium island shape can be determined by using the Kaishew approach [71] that is also often referred to as the Winterbottom construction [133]. We compare the numerical equilibrium island shape with the theoretical predictions as a function of the number of markers N employed in the description of the island shape. Figure 2.4 and Table 2.2 show the numerical convergence results.

As showed in Fig. 2.4, the numerical equilibrium states converge to the theoretical
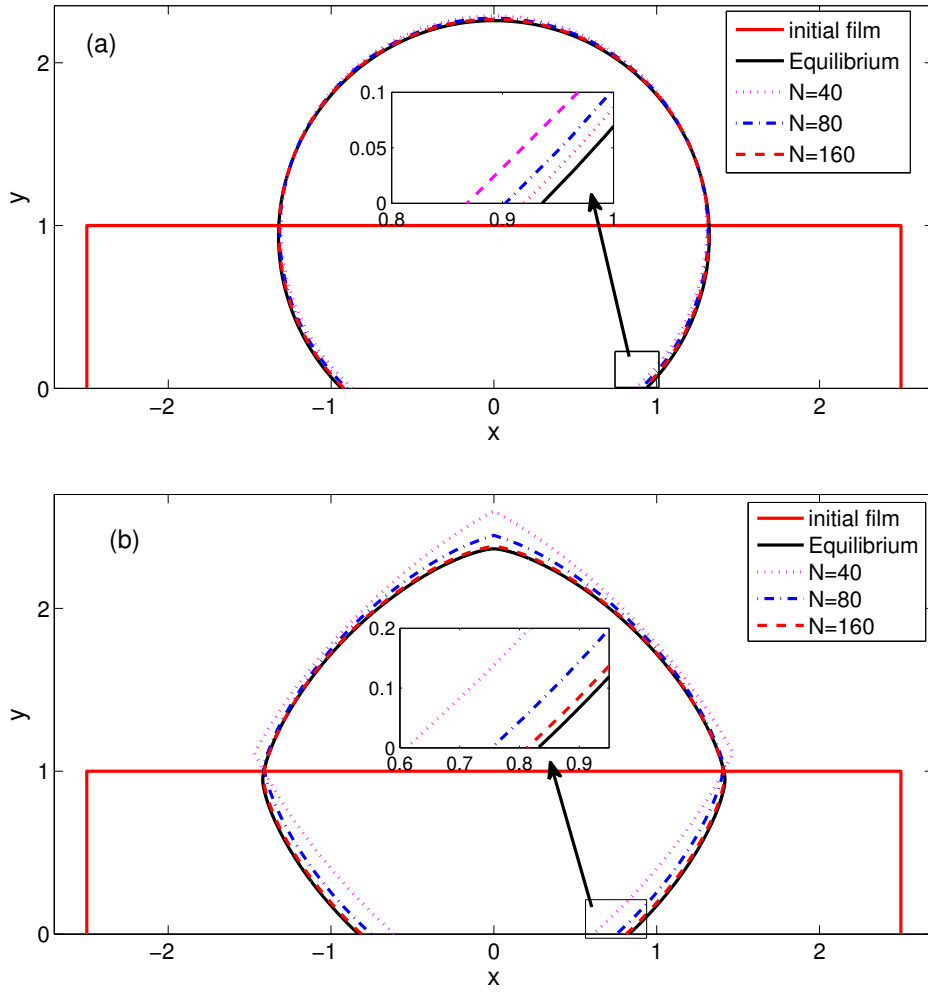
Figure 2.4: Comparison of the long time numerical solution of the dynamic island shape with the theoretical equilibrium shape (from the Winterbottom construction, shown in blue) for several values of the number of computational marker points N for: (a) the isotropic surface energy case with $\beta = 0$ and $\theta_i = 3\pi/4$; and (b) the weakly surface energy case with $\beta = 0.06$, $\theta_i = 3\pi/4$ and $m = 4$.

N	Isotropic			Anisotropic		
	40	80	160	40	80	160
α_{err}	7.21E-2	3.54E-2	1.75E-2	2.64E-1	9.37E-2	2.27E-2
d_{err}	6.75E-2	3.31E-2	1.63E-2	2.34E-1	8.32E-2	1.89E-2

Table 2.2: Convergence of the long time simulation island shape with the theoretical equilibrium shape (Winterbottom construction) as a function of the number of marker points N. The error measures α_{err} and d_{err} are defined in the text.

equilibrium states (Winterbottom construction, shown by the black curves) with increasing number of marker points from $N = 40$ to $N = 160$ in both the isotropic and weakly anisotropic cases; this is a clear demonstration of the convergence of our numerical scheme. We also computed the relative error α_{err} of the right contact point position between the numerical equilibrium state $x_{c,n}^r$ and the theoretical equilibrium state $x_{c,e}^r$, and the maximum distance error d_{err} between the two equilibrium shapes measured by marker points. We define the relative error as $\alpha_{\text{err}} = |(x_{c,n}^r - x_{c,e}^r)/x_{c,e}^r|$. Table 2.2 shows the convergence of the numerical equilibrium shape to the theoretical equilibrium shape. From Table 2.2, we see that the shapes are determined more accurately in the isotropic than in the anisotropic case for the same number of marker points. This can be understood by noting that in the anisotropic surface energy case, more marker points are required to capture the anisotropic morphology than in the smoother isotropic case. In addition, we also computed the temporal evolution of the normalized total free energy $\overline{W}(t)$ and the normalized island size (area) $\overline{A}(t)$ in the weakly anisotropic case shown in Figure 2.5 which demonstrates that the area occupied by the island is conserved (mass conservation) during the entire simulation and that the total free energy of the system decays monotonically during the evolution.
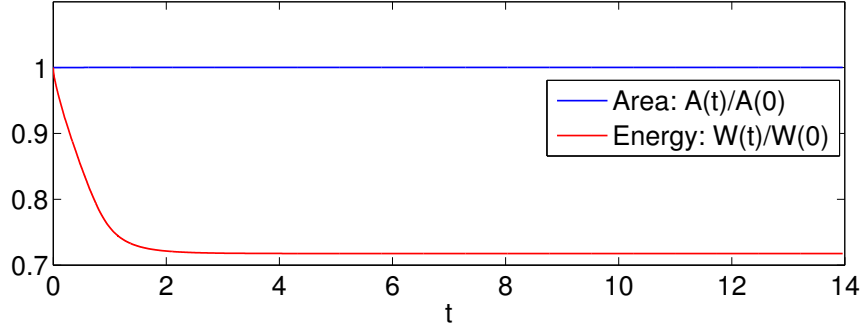
Figure 2.5: The temporal evolution of the normalized total free energy and the normalized area occupied by the island for the weakly anisotropic case with $N = 80$ and $\beta = 0.06$ presented in Fig. 2.4b.

2.5.3   Convergence test of PFEM

We now turn to the numerical convergence rate of the proposed parametric FEM by performing simulations for a closed or open curve evolution under the surface diffusion flow. The governing equations for a closed curve evolution are given by Eq. (2.4.2), and the solid-state dewetting problem can be described as an open curve evolution, which governing equations are the same as those for a closed curve evolution, but need to couple with the boundary conditions (2.1.24), (2.1.25) and (2.1.27).

In this section, we use essentially uniform time steps in our numerical simulations, i.e, $t_{m+1} - t_m = k$, $m = 0, 1, \ldots, M - 1$. In order to compute the convergence order at any fixed time, we define the following numerical approximation solution in any time interval as:

$$\mathbf{X}_{h,k}(q_j, t) = \frac{t - t_{m-1}}{k}\mathbf{X}^m(q_j) + \frac{t_m - t}{k}\mathbf{X}^{m-1}(q_j), \quad j = 0, 1, \ldots, N, \quad t \in [t_{m-1}, t_m],$$

where h and k denote the uniform spatial grid size and time step, respectively. The numerical error $e_{h,k}(t)$ in the L^∞ norm can be measured as:

$$e_{h,k}(t) = \parallel \mathbf{X}_{h,k} - \mathbf{X}_{\frac{h}{2}, \frac{k}{4}} \parallel_{L^\infty} = \max_{0 \leq j \leq N} \min_{p \in [0,1]} |\mathbf{X}_{h,k}(q_j, t) - \mathbf{X}_{\frac{h}{2}, \frac{k}{2}}(p, t)|,$$

where the curve $\mathbf{X}_{\frac{h}{2}, \frac{k}{2}}(p, t)$ belongs to the piecewise linear finite element vector spaces and at the interval nodes $p = q_j$, the curve satisfies the equations: $\mathbf{X}_{\frac{h}{2}, \frac{k}{2}}(p = $

$q_j, t) = \mathbf{X}_{\frac{h}{2}, \frac{k}{2}}(q_j, t)$. On the other hand, compared to the traditional explicit finite difference method (e.g., MPM) for computing the fourth-order geometric evolution PDEs [43, 134], which imposes the extremely strong stability restriction on the time step, i.e., $k \sim \mathcal{O}(h^4)$, the proposed semi-implicit parametric mixed FEM can greatly alleviate the stability restriction and numerical experiments indicate that the time step only needs to choose as $k \sim \mathcal{O}(h^2)$ to maintain the numerical stability.

As far as we know, there exists rare literature which has reported the numerical convergence rate about numerical schemes for solving surface diffusion equations. In the following, we will present convergence order results of the proposed parametric FEM for simulating surface diffusion flow, including the two different cases: closed curve evolution and open curve evolution (i.e., solid-state dewetting).

In order to test the convergence order of the proposed numerical scheme, the computational set-up is prepared as follows: for a closed curve evolution, including the isotropic (shown in Table 2.3) and anisotropic (shown in Table 2.5) cases, the initial shape of thin film is chosen as a closed tube, i.e., a rectangle of length 4 and width 1 adding two semi-circles with radii of 0.5 to its left and right sides, and the time step and grid size are chosen as $h_0 = (8 + \pi)/120$ and $k_0 = 0.01$; for an open curve evolution, also including the isotropic (shown in Table 2.4) and anisotropic (shown in Table 2.6) cases, the initial shape of thin film is chosen as a rectangle island of length 5 and thickness 1, and the time step and grid size are chosen as $h_0 = 0.1$ and $k_0 = 0.01$.

We compare the convergence results for the above four cases under three different time levels, i.e. $t = 0.5$, 2.0 and 5.0. As shown from Table 2.3 to Table 2.6, we can clearly observe that: for closed curve evolution cases, the convergence rate can almost perfectly attain the second-order in the L^∞ norm sense under the isotropic surface energy (see Table 2.3), but numerical experiments indicate that the surface energy anisotropy may diminish the convergence rate of the numerical scheme to about 1.5 (see Table 2.5); for open curve evolution cases, the convergence rates of the numerical scheme may further diminish to only first-order for the isotropic

$e_{h,k}(t)$	$h = h_0$ $k = k_0$	$h_0/2$ $k_0/2^2$	$h_0/2^2$ $k_0/2^4$	$h_0/2^3$ $k_0/2^6$	$h_0/2^4$ $k_0/2^8$
$e_{h,k}(t = 0.5)$	4.58E-3	1.09E-3	2.63E-4	6.40E-5	1.58E-5
order	–	2.07	2.05	2.04	2.02
$e_{h,k}(t = 2.0)$	3.61E-3	9.43E-4	2.45E-4	6.31E-5	1.61E-5
order	–	1.94	1.95	1.96	1.97
$e_{h,k}(t = 5.0)$	3.63E-3	9.47E-4	2.46E-4	6.33E-5	1.62E-5
order	–	1.94	1.95	1.96	1.97

Table 2.3: The numerical convergence orders in the L^∞ norm sense for a closed curve evolution under the isotropic surface diffusion flow.

$e_{h,k}(t)$	$h = h_0$ $k = k_0$	$h_0/2$ $k_0/2^2$	$h_0/2^2$ $k_0/2^4$	$h_0/2^3$ $k_0/2^6$	$h_0/2^4$ $k_0/2^8$
$e_{h,k}(t = 0.5)$	2.04E-2	2.59E-2	1.32E-2	6.52E-3	3.29E-3
order	–	-0.34	0.97	1.01	0.99
$e_{h,k}(t = 2.0)$	3.00E-2	2.39E-2	1.22E-2	6.10E-3	3.07E-3
order	–	0.33	0.97	1.00	0.99
$e_{h,k}(t = 5.0)$	3.33E-2	1.91E-2	9.67E-3	4.84E-3	2.43E-3
order	–	0.75	0.98	1.00	0.99

Table 2.4: The numerical convergence orders in the L^∞ norm sense for an open curve evolution under the isotropic surface diffusion flow (solid-state dewetting with isotropic surface energies), where the computational parameters are chosen as: $\beta = 0, \theta_i = 5\pi/6$.

and anisotropic cases (see Table 2.4 and 2.6), and this may be explained as that because of the high nonlinearity of the problem, we use the forward Euler scheme to discretize the relaxed contact angle boundary condition, i.e. Eq. (2.1.25). But the subtle understanding may need detailed numerical analysis, and we hope our work

$e_{h,k}(t)$	$h = h_0$ $k = k_0$	$h_0/2$ $k_0/2^2$	$h_0/2^2$ $k_0/2^4$	$h_0/2^3$ $k_0/2^6$	$h_0/2^4$ $k_0/2^8$
$e_{h,k}(t = 0.5)$	3.82E-2	1.43E-2	6.05E-3	2.19E-3	6.76E-4
order	–	1.41	1.24	1.47	1.69
$e_{h,k}(t = 2.0)$	1.80E-2	6.48E-3	2.47E-3	7.99E-4	2.24E-4
order	–	1.47	1.39	1.63	1.83
$e_{h,k}(t = 5.0)$	1.74E-2	6.19E-3	2.36E-3	7.60E-4	2.12E-4
order	–	1.49	1.39	1.64	1.84

Table 2.5: The numerical convergence orders in the L^∞ norm sense for a closed curve evolution under the anisotropic surface diffusion flow, where the parameters of the surface energy are chosen as: $m = 4, \beta = 0.06, \phi = 0$.

$e_{h,k}(t)$	$h = h_0$ $k = k_0$	$h_0/2$ $k_0/2^2$	$h_0/2^2$ $k_0/2^4$	$h_0/2^3$ $k_0/2^6$	$h_0/2^4$ $k_0/2^8$
$e_{h,k}(t = 0.5)$	2.80E-1	3.91E-2	1.73E-2	7.52E-3	3.40E-3
order	–	2.84	1.17	1.20	1.16
$e_{h,k}(t = 2.0)$	7.87E-2	3.58E-2	1.73E-2	7.71E-3	3.46E-3
order	–	1.14	1.05	1.17	1.15
$e_{h,k}(t = 5.0)$	1.37E-1	2.75E-2	1.39E-2	6.61E-3	3.10E-3
order	–	2.31	0.98	1.07	1.09

Table 2.6: The numerical convergence orders in the L^∞ norm sense for an open curve evolution under the anisotropic surface diffusion flow (solid-state dewetting with anisotropic surface energies), where the computational parameters are chosen as: $k = 4, \beta = 0.06, \phi = 0, \theta_i = 5\pi/6$.

can motivate researchers' interest on the topic.

At last, similar to that for MPM, we list the convergence result of PFEM in Table 2.7, compared to the Winterbottom construction. As can be seen that for

a fixed N, there is almost no difference in the error between the isotropic and anisotropic cases, which implies that no refinement of the mesh is needed in the anisotropic case. Moreover, since the stability constraint is not so severe as that for MPM, we can employ a fine mesh ($N = 320$ or more).

	Isotropic			Anisotropic		
N	80	160	320	80	160	320
α_{err}	3.52E-2	1.80E-2	8.92E-3	3.22E-2	1.72E-2	8.78E-3
d_{err}	3.76E-2	1.92E-2	9.54E-3	4.00E-2	2.06E-2	1.05E-2

Table 2.7: Convergence of the numerical equilibrium island shape with the theoretical equilibrium shape (Winterbottom construction) as a function of the number of grid points N by using the proposed parametric FEM. The error measures α_{err} and d_{err} are defined the same as that for the MPM.

2.6 Island/film evolution simulation results

We now examine dewetting in several geometries using the mathematical model described above for weakly anisotropic surface energies. First, we examine the evolution of small islands on a flat substrate for "smooth" $\gamma(\theta)$ with different degrees of anisotropy, m-fold crystal symmetries and rotation angles, as well as the "cusped" $\gamma(\theta)$. In this chapter, by saying "smooth", we mean the $\gamma(\theta)$ of form as in Eq. 1.2.2, and "cusped" $\gamma(\theta)$ is of form as in Eq. (1.2.3). Next, we perform numerical simulations for the evolution of large islands and semi-infinite films on a substrate, where pinch-off occurs. Then, we examine the relationship among the number of agglomerates resulting from the evolution of islands, the initial island size L and the isotropic Young angle θ_i. Finally, we examine the evolution of an infinite long thin film containing holes.

2.6.1   Small islands

1. Smooth $\gamma(\theta)$:

The evolution of small rectangular islands towards their equilibrium shapes is shown in Fig. 2.6 for the smooth $\gamma(\theta)$ with $m = 4, \beta = 0.06, \theta_i = 2\pi/3$. (a1-a4) shows the evolution for $\phi = 0$, and (b1-b4) is for $\phi = \pi/4$. In both cases, i) the dynamic contact angle θ_d rapidly converges to the equilibrium contact angle θ_a and then remains fixed throughout the remainder of the island shape evolution; ii) the edges quickly form anisotropic shapes instead of just becoming rounded and thickened as in the isotropic case [66, 134].

Fig. 2.7 shows the numerical equilibria for several different anisotropy strengths β and m-fold crystalline symmetries for fixed $\theta_i = 3\pi/4$. As the anisotropy β increases from 0.02 to 0.06 (Fig. 2.7a–c), the equilibrium island shape changes from smooth and nearly circular to an increasingly anisotropic shape with increasingly sharp corners, as expected based upon the anisotropic surface energy. As the rotational symmetry m (Fig. 2.7d–f) is increased, the number of facets in the equilibrium shape increases.

Fig. 2.8a shows the equilibrium shapes of small islands (initially rectangular with $L = 5$, $h = 1$) for different values of the isotropic Young angle $0 \leq \theta_i \leq \pi$ for $\beta = 0.06, m = 4$. Unlike in the isotropic case (even though $\theta_i = 0$ or π), complete wetting (or dewetting) does not occur with anisotropic surface energies. This can be understood by noting that the bending term which appears in the anisotropic Young equation (2.1.22) and is absent in its isotropic analogue, leads to an equilibrium angle θ_a that differs from θ_i, and is not 0 or π even when $\theta_i = 0$ or π (Fig. 2.8b).

We also performed numerical simulations of the evolution of small islands with finite values of ϕ in Eq. (1.2.2) for the weakly anisotropic cases for $\beta = 0.06, m = 4$ — this corresponds to different rotations of the crystalline axis of the island relative to the substrate normal. The numerical equilibrium shapes for different θ_i and phase shift angles ϕ are shown in Figs. 2.9a and 2.9b, respectively. The asymmetry of the equilibrium shapes is clearly seen in the two figures, resulting from breaking
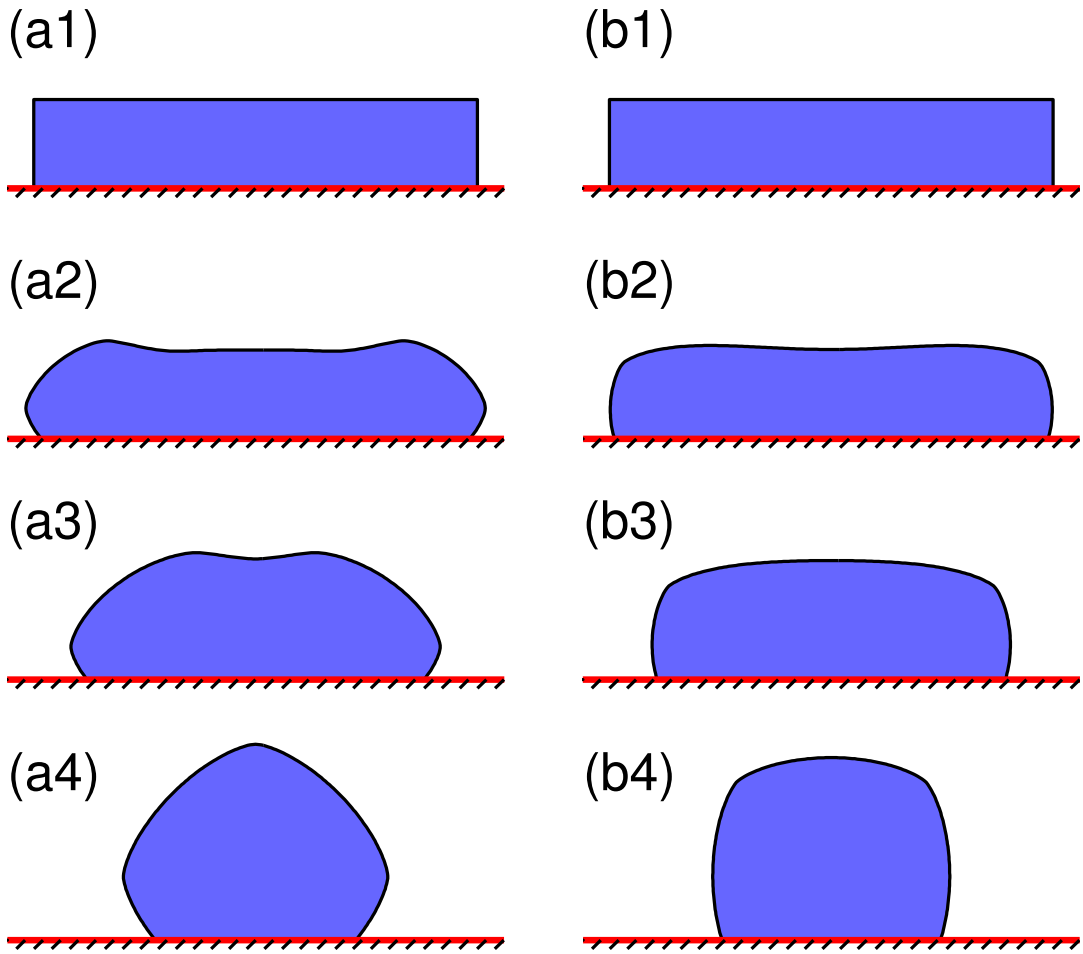
Figure 2.6: Evolution of thin island films with smooth weakly anisotropic surface energy for different values of ϕ. (a1-a4) is for $\phi = 0$; (b1-b4) is for $\phi = \pi/4$. $m = 4, \beta = 0.06, \theta_i = 2\pi/3$ for both cases.

the symmetry of the surface energy anisotropy (see Eq. (1.2.2)) with respect to the substrate normal. The numerical results confirm that the left and right equilibrium contact angles are two roots of the anisotropic Young equation (2.1.22). In general, it is possible for a crystal island with an m-fold rotation symmetry to exhibit 0 to $m - 1$ corners upon rotation of the crystal axes with respect to the substrate ϕ and the isotropic Young angle θ_i.
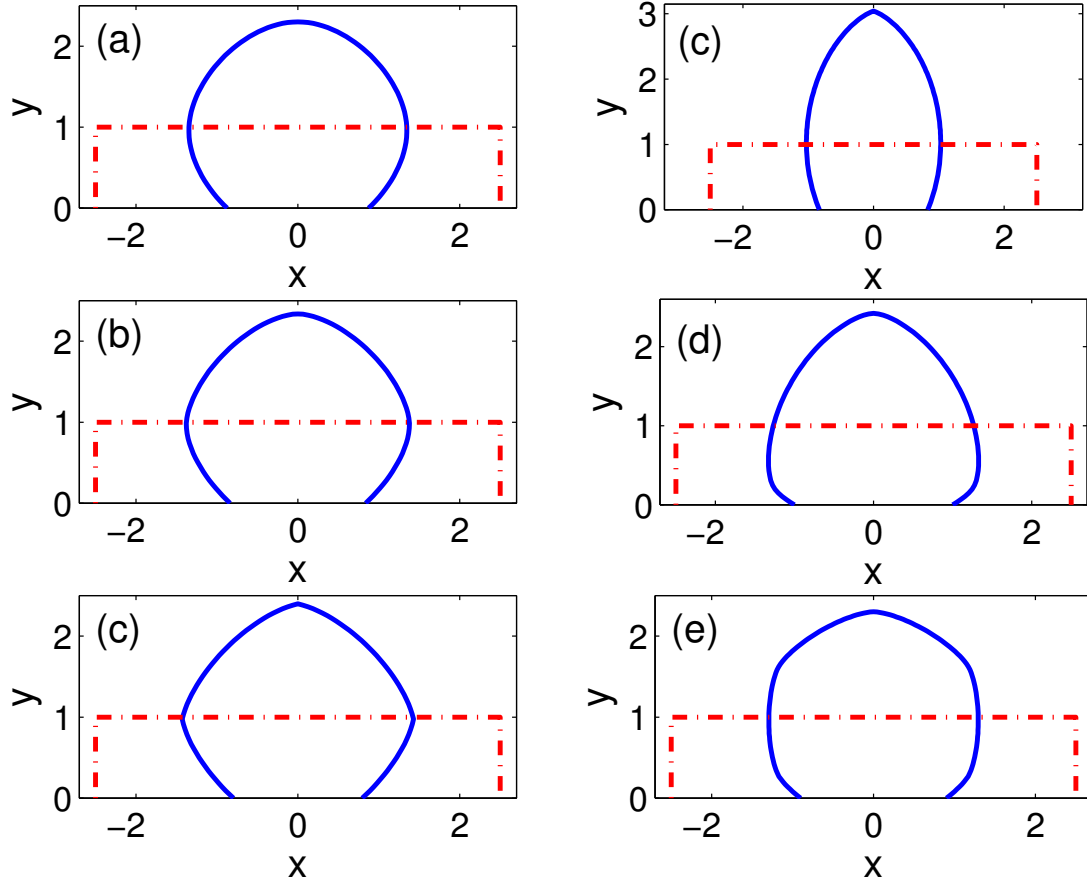
Figure 2.7: Equilibrium morphologies (blue solid curves) of the initial $L = 5$ islands (red dash-dot lines) for different anisotropies β and crystalline rotational symmetry orders m ($\theta_i = 3\pi/4$ in all cases). Figures (a) - (c) are results for $\beta = 0.02, 0.04, 0.06$ ($m = 4$ are fixed). Figures (d) - (f) are simulation results for (d) $m = 2, \beta = 0.32$, (e) $m = 3, \beta = 0.1$, and (f) $m = 6, \beta = 0.022$, respectively.

2. Cusped $\gamma(\theta)$:

In addition, we performed simulations for the regularized cusped $\gamma(\theta)$ of form (Eq. (1.2.4))

$$\gamma(\theta) = \sum_{i=1}^{n} \sqrt{\varepsilon + (1 - \varepsilon)\sin^2(\theta - \alpha_i)}.$$

The morphological evolution is shown in Fig. 2.10 with fixed $n = 2, \theta_i = 2\pi/3, \varepsilon = 10^{-2}$ for (a1-a4) $\alpha_{1,2} = \pi/4, 3\pi/4$ and (b1-b4) $\alpha_{1,2} = 0, \pi/2$. The evolution of both
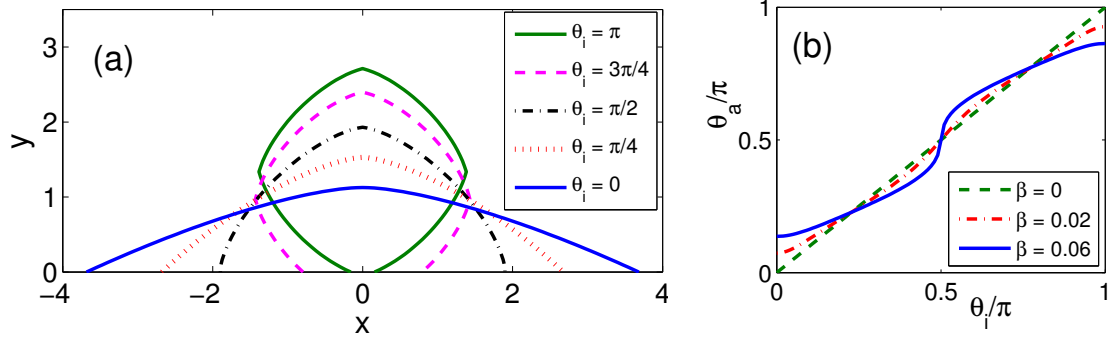
Figure 2.8: Equilibrium morphologies resulting from the evolution of several small $L = 5$ islands. Figure (a) shows the results for different values of θ_i ($\beta = 0.06, m = 4$). Figure (b) shows the relationship between the anisotropic equilibrium contact angle θ_a and θ_i for different magnitude of anisotropies β.
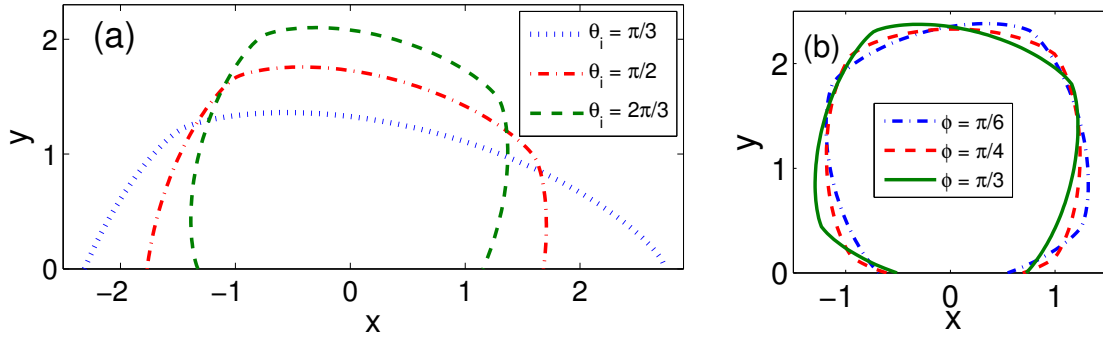
Figure 2.9: (a) Equilibrium island morphologies for small ($L = 5$) islands with a rotation of the crystal relative to the surface normal of $\phi = \pi/3$ for different values of θ_i. (b) Equilibrium island morphologies for small ($L = 5$) islands with $\theta_i = 5\pi/6$ for several different crystal rotations ϕ (phase shifts). In both figures, $\beta = 0.06$ and $m = 4$.

the dynamical contact angle and the edges is similar to that in the smooth $\gamma(\theta)$ cases. But the facets are much flatter than that in 2.6.

Fig. 2.11a-c show the numerical equilibria with $n = 2, \alpha_{1,2} = 0, \pi/2$ for different ε. As can be seen that the facets become flatter and the corners become shaper as ε decreases from 10^{-1} to 10^{-3}. This implies that the parameter ε plays a role similar
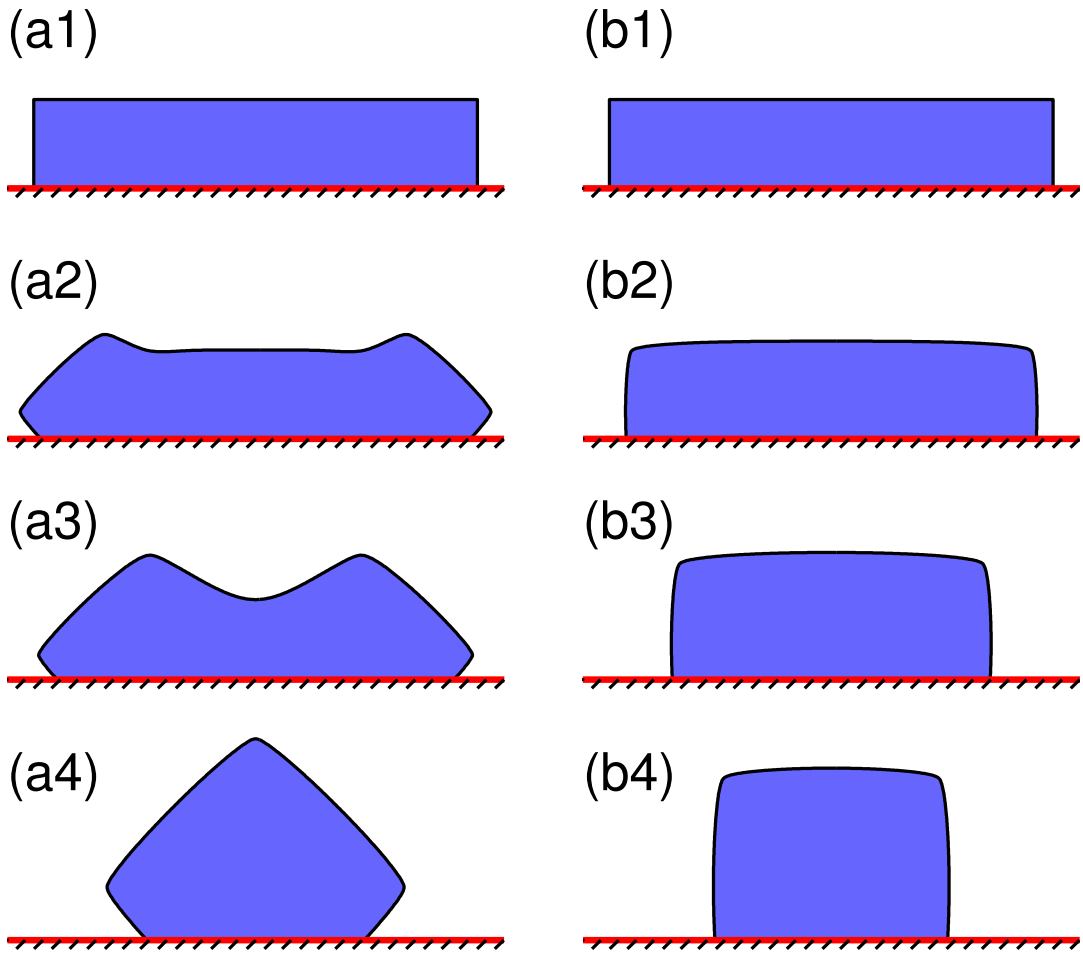
Figure 2.10: Evolution of thin island films with cusped weakly anisotropic surface energy for different values of α_i. (a1-a4) is for $\alpha_{1,2} = \pi/4, 3\pi/4$; (b1-b4) is for $\alpha_{1,2} = 0, \pi/2$. $n = 2, \varepsilon = 10^{-2}, \theta_i = 2\pi/3$ for both cases.

to β in the smooth case, which controls the flatness of the facets. Fig. 2.11d-f show the equilibria with $\varepsilon = 10^{-2}$ for different n, α_i. It can be seen that i) for the fixed n, the orientations of the facets change as we change the α_i, ii) the number of facets increases as n increases.
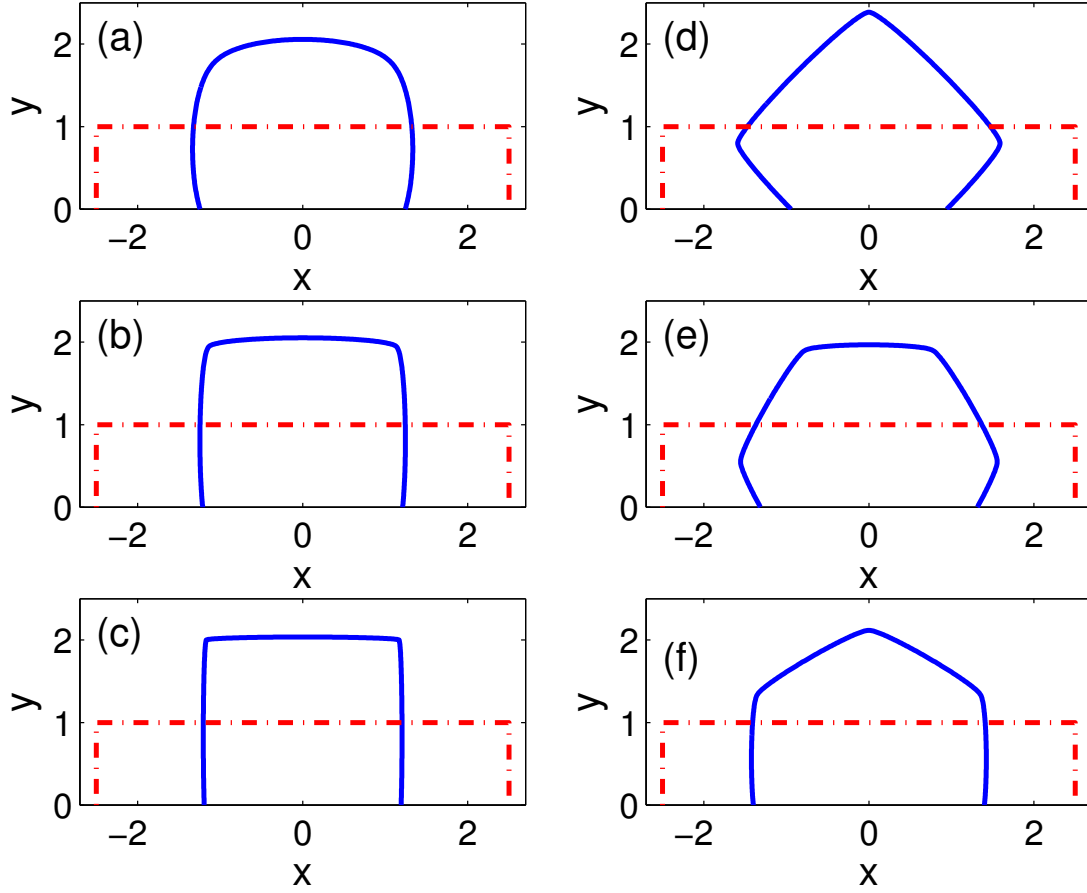
Figure 2.11: Equilibrium morphologies (blue solid curves) of the initial $L = 5$ islands (red dash-dot lines) with (regularized) cusped $\gamma(\theta)$ of form as in Eq. (1.2.4). Figures (a) - (c) are results for $\varepsilon = 10^{-1}$, 10^{-2}, $10^{-3}(n = 2,\ \alpha_{1,2} = 0, \pi/2$ are fixed). Figures (d) - (f) are simulation results ($\varepsilon = 10^{-2}$ is fixed) for (d) $n = 2,\ \alpha_{1,2} = \pi/4, 3\pi/4$, (e) $n = 3,\ \alpha_{1,2,3} = 0, \pi/3, 2\pi/3$, and (f) $n = 3,\ \alpha_{1,2,3} = \pi/6, \pi/2, 5\pi/6$, respectively. $\theta_i = 3\pi/4$ for all cases.

2.6.2 Large islands and pinch-off

As noted in the papers [41, 66], when the aspect ratios of islands are larger than critical values, the islands pinch-off leaving two, three or more islands. Figure 2.12a shows the temporal evolution of a very large (thin) island (aspect ratio of 60) with weakly anisotropic surface energy (similar to the experimental result shown in 1.3 in [137]). Figure 2.12a shows that surface diffusion kinetics very quickly leads to

the formation of ridges at the island edges followed by valleys. As time evolves and the island contact point retracts, these two features become increasing exaggerated, then two valleys merge near the island center. Eventually, the valley at the center of the islands deepens until it touches the substrate, leading to a pinch-off event that separates the initial island into a pair of islands. The corresponding evolution of the normalized total free energy and the normalized enclosed area are shown in Fig. 2.12b. During the dewetting process, the area (mass) is conserved and the energy decays. The energy undergoes a sharp drop at $t = 374$ – the moment when the pinch-off event occurs.

In addition to the aspect ratio, the parameter θ_i plays an important role in determining the number of pinch-off events that will occur. We performed a series of numerical simulations for large islands with different aspect ratios and different values of θ_i; the results are shown in Figs. 2.13 for both the isotropic case and the weakly anisotropic case and compare these with the results of Dornel [41] (shown in Fig. 1.18). In the numerical results, we observe distinct boundaries between 1, 2 and 3 (or more) islands at late times.

For the isotropic case, our numerical results (i.e., the lines that divide between different number of islands - shown in Fig. 2.13(a)) are consistent with the numerical results of Dornel [41] (the left one of Fig. 1.18), by observing that in Fig. 2.13(a) the solid lines represent Dornel's numerical results.

For the anisotropic case, our linear curve fittings (shown in Fig. 2.13(b)) identify that the 1-2 islands and 2-3 islands boundary lines are respectively $L = 24.46/\sin(\theta_i/2) + 25.91$ and $L = 73.59/\sin(\theta_i/2) + 12.74$, and these results are different from the numerical results of Dornel (the right one of Fig. 1.18). By comparing our numerical results in the isotropic and anisotropic cases in Figs. 2.13(a)-(b), we can clearly see that for the same value of θ_i an island tends to evolve into a larger number of islands in the anisotropic case than in the isotropic case, but this conclusion is just the opposite to the observations of numerical results of Dornel (shown in the right one of Fig. 1.18).
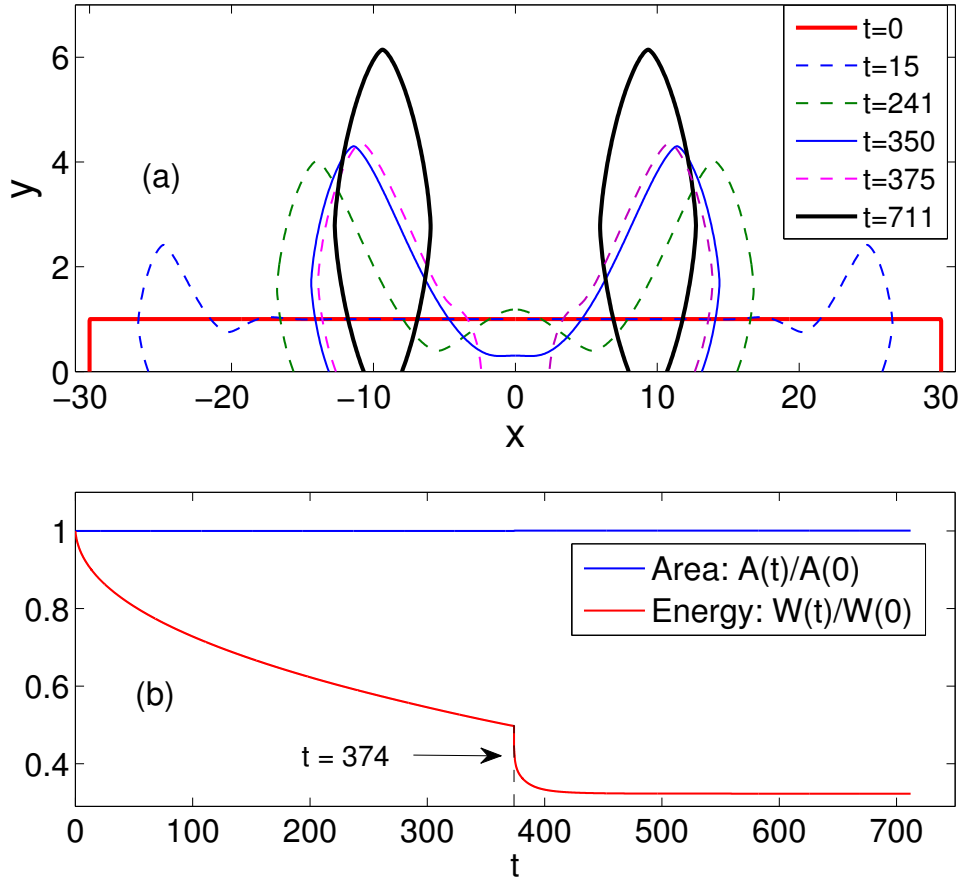
Figure 2.12: (a) The evolution of a long, thin island (aspect ratio of 60) with weakly anisotropic surface energy ($\beta = 0.06, m = 4, \theta_i = 5\pi/6$). Note the difference in vertical and horizontal scales. (b) The corresponding temporal evolution of the normalized total free energy and the normalized area (mass).

This difference of numerical results in the anisotropic case may be caused by the phase shift angle ϕ. We used $m = 4, \phi = 0$, which leads to the diamond equilibrium shown in Fig. 2.6(a4), where $\theta = 0, \pi/2$ (in the initial state) are characterized by a maximum of the surface energy. While they used $m = 8, \phi = \pi/8$, where $\theta = 0, \pi/2$ are of minimum surface energy. We later performed simulations for $\phi = \pi/4$, where $\theta = 0, \pi/2$ are also of minimum surface energy, and we can draw the same conclusion as Dornel *et al.* from the phase diagram of the number of agglomerates shown in Fig. 2.14.
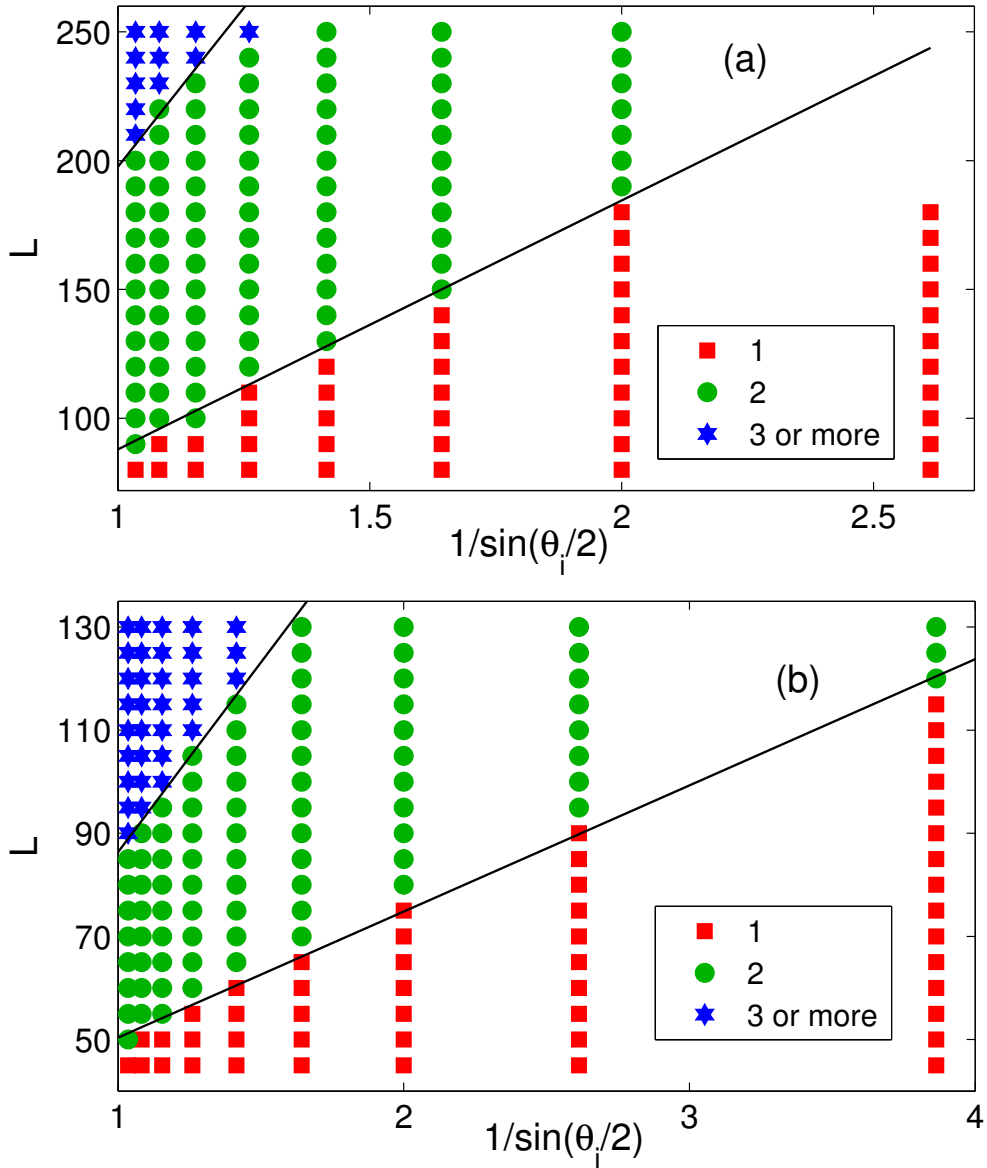
Figure 2.13: The number of islands formed from the retraction of a high aspect ratio island as a function of initial length L and θ_i ($h = 1$) (a) for the isotropic case and (b) anisotropic case with $\beta = 0.06, m = 4$. In (a), the solid lines are numerical results of Dornel [41]. In (b), the 1-2 islands and 2-3 islands boundaries (solid lines) are linear curve fittings to our numerical results — $L = 24.46/\sin(\theta_i/2) + 25.91$ and $L = 73.59/\sin(\theta_i/2) + 12.74$, respectively.
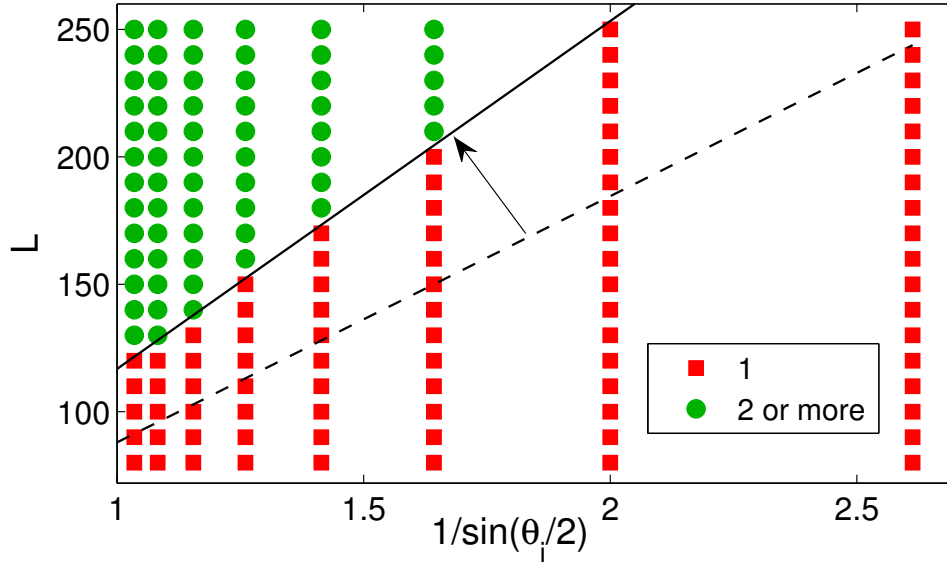
Figure 2.14: The number of islands formed from the retraction of a high aspect ratio island as a function of initial length L and θ_i ($h = 1$) for the weakly anisotropic case with $\beta = 0.06, m = 4, \phi = \pi/4$. The dash line is the 1-2 island boundary in Fig. 2.13(a). The solid line is the fitting for 1-2 islands boundary: $L = 136.5/\sin(\theta_i/2) - 19.73$.

2.6.3   Semi-infinite films

Several earlier studies have shown that a discontinuous film (i.e., a semi-infinite film) retracts such that the retraction distance scales with time according to a power law relation $l \sim t^n$ for sufficiently long time. For the isotropic case, analytical predictions in the small film surface slope limit suggest $n = 1/4$ by Srolovitz [118] and $n = 2/5$ by Wong [134]. On the other hand, numerical simulations using the sharp interface model [134] and phase field model [66] both suggest that $n \approx 0.4$ in the isotropic limit. A study of the anisotropic case also found $n \approx 0.4$ in physical experiments on the dewetting of single crystal nickel films [75] and silicon-on-insulator films [85].

We simulated the evolution of a discontinuous film (semi-infinite flat film with a step) with the anisotropic surface energy $\gamma(\theta) = 1 + \beta \cos(4\theta)$ and observed a
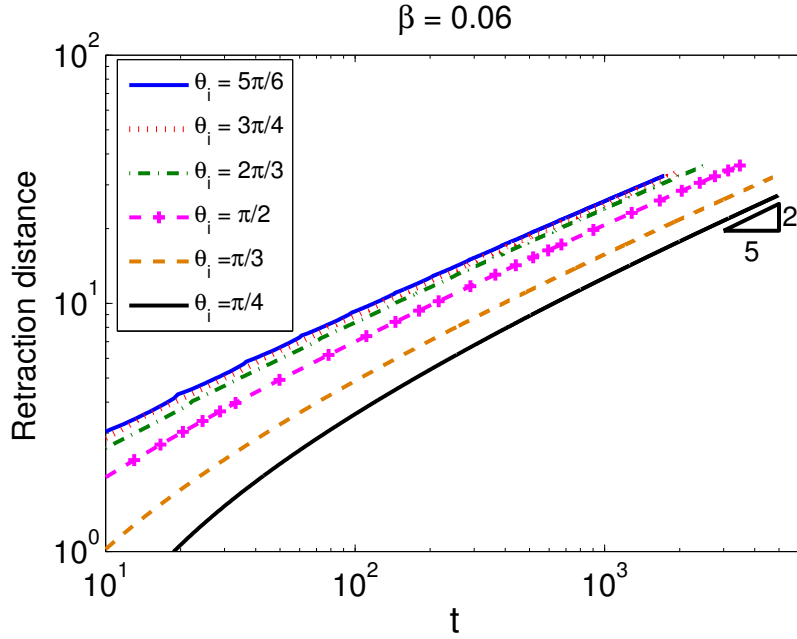
Figure 2.15: Retraction distance (the moving distance of the contact point) l vs time t for $\beta = 0.06$.

power-law retraction rate. Figure 2.15 shows a typical log-log plot for computing the exponent n of power law under $\beta = 0.06$ with different isotropic Young angles. Figure 2.16 shows the exponent n as a function of θ_i for different degrees of anisotropy β. As shown in Fig. 2.16, the power law exponent n are all in the 0.4-0.5 range, depending on θ_i but nearly independent of the strength of the anisotropy.

2.6.4 Infinite films with a hole

At last, we performed numerical simulations for the evolution of an initially continuous thin film containing a single hole from the free surface to the substrate. As reported previously [66, 118], there exists a critical hole size above which the hole gets larger (i.e., Case I - *dewetting*, shown in Fig. 2.17a) or the hole shrinks and closes (Case II - *wetting*, shown in Fig. 2.17b).

Interestingly, we find a third case where the two sides of the hole touch and merge, leaving a covered hole/void/bubble at the continuous film-substrate interface (Case
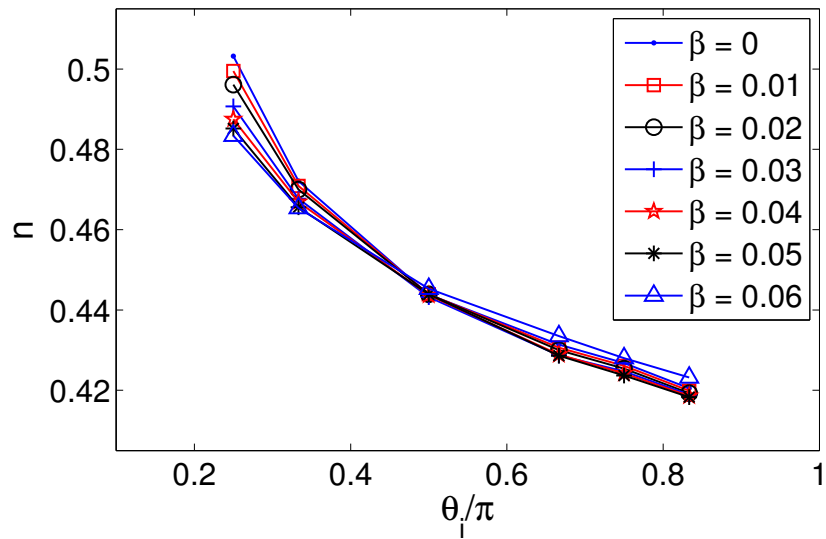
Figure 2.16: The exponent n obtained by fitting the simulation data for the retraction distance of an initially semi-infinite thin film ($l \sim t^n$) versus the corresponding isotropic Young contact angles θ_i for the case of a weakly anisotropic surface energy with different degrees of anisotropy β.

III - *void*, shown in Fig. 2.17c). In this case, if $\theta_a < \pi$, the void is stable and of finite extent, but if $\theta_a = \pi$ the void will grow leaving a continuous film disconnected from the substrate. We note that the case applies for $f(\theta) > 0$ for all θ (see Eq. (2.1.22) for definition of $f(\theta)$). The occurrence of these three behaviors depends on θ_i (or θ_a) and the initial size of the hole. Figure 2.18 shows the phase diagram for the relation among the occurrence of the three cases, the parameters θ_i and the initial hole size d for the isotropic and an anisotropic surface energy cases. As revealed by the figure, it is easier to form a void at the interface (Case III) for thin films with anisotropic surface energy than when the surface energy is isotropic under the same conditions.
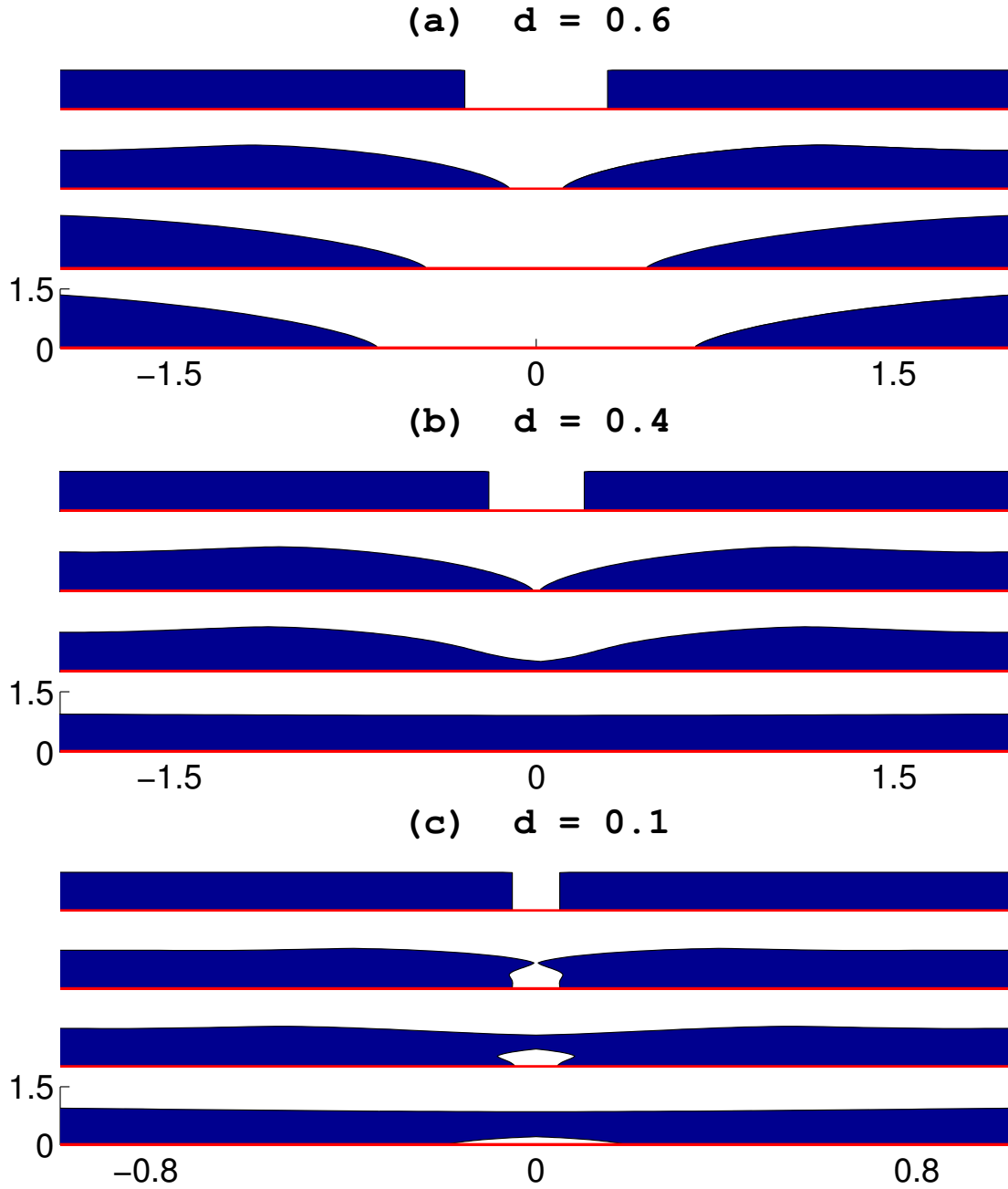
Figure 2.17: Three different types of morphological evolution of an infinite film with a hole of diameter d under anisotropic surface energy conditions, $\gamma(\theta) = 1 + 0.06\cos(4\theta)$ and $\theta_i = \pi/2$, (a) Case I: dewetting; (b) Case II: wetting; (c) Case III: void. Note that the vertical and horizontal scales are different.
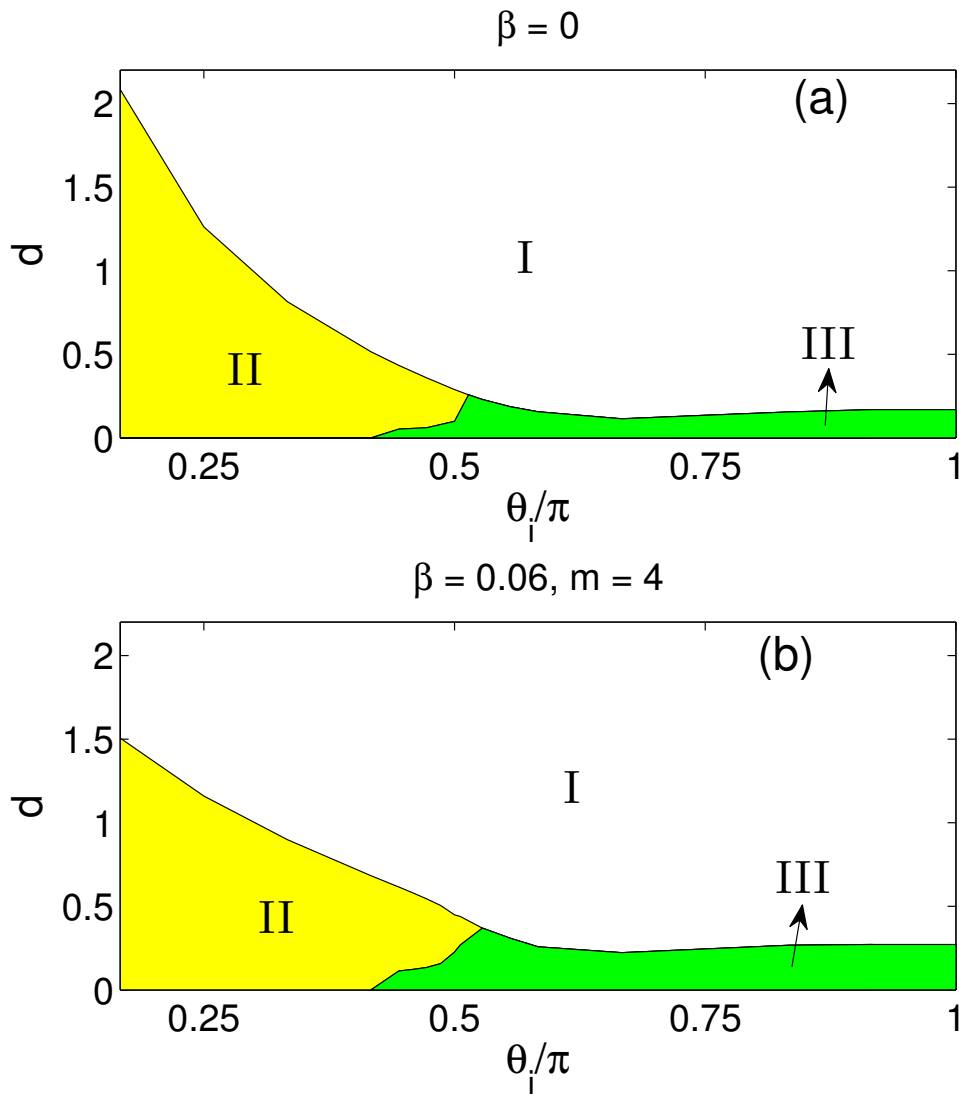
Figure 2.18: Diagram showing the conditions (d and θ_i) for the occurrence of the three Cases, I-*dewetting*, II-*wetting* and III-*void* for (a) isotropic and (b) anisotropic surface energies (shown by Fig. 2.17).

Extension to Strongly Anisotropic Case

As mentioned in Chapter 2, the governing equation will become ill-posed in the strongly anisotropic case, then either the total free energy of the system [27, 126] or the surface energy density $\gamma(\theta)$ needs to be regularized [48]. In this section, we first show the detailed derivation of the model for the strongly anisotropic case by regularizing the total free energy; Then we show the energy dissipation property of the proposed model; Next, we discuss the multiple equilibria construction; At last, we introduce the parametric finite element method (PFEM) for the proposed model and report the simulation results, focusing on the multiple anisotropic Young angles and equilibria.

3.1 The sharp interface model

We add the Willmore energy W_{w} into the original total free energy (2.1.1):

$$W_{\mathrm{w}} = \int_{\Gamma} \frac{\varepsilon^2}{2} \kappa^2 \, d\Gamma, \tag{3.1.1}$$

where ε is a regularization parameter and κ is the curvature of the curve Γ.

Following with the same approach presented in Chapter 2, the curve $\Gamma(t)$ is perturbed to the new curve $\Gamma^\epsilon(t)$ along its normal and tangent directions. We can define the curvature κ^ϵ of the new curve $\Gamma^\epsilon(t)$ due to the infinitesimal perturbation

defined in Eq. (2.1.2) as:

$$\kappa^\epsilon = \frac{-(y_{ss} + \epsilon v_{ss})(x_s + \epsilon u_s) + (x_{ss} + \epsilon u_{ss})(y_s + \epsilon v_s)}{[(x_s + \epsilon u_s)^2 + (y_s + \epsilon v_s)^2]^{3/2}}, \tag{3.1.2}$$

when $\epsilon = 0$, the curvature κ^ϵ reduces to the curvature of perturbed curve $\Gamma(s,t)$, i.e. $\kappa = -y_{ss}x_s + x_{ss}y_s$. The perturbed Willmore energy becomes

$$W_w^\epsilon = \frac{\varepsilon^2}{2} \int_{\Gamma^\epsilon} (\kappa^\epsilon)^2 \, d\Gamma^\epsilon = \frac{\varepsilon^2}{2} \int_0^L (\kappa^\epsilon)^2 \sqrt{(x_s + \epsilon u_s)^2 + (y_s + \epsilon v_s)^2} \, ds. \tag{3.1.3}$$

Then we can calculate the energy change rate of the regularization term W_w about the curve $\Gamma(s,t)$ due to the infinitesimal perturbation with respect to ϵ at the time t:

$$
\begin{aligned}
\frac{dW_w^\epsilon}{d\epsilon}\Big|_{\epsilon=0} &= \lim_{\epsilon \to 0} \frac{W_w^\epsilon - W_w}{\epsilon} \\
&= \frac{\varepsilon^2}{2} \lim_{\epsilon \to 0} \frac{1}{\epsilon} \left\{ \int_0^L (\kappa^\epsilon)^2 \sqrt{(x_s + \epsilon u_s)^2 + (y_s + \epsilon v_s)^2} \, ds - \int_0^L \kappa^2 \, ds \right\} \\
&= \frac{\varepsilon^2}{2} \int_0^L \left\{ \lim_{\epsilon \to 0} \frac{1}{\epsilon} \left[(\kappa^\epsilon)^2 \sqrt{(x_s + \epsilon u_s)^2 + (y_s + \epsilon v_s)^2} - \kappa^2 \right] \right\} ds \\
&= \frac{\varepsilon^2}{2} \int_0^L 2\kappa \Big(\frac{d\kappa^\epsilon}{d\epsilon} \Big) \Big|_{\epsilon=0} \, ds \\
&\quad + \frac{\varepsilon^2}{2} \int_0^L \kappa^2 \Big(\frac{d}{d\epsilon} \sqrt{(x_s + \epsilon u_s)^2 + (y_s + \epsilon v_s)^2} \Big) \Big|_{\epsilon=0} \, ds \\
&= \frac{\varepsilon^2}{2} \int_0^L 2\kappa \big(\kappa_s \psi - \kappa^2 \varphi - \varphi_{ss} \big) \, ds + \frac{\varepsilon^2}{2} \int_0^L \kappa^2 \big(\kappa\varphi + \psi_s \big) \, ds \\
&= \int_0^L \varepsilon^2 \kappa \kappa_s \psi \, ds - \int_0^L \varepsilon^2 \kappa^3 \varphi \, ds - \big(\varepsilon^2 \kappa \varphi_s \big) \Big|_0^L + \big(\varepsilon^2 \kappa_s \varphi \big) \Big|_0^L - \int_0^L \varepsilon^2 \kappa_{ss} \varphi \, ds \\
&\quad + \int_0^L \frac{\varepsilon^2}{2} \kappa^3 \varphi \, ds + \Big(\frac{\varepsilon^2}{2} \kappa^2 \psi \Big) \Big|_0^L - \int_0^L \varepsilon^2 \kappa \kappa_s \psi \, ds \\
&= -\int_0^L \varepsilon^2 \Big[\kappa_{ss} + \frac{\kappa^3}{2} \Big] \varphi \, ds - \big(\varepsilon^2 \kappa \varphi_s \big) \Big|_0^L + \big(\varepsilon^2 \kappa_s \varphi \big) \Big|_0^L + \Big(\frac{\varepsilon^2}{2} \kappa^2 \psi \Big) \Big|_0^L, \tag{3.1.4} \\
&= -\int_0^L \varepsilon^2 \Big[\kappa_{ss} + \frac{\kappa^3}{2} \Big] \varphi \, ds + \big(\varepsilon^2 \kappa_s \varphi \big) \Big|_0^L. \tag{3.1.5}
\end{aligned}
$$

Note here that φ_s is an arbitrary smooth function and if we want this term to disappear, the most natural way is to let the curvature κ be zero at the two contact points. We refer to this as the "Zero-curvature" condition. So the κ terms vanished, and Eq. (3.1.4) became Eq. (3.1.5).

Similarly, making use of Eq. (2.1.12), the boundary terms in Eq. (3.1.5) can be rewritten into

$$\varepsilon^2 \Big(\kappa_s \varphi \Big) \Big|_0^L = \varepsilon^2 (u(0,t)\kappa_s(\theta_d^l) \sin \theta_d^l - u(L,t)\kappa_s(\theta_d^r) \sin \theta_d^r). \qquad (3.1.6)$$

Therefore, under the strongly anisotropic cases, by combining Eq. (3.1.5) with Eq. (2.1.9), we can obtain the first variation of the total free energy $W + W_{\mathrm{w}}$ with respect to the moving curve Γ and the right contact point x_c^r and left contact point x_c^l as follows:

$$\frac{\delta(W + W_{\mathrm{w}})}{\delta \Gamma} = \Big(\gamma(\theta) + \gamma''(\theta) \Big) \kappa - \varepsilon^2 \Big[\frac{\partial^2 \kappa}{\partial s^2} + \frac{\kappa^3}{2} \Big], \qquad (3.1.7)$$

$$\frac{\delta(W + W_{\mathrm{w}})}{\delta x_c^r} = \gamma(\theta_d^r) \cos \theta_d^r - \gamma'(\theta_d^r) \sin \theta_d^r + \Big(\gamma_{FS} - \gamma_{VS} \Big)$$

$$- \varepsilon^2 \frac{\partial \kappa}{\partial s}(\theta_d^r) \sin \theta_d^r, \qquad (3.1.8)$$

$$\frac{\delta(W + W_{\mathrm{w}})}{\delta x_c^l} = - \Big[\gamma(\theta_d^l) \cos \theta_d^l - \gamma'(\theta_d^l) \sin \theta_d^l + \Big(\gamma_{FS} - \gamma_{VS} \Big)$$

$$- \varepsilon^2 \frac{\partial \kappa}{\partial s}(\theta_d^l) \sin \theta_d^l \Big], \qquad (3.1.9)$$

Similar to the weakly anisotropic case, after obtaining the first variation of $W + W_{\mathrm{w}}$, we can define the chemical potential of the system as:

$$\mu = \Omega_0 \frac{\delta(W + W_{\mathrm{w}})}{\delta \Gamma} = \Omega_0 \Big[\Big(\gamma(\theta) + \gamma''(\theta) \Big) \kappa - \varepsilon^2 \Big(\frac{\partial^2 \kappa}{\partial s^2} + \frac{\kappa^3}{2} \Big) \Big], \qquad (3.1.10)$$

and the normal velocity V_n of the moving interface as:

$$V_n = \frac{D_s \nu \Omega_0^2}{k_B T_e} \frac{\partial^2}{\partial s^2} \Big[\Big(\gamma(\theta) + \gamma''(\theta) \Big) \kappa - \varepsilon^2 \Big(\frac{\partial^2 \kappa}{\partial s^2} + \frac{\kappa^3}{2} \Big) \Big]. \qquad (3.1.11)$$

Under the same dimensionless scaling as in the weakly anisotropic case, we can describe the solid-state dewetting of a thin film on a flat, rigid substrate by the following dimensionless sharp interface model:

$$\begin{cases} \dfrac{\partial \mathbf{X}}{\partial t} = V_n \mathcal{N} = \dfrac{\partial^2 \mu}{\partial s^2} \mathcal{N}, \\ \mu = \Big(\gamma(\theta) + \gamma''(\theta) \Big) \kappa - \varepsilon^2 \Big(\dfrac{\partial^2 \kappa}{\partial s^2} + \dfrac{\kappa^3}{2} \Big). \end{cases} \qquad (3.1.12)$$

Again, note here that $\mathbf{X}, t, V_n, s, \kappa, \mu, \gamma$ are dimensionless variables, ε and η are two dimensionless parameters, and we still use the same notations for brevity. The above governing equation (3.1.12) are subject to the following dimensionless conditions:

(i) Contact point condition (**BC1**)

$$y(x_c^l, t) = 0, \qquad y(x_c^r, t) = 0, \tag{3.1.13}$$

this is the same as the one in the weakly anisotropic case.

(ii) Relaxed contact angle condition (**BC2**)

$$\frac{dx_c^l}{dt} = \eta f_\varepsilon(\theta_d^l), \qquad \frac{dx_c^r}{dt} = -\eta f_\varepsilon(\theta_d^r), \tag{3.1.14}$$

this condition is similar to the one in the weakly anisotropic case. The difference is that the function $f(\theta)$ in (2.1.25) changes to the function f_ε which is defined as:

$$f_\varepsilon(\theta) := \gamma(\theta)\cos\theta - \gamma'(\theta)\sin\theta - \sigma - \varepsilon^2 \frac{\partial\kappa}{\partial s}(\theta)\sin\theta, \tag{3.1.15}$$

and the dimensionless material parameter σ is defined as in (2.1.26).

(iii) Zero-mass flux condition (**BC3**)

$$\frac{\partial\mu}{\partial s}(x_c^l, t) = 0, \qquad \frac{\partial\mu}{\partial s}(x_c^r, t) = 0, \tag{3.1.16}$$

this condition is similar to the weakly anisotropic case with a different μ, it also ensures that the total mass of the thin film is conserved.

(iv) Zero-curvature condition (**BC4**)

$$\kappa(x_c^l, t) = 0, \qquad \kappa(x_c^r, t) = 0. \tag{3.1.17}$$

It should be noted that the dynamical evolution equation for the strongly anisotropic case becomes to a sixth-order PDE, compared to the fourth-order PDE in the weakly anisotropic case (2.1.23). To make the system well-posed, we need one more boundary condition (**BC4**), which comes from the derivation of the model (from Eq. (3.1.4) to Eq. (3.1.5)). This condition ensures the total free energy to be dissipative during the evolution.

3.2   Mass conservation and energy dissipation

We use the same notations introduced in section 2.2. Since the proof of mass conservation is almost the same as the weakly anisotropic case, we omit the proof here, and we focus on proving the energy dissipation for the strongly anisotropic case.

Proof of energy dissipation. The total free energy of the system for solid-state dewetting problems under the strongly anisotropic case is $W(t) + W_{\mathrm{w}}(t)$ with

$$W(t) = \int_0^1 \gamma(\theta) s_p \, dp + (\gamma_{FS} - \gamma_{VS})(x_c^r - x_c^l),$$

$$W_{\mathrm{w}}(t) = \frac{\varepsilon^2}{2} \int_0^1 \kappa^2 s_p \, dp.$$

As shown in section 2.2 that

$$
\begin{aligned}
\frac{dW(t)}{dt} = & \int_0^{L(t)} \kappa\big(\gamma(\theta) + \gamma''(\theta)\big) \mathbf{X}_t \cdot \mathcal{N} \, ds \\
& + \frac{dx_c^r}{dt}\bigg(\gamma(\theta)\cos\theta - \gamma'(\theta)\sin\theta + \gamma_{FS} - \gamma_{VS}\bigg)_{\theta=\theta_d^r} \\
& - \frac{dx_c^l}{dt}\bigg(\gamma(\theta)\cos\theta - \gamma'(\theta)\sin\theta + \gamma_{FS} - \gamma_{VS}\bigg)_{\theta=\theta_d^l}.
\end{aligned}
\tag{3.2.1}
$$

Note that the following equations hold:

$$\kappa_t s_p = -\theta_{pt} - \kappa s_{pt},$$

$$\theta_t s_p = \mathbf{X}_{pt} \cdot \mathcal{N}, \quad s_{pt} = \mathbf{X}_{pt} \cdot \mathcal{T},$$

$$\mathcal{N}_s = \kappa \mathcal{T}, \quad \mathcal{T}_s = -\kappa \mathcal{N}$$

We can calculate the change rate of $W_{\mathrm{w}}(t)$ as follows:

$$
\begin{aligned}
\frac{dW_{\mathrm{w}}(t)}{dt} &= \frac{\varepsilon^2}{2} \int_0^1 \left(2\kappa\kappa_t s_p + \kappa^2 s_{pt} \right) dp \\
&= \varepsilon^2 \int_0^1 \left(-\kappa\theta_{pt} - \kappa^2 s_{pt} + \frac{1}{2}\kappa^2 s_{pt} \right) dp \\
&= \varepsilon^2 \int_0^1 \left(-\kappa\theta_{pt} - \frac{1}{2}\kappa^2 s_{pt} \right) dp \tag{3.2.2} \\
&= \varepsilon^2 \left(-\kappa\theta_t \Big|_{p=0}^{p=1} + \int_0^1 \left(\kappa_s s_p \theta_t - \frac{1}{2}\kappa^2 s_{pt} \right) dp \right) \tag{3.2.3} \\
&= \varepsilon^2 \left(-\kappa\theta_t \Big|_{p=0}^{p=1} + \int_0^1 \mathbf{X}_{pt} \cdot \left(\kappa_s \mathcal{N} - \frac{1}{2}\kappa^2 \mathcal{T} \right) dp \right) \tag{3.2.4} \\
&= -\varepsilon^2 \int_0^1 \mathbf{X}_t \cdot \left(\kappa_{ss} s_p \mathcal{N} + \kappa_s \mathcal{N}_s s_p - \kappa\kappa_s s_p \mathcal{T} - \frac{1}{2}\kappa^2 \mathcal{T}_s s_p \right) dp \\
&\quad + \varepsilon^2 \left(-\kappa\theta_t + \mathbf{X}_t \cdot \left(\kappa_s \mathcal{N} - \frac{1}{2}\kappa^2 \mathcal{T} \right) \right)\Bigg|_{p=0}^{p=1} \tag{3.2.5} \\
&= -\varepsilon^2 \int_0^{L(t)} (\kappa_{ss} + \frac{1}{2}\kappa^3) \mathbf{X}_t \cdot \mathcal{N}\, ds \\
&\quad - \varepsilon^2 \frac{dx_c^r}{dt} \left(\kappa_s \sin\theta + \frac{1}{2}\kappa^2 \cos\theta \right)_{\theta=\theta_d^r} - \varepsilon^2 \kappa\theta_t \Big|_{p=1} \\
&\quad + \varepsilon^2 \frac{dx_c^l}{dt} \left(\kappa_s \sin\theta + \frac{1}{2}\kappa^2 \cos\theta \right)_{\theta=\theta_d^l} + \varepsilon^2 \kappa\theta_t \Big|_{p=0} \tag{3.2.6} \\
&= -\varepsilon^2 \int_0^{L(t)} (\kappa_{ss} + \frac{1}{2}\kappa^3) \mathbf{X}_t \cdot \mathcal{N}\, ds \\
&\quad - \varepsilon^2 \frac{dx_c^r}{dt} \left(\kappa_s \sin\theta \right)_{\theta=\theta_d^r} + \varepsilon^2 \frac{dx_c^l}{dt} \left(\kappa_s \sin\theta \right)_{\theta=\theta_d^l}. \tag{3.2.7}
\end{aligned}
$$

In the above calculation, we use integration by parts for the term $\kappa\theta_{pt}$ in (3.2.2) to get (3.2.3), then we apply integration by parts for (3.2.4) to obtain (3.2.5). (3.2.7) is obtained by applying the zero-curvature boundary condition (3.1.17).

Therefore, combining Eqs. (3.2.1) and (3.2.7) and making use of the governing equation (3.1.12) and the corresponding boundary conditions (3.1.13)-(3.1.16), we have the change rate of the total free energy:

$$\begin{aligned}
\frac{d(W + W_w)}{dt} &= \int_0^{L(t)} \left(\kappa\big(\gamma(\theta) + \gamma''(\theta)\big) - \varepsilon^2\big(\kappa_{ss} + \frac{1}{2}\kappa^3\big) \right) \mathbf{X}_t \cdot \mathcal{N}\, ds \\
&\quad + \frac{dx_c^r}{dt} \left(\Big(\gamma(\theta)\cos\theta - \gamma'(\theta)\sin\theta + \gamma_{FS} - \gamma_{VS}\Big) - \varepsilon^2 \kappa_s \sin\theta \right)_{\theta=\theta_d^r} \\
&\quad - \frac{dx_c^l}{dt} \left(\Big(\gamma(\theta)\cos\theta - \gamma'(\theta)\sin\theta + \gamma_{FS} - \gamma_{VS}\Big) - \varepsilon^2 \kappa_s \sin\theta \right)_{\theta=\theta_d^l} \\
&= \int_0^{L(t)} \mu\mu_{ss}\, ds - C\left[\left(\frac{dx_c^r}{dt}\right)^2 + \left(\frac{dx_c^l}{dt}\right)^2 \right] \\
&= -\int_0^{L(t)} \mu_s^2\, ds - C\left[\left(\frac{dx_c^r}{dt}\right)^2 + \left(\frac{dx_c^l}{dt}\right)^2 \right] \leq 0.
\end{aligned}$$

Hence, the total free energy decreases with the given governing equation and the corresponding boundary conditions.

$\square$

3.3 Multiple equilibria

According to the proposed contact angle boundary condition (**BC2**), the dynamical contact angle should converge to a root of $f_\varepsilon(\theta) = 0$. And by comparing Eq. (3.1.15) and Eq. (2.1.26), we can clearly observe that

$$f_\varepsilon(\theta) \to f(\theta) = \gamma(\theta)\cos\theta - \gamma'(\theta)\sin\theta - \sigma, \quad \text{as} \quad \varepsilon \to 0.$$

This implies that the dynamical contact angle in the strongly anisotropic case should also converge to the anisotropic Young angle θ_a, which is the root of the following anisotropic Young equation (same as Eq. (2.1.22)):

$$f(\theta) = \gamma(\theta)\cos\theta - \gamma'(\theta)\sin\theta - \sigma = 0. \tag{3.3.1}$$

When we take derivative for $f(\theta)$, we have

$$f'(\theta) = -\Big(\gamma(\theta) + \gamma''(\theta)\Big)\sin\theta. \tag{3.3.2}$$

Therefore,

- When $0 \leq \beta < \frac{1}{(m^2-1)}$, which is the weakly anisotropic (including isotropic) case, $f(\theta)$ is a monotone function.So, Eq. (3.3.1) has at most one root.

- However, unlike in the weakly anisotropic case, when $\frac{1}{(m^2-1)} < \beta < 1$, which belongs to the strongly anisotropic case, Eq. (3.3.1) has multiple roots for some σ since $f(\theta)$ is no longer monotone.

- Since the root determines the static contact angle in the equilibrium state, the equilibrium in the weakly anisotropic case is unique, but multiple equilibria may exist in the strongly anisotropic case.

In the following of this section, we study the number of possible static contact angles, i.e., the number of roots to the anisotropic Young equation, and then discuss the construction of stable equilibrium shapes in next.

We take the following dimensionless energy density as example (the variables are defined the same as in Chapter 1 and 2)

$$\gamma(\theta) = 1 + \beta \cos(m\theta), \qquad \theta \in [-\pi, \pi],$$

where m is chosen to be 2, 3, 4, 6. And we restrict the discussion to $0 \leq \beta < 1$, this is because there is no convex Wulff construction when $\beta \geq 1$ (an example is shown in Fig. 3.1), which is referred as meaningless.

3.3.1 The number of static contact angles

Since $f(\theta)$ is an even function and the θ we introduced varies from $-\pi$ to π, the following discussion is restricted on $\theta \in [0, \pi]$ and the extension to a wider interval is similar.

The number of roots to the anisotropic Young equation is related to the competition of the extreme points/values of $f(\theta)$, i.e., zeros of

$$f'(\theta) = -\left(1 - (m^2 - 1)\beta \cos(m\theta)\right) \sin \theta = 0.$$
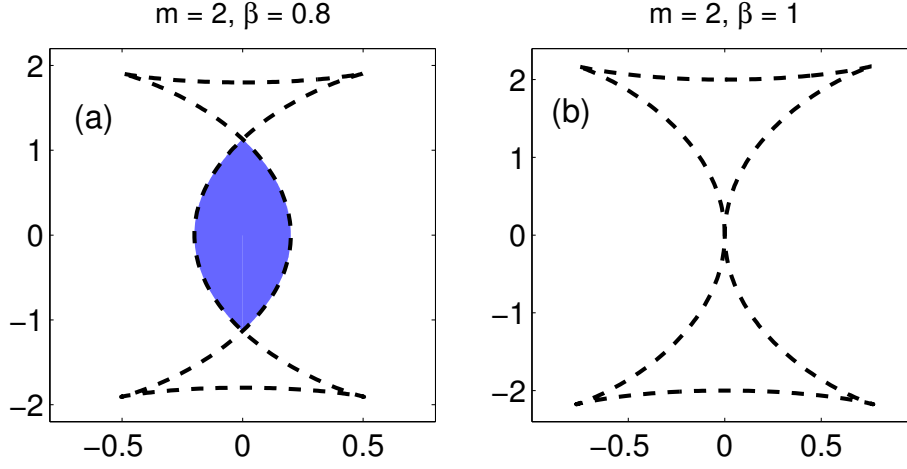
Figure 3.1: (a) Wulff envelope (black dash line) for $\beta < 1$ with the Wulff shape (the shaded area); (b) Wulff envelope for $\beta = 1$, which has no Wulff shape.

It can be seen that $f(\theta)$ has $m + 2$ extreme points: $0, \pi, \theta_j, j = 1, ..., m$ where θ_j satisfies

$$\cos(m\theta_j) = \frac{1}{(m^2 - 1)\beta}, \quad \theta_j < \theta_{j+1}, \; j = 1, ..., m - 1.$$

- $m = 2$:

  For $m = 2$, $f(\theta)$ reaches its maximum at $\theta = \theta_1$ and minimum at θ_2 (as shown in Fig. 3.2, where

  $$\theta_1 = \frac{1}{2} \arccos\left(\frac{1}{3\beta}\right), \quad \theta_2 = \pi - \theta_1.$$

  Hence, Eq. (3.3.1) has a unique root for $\sigma \in \{f(\theta_1), f(\theta_2)\} \cup (-1 - \beta, 1 + \beta)$, two roots for $\sigma \in [1 + \beta, f(\theta_1)) \cup (f(\theta_2), -1 - \beta]$ and no root for other σ (as shown in Fig. 3.3).

- $m = 3$:

  For $m = 3$, when β is small such that $f(\pi) = -1 + \beta < f(\theta_2)$, $f(\theta)$ reaches its maximum at $\theta = \theta_1$ and minimum at $\theta = \pi$, and it has a local minimum at θ_2 and a local maximum at θ_3 (as shown in Fig. 3.4(a)), where

  $$\theta_1 = \frac{1}{3} \arccos\left(\frac{1}{8\beta}\right), \quad \theta_2 = \frac{2\pi}{3} - \theta_1, \quad \theta_3 = \frac{2\pi}{3} + \theta_1.$$
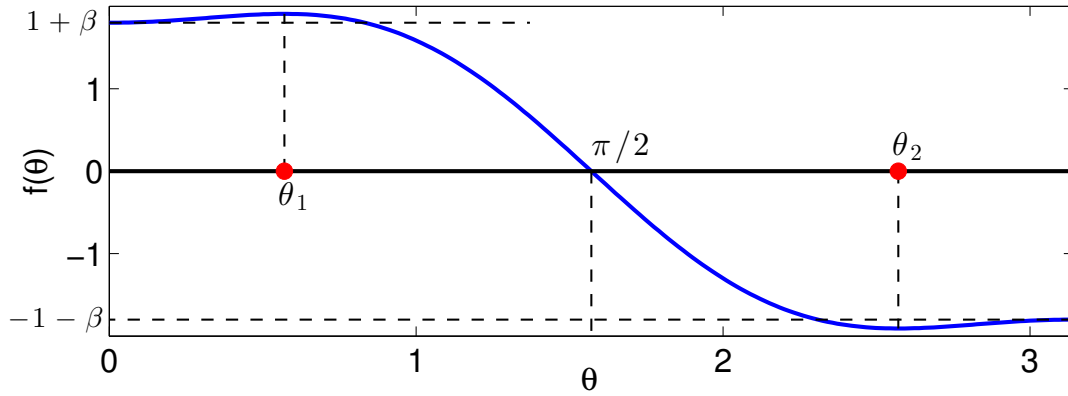
Figure 3.2: Sketch of $f(\theta)$ against θ with $m = 2, \sigma = 0$.
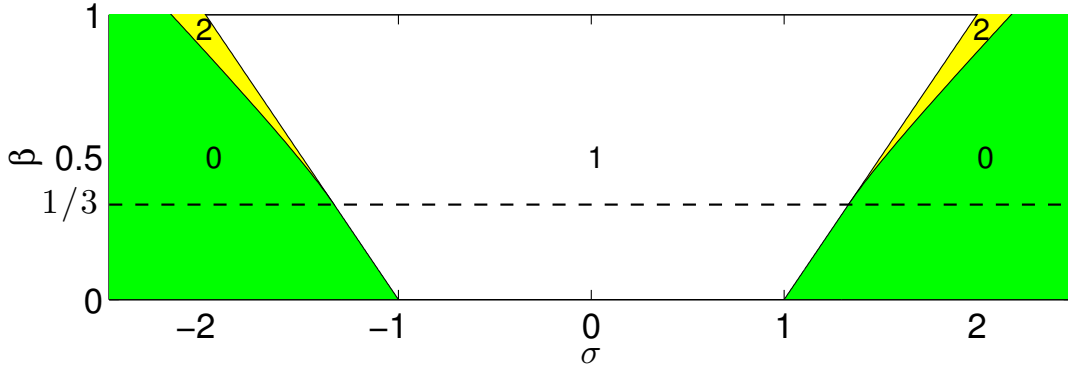
Figure 3.3: Phase diagram of the number of roots to Eq. (3.3.1) with $m = 2$ for different σ and β. The dash line $\beta = 1/3$ is the boundary of the weakly and strongly anisotropic cases.

As β goes larger, $f(\theta_2)$ becomes to a global minimum shown in Fig. 3.4(b). Hence, for different σ, Eq. (3.3.1) has at most 3 roots and the phase diagram is shown in Fig. 3.3.

- $m = 4$ and $m = 6$:

    For $m = 4$ and $m = 6$, we did similar discussion as for $m = 3$ and obtained the phase diagram (Fig. 3.6) of the number of roots to the anisotropic Young equation.

Remark: Instead of analyze the monotone intervals of $f(\theta)$, the number of roots
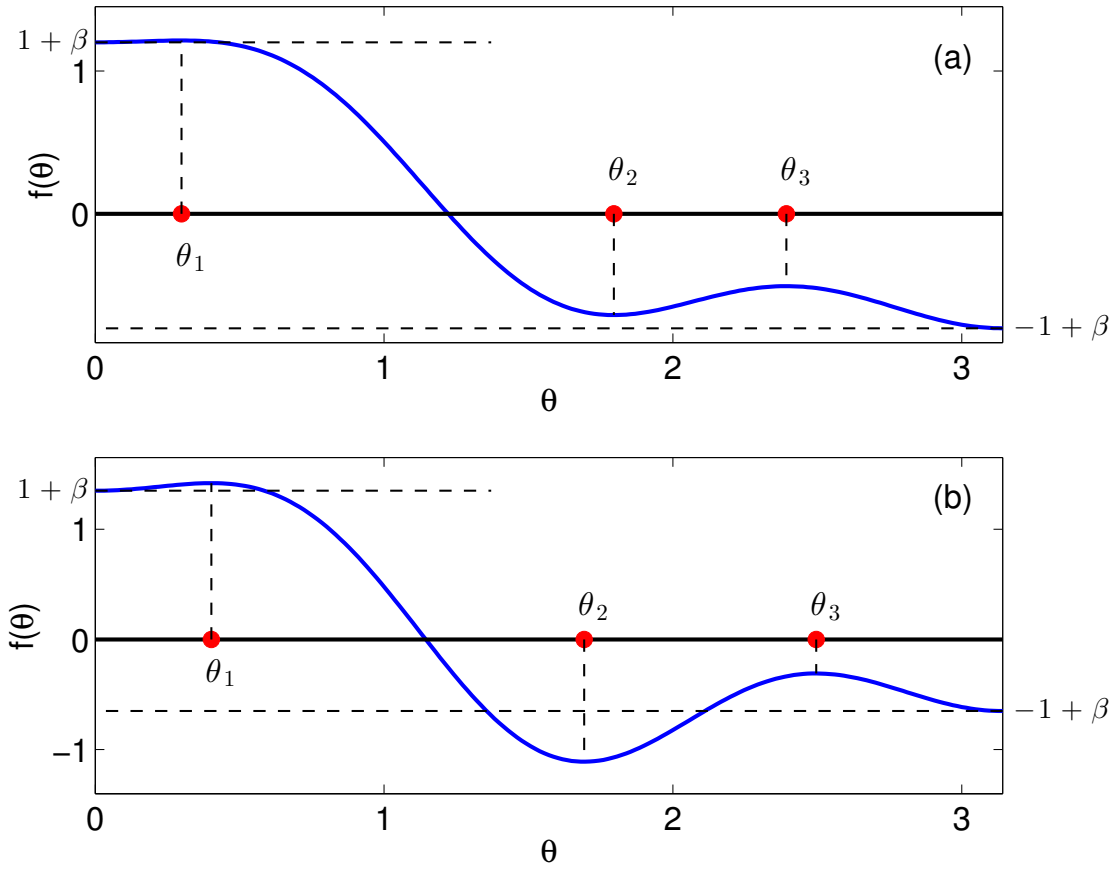
Figure 3.4: Sketch of $f(\theta)$ against θ with $m = 3, \sigma = 0$. (a) is for small β, (b) is for large β.

can be obtained by counting the intersections of the Wulff envelope and the line $y = \sigma$. This is because that the Wulff envelope has the following expression (which is Eq. (1.3.5).)

$$\begin{cases} x(\theta) = -\gamma(\theta) \sin \theta - \gamma'(\theta) \cos \theta, \\ y(\theta) = \gamma(\theta) \cos \theta - \gamma'(\theta) \sin \theta. \end{cases}$$

It can be seen that $y(\theta) = \sigma$ is the anisotropic Young equation for a fixed σ.
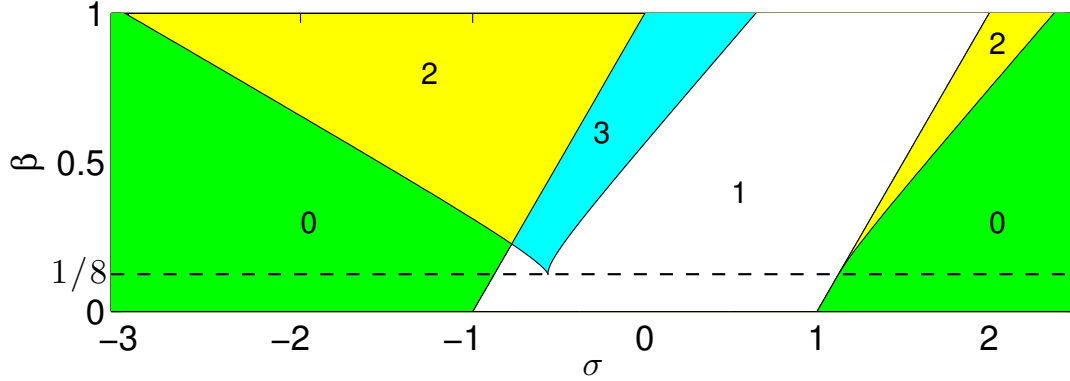
Figure 3.5: Phase diagram of the number of roots to Eq. (3.3.1) with $m = 3$ for different σ and β. The dash line $\beta = 1/8$ is the boundary of the weakly and strongly anisotropic cases.

3.3.2 Generalized Winterbottom construction

We can calculate the second variation of the total interfacial energy (without regularization) to analyze the sufficient and necessary condition for a stable equilibrium.

Recall that

$$
\frac{dW^\epsilon}{d\epsilon} = \int_0^L \left(\gamma'(\theta^\epsilon) \frac{d\theta^\epsilon}{d\epsilon} \sqrt{(x_s + \epsilon u_s)^2 + (y_s + \epsilon v_s)^2} \right.
$$
$$
\left. + \gamma(\theta^\epsilon) \frac{x_s u_s + y_s v_s + \epsilon(u_s^2 + v_s^2)}{\sqrt{(x_s + \epsilon u_s)^2 + (y_s + \epsilon v_s)^2}} \right) ds, \tag{3.3.3}
$$

where

$$
\frac{d\theta^\epsilon}{d\epsilon} = \frac{x_s v_s - y_s u_s}{(x_s + \epsilon u_s)^2 + (y_s + \epsilon v_s)^2}. \tag{3.3.4}
$$

We can further calculate
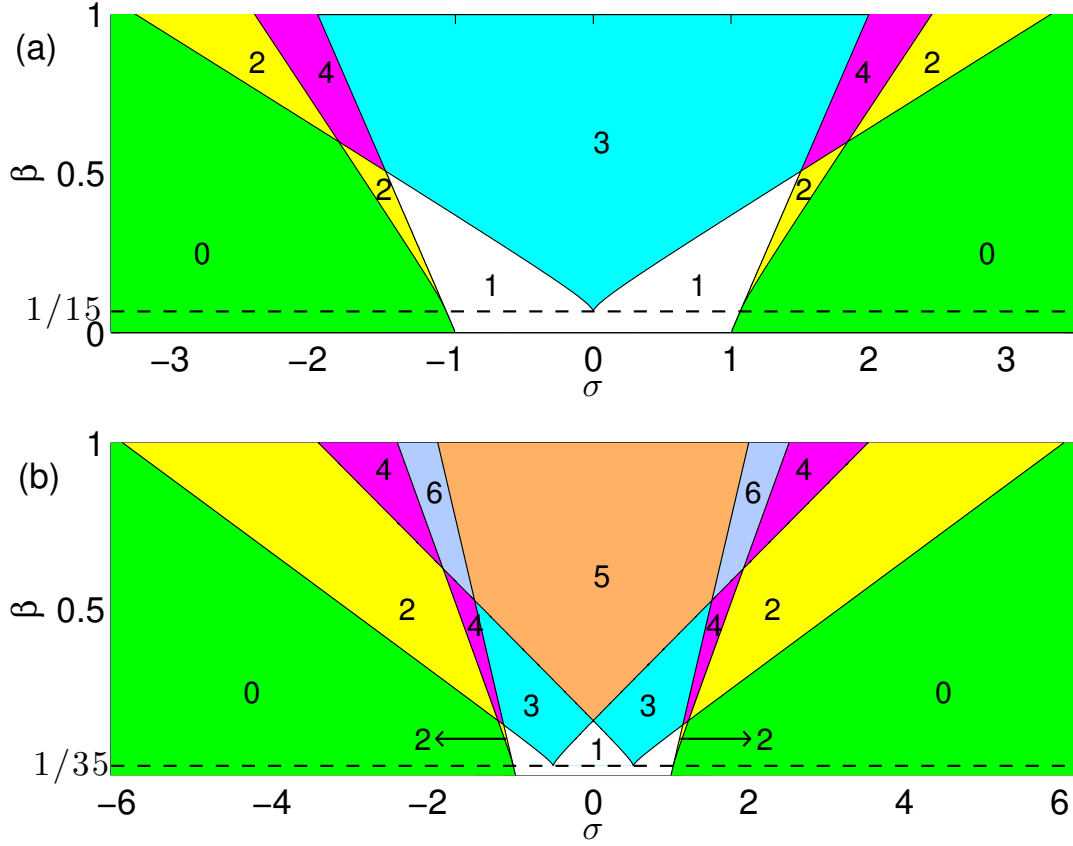
Figure 3.6: Phase diagram of the number of roots to Eq. (3.3.1) with (a) $m = 4$, (b)$m = 6$ for different σ and β.

$$
\begin{aligned}
\frac{d^2 W^\epsilon}{d\epsilon^2} \ = \ & \int_0^L \Bigg(\gamma''(\theta^\epsilon) \Big(\frac{d\theta^\epsilon}{d\epsilon}\Big)^2 \sqrt{(x_s + \epsilon u_s)^2 + (y_s + \epsilon v_s)^2} \\
& + \ \gamma'(\theta) \frac{d^2\theta^\epsilon}{d\epsilon^2} \sqrt{(x_s + \epsilon u_s)^2 + (y_s + \epsilon v_s)^2} \\
& + \ 2\gamma'(\theta^\epsilon) \frac{d\theta^\epsilon}{d\epsilon} \frac{x_s u_s + y_s v_s + \epsilon(u_s^2 + v_s^2)}{\sqrt{(x_s + \epsilon u_s)^2 + (y_s + \epsilon v_s)^2}} \\
& + \ \gamma(\theta^\epsilon) \frac{u_s^2 + v_s^2}{\sqrt{(x_s + \epsilon u_s)^2 + (y_s + \epsilon v_s)^2}} \\
& - \ \gamma(\theta^\epsilon) \frac{\Big(x_s u_s + y_s v_s + \epsilon(u_s^2 + v_s^2)\Big)^2}{\Big((x_s + \epsilon u_s)^2 + (y_s + \epsilon v_s)^2\Big)^{3/2}} \Bigg) ds,
\end{aligned}
$$

where

$$\frac{d^2\theta^\epsilon}{d\epsilon^2} = -2\frac{(x_s v_s - y_s u_s)\Big(x_s u_s + y_s v_s + \epsilon(u_s^2 + v_s^2)\Big)}{\Big((x_s + \epsilon u_s)^2 + (y_s + \epsilon v_s)^2\Big)^2}.$$

Therefore, we have

$$
\begin{aligned}
\frac{d^2 W^\epsilon}{d\epsilon^2}\Big|_{\epsilon=0} &= \int_0^L \Big(\gamma''(\theta)(x_s v_s - y_s u_s)^2 + \gamma'(\theta)\big(-2(x_s v_s - y_s u_s)(x_s u_s + y_s v_s)\big) \\
&\quad + 2\gamma'(\theta)(x_s v_s - y_s u_s)(x_s u_s + y_s v_s) \\
&\quad + \gamma(\theta)\big((u_s^2 + v_s^2) - (x_s u_s + y_s v_s)^2\big)\Big) ds \\
&= \int_0^L \Big(\gamma(\theta) + \gamma''(\theta)\Big)(x_s v_s - y_s u_s)^2 \, ds \\
&= \int_0^L \widetilde{\gamma}(\theta)(\varphi_s - \kappa\psi)^2 \, ds. \quad\quad (3.3.5)
\end{aligned}
$$

According to the above equation (3.3.5) and Eq. (2.1.9), we have the following theorem, providing the sufficient and necessary condition for a stable equilibrium.

Theorem 3.3.1. $\Gamma_e := \big(x(s),\, y(s)\big),\ s \in [0, L]$ *is a stable equilibrium shape (without scaling, film/vapor interface) of the solid-state dewetting problem with film/vapor interface energy density* $\gamma(\theta)$ *if and only if the following three conditions are satisfied:*

$$\mu(s) = \widetilde{\gamma}(\theta(s))\kappa(s) \equiv C, \qquad s \in [0, L], \quad\quad (3.3.6)$$

$$\widetilde{\gamma}(\theta(s)) \geq 0, \qquad s \in [0, L], \quad\quad (3.3.7)$$

$$f(\theta) = 0, \qquad \theta = \theta_c^l, \theta_c^r, \qu\quad (3.3.8)$$

where C *is a constant,* θ_c^l, θ_c^r *are the left and right (static) contact angles of* Γ_e.

As we know that the Wulff envelope which solves the minimization Problem (1.3.2) is of equipotential. Therefore, condition (3.3.6) is equivalent to that Γ_e should be a continuous segment of the Wulff envelope (shown as black solid curve in Fig. 3.7(a)) given by Eq. (1.3.5).

Condition (3.3.7) requires all the orientations appears in Γ_e to be of positive surface stiffness. We refer to these orientations as stable orientations. Therefore,
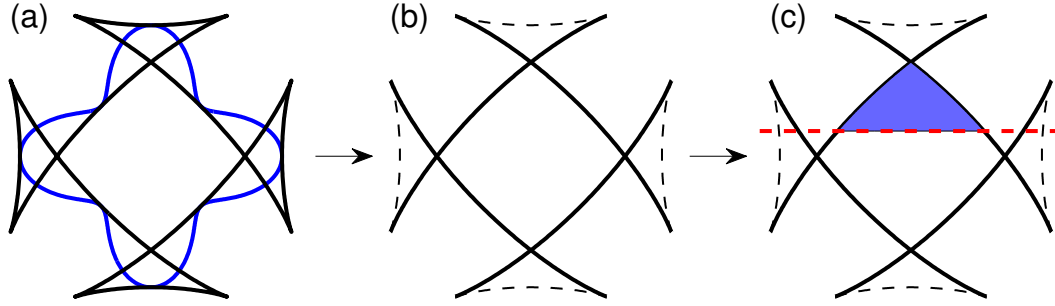
Figure 3.7: Illustration of steps for getting a stable equilibrium shape. Step (a) gives a γ-plot (blue solid curve) and the corresponding Wulff envelope with "ears" (black solid curve); Step (c) eliminates the unstable orientations (black dash curves); Step (b) adds a substrate (red dash line) and results in a unique stable equilibrium (blue shaded region).

instead of using the Wulff envelope with "ears", Γ_e should be constructed by the Wulff envelope with stable orientations (shown as solid black curves in Fig. 3.7(b)).

Eq. (3.3.8), which is referred to as the anisotropic Young equation, determines the static contact angles. We observe that the equation can also be viewed as $y(\theta) = \sigma$ where $y(\theta)$ is the y-coordinate of Wulff envelope given by Eq. (1.3.5). That is, the line $y = \sigma$ intersects Wulff envelope at the point(s) $\bigl(x(\theta_a),\ y(\theta_a)\bigr)$ with normal angle θ_a (viewing in clockwise direction), where θ_a solves Eq. (3.3.8). Therefore, Γ_e can be constructed by cutting the Wulff envelope with stable orientations by the substrate line $y(\theta) = \sigma$ (shown in Fig. 3.7(c)). Finally, Γ_e is a continuous curve which can be physically attained, and the corresponding equilibrium is the region enclosed by Γ_e and $y(\theta) = \sigma$ (shown in Fig. 3.7(c)).

We refer to this process as the generalized Winterbottom construction. And we can define the angles which can be attained in the generalized Winterbottom construction to be stable. Here, we want to highlight the case that the substrate line intersects with the bottom "ear". According to the generalized Winterbottom construction, we obtain a self-intersection curve which is not physically attained. However, the thin film should still alter its shape in an effort to reach this equilibrium

since it is of minimum energy (unique minimum). As a result, the two contact points will meet within a finite period. Therefore, we refer to this case as a complete dewetting with a stable anisotropic Young angle.

A detailed explanation for $m = 2, 3, 4, 6$ is as follows.

- $m = 2$:

  For a given β, Fig. 3.8 shows all the equilibrium shapes that we can obtain by the generalized Winterbottom construction (adding a substrate to the Wulff envelope) except for the complete wetting case. It can be seen that: i) usually the equilibrium is the shape between the substrate and the top point of the Wulff shape (Fig. 3.8(b, c)), ii) when the substrate is above the Wulff shape (Fig. 3.8(a)), we refer to the shape between the top point of the Wulff shape and the substrate as the inverted equilibrium shape (shown in Fig. 3.9). It is noted that this equilibrium is concave. iii) when the substrate is below the bottom point of Wulff shape(Fig. 3.8(d)), the convex Wulff shape is referred to as the equilibrium.

  According to the generalized Winterbottom construction (Fig. 3.8), we provide a visual illustration of the stable and unstable roots via the Wulff envelope in Fig. 3.10(a), and the relation between the roots and σ is shown in Fig. 3.10(b) by taking $\beta = 0.8$. It can be seen that the anisotropic Young equation has at most one stable root for $m = 2$. Therefore, for different σ, β, the phase diagram of the number of stable roots is shown in Fig. 3.11.

- $m = 3$:

  For small β that $f(\pi) < f(\theta_2)$, according to the generalized Winterbottom construction, all the equilibrium shapes (without complete wetting and dewetting) for $m = 3$ are shown in Fig. 3.12(a-d). It can be seen that the complete dewetting occurs only when the substrate does not intersect with the Wulff envelope, which is different with that in the $m = 2$ case. In addition, multiple equilibria become possible, which implies that there are multiple stable roots
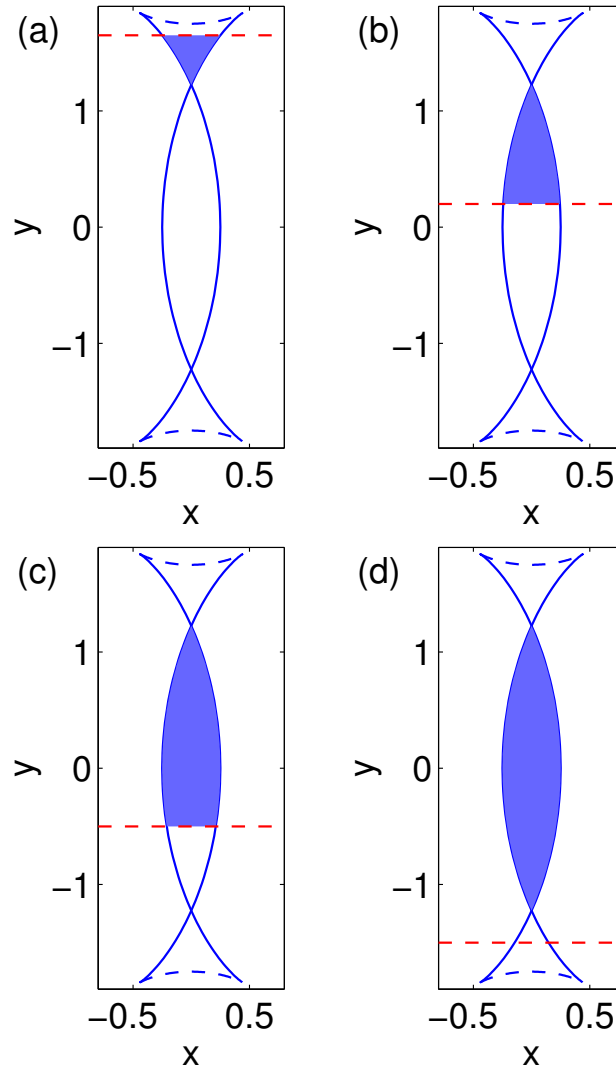
Figure 3.8: Schematic view of the equilibria for different σ with $m = 2$.

for the anisotropic Young equation.

When β is large enough such that $f(\theta_2) > f(\pi)$, then we can obtain equilibria shown in Fig. 3.12(e, f) instead of (c, d). As can be seen that complete dewetting may occur when the substrate and the Wulff envelope intersect.

Similar to the $m = 2$ case, we show a visual illustration of the stable and unstable roots in Fig. 3.13(a), the relation between the roots and σ in Fig. 3.13(b), and the phase diagram of the number of stable roots different σ, β in Fig. 3.14.
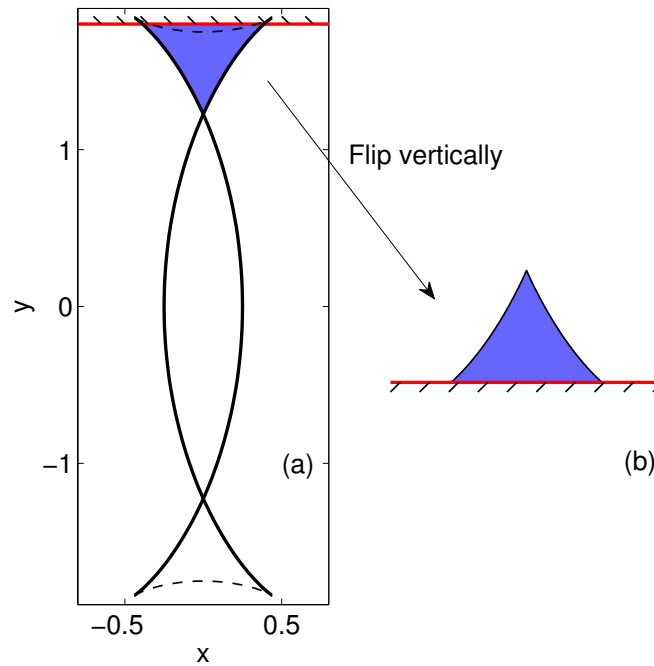
Figure 3.9: Schematic view of the equilibrium when the substrate is above the Wulff shape.
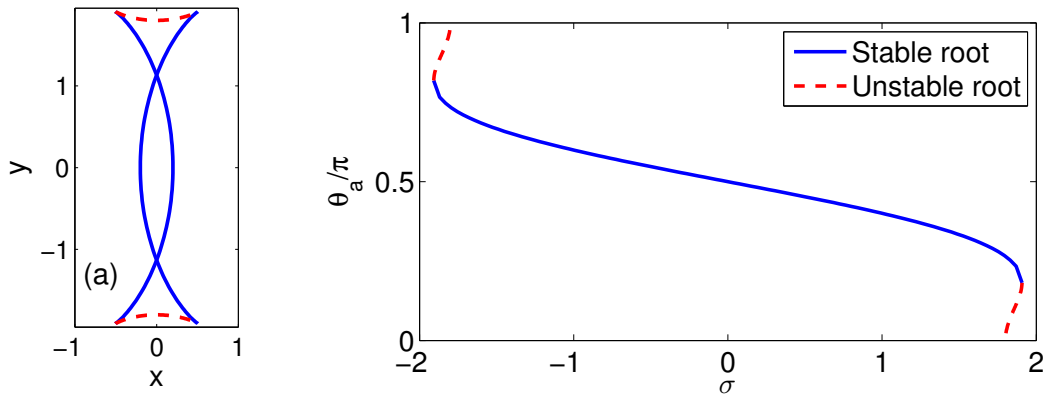
Figure 3.10: (a) A schematic view of the stable roots and unstable roots via Wulff envelope. (b) The plot of roots to Eq. (3.3.1) against σ for $m = 2, \beta = 0.8$. The blue solid line is the stable root, and the red dash line is the unstable root.

- $m = 4, 6$:

  For $m = 4, 6$, although the ears may intersect when β becomes large enough,
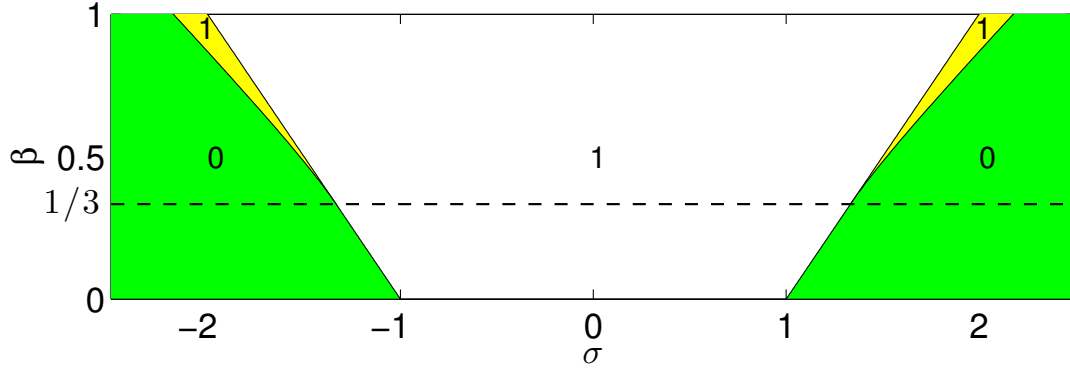
Figure 3.11: Phase diagram of the number of stable roots to Eq. (3.3.1) with $m = 2$ for different σ and β. The number in each region is the number of stable roots.

which is different with the $m = 2, 3$ cases, the discussion is still similar. For simplicity, we do not distinguish the ear-intersected cases from the non-intersected cases. Similarly, we can obtain the equilibria (we only list some of the equilibria since they are similar to the $m = 2, 3$ cases.) according to the generalized Winterbottom construction for $m = 4, 6$ in Fig. 3.15 and Fig. 3.18, respectively. Then we provide the schematic view of the stable and unstable roots via the Wulff envelope in Fig. 3.16 and Fig. 3.19. In addition, the phase diagrams for the number of stable roots to the anisotropic Young equation are shown in Fig. 3.17 and Fig. 3.20.

Although our analysis for the multiple roots and the definition for the stability are focused on the energy density of form $\gamma(\theta) = 1 + \beta \cos(m(\theta + \phi))$ with $\phi = 0$, the extension to non-zero ϕ and other kinds of energy density is similar.

Based on the above analysis, we find that the classification of the types of wetting/dewetting (reviewed in section 1.3.3, shown in Fig. 1.13) may not be precise. Therefore, we re-classify the types of dewetting with an schematic illustration (taking $m = 4$) shown in Fig. 3.21:

- Case I: *Complete Wetting.* The substrate line falls above the Wulff envelope such that $f(\theta)$ in (3.3.1) is always less than zero. In this case, for any initial
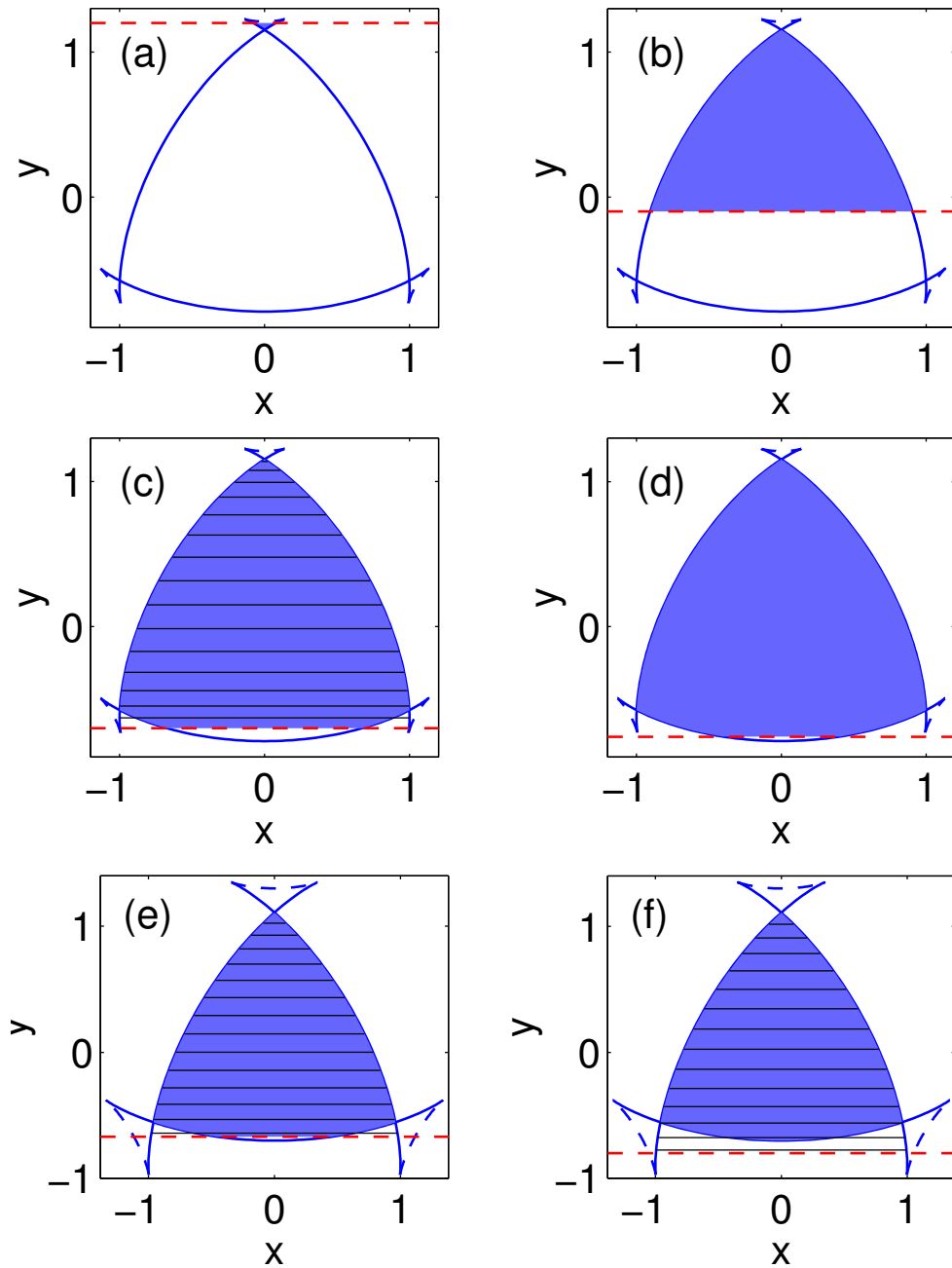
Figure 3.12: Schematic view of the equilibria for different σ with $m = 3$. (a-d) are for small β, (e-f) are for big β.

island shape, the contact points will move outward and there is no stable shape; the island tends to cover the substrate.
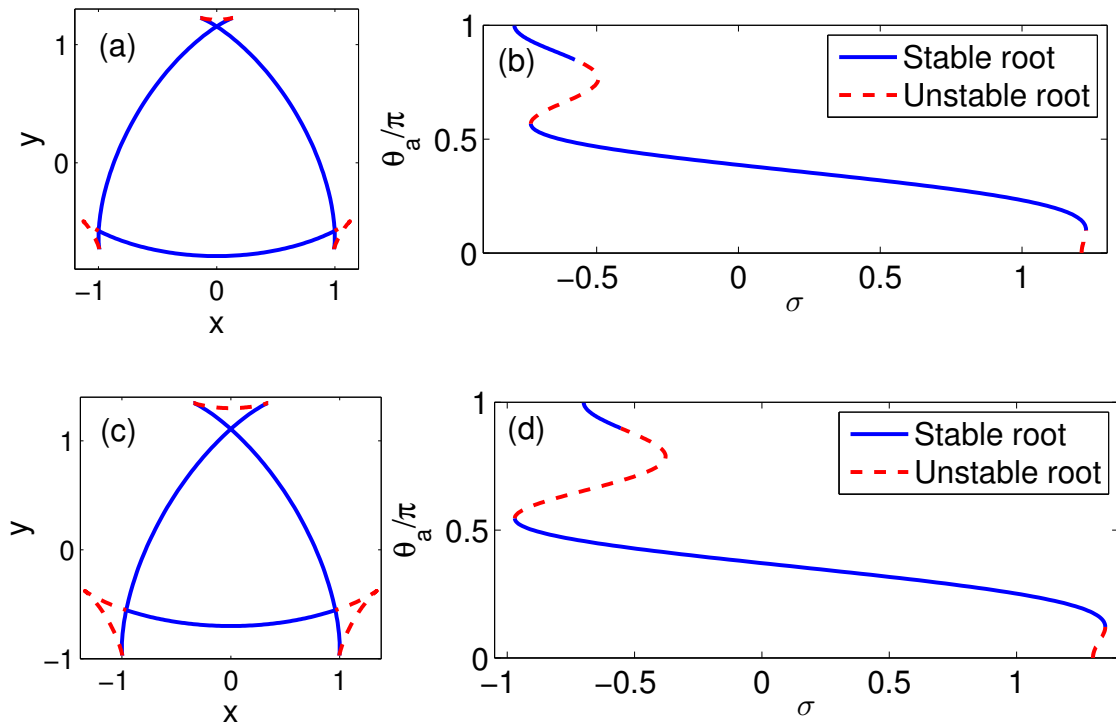
Figure 3.13: A schematic view of the stable roots and unstable roots via Wulff envelope for (a) $f(\pi) < f(\theta_2)$ (c) $f(\pi) > f(\theta_2)$. The plot of roots to Eq. (3.3.1) against σ for $m = 3$ (b)$\beta = 0.21$, (d) $\beta = 0.3$.
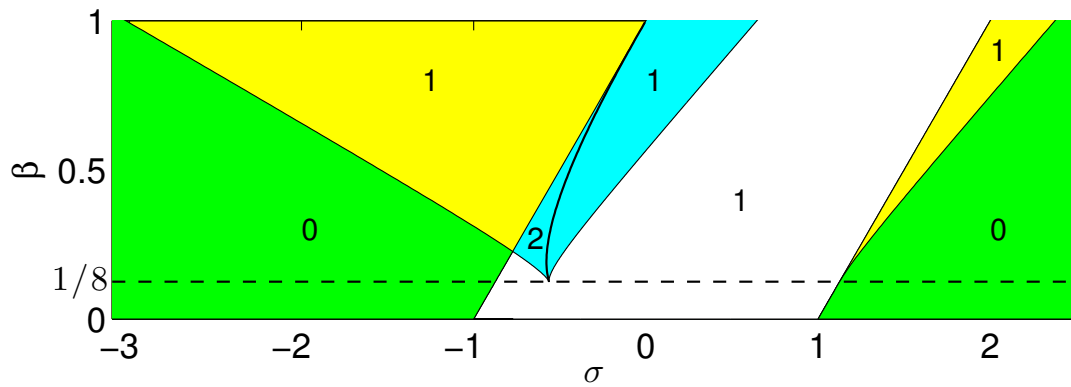
Figure 3.14: Phase diagram of the number of stable roots to Eq. (3.3.1) with $m = 3$ for different σ and β.
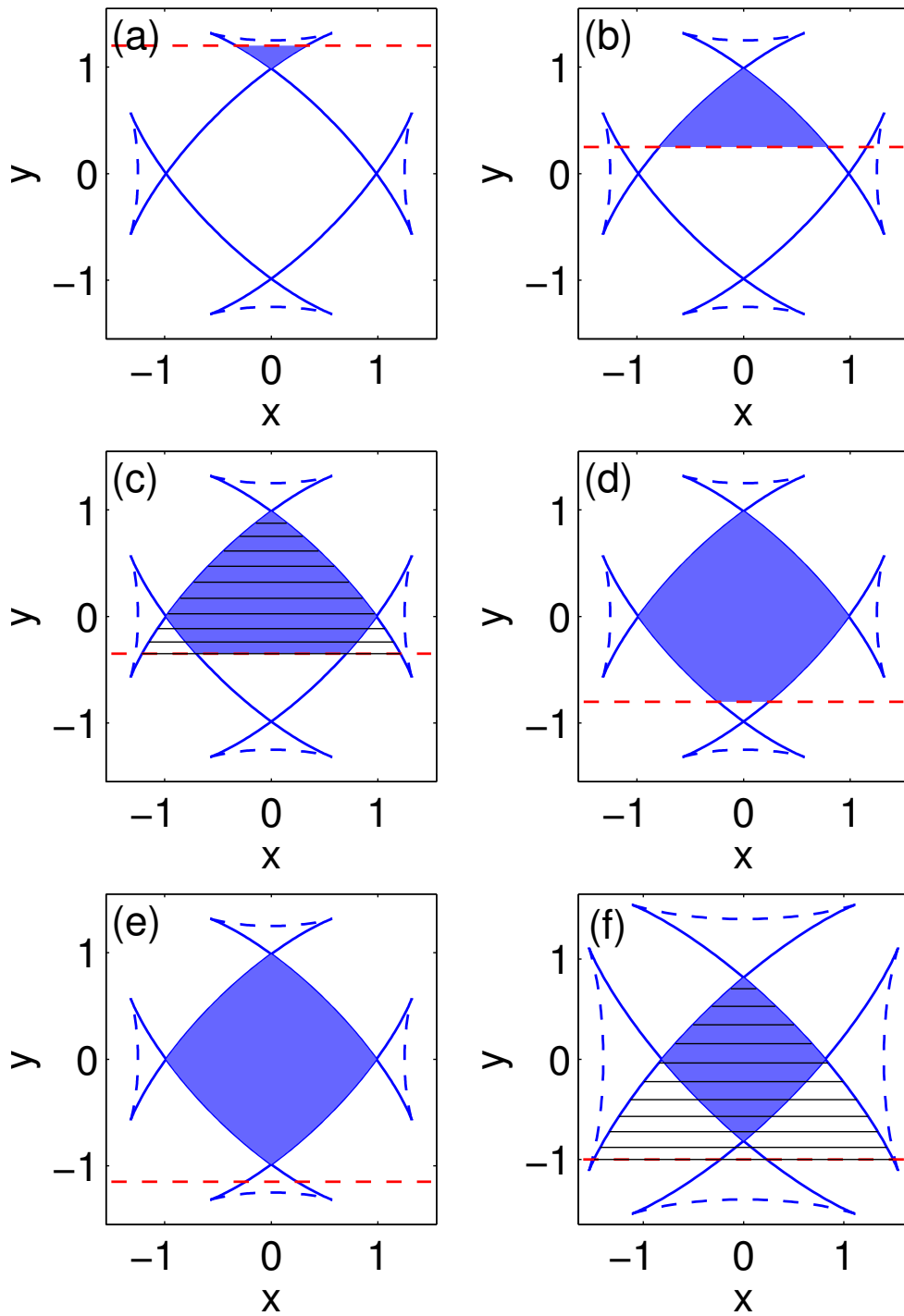
Figure 3.15: Schematic view of the equilibria for different σ with $m = 4$. (a-e) are for small β, (f) is for big β.
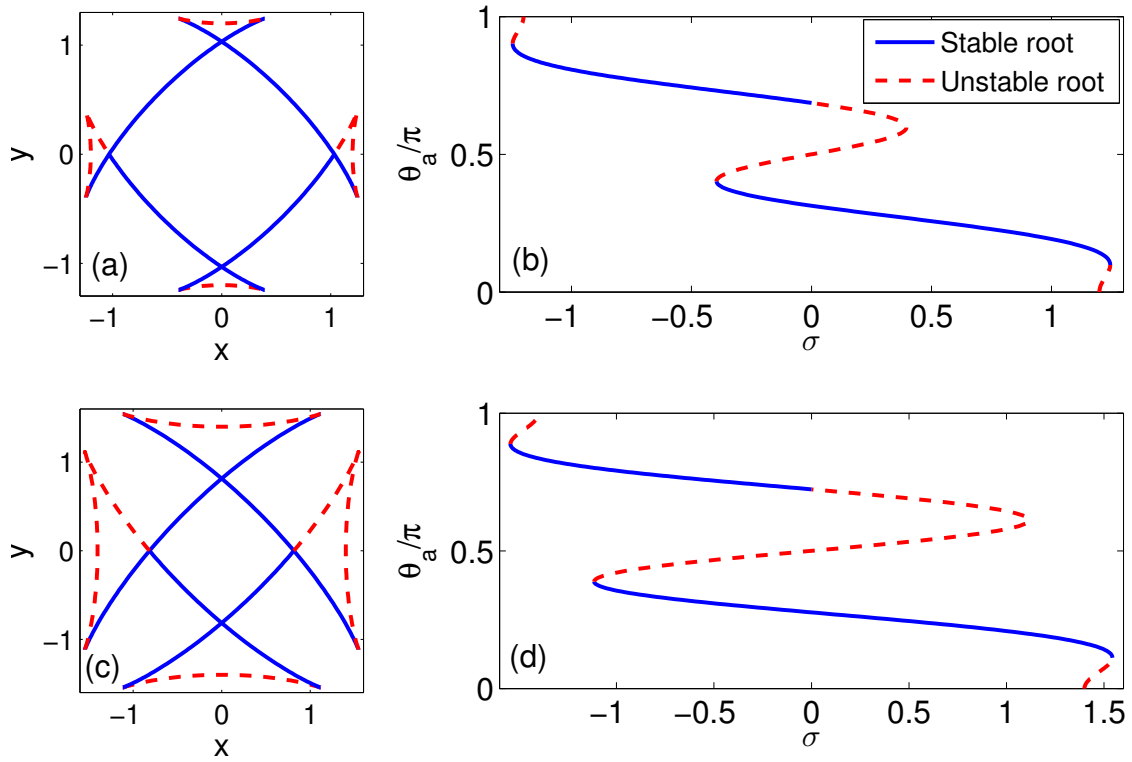
Figure 3.16: A schematic view of the stable roots and unstable roots via Wulff envelope for (a) small β (c) big β. The plot of roots to Eq. (3.3.1) against σ for $m = 4$ (b)$\beta = 0.2$, (d) $\beta = 0.4$.
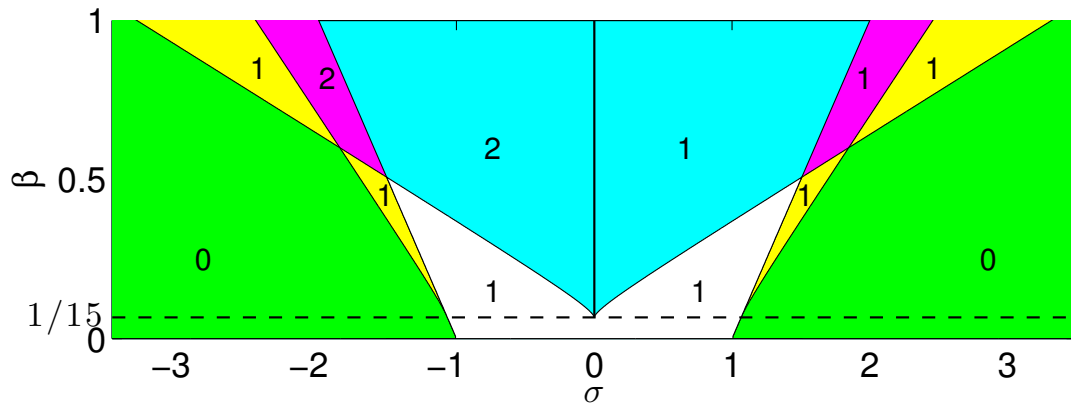
Figure 3.17: Phase diagram of the number of stable roots to Eq. (3.3.1) with $m = 4$ for different σ and β.
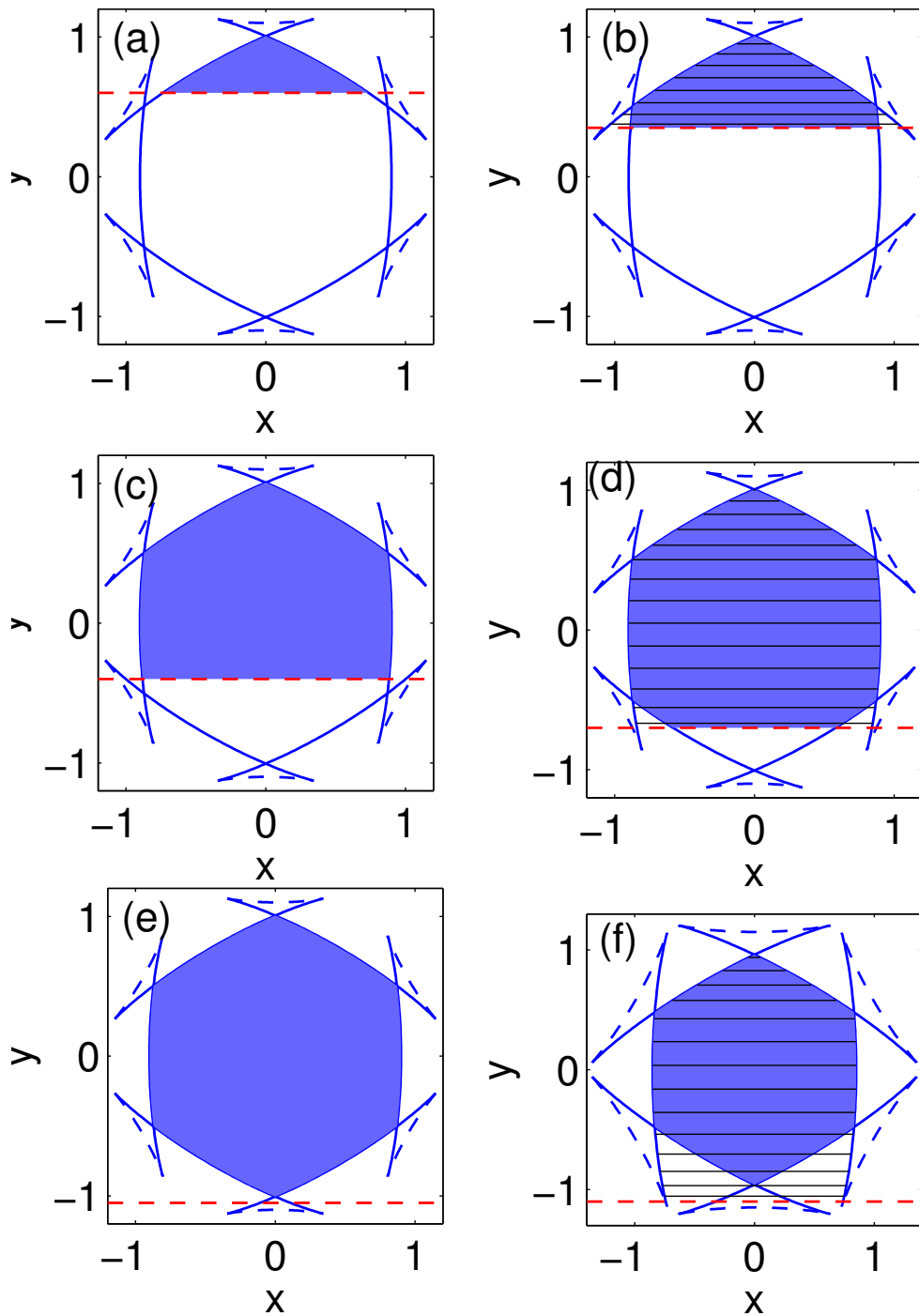
Figure 3.18: Schematic view of some of the equilibria for different σ with $m = 6$. (a-e) are for small β, (f) is for big β.
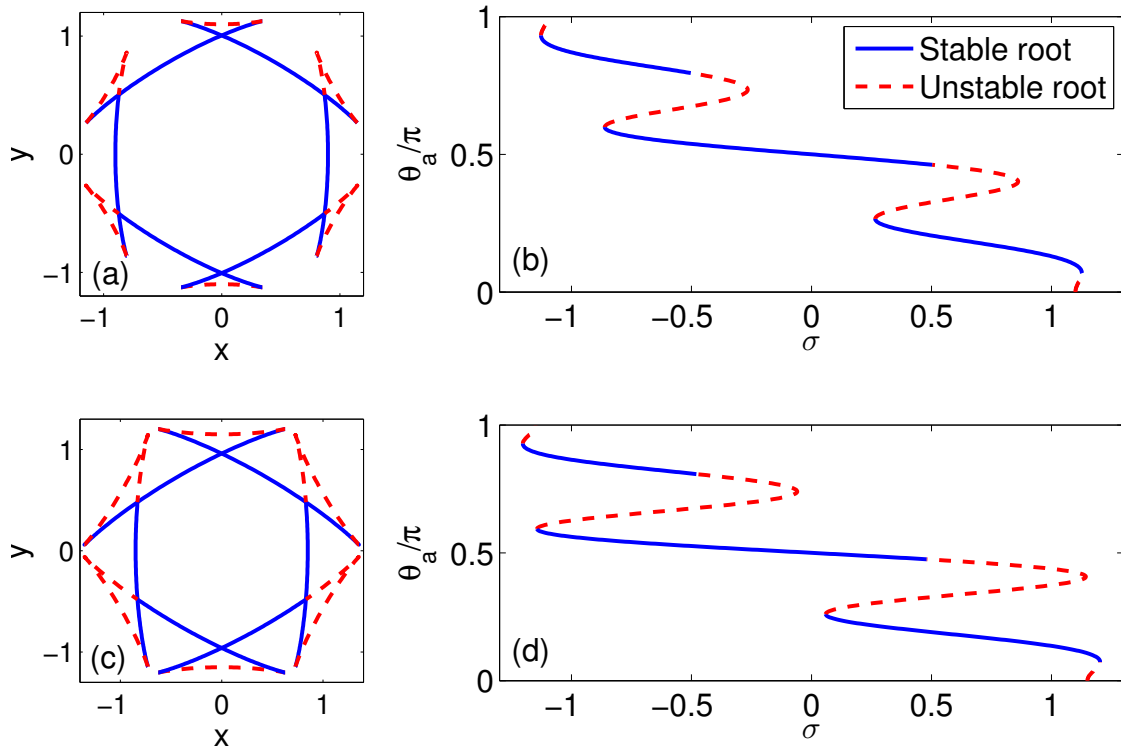
Figure 3.19: A schematic view of the stable roots and unstable roots via Wulff envelope for (a) small β (c) big β. The plot of roots to Eq. (3.3.1) against σ for $m = 6$ (b)$\beta = 0.1$, (d) $\beta = 0.18$.
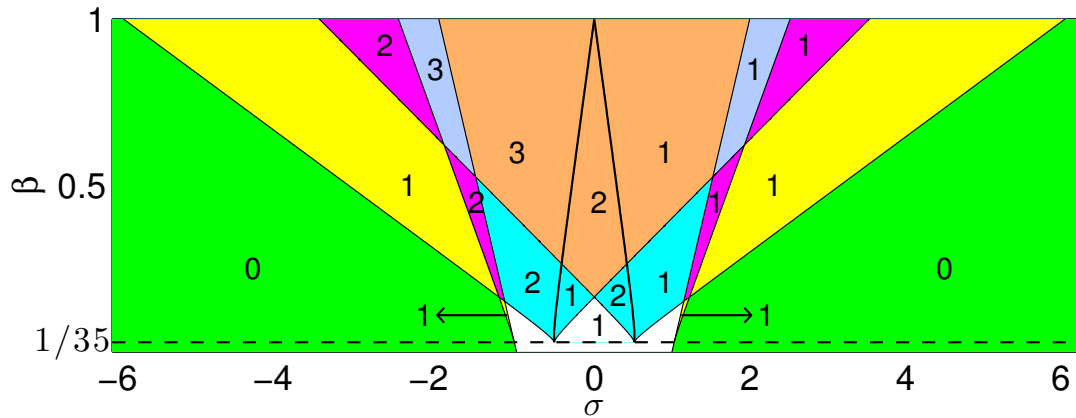
Figure 3.20: Phase diagram of the number of stable roots to Eq. (3.3.1) with $m = 6$ for different σ and β.

- Case II: *Partial Wetting*, $\theta_a \in (0, \pi/2)$. The equilibrium shape is found by flipping over the part of the Wulff envelope truncated by the substrate line that lies between L_1 and Line L_2 in Fig. 3.21, as indicated by the blue shaded region in Fig. 3.15(a) for the red dashed substrate line. We distinguish this case from Case III since it can be clearly seen that the equilibrium is not convex.

- Case III: *Partial Wetting*, $\theta_a \in (0, \pi/2)$. The equilibrium shape can be directly obtained from the section of the Wulff shape delimited by the substrate line between L_2 and Line L_3 in Fig. 3.21, as shown by the blue shaded region in Fig. 3.15(b).

- Case IV (or IV′): *Multiple Equilibrium Shapes.* In these cases, multiple stable shapes exist, which can be determined by proper truncation of the Wulff envelope (shown in Fig. 3.15(c)). In this case, there are two "stable" equilibrium contact angles $\theta_a \in (0, \pi/2)$ which yield three possible equilibrium shapes. Referring to Fig. 3.15(c), the stable shapes are (i) the blue shaded region (i.e., the equilibrium Winterbottom shape), (ii) the striped region, (iii) the left side of the island corresponds to the striped and the right side to the blue regions, and (iv) the right side of the island corresponds to the striped and the left side to the blue regions (the mirror of case (iii)).

- Case V: *Partial Wetting*, $\theta_a \in (\pi/2, \pi)$ The equilibrium shape is obtained from the section of the Wulff shape delimited by the substrate line between Lines L_4 and L_5 in Fig. 3.21, as shown by the blue shading in Fig. 3.15(d).

- Case VI: *Complete Dewetting.* This case corresponds to complete dewetting (shown in Fig. 3.15(e)).
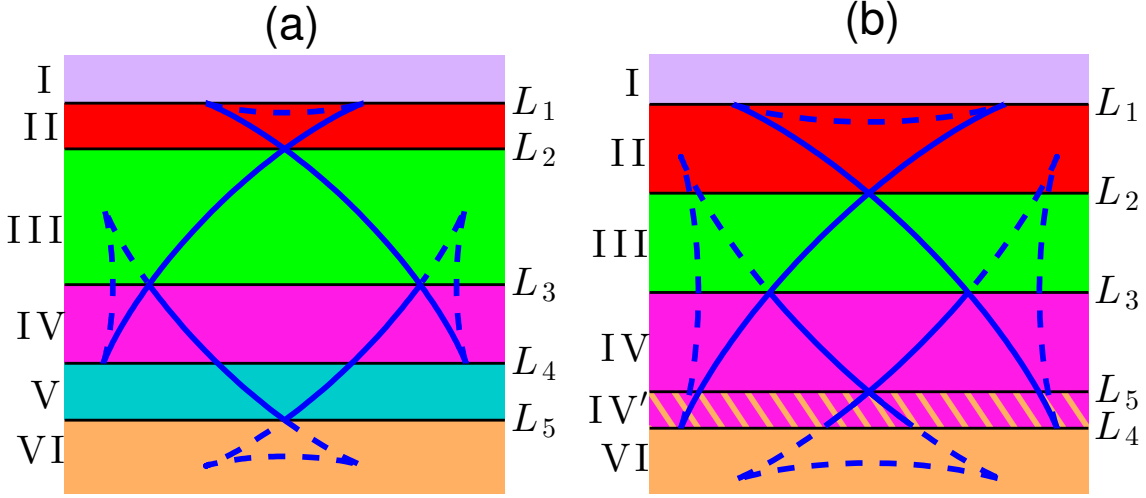
Figure 3.21: Classification of the wetting/dewetting into six different cases for a four-fold crystalline thin film: (a) β is not very large, (b) β is very large (i.e., large ears). Here, the blue curves represent the Wulff envelope, and the dashed blue curves correspond to unstable roots of the anisotropic Young equation, Eq. (3.3.1).

3.4 The parametric finite element method (PFEM)

The notations we use in this section are the same as that in Chapter 2. We first rewrite the governing equation (3.1.12) as

$$\mathbf{X}_t \cdot \mathcal{N} = \mu_{ss}, \tag{3.4.1a}$$

$$\mu = \widetilde{\gamma}(\theta)\kappa - \varepsilon^2\left(\kappa_{ss} + \frac{\kappa^3}{2}\right), \tag{3.4.1b}$$

$$\kappa\mathcal{N} = -\mathbf{X}_{ss}. \tag{3.4.1c}$$

It can be seen that only the equation for μ changes, compared to the equations for the weakly anisotropic case.

The weak solution of the problem is defined by the following weak formulation: Given $\Gamma(0) = \mathbf{X}(I,0)$, for all $t \in (0,T]$ find $\Gamma(t) = \mathbf{X}(I,t)$ with $\mathbf{X}(t) \in H^1_{l,r} \times H^1_0$ (l

and r stand for x_c^l, x_c^r, respectively), $\mu(t) \in H^1$, $\kappa(t) \in H_0^1$ such that

$$(\mathbf{X}_t \cdot \mathcal{N}, \ \varphi)_\Gamma + a_\Gamma(\mu, \ \varphi) = 0, \qquad \forall \varphi \in H^1, \tag{3.4.2a}$$

$$(\mu, \ \phi)_\Gamma - (\widetilde{\gamma}(\theta)\kappa - \frac{\varepsilon^2}{2}\kappa^3, \ \phi)_\Gamma - \varepsilon^2 a_\Gamma(\kappa, \ \phi) = 0, \qquad \forall \phi \in H_0^1, \tag{3.4.2b}$$

$$(\kappa\mathcal{N}, \ \mathbf{w})_\Gamma - a_\Gamma(\mathbf{X}, \ \mathbf{w}) = 0, \qquad \forall \mathbf{w} \in H_0^1 \times H_0^1. \tag{3.4.2c}$$

Note that the space for ϕ changes from H^1 in Eq. (2.4.3b) to H_0^1 in Eq. (3.4.2b). This is because that we introduced the "zero-curvature" condition for the moving contact line.

The finite element approximation to Eq. (3.4.2) can be written as follows. For $m \geq 0$, given $\Gamma^m = \mathbf{X}^m \in V_{l,r}^h \times V_0^h$ with $l = x_c^l(t_m), r = x_c^r(t_m)$, $\mu^m \in V^h$, $\kappa^m \in V_0^h$, find $\Gamma^{m+1} = \mathbf{X}^{m+1} \in V_{l,r}^h \times V_0^h$ with $l = x_c^l(t_{m+1}), r = x_c^r(t_{m+1})$, and $\mu^{m+1} \in V^h$, $\kappa^{m+1} \in V_0^h$ such that

$$(\frac{\mathbf{X}^{m+1} - \mathbf{X}^m}{t_{m+1} - t_m} \cdot \mathcal{N}^m, \ \varphi)_{\Gamma^m} + a_{\Gamma^m}(\mu^{m+1}, \ \varphi) = 0, \qquad \forall \varphi \in V^h, \tag{3.4.3a}$$

$$(\mu^{m+1}, \ \phi)_{\Gamma^m} - (\widetilde{\gamma}(\theta^m)\kappa^{m+1}, \ \phi)_{\Gamma^m} + \frac{\varepsilon^2}{2}((\kappa^m)^2\kappa^{m+1}, \ \phi)_{\Gamma^m}$$
$$- \varepsilon^2 a_{\Gamma^m}(\kappa^{m+1}, \ \phi) = 0, \qquad \forall \phi \in V_0^h, \tag{3.4.3b}$$

$$(\kappa^{m+1}\mathcal{N}^m, \ \mathbf{w})_{\Gamma^m} - a_{\Gamma^m}(\mathbf{X}^{m+1}, \ \mathbf{w}) = 0, \qquad \forall \mathbf{w} \in V_0^h \times V_0^h. \tag{3.4.3c}$$

$x_c^l(t_{m+1})$ and $x_c^r(t_{m+1})$ are also computed previously by discretizing Eq. (3.1.14).

3.5 Convergence test and numerical results

3.5.1 Convergence test

Since the convergence of PFEM and the contact line mobility are already shown in Chapter 2, we here only address the issue of convergence of the proposed model with respect to the regularization parameter ε (with fixed $\eta = 100$).

Fig. 3.22 shows by numerically solving the proposed model, the numerical equilibrium shapes of a strongly anisotropic thin island film for different regularization
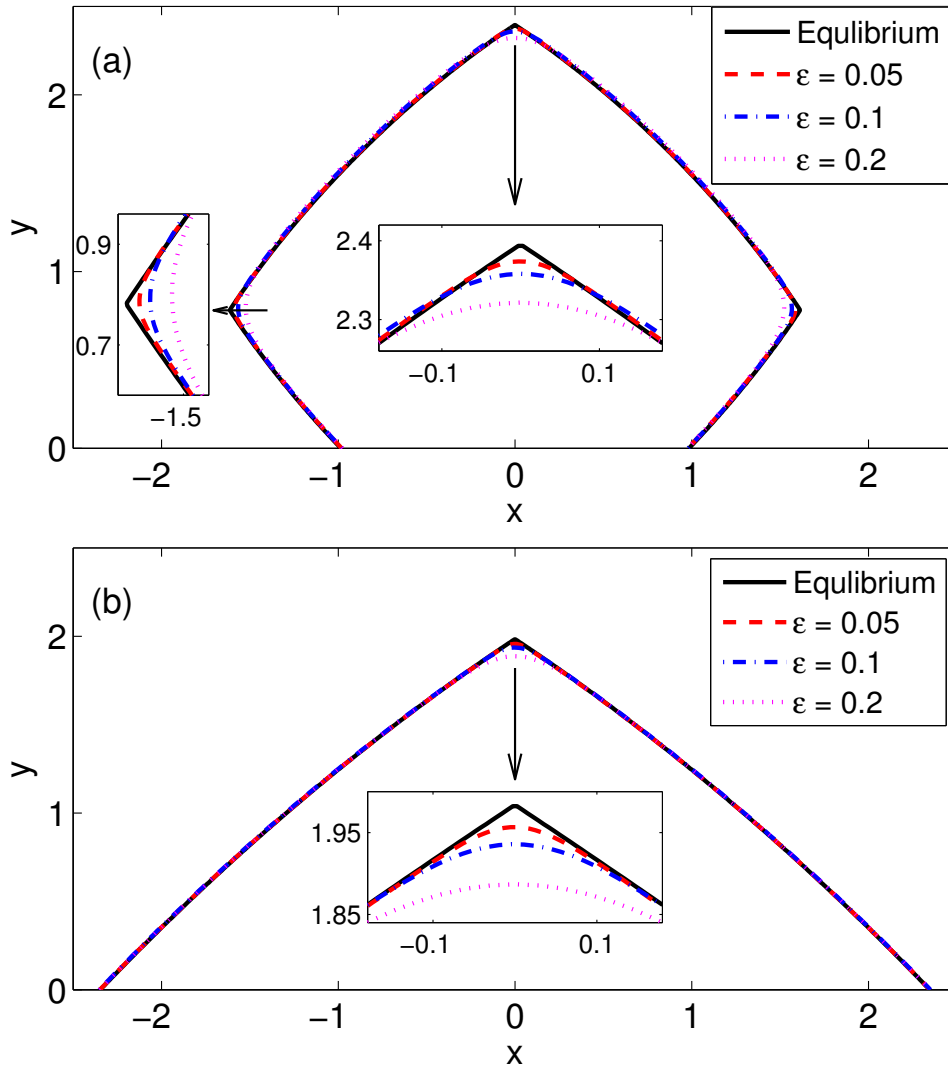
Figure 3.22: Comparison of the numerical equilibrium shapes of thin film with the theoretical equilibrium shape for several values of the regularization parameters ε, where the solid black lines represent the theoretical equilibrium shapes and colored lines represent the numerical equilibrium shapes, and the parameters are chosen as (a): $m = 4, \beta = 0.2, \sigma = -0.5$; (b): $m = 4, \beta = 0.2, \sigma = 0.5$.

parameters ε under the energy density (1.2.2) with the parameters $m = 4, \beta = 0.2, \sigma = -0.5$ (Fig. 3.22(a)) and $m = 4, \beta = 0.2, \sigma = 0.5$ (Fig. 3.22(b)). Initially, the shape of thin island film is a rectangle with the length 5 and height 1, and we let

it evolve into the equilibrium shape. Then, we compare the numerical equilibrium shapes as a function of different parameters ε with the theoretical equilibrium shape (generalized Winterbottom construction, shown by the solid black lines in Fig. 3.22).

As clearly shown in Fig. 3.22, the numerical equilibrium shapes converge to the theoretical equilibrium shapes (especially at the corners) with decreasing the small parameter ε in the proposed model from $\varepsilon = 0.2$ to $\varepsilon = 0.05$ in the two cases. This implies that the smaller ε we choose, the better (closer to the non-regularization case) numerical results will be. We did not compare the convergence at the contact points since the theoretical equilibrium may not satisfy the zero-curvature condition. However, we do not suggest to choose too small ε by taking the computational cost into consideration. This is because that the mesh size has to be chosen proportional to the small parameter ε due to the stability constraint. Therefore, ε is chosen to be 0.1 in the following simulations unless stated.

3.5.2   Small islands

Similar to the weakly anisotropic case, we first examine and report the evolution of small islands under the energy density (1.2.2) with different degrees of anisotropy, m-fold crystal symmetries and rotation angles.

Figs. 3.23 and 3.24 show the evolutions of small islands with strongly anisotropic surface energy for $\phi = 0, \pi/4$, respectively. It can be seen that the evolution of the $\phi = 0$ case is quite different with that in the isotropic and weakly anisotropic cases. Many ridges and valleys are formed after a very short time. This may be because that when $\phi = 0$, the energy density of $\theta = 0$ orientation (initial orientation of the facet) is too big so that this orientation becomes unstable or metastable. The ridges and valleys are formed to avoid the $\theta = 0$ orientation. Besides the flatten of the facets, the evolution of the $\phi = \pi/4$ case is similar to that in the weakly anisotropic case (Fig. 2.6).

Fig. 3.25 shows the equilibria of thin films with strongly anisotropic surface energy density for different m and β. In the figure, the equilibria are compared with the
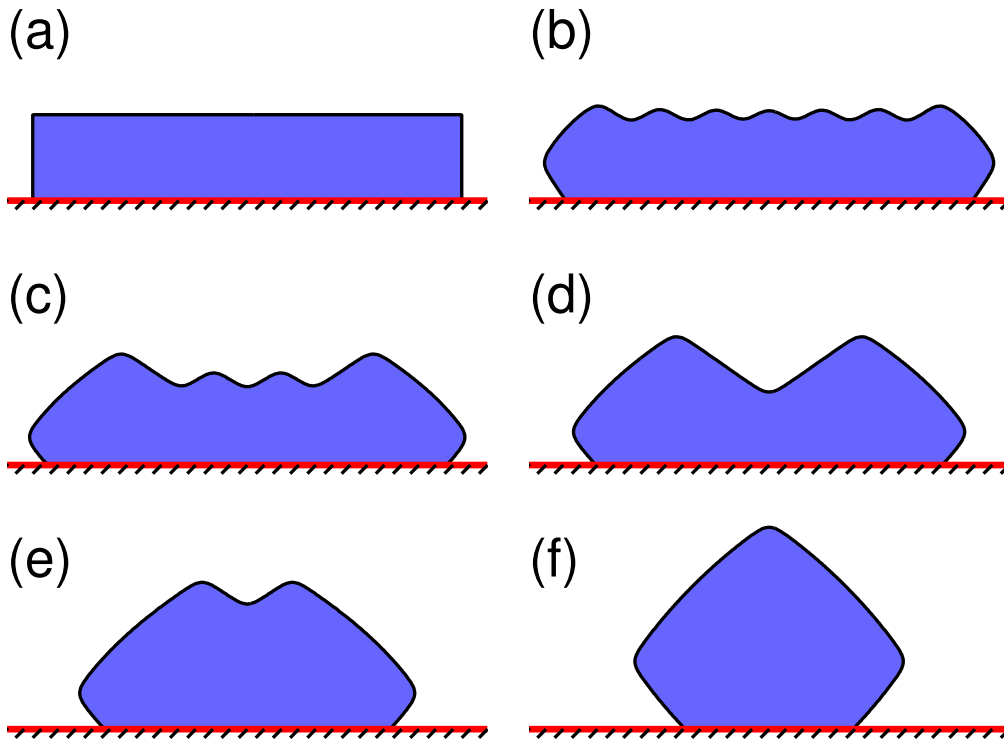
Figure 3.23: Evolution of a thin island film with strongly anisotropic surface energy, the initial length is 5, the parameters are $m = 4, \beta = 0.2, \sigma = -0.5, \phi = 0$. The time for each subplot is (a) $t = 0$, (b) $t = 0.002$, (c) $t = 0.1$, (d) $t = 0.4$, (e)$t = 1$, (f) $t = 20$.

Wulff envelope instead of the Winterbottom construction. This is because we find that it is the generalized Winterbottom construction (Wulff envelope with "ears") that matches the equilibrium for $m = 3$, instead of the Winterbottom construction. For fixed $m = 4$, it can be seen that the edges become flatter, the corners become sharper and the contact points go closer as β increases. When we increase β to 0.5, the two contact points meet before evolving to the equilibrium (shown in Fig. 3.26). This implies that the completely dewetting may occur when the isotropic Young angle $\theta_i < \pi$ in the strongly anisotropic case, while it will not occur in the weakly anisotropic case. Moreover, we verified that the contact angles all converged to one of the anisotropic Young angles, a root to Eq. (3.3.1). In general, the equilibrium
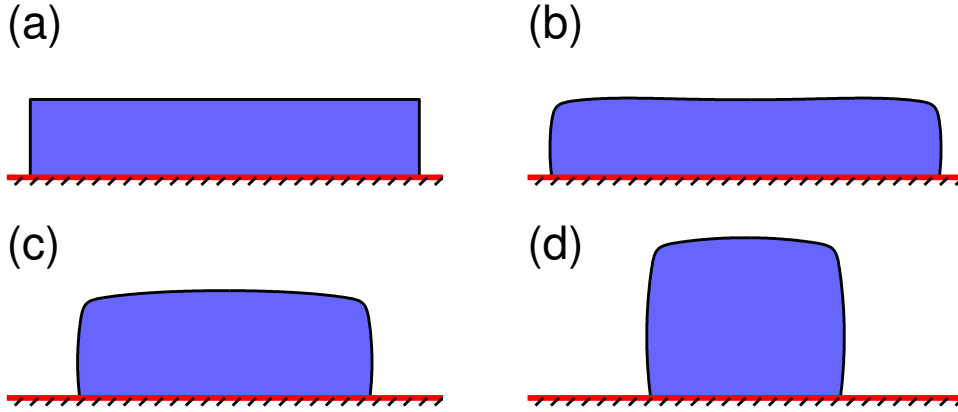
Figure 3.24: Evolution of a thin island film with strongly anisotropic surface energy, the initial length is 5, the parameters are $m = 4, \beta = 0.2, \sigma = -0.5, \phi = \pi/4$. The time for each subplot is (a) $t = 0$, (b) $t = 0.01$, (c) $t = 1$, (d) $t = 11$.

shape are all convex and match the Wulff envelope well.

Unlike the convex equilibria shown in Fig. 3.25, when we take $m = 4, \beta = 0.3, \sigma = 1.3$, the numerical equilibrium becomes concave as shown in Fig. 3.27, compared with the inverted Wulff envelope. As can be seen that it matches the inverted Wulff envelope well, which is just as our prediction by the generalized Winterbottom construction, while the Winterbottom construction suggests a complete wetting for σ of this value. Therefore, the classification (reviewed in section 1.3.3) based on the Winterbottom construction is indeed not accurate, and our classification based on the generalized Winterbottom construction seems more precise.

In general, the above equilibrium shapes are all consistent with our predictions based on the generalized Winterbottom construction in section 3.3. Therefore, the equilibria of thin films with different θ_i/σ and ϕ are not shown here. Instead, we study something new and interesting for the strongly anisotropic case, which is about the multiple anisotropic Young angles.

As we mentioned in section 3.3, the anisotropic Young equation may have multiple roots, which are the anisotropic Young angles, in the strongly anisotropic case. Among all the anisotropic Young angles, which one can or cannot be obtained during
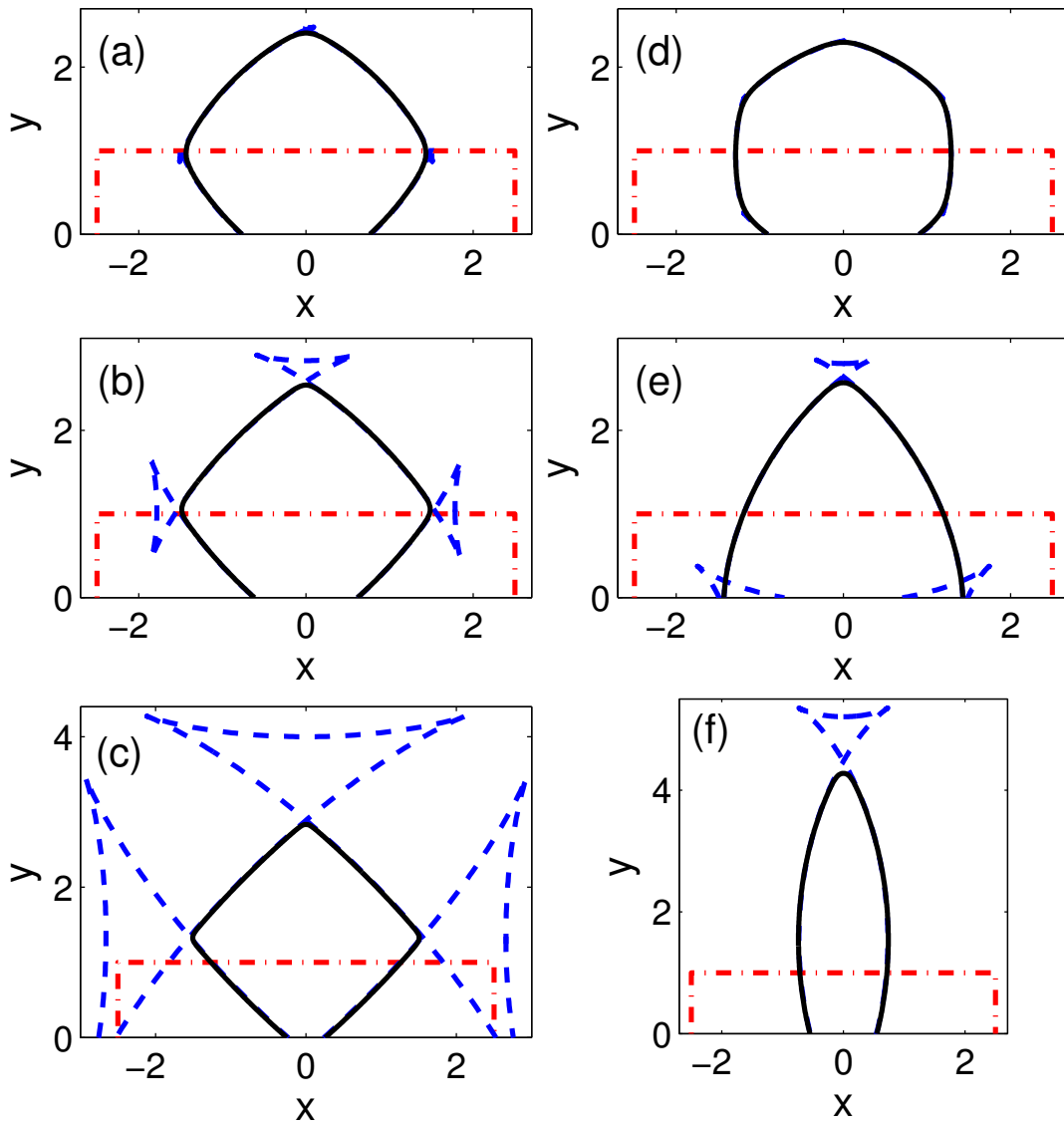
Figure 3.25: Equilibria (black solid lines) of thin films with initial length 5, $\theta_i = 3\pi/4$ in all cases. The red dash-dot line shows the initial shape and the blue dash line is the scaled Wulff envelope. (a) - (c) are equilibria for $\beta = 0.1,\ 0.2,\ 0.4$ ($m = 4$ are fixed). (d) - (f) are simulation results for (d) $m = 6,\ 3,\ 2$ ($(m^2 - 1)\beta = 2$ are fixed).

evolutions is of great concern to many researchers. Therefore, simulations are performed for thin films of different initial shapes to study this problem for $m = 2, 3, 4, 6$. The initial shape of the thin film is chosen to be a trapezoid with the base angles
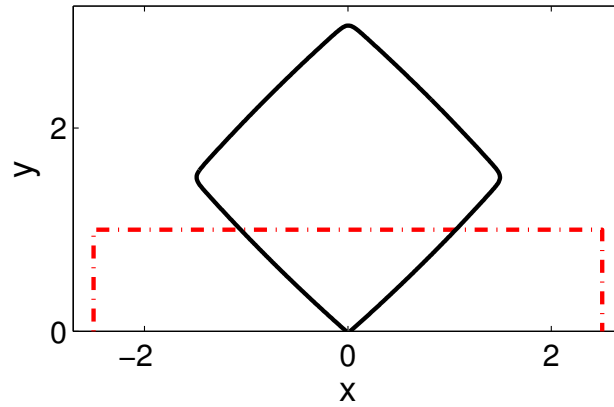
Figure 3.26: The terminating state of a dewetting thin film with $m = 4, \beta = 0.5, \theta_i = 3\pi/4$. Simulation terminates when the two contact points meet.
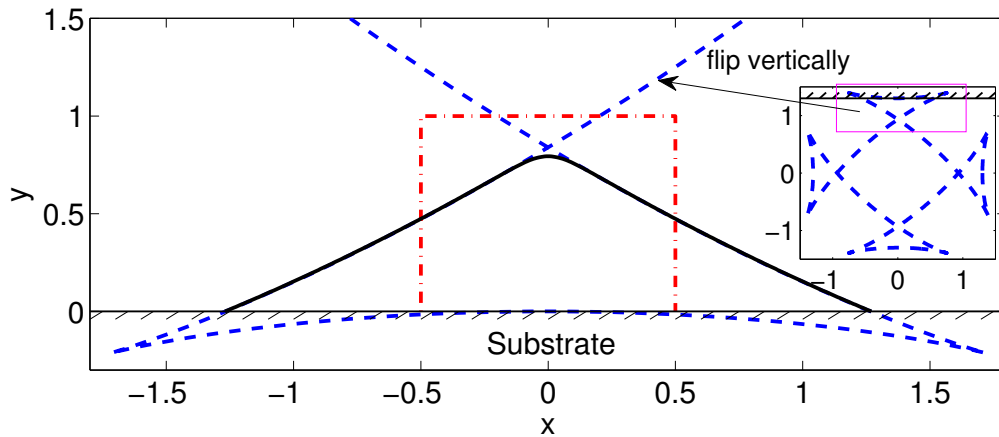
Figure 3.27: Equilibrium (black solid lines) of thin films with initial length 1, $m = 4, \beta = 0.3, \sigma = 1.3$. The red dash-dot line shows the initial shape and the blue dash line is the scaled inverted Wulff envelope.

varying from $\pi/4$ to $3\pi/4$. We first report the simulation results for the $\phi = 0$ case and then we show several results for some nonzero ϕ's.

Combining the phase diagrams (Figs. 3.3, 3.5 and 3.6) of the number of roots to the anisotropic equation and the visual illustrations (Figs. 3.11, 3.14, 3.17 and 3.20)

of the stable/unstable roots, we find that the anisotropic Young equation has multiple roots only when the substrate $y = \sigma$ intersects with the ears of the Wulff envelope, that is, when the substrate is either away from (above/below) the Wulff shape or near the corners of the Wulff shape.

1. *The substrate $y = \sigma$ is above the Wulff shape*

   Fig. 3.28 shows the numerical equilibria with different initial shapes, compared with the inverted Wulff envelopes, for $m = 2, \beta = 0.7, \sigma = 1.75$ when the anisotropic Young equation has two roots and $m = 4, \beta = .2, \sigma = 1.22$ when the equation has three roots. It can be seen that the dynamic contact angle always converges to the stable root no matter what the initial shape is.

2. *The substrate $y = \sigma$ is below the Wulff shape*

   By taking $m = 2, \beta = 0.7, \sigma = -1.75$; $m = 3, \beta = 0.3, \sigma = -0.8$; $m = 4, \beta = 0.4, \sigma = -\sqrt{3}/2$ and $m = 6, \beta = 0.15, \sigma = -1.05$, we show the numerical equilibria or the terminating states in Figs. 3.29 and 3.30. As can be seen that the complete dewetting must occur as long as we choose proper initial state (big initial contact angles). The dynamic contact angle in the complete dewetting cases converges to the stable root that we defined before terminating. This demonstrates that although complete dewetting occurs, the root that we defined as stable is really a stable root.

3. *The substrate $y = \sigma$ is near and above the corners of the Wulff shape*

   Choosing $m = 3, \beta = 0.3, \sigma = -0.45$; $m = 4, \beta = 0.3, \sigma = 0.4$; $m = 6, \beta = 0.1, \sigma = 0.6$ and -0.4, we can see from Figs. 3.31 and 3.32 that there is only one equilibrium shape no matter what initial shape we choose, and the contact angle is the stable one that we defined.

4. *The substrate $y = \sigma$ is near and below the corners of the Wulff shape*

   Taking $m = 3, \beta = 0.3, \sigma = -0.65$; $m = 4, \beta = 0.3, \sigma = -0.5$; $m = 6, \beta = 0.1, \sigma = 0.35$ and -0.7, Figs. 3.33 and 3.34 show the corresponding numerical equilibria compared with the scaled Wulff envelope, as well as the initial state.
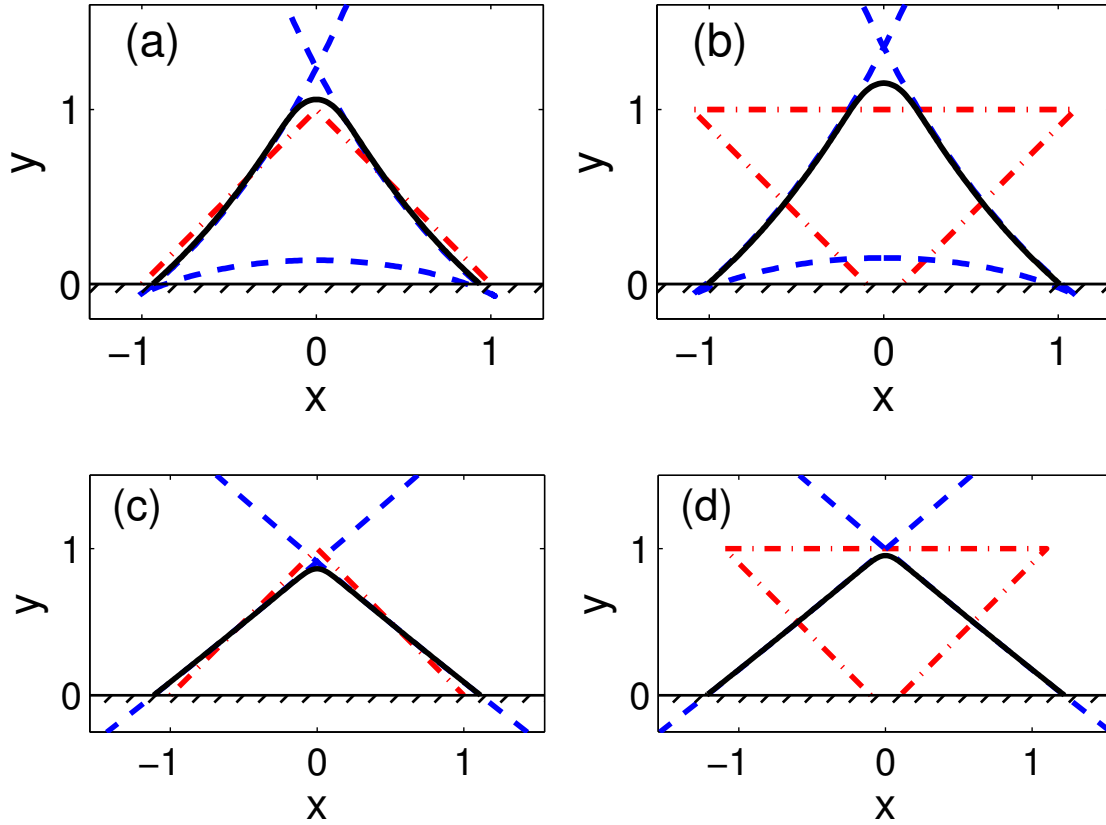
Figure 3.28: Equilibria (black solid curve) of dewetting thin films with (a, b)$m = 2, \beta = 0.7, \sigma = 1.75$; (c, d) $m = 4, \beta = 0.4, \sigma = 0.95$. The red dash-dot lines are the initial states with base angles (a, c) $\pi/4$ and (b, d) $3\pi/4$, blue dash curves are the inverted Wulff envelopes.

It can be seen that thin films all evolve to different equilibria only with different initial shapes. Moreover, these equilibrium shapes are all consistent with the generalized Winterbottom construction in section 3.3.

Apart from the above symmetric initial shapes, we find that asymmetric initial shapes may result in asymmetric equilibria which can also be predicted according to the generalized Winterbottom construction. Here, we only show two examples in Fig. 3.35.

At last, we report two simulation results with nonzero ϕ shown in Figs. 3.36,
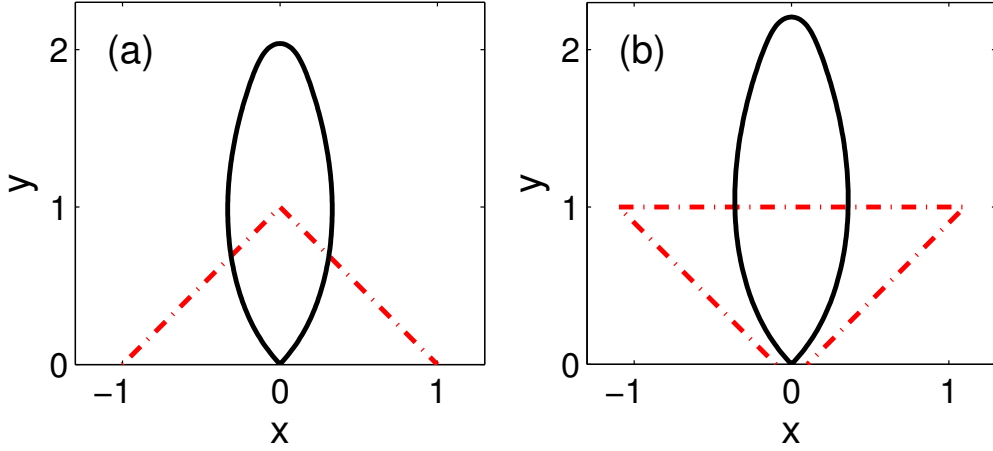
Figure 3.29: Terminating state (black solid curve) of dewetting thin films with $m = 2, \beta = 0.7, \sigma = -1.75$.

3.37. Similar to the symmetric cases that by choosing different initial states, we can find all the possible equilibria predicted by generalized Winterbottom construction.

In summary, these simulations validate the proposed generalized Winterbottom construction, the stable roots to the anisotropic Young equation and the classification of dewetting. Moreover, the consistency of the simulation results and our prediction by the generalized Winterbottom construction implies that the generalized Winterbottom construction can predict all the possible equilibria for an arbitrary energy density γ.

3.5.3 Large islands and pinch-off

Similar to the weakly anisotropic case, pinch-off occurs when we enlarge the length of the thin film. Fig. 3.38 shows the pinch-off process of a thin film of initial length $L = 15$. The evolution is the same as that of the small islands before pinch-off: initially many ridges and valleys are formed, then they merge and the valleys deepen until the film touches the substrate. After pinch-off, the two agglomerates evolve to equilibria independently. The two equilibria are of same shape since there is only one equilibrium shape for $m = 4, \beta = 0.2, \sigma = -\sqrt{3}/2$.
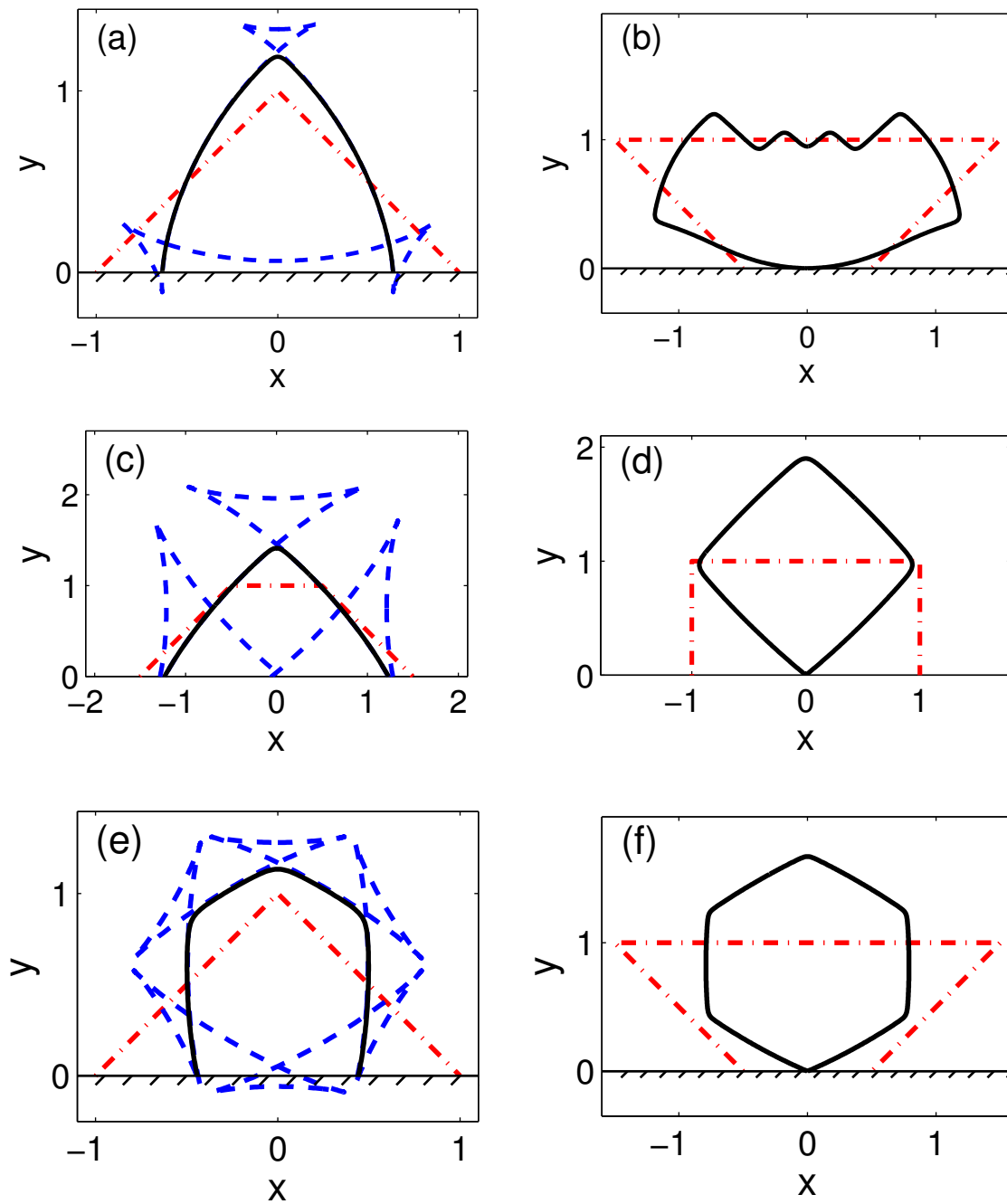
Figure 3.30: (a, c, e) Equilibria/ (b, d, f) Terminating state (black solid curve) of dewetting thin films with (a, b)$m = 3, \beta = 0.3, \sigma = -0.8$; (c, d) $m = 4, \beta = 0.4, \sigma = -\sqrt{3}/2$; (e, f) $m = 6, \beta = 0.15, \sigma = -1.05$.
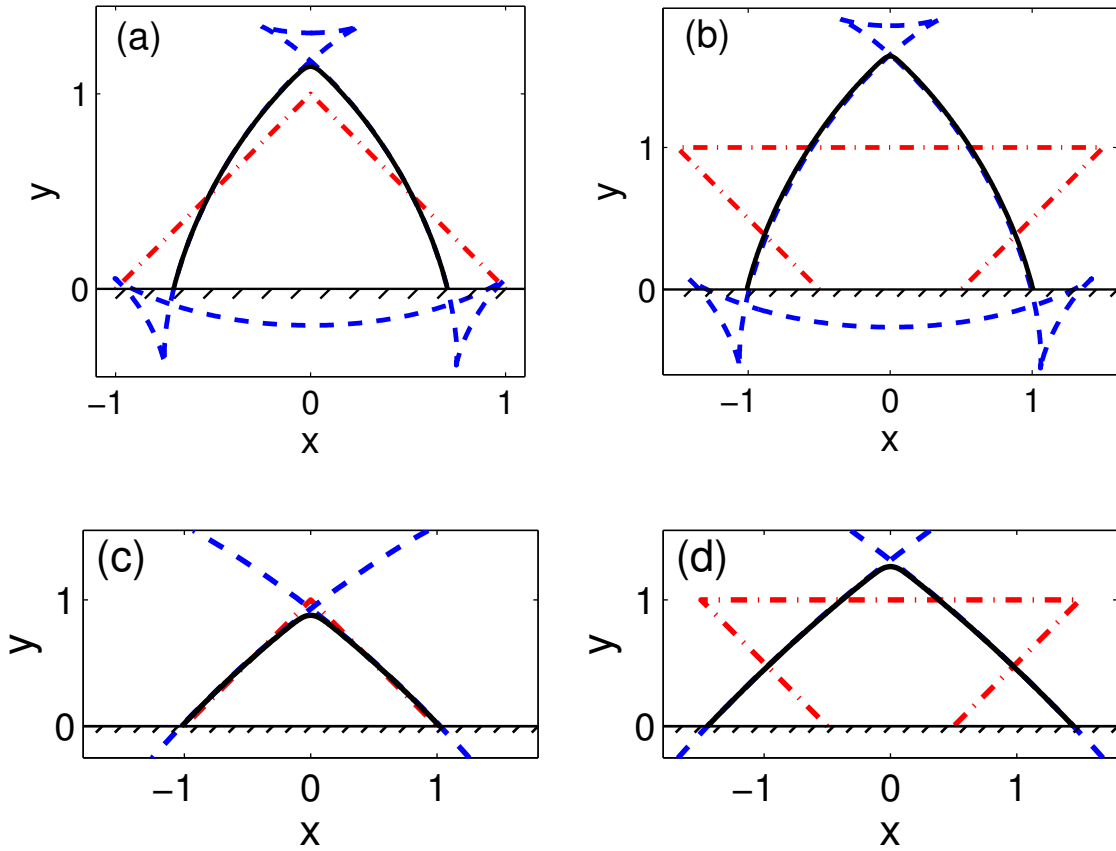
Figure 3.31: Equilibria (black solid curve) of dewetting thin films with (a, b) $m = 3, \beta = 0.3, \sigma = -0.45$; (c, d) $m = 4, \beta = 0.3, \sigma = 0.4$.

When we choose the parameters such that multiple equilibria exist, the equilibrium states of large islands of different initial states are shown in Figs. 3.39. The thin film in (a) pinches off to three agglomerates of the same equilibrium shape (when they are scaled to same size); In (b), the thin film also pinches off to three agglomerates, but of different equilibrium shapes; The thin film in (c) is asymmetric initially, it only pinches off to two agglomerates of different equilibrium shapes. Moreover, it is noted that although the large thin films pinch off and may evolve to different equilibrium shapes, all the central contact angles are the same. This implies that the initial shape only affect the shape near the edge (contact angle) of the long film. That is, if the thin film pinches off to many agglomerates, the central
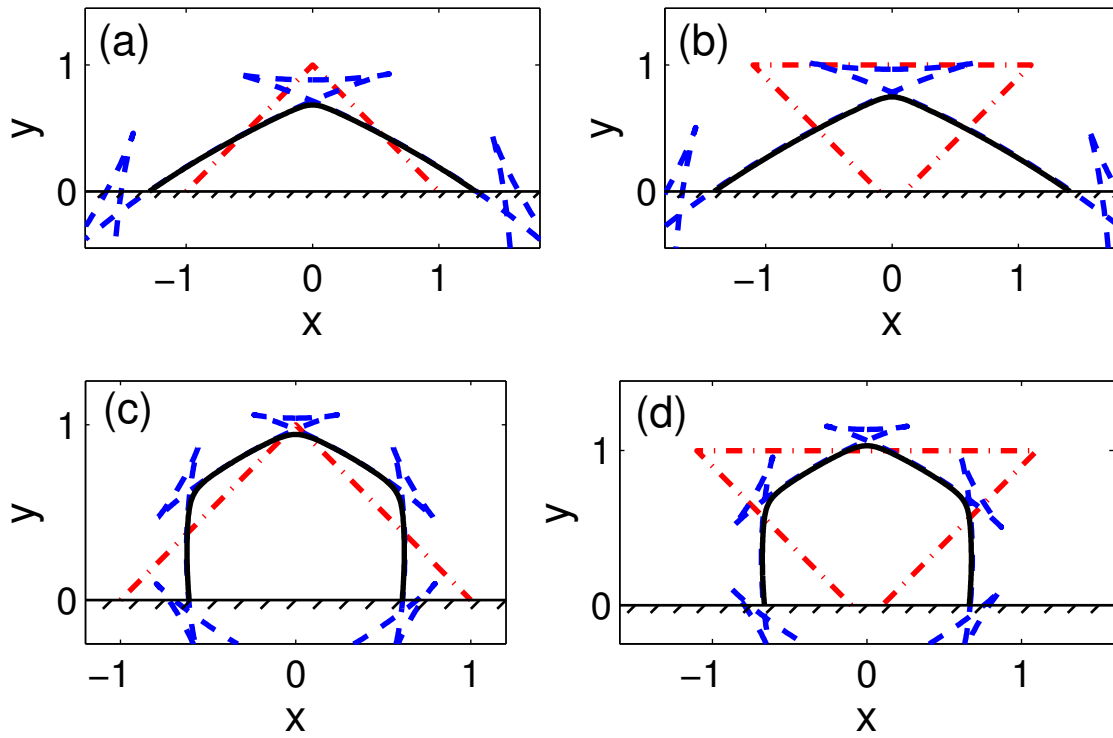
Figure 3.32: Equilibria (black solid curve) of dewetting thin films with $m = 6, \beta = 0.1$, (a, b) $\sigma = 0.6$; (c, d) $\sigma = -0.4$.

ones should be of same shape.
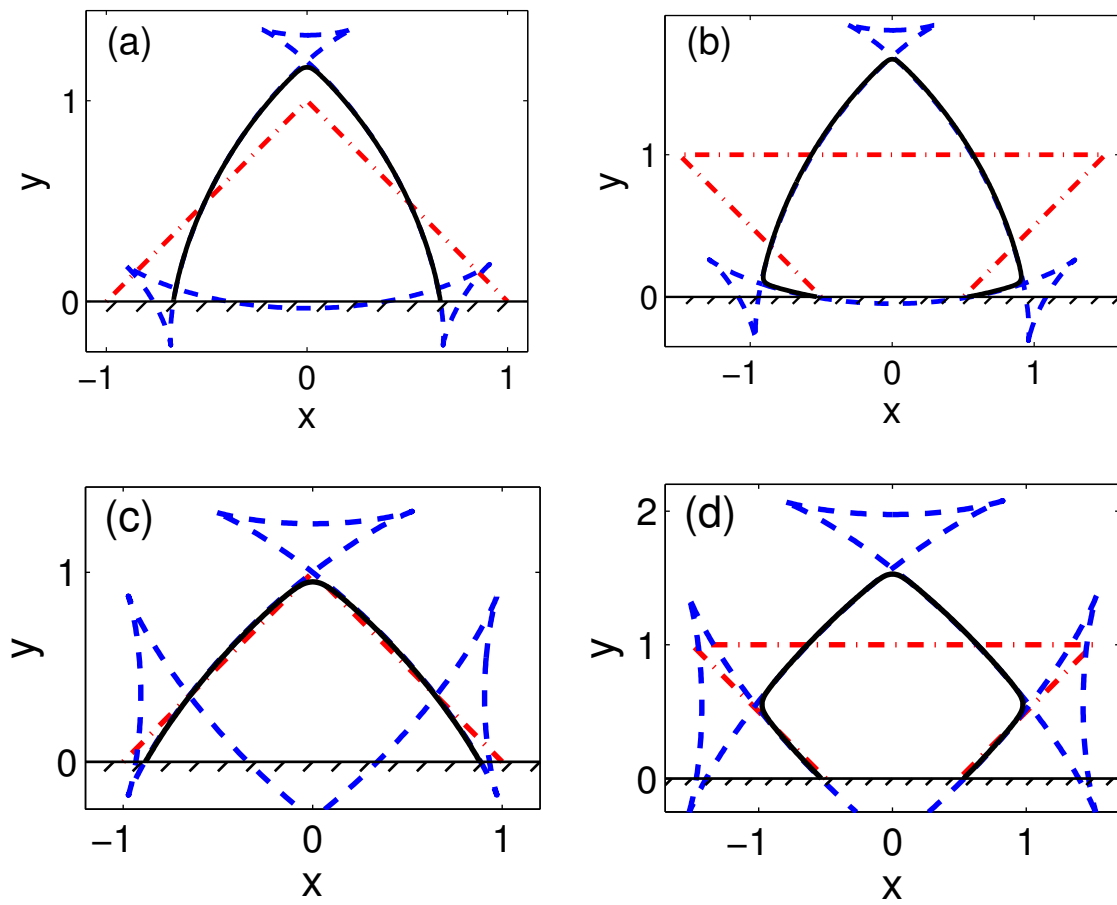
Figure 3.33: Equilibria (black solid curve) of dewetting thin films with (a, b) $m = 3, \beta = 0.3, \sigma = -0.65$; (c, d) $m = 4, \beta = 0.3, \sigma = -0.5$.
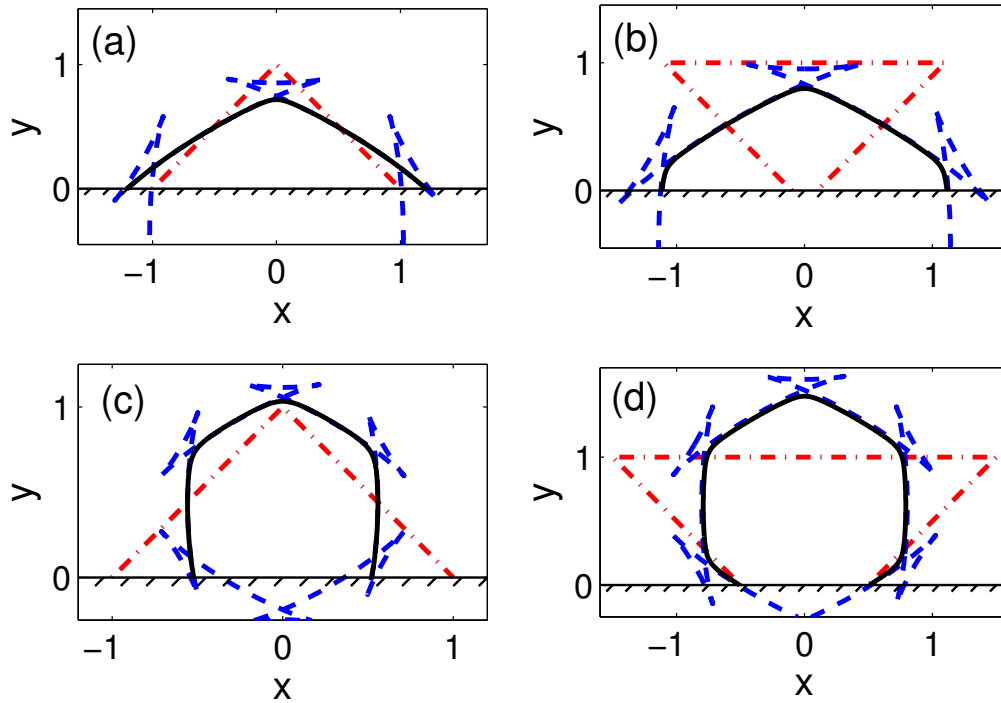
Figure 3.34: Equilibria (black solid curve) of dewetting thin films with $m = 6, \beta = 0.1$, (a, b) $\sigma = 0.35$; (c, d) $\sigma = -0.7$.
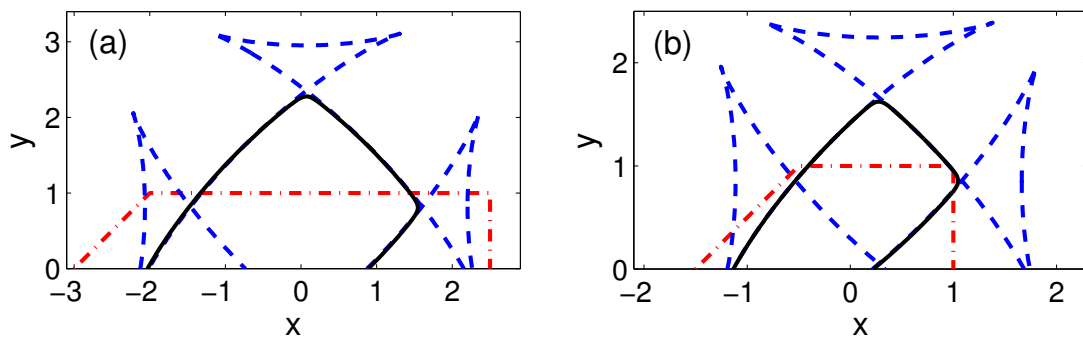
Figure 3.35: Equilibria (black solid curve) of dewetting thin films with $m = 4$ (a)$\beta = 0.3, \sigma = -0.5$, (b) $\beta = 0.4, \sigma = -\sqrt{3}/2$.
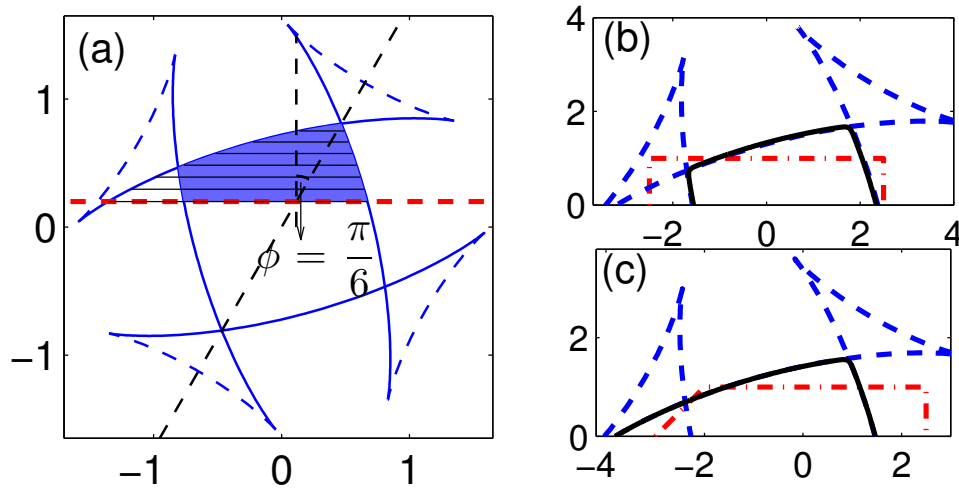
Figure 3.36: (a) Schematic view of the Equilibria with a nonzero $\phi = \pi/6$ and a given σ when $m = 4$. (b, c) Equilibria (black solid curve) of dewetting thin films with different initial shapes. The parameters are $m = 4, \beta = 0.3, \sigma = 0.2$.
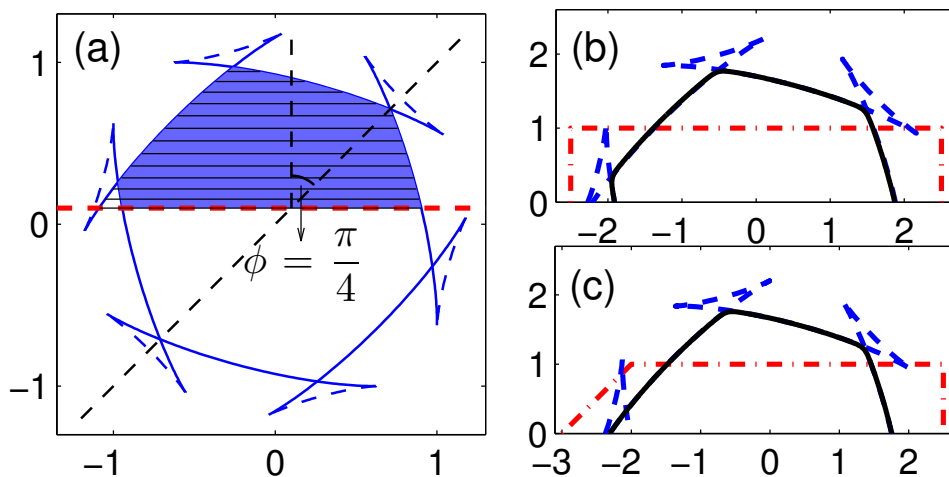
Figure 3.37: (a) Schematic view of the Equilibria with a nonzero $\phi = \pi/4$ and a given σ when $m = 6$. (b, c) Equilibria (black solid curve) of dewetting thin films with different initial shapes. The parameters are $m = 6, \beta = 0.1, \sigma = 0.1$.
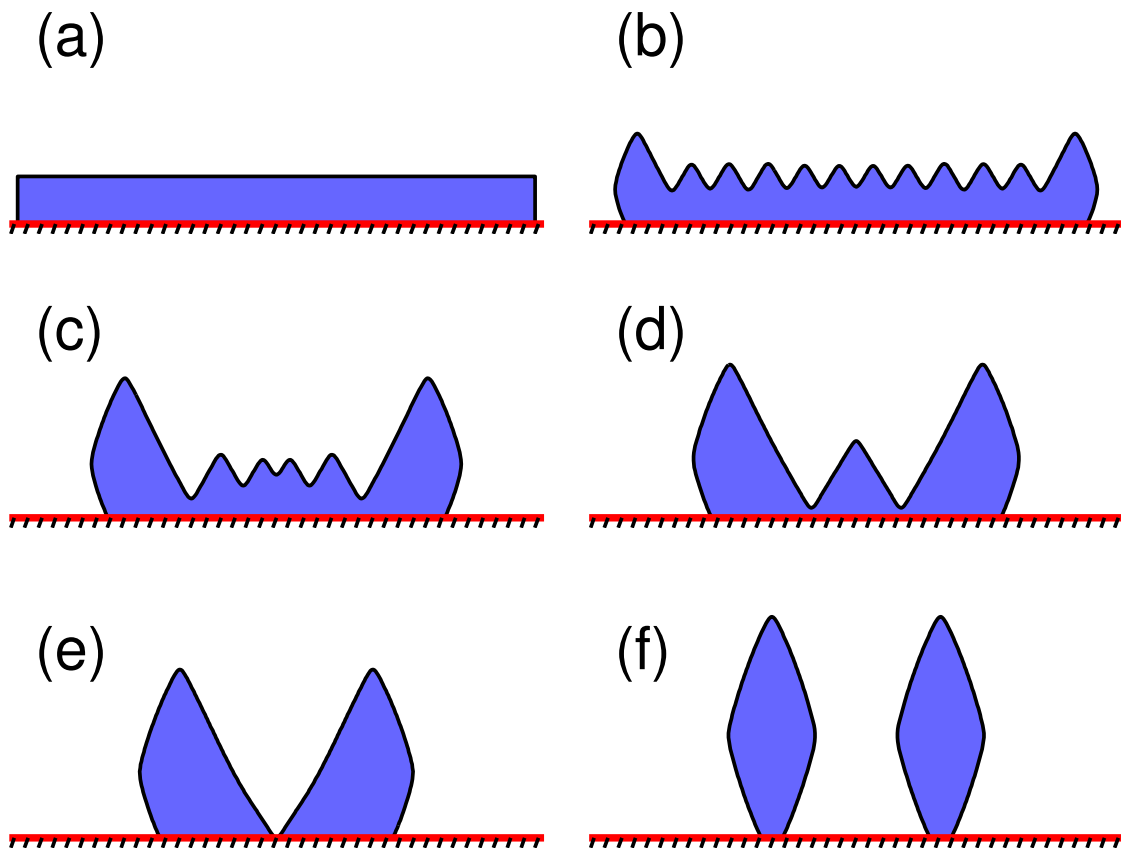
Figure 3.38: Evolution and pinch-off of a large island with initial length $L = 15$. $m = 4, \beta = 0.2, \sigma = -\sqrt{3}/2$.
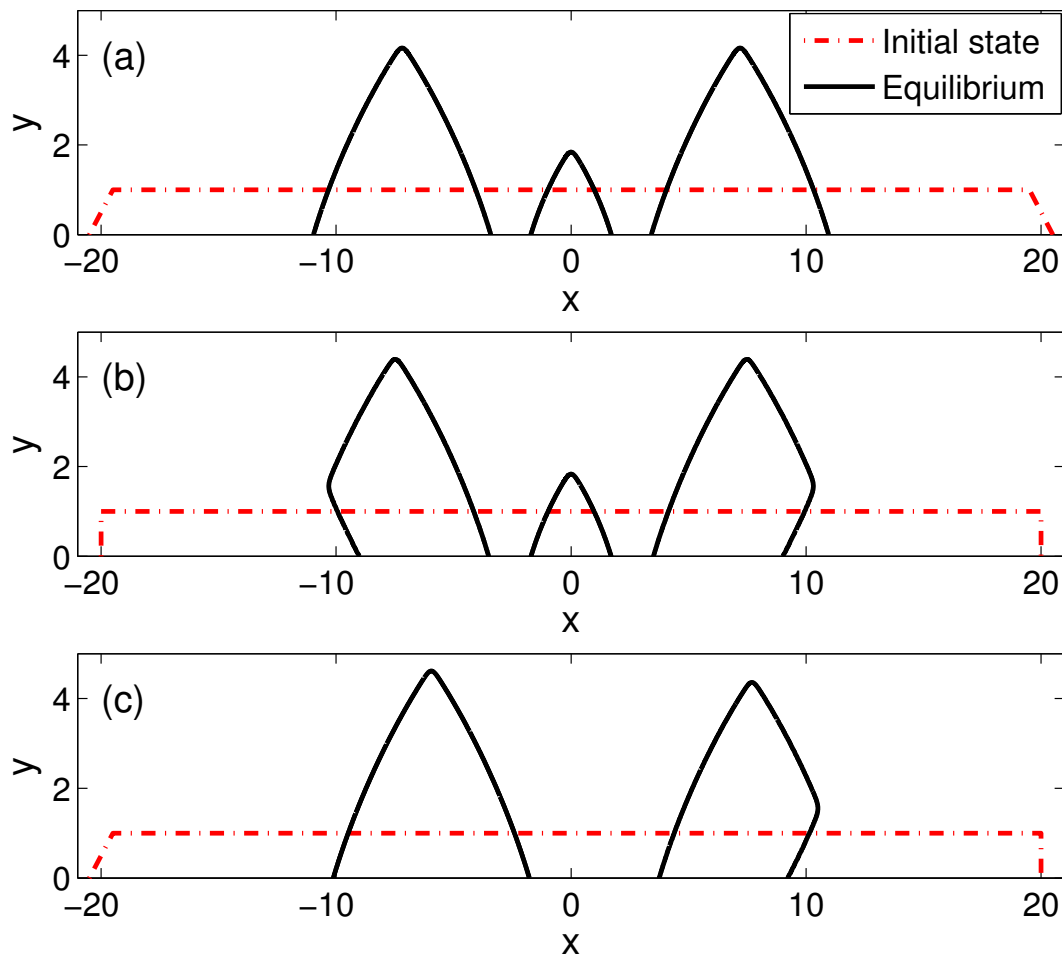
Figure 3.39: Equilibrium states of large islands with different initial states. $m = 4, \beta = 0.3, \sigma = -1/2$ and area 40 for all cases.

Chapter 4

Extension to Curved Substrates

In this chapter, we consider a thin solid film lying on a rigid curved solid substrate in 2D, as illustrated in Fig. 4.1.
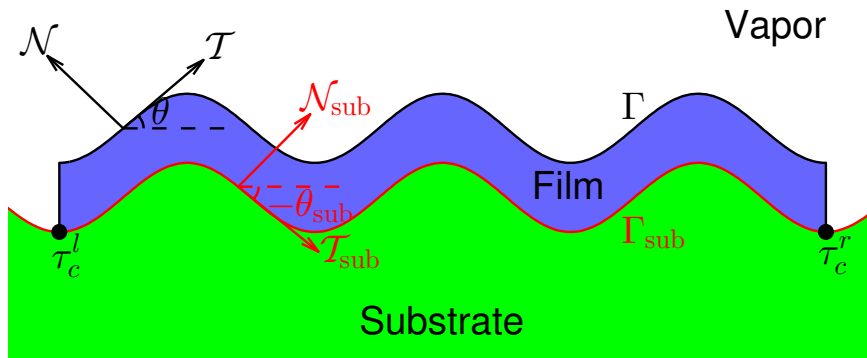
Figure 4.1: A schematic illustration of a solid thin film on a rigid, curved substrate in 2D.

The moving film/vapor interface is described by $\Gamma = \Gamma(t) := \mathbf{X}(s,t) = \big(x(s,t), y(s,t)\big)$ with arc length $s \in [0, L(t)]$. The unit tangent vector and unit outer normal vector of $\Gamma(t)$ are $\mathcal{T}(s,t) := (x_s, y_s)$ and $\mathcal{N}(s,t) := (-y_s, x_s)$, respectively. $\theta(s,t) \in (-\pi, \pi]$ is defined to be the tangent (normal) angle of the interface.

The fixed curved substrate is denoted as $\Gamma_{\mathrm{sub}} := \mathbf{X}_{\mathrm{sub}}(\tau) = \big(x_{\mathrm{sub}}(\tau), y_{\mathrm{sub}}(\tau)\big)$ with arc length $\tau \in [0, L_{\mathrm{sub}}]$. The unit tangent vector and unit outer normal vector

are denoted as $\mathcal{T}_{\mathrm{sub}}(\tau)$ and $\mathcal{N}_{\mathrm{sub}}(\tau)$, respectively. $\theta_{\mathrm{sub}}(\tau) \in (-\pi, \pi]$ is the tangent angle of the substrate curve.

The two contact points can be described as the $s = 0$ and $s = L(t)$ points on $\Gamma(t)$, or the $\tau = \tau_c^l(t)$ and $\tau = \tau_c^r(t)$ on Γ_{sub}. For simplicity, we denote them as τ_c^l and τ_c^r, and we use the following notations

$$\theta^l = \theta(0, t), \quad \theta^r = \theta(L, t),$$

$$\theta_{\mathrm{sub}}^l = \theta_{\mathrm{sub}}(\tau_c^l), \quad \theta_{\mathrm{sub}}^r = \theta_{\mathrm{sub}}(\tau_c^r).$$

The left and right dynamical contact angles are defined as

$$\theta_d^l = \theta_d^l(t) := \theta^l - \theta_{\mathrm{sub}}^l, \quad \theta_d^r = \theta_d^r(t) := \theta^r - \theta_{\mathrm{sub}}^r. \tag{4.0.1}$$

This is consistent with the definition in the flat substrate case [130] where $\theta_{\mathrm{sub}}^l = \theta_{\mathrm{sub}}^r = 0$.

4.1 The sharp interface models

4.1.1 Isotropic/weakly anisotropic case

The total free energy of the system for solid-state dewetting problems with weakly anisotropic surface energies on rigid curved substrates can be written as:

$$W = \int_\Gamma \gamma(\theta)\, d\Gamma + \big(\gamma_{FS} - \gamma_{VS}\big)(\tau_c^r - \tau_c^l), \tag{4.1.1}$$

where γ_{FS} and γ_{VS} are, respectively, the surface energy densities of the film/substrate and vapor/substrate interfaces. Here, we assume that the film/vapor interface energy (density) γ_{FV} is a function only of the interface tangent angle, i.e. $\gamma_{FV} = \gamma(\theta)$.

Consider an infinitesimal perturbation of the curve $\Gamma(t)$ along its normal and tangent directions:

$$\Gamma^\epsilon(t) = \Gamma(t) + \epsilon\varphi(s)\mathcal{N} + \epsilon\psi(s)\mathcal{T},$$

where ϵ is an infinitesimal number, and $\varphi(s), \psi(s)$ are arbitrary smooth functions with respect to arc length s. Then the two components of the new curve $\Gamma^\epsilon(t)$ can be expressed as follows:

$$
\begin{aligned}
\Gamma^\epsilon(t) &= (x^\epsilon(s,t), y^\epsilon(s,t)) \\
&= (x(s,t) + \epsilon u(s,t), y(s,t) + \epsilon v(s,t)),
\end{aligned}
$$

where the two component increments along the $x-$aixs and $y-$axis are defined as

$$
\begin{cases}
u(s,t) = -y_s(s,t)\varphi(s) + x_s(s,t)\psi(s), \\
v(s,t) = x_s(s,t)\varphi(s) + y_s(s,t)\psi(s).
\end{cases}
\tag{4.1.2}
$$

Assume that the contact points move along the tangent direction of substrate (If the substrate is not smooth, regularization is needed.), so the increments at the two contact points must be parallel to the tangent vectors of Γ_{sub}, that is,

$$
\begin{cases}
\big(u(0,t),\ v(0,t)\big) &= \lambda_l\ \mathcal{T}_{\text{sub}}(\tau_c^l), \\
\big(u(L,t),\ v(L,t)\big) &= \lambda_r\ \mathcal{T}_{\text{sub}}(\tau_c^r).
\end{cases}
\tag{4.1.3}
$$

Therefore, the increments in the arc length of the two contact points (taking Γ_{sub} as reference) are

$$
\begin{cases}
\epsilon\sqrt{u^2(0,t) + v^2(0,t)} = \epsilon\lambda_l|\mathcal{T}_{\text{sub}}(\tau_c^l)| = \epsilon\lambda_l, \\
\epsilon\sqrt{u^2(L,t) + v^2(L,t)} = \epsilon\lambda_r|\mathcal{T}_{\text{sub}}(\tau_c^r)| = \epsilon\lambda_r.
\end{cases}
$$

Here, λ_r, λ_l are arbitrary constants that measures the perturbation of the contact points.

Then, the total free energy W^ϵ of the new curve $\Gamma^\epsilon(t)$ becomes:

$$
\begin{aligned}
W^\epsilon &= \int_{\Gamma^\epsilon} \gamma(\theta^\epsilon)\, d\Gamma^\epsilon + \big(\gamma_{FS} - \gamma_{VS}\big)\Big[\big(\tau_c^r + \epsilon\lambda_r\big) - \big(\tau_c^l + \epsilon\lambda_l\big)\Big] \\
&= \int_0^L \gamma\Big(\arctan2\big(\frac{y_s + \epsilon v_s}{x_s + \epsilon u_s}\big)\Big)\sqrt{(x_s + \epsilon u_s)^2 + (y_s + \epsilon v_s)^2}\, ds \\
&\quad + \big(\gamma_{FS} - \gamma_{VS}\big)\Big[\big(\tau_c^r + \epsilon\lambda_r\big) - \big(\tau_c^l + \epsilon\lambda_l\big)\Big],
\end{aligned}
\tag{4.1.4}
$$

where the operator arctan2 is defined in Eq. (2.1.8). Then we can calculate the change rate of total free energy about the curve $\Gamma(t)$ because of this infinitesimal perturbation with respect to ϵ at the time t:

$$
\begin{aligned}
\frac{dW^\epsilon}{d\epsilon}\bigg|_{\epsilon=0} &= \int_0^L \Big(\gamma'(\theta)(v_s x_s - y_s u_s) + \gamma(\theta)(x_s u_s + y_s v_s)\Big)\,ds + \big(\gamma_{FS} - \gamma_{VS}\big)(\lambda_r - \lambda_l) \\
&= \int_0^L \Big[\gamma'(\theta)(\varphi_s - \kappa\psi) + \gamma(\theta)(\kappa\varphi + \psi_s)\Big]\,ds + \big(\gamma_{FS} - \gamma_{VS}\big)(\lambda_r - \lambda_l) \\
&= \int_0^L \big(\gamma(\theta) + \gamma''(\theta)\big)\kappa\varphi\,ds \\
&\quad + \Big(\big(\gamma'(\theta)\varphi\big)_{s=L} + \big(\gamma(\theta)\psi\big)_{s=L} + \big(\gamma_{FS} - \gamma_{VS}\big)\lambda_r\Big) \\
&\quad - \Big(\big(\gamma'(\theta)\varphi\big)_{s=0} + \big(\gamma(\theta)\psi\big)_{s=0} + \big(\gamma_{FS} - \gamma_{VS}\big)\lambda_l\Big), \quad (4.1.5)
\end{aligned}
$$

where the curvature of the curve is defined as $\kappa = -y_{ss}x_s + x_{ss}y_s$.

Since the two contact points are required to move along the tangent direction of substrate, we can obtained the following relations between φ, ψ and u, v at $s = 0, L$ by combining Eq. (4.1.2) and Eq. (4.1.3).

$$\varphi(0) = \big(u(0,t), v(0,t)\big) \cdot \mathcal{N}(0,t) = -\lambda_l \sin\theta_d^l, \qquad (4.1.6a)$$

$$\psi(0) = \big(u(0,t), v(0,t)\big) \cdot \mathcal{T}(0,t) = \lambda_l \cos\theta_d^l, \qquad (4.1.6b)$$

$$\varphi(L) = \big(u(L,t), v(L,t)\big) \cdot \mathcal{N}(L,t) = -\lambda_r \sin\theta_d^r, \qquad (4.1.6c)$$

$$\psi(L) = \big(u(L,t), v(L,t)\big) \cdot \mathcal{T}(L,t) = \lambda_r \cos\theta_d^r. \qquad (4.1.6d)$$

Therefore, Eq. (4.1.5) becomes

$$
\begin{aligned}
\frac{dW^\epsilon}{d\epsilon}\bigg|_{\epsilon=0} &= \int_0^L \big(\gamma(\theta) + \gamma''(\theta)\big)\kappa\varphi\,ds \\
&\quad + \Big(\gamma(\theta^r)\cos\theta_d^r - \gamma'(\theta^r)\sin\theta_d^r + \big(\gamma_{FS} - \gamma_{VS}\big)\Big)\lambda_r \\
&\quad - \Big(\gamma(\theta^l)\cos\theta_d^l - \gamma'(\theta^l)\sin\theta_d^l + \big(\gamma_{FS} - \gamma_{VS}\big)\Big)\lambda_l. \quad (4.1.7)
\end{aligned}
$$

From Eq. (4.1.7) we can define the first variation of the total free energy W with respect to the moving film/vapor interface Γ and the right contact point τ_c^r and the

left contact point τ_c^l as follows:

$$\frac{\delta W}{\delta \Gamma} = \Big(\gamma(\theta) + \gamma''(\theta)\Big)\kappa, \tag{4.1.8}$$

$$\frac{\delta W}{\delta \tau_c^r} = \gamma(\theta^r)\cos\theta_d^r - \gamma'(\theta^r)\sin\theta_d^r + \big(\gamma_{FS} - \gamma_{VS}\big), \tag{4.1.9}$$

$$\frac{\delta W}{\delta \tau_c^l} = -\Big(\gamma(\theta^l)\cos\theta_d^l - \gamma'(\theta^l)\sin\theta_d^l + \big(\gamma_{FS} - \gamma_{VS}\big)\Big). \tag{4.1.10}$$

It can be seen that the first equation is the same as Eq. (2.1.15) in the flat substrate case, and Eqs. (4.1.9, 4.1.10) collapse to Eqs. (2.1.16, 2.1.17) when the substrate is flat, that is, $\theta_d^r = \theta^r, \theta_d^l = \theta^l$. Therefore, the chemical potential μ and the normal velocity V_n of the film/vapor interface are defined the same as in the flat substrate case as follows:

$$\mu = \Omega_0\frac{\delta W}{\delta \Gamma} = \Omega_0\Big(\gamma(\theta) + \gamma''(\theta)\Big)\kappa = \Omega_0\tilde{\gamma}(\theta)\kappa, \tag{4.1.11}$$

$$V_n = \frac{D_s\nu\Omega_0^2}{k_BT_e}\frac{\partial^2}{\partial s^2}\Big[\big(\gamma(\theta) + \gamma''(\theta)\big)\kappa\Big]. \tag{4.1.12}$$

Analogous with the weakly anisotropic case, we can describe the relaxed contact angle boundary conditions as

$$\frac{d\tau_c^l(t)}{dt} = -\eta\frac{\delta W}{\delta \tau_c^l}, \quad \text{at} \quad \tau = \tau_c^l, \tag{4.1.13}$$

$$\frac{d\tau_c^r(t)}{dt} = -\eta\frac{\delta W}{\delta \tau_c^r}, \quad \text{at} \quad \tau = \tau_c^r. \tag{4.1.14}$$

By choosing the time scale to be $R_0^4/(B\gamma_0)$ and the contact line mobility scale to be B/R_0^3, where R_0, γ_0 are unit scales of the length and the film/vapor energy density, respectively, and $B = D_s\nu\gamma_{FV}\Omega_0^2/(k_BT_e)$ is defined the same as in the flat substrate case, the two-dimensional solid-state dewetting of a thin film with weakly anisotropic surface energies on a rigid curved solid substrate can be described in the following dimensionless form by the sharp interface model:

$$\begin{cases} \dfrac{\partial \mathbf{X}}{\partial t} = V_n\mathcal{N} = \dfrac{\partial^2\mu}{\partial s^2}\mathcal{N}, \\ \mu = \tilde{\gamma}(\theta)\kappa = \Big(\gamma(\theta) + \gamma''(\theta)\Big)\kappa. \end{cases} \tag{4.1.15}$$

Note that $\mathbf{X}, t, V_n, s, \mu, \widetilde{\gamma}, \gamma$ and η are dimensionless variables, and we still use the same notations for brevity.

The governing equation (4.1.15) for the solid-state dewetting problem is subject to the following dimensionless conditions:

(i) Contact point condition (**BC1**)

$$\mathbf{X}(0, t) = \mathbf{X}_{\text{sub}}(\tau_c^l), \qquad \mathbf{X}(L, t) = \mathbf{X}_{\text{sub}}(\tau_c^r). \tag{4.1.16}$$

This condition, which shows two expressions of the contact points by taking different curve as reference, means that the two moving contact points always lie on the substrate.

(ii) Relaxed (or dissipative) contact angle condition (**BC2**)

$$\frac{d\tau_c^l}{dt} = \eta f(\theta^l, \theta_d^l), \qquad \frac{d\tau_c^r}{dt} = -\eta f(\theta^r, \theta_d^r), \tag{4.1.17}$$

where the two-variable-function f is defined as

$$f(\theta, \theta_d) := \gamma(\theta) \cos \theta_d - \gamma'(\theta) \sin \theta_d - \sigma$$

with the dimensionless coefficient $\sigma := (\gamma_{VS} - \gamma_{FS})/\gamma_0$ the same as in previous chapters. The variables θ^l, θ_d^l should satisfy Eq. (4.0.1).

(iii) Zero-mass flux condition (**BC3**)

$$\frac{\partial \mu}{\partial s}(s = 0, t) = 0, \qquad \frac{\partial \mu}{\partial s}(s = L, t) = 0, \tag{4.1.18}$$

This condition implies that the area (mass) of the thin film is conserved.

It should be noted that according to the relaxed contact angle condition here, the movement of the contact line (taking the left contact point as example) depends on two variables, both θ^l (or equivalently θ_{sub}^l) and θ_d^l. That is, for the equilibrium configuration, a generalized Young equation

$$f(\theta, \theta_d) = \gamma(\theta) \cos \theta_d - \gamma'(\theta) \sin \theta_d - \sigma = 0 \tag{4.1.19}$$

should be satisfied, instead of the traditional Young equation. This implies that in the equilibrium configuration, the contact angle can not be determined unless we fix the contact line position (or θ^l_{sub}).

The generalized Young equation can be simplified in the following two cases. One is the isotropic case, i.e.,. $\gamma(\theta) = 1$, and $\gamma'(\theta) = 0$. In this case, Eq. (4.1.19) will collapse to the well-known isotropic Young equation. It implies that in the isotropic case, the isotropic Young equation still works for curved substrates. The other simplified case is that the substrate tangent angle is fixed to be a constant θ_{sub}, then the generalized Young equation (i.e., Eq. (4.1.19)) becomes to the following equation:

$$\gamma(\theta_d + \theta_{\text{sub}}) \cos \theta_d - \gamma'(\theta_d + \theta_{\text{sub}}) \sin \theta_d - \sigma = 0, \tag{4.1.20}$$

which can be used for determining the static contact angle in the equilibrium configuration. And when the $\theta_{\text{sub}} = 0$, this case further collapses to the (traditional) isotropic/anisotropic Young equation in the flat substrate case. Moreover, it should be noted that when we choose $\gamma(\theta)$ of the form as in Eq. (1.2.2), the above equation with a nonzero θ_{sub} and $\phi = 0$ is equivalent to the traditional Young equation in the flat substrate case with $\phi = \theta_{\text{sub}}$.

4.1.2 Strongly anisotropic case

Similar to the flat substrate cases, for strongly anisotropic surface energies, the total free energy of the system is regularized by adding the Willmore energy W_{w} into Eq. (4.1.1):

$$W_{\text{w}} = \int_{\Gamma} \frac{\varepsilon^2}{2} \kappa^2 \, d\Gamma, \tag{4.1.21}$$

where ε is a regularization parameter and κ is the curvature of the curve Γ.

Following with the same perturbation approach presented above, we can calculate the change rate of the regularization term W_{w} about the curve $\Gamma(t)$ due to the

infinitesimal perturbation with respect to ϵ at the time t.

$$
\begin{aligned}
\frac{dW_{\mathrm{w}}^{\epsilon}}{d\epsilon}\bigg|_{\epsilon=0} &= -\int_0^L \varepsilon^2\Big(\kappa_{ss}+\frac{\kappa^3}{2}\Big)\varphi\,ds \\
&\quad - \Big(\varepsilon^2\kappa\varphi_s\Big)\Big|_0^L + \Big(\varepsilon^2\kappa_s\varphi\Big)\Big|_0^L + \Big(\frac{\varepsilon^2}{2}\kappa^2\psi\Big)\Big|_0^L \\
&= -\int_0^L \varepsilon^2\Big(\kappa_{ss}+\frac{\kappa^3}{2}\Big)\varphi\,ds \\
&\quad - \varepsilon^2\Big(\kappa_s(s=L)\cos\theta_d^r\lambda_r - \kappa_s(s=0)\cos\theta_d^l\lambda_l\Big)
\end{aligned}
\tag{4.1.22}
$$

We do not show the calculation steps in detail since it is almost the same as the flat substrate (strongly anisotropic) case. Note that in the last step of the above calculation, we make use of Eq. (4.1.6) and we also introduce the zero-curvature condition $\kappa(s=0,t)=\kappa(s=L,t)=0$ as in the flat substrate (strongly anisotropic) case.

Then, combining Eq. (4.1.7) and Eq. (4.1.22), we can obtain the first variation of the total free energy $W + W_{\mathrm{w}}$ with respect to the moving film/vapor interface Γ and the right and left contact points τ_c^r, τ_c^l as follows:

$$
\frac{\delta(W + W_{\mathrm{w}})}{\delta\Gamma} = \Big(\gamma(\theta) + \gamma''(\theta)\Big)\kappa - \varepsilon^2\Big(\frac{\partial^2\kappa}{\partial s^2}+\frac{\kappa^3}{2}\Big),
\tag{4.1.23}
$$

$$
\frac{\delta(W + W_{\mathrm{w}})}{\delta\tau_c^r} = \Big[\gamma(\theta^r)\cos\theta_d^r - \gamma'(\theta^r)\sin\theta_d^r + \big(\gamma_{FS}-\gamma_{VS}\big)
$$
$$
\qquad\qquad - \varepsilon^2\frac{\partial\kappa}{\partial s}\sin\theta_d^r\Big]_{s=L},
\tag{4.1.24}
$$

$$
\frac{\delta(W + W_{\mathrm{w}})}{\delta\tau_c^l} = -\Big[\gamma(\theta^l)\cos\theta_d^l - \gamma'(\theta^l)\sin\theta_d^l + \big(\gamma_{FS}-\gamma_{VS}\big)
$$
$$
\qquad\qquad - \varepsilon^2\frac{\partial\kappa}{\partial s}\sin\theta_d^l\Big]_{s=0}.
\tag{4.1.25}
$$

Then, by the same dimensionless procedure as in the weakly anisotropic case, the two-dimensional solid-state dewetting of a thin film with strongly anisotropic surface energies on a curved solid substrate can be described in the following dimensionless form by the sharp interface model:

$$
\begin{cases}
\dfrac{\partial \mathbf{X}}{\partial t} = V_n\mathcal{N} = \dfrac{\partial^2\mu}{\partial s^2}\mathcal{N}, \\[2mm]
\mu = \Big(\gamma(\theta) + \gamma''(\theta)\Big)\kappa - \varepsilon^2\Big(\dfrac{\partial^2\kappa}{\partial s^2}+\dfrac{\kappa^3}{2}\Big).
\end{cases}
\tag{4.1.26}
$$

Again, $\mathbf{X}, t, V_n, s, \mu, \gamma$ and η are dimensionless variables, and we still use the same notations for brevity.

The governing equation (4.1.26) for the solid-state dewetting problem is subject to the following dimensionless conditions:

(i) Contact point condition (**BC1**)

$$\mathbf{X}(0, t) = \mathbf{X}_{\text{sub}}(\tau_c^l), \qquad \mathbf{X}(L, t) = \mathbf{X}_{\text{sub}}(\tau_c^r). \tag{4.1.27}$$

(ii) Relaxed (or dissipative) contact angle condition (**BC2**)

$$\frac{d\tau_c^l}{dt} = \eta f_\varepsilon(\theta^l, \theta_d^l), \qquad \frac{d\tau_c^r}{dt} = -\eta f_\varepsilon(\theta^r, \theta_d^r), \tag{4.1.28}$$

where the two-variable-function f_ε is defined as

$$f_\varepsilon(\theta, \theta_d) := \gamma(\theta) \cos \theta_d - \gamma'(\theta) \sin \theta_d - \sigma - \varepsilon^2 \frac{\partial \kappa}{\partial s}(\theta) \sin \theta_d,$$

where σ is defined the same as the one in Eq. (4.1.17). Analogously, this condition is consistent with condition (3.1.14) when the substrate becomes flat, and the $f_\varepsilon(\theta, \theta_d)$ converges to $f(\theta, \theta_d)$ in Eq. (4.1.17) as ε approaches 0.

(iii) Zero-mass flux condition (**BC3**)

$$\frac{\partial \mu}{\partial s}(s = 0, t) = 0, \qquad \frac{\partial \mu}{\partial s}(s = L, t) = 0, \tag{4.1.29}$$

(iv) Zero curvature condition(**BC4**)

$$\kappa(s = 0, t) = 0, \qquad \kappa(s = L, t) = 0. \tag{4.1.30}$$

4.2 Mass conservation and energy dissipation

Proof of mass conservation. The following proof is suitable for both the weakly and strongly anisotropic case.

The area(mass) of the thin film is defined as

$$A(t) = \int_0^1 y x_p \, dp - \int_{\tau_c^l}^{\tau_c^r} y_{\text{sub}}(x_{\text{sub}})_\tau \, d\tau.$$

Then the change rate of the area can be calculated as

$$
\begin{aligned}
\frac{dA}{dt} &= \int_0^1 (y_t x_p + y x_{pt})\, dp - \left(y_{\text{sub}}(x_{\text{sub}})_\tau \frac{d\tau_c^r}{dt} \right)_{\tau=\tau_c^r} + \left(y_{\text{sub}}(x_{\text{sub}})_\tau \frac{d\tau_c^r}{dt} \right)_{\tau=\tau_c^l} \\
&= \int_0^1 (y_t x_p - y_p x_t)\, dp + y x_t \Big|_{p=0}^{p=1} - y_{\text{sub}}(\tau_c^r)\frac{dx_{\text{sub}}(\tau_c^r)}{dt} + y_{\text{sub}}(\tau_c^l)\frac{dx_{\text{sub}}(\tau_c^l)}{dt} \\
&= \int_0^1 (x_t, y_t) \cdot (-y_p, x_p)\, dp + y x_t \Big|_{p=0}^{p=1} - y(1)x_t(1) + y(0)x_t(0) \\
&= \int_0^{L(t)} \mathbf{X}_t \cdot \mathcal{N}\, ds \\
&= \int_0^{L(t)} \mu_{ss}\, ds \\
&= \mu_s\big(L(t), t\big) - \mu_s\big(0, t\big) = 0
\end{aligned}
$$

In the above calculation, we make use of that the following two notations (Left side is the notation at Γ, and right side is the notation for Γ_{sub}.) for the contact points are equivalent.

$$
\big(x(p=0),\ y(p=0)\big) = \big(x_{\text{sub}}(\tau_c^l),\ y_{\text{sub}}(\tau_c^l)\big),
$$
$$
\big(x(p=1),\ y(p=1)\big) = \big(x_{\text{sub}}(\tau_c^r),\ y_{\text{sub}}(\tau_c^r)\big).
$$

Hence, the area(mass) of the thin film is conserved under the condition $\mu_s(0, t) = \mu_s(L, t) = 0$. $\qquad\square$

Proof of energy dissipation for the weakly anisotropic case. The total energy in the weakly case (4.1.1) can be rewritten as:

$$
W(t) = \int_0^1 \gamma(\theta) s_p\, dp + \big(\gamma_{FS} - \gamma_{VS}\big)\big(\tau_c^r - \tau_c^l\big),
$$

Making using of the same identities we used in the flat substrate case, we can

calculate the change rate of the total free energy as follows:

$$
\begin{aligned}
\frac{dW}{dt} &= \int_0^1 \Big(\gamma'(\theta)\theta_t s_p + \gamma(\theta)s_{pt}\Big)\,dp + (\gamma_{FS} - \gamma_{VS})\Big(\frac{d\tau_c^r}{dt} - \frac{d\tau_c^l}{dt}\Big) \\
&= \int_0^1 \mathbf{X}_{pt} \cdot \big(\gamma'(\theta)\,\mathcal{N} + \gamma(\theta)\,\mathcal{T}\big)\,dp + (\gamma_{FS} - \gamma_{VS})\Big(\frac{d\tau_c^r}{dt} - \frac{d\tau_c^l}{dt}\Big) \\
&= -\int_0^1 \mathbf{X}_t \cdot \Big(\big(\gamma''(\theta)\theta_p\mathcal{N} + \gamma'(\theta)\kappa s_p\mathcal{T}\big) + \big(\gamma'(\theta)\theta_p\mathcal{T} - \gamma(\theta)\kappa s_p\mathcal{N}\big)\Big)\,dp \\
&\quad + \Big(\mathbf{X}_t \cdot \big(\gamma'(\theta)\,\mathcal{N} + \gamma(\theta)\,\mathcal{T}\big)\Big)\Big|_{p=0}^{p=1} + (\gamma_{FS} - \gamma_{VS})\Big(\frac{d\tau_c^r}{dt} - \frac{d\tau_c^l}{dt}\Big) \\
&= \int_0^{L(t)} \kappa\Big(\gamma(\theta) + \gamma''(\theta)\Big)\,\mathbf{X}_t \cdot \mathcal{N}\,ds \\
&\quad + \frac{d\tau_c^r}{dt}\Big(\gamma(\theta^r)\cos\theta_d^r - \gamma'(\theta^r)\sin\theta_d^r + \gamma_{FS} - \gamma_{VS}\Big) \\
&\quad - \frac{d\tau_c^l}{dt}\Big(\gamma(\theta^l)\cos\theta_d^l - \gamma'(\theta^l)\sin\theta_d^l + \gamma_{FS} - \gamma_{VS}\Big) \\
&= \int_0^{L(t)} \mu\mu_{ss}\,ds - C\Big[\Big(\frac{d\tau_c^r}{dt}\Big)^2 + \Big(\frac{d\tau_c^l}{dt}\Big)^2\Big] \\
&= \mu\mu_s\Big|_{s=0}^{s=L(t)} - \int_0^{L(t)} \mu_s^2\,ds - C\Big[\Big(\frac{d\tau_c^r}{dt}\Big)^2 + \Big(\frac{d\tau_c^l}{dt}\Big)^2\Big] \\
&= -\int_0^{L(t)} \mu_s^2\,ds - C\Big[\Big(\frac{d\tau_c^r}{dt}\Big)^2 + \Big(\frac{d\tau_c^l}{dt}\Big)^2\Big] < 0, \tag{4.2.1}
\end{aligned}
$$

where C is a positive constant.

Hence, the total free energy of the system decreases in the weakly anisotropic case when following our proposed model.

$\square$

Proof of energy dissipation for the strongly anisotropic case. The Willmore regularization (4.1.21) can be rewritten as

$$
W_{\mathrm{w}}(t) = \int_0^1 \frac{\varepsilon^2}{2}\kappa^2 s_p\,dp.
$$

So the change rate of $W_{\mathrm{w}}(t)$ can be calculated as follows:

$$
\begin{aligned}
\frac{dW_{\mathrm{w}}}{dt} &= -\varepsilon^2 \int_0^{L(t)} (\kappa_{ss} + \frac{1}{2}\kappa^3)\mathbf{X}_t \cdot \mathcal{N} \, ds \\
&\quad + \varepsilon^2 \Big(-\kappa\theta_t + \kappa_s \mathbf{X}_t \cdot \mathcal{N} - \frac{1}{2}\kappa^2 \mathbf{X}_t \cdot \mathcal{T} \Big) \Big|_{p=0}^{p=1} \qquad (4.2.2) \\
&= -\varepsilon^2 \int_0^{L(t)} (\kappa_{ss} + \frac{1}{2}\kappa^3)\mathbf{X}_t \cdot \mathcal{N} \, ds \\
&\quad - \varepsilon^2 \Big(\kappa_s(s=L)\sin\theta_d^r \frac{d\tau_c^r}{dt} - \kappa_s(s=0)\sin\theta_d^l \frac{d\tau_c^l}{dt} \Big) \qquad (4.2.3)
\end{aligned}
$$

Again, we do not show the detailed calculation steps since it is the same as the flat substrate cases. From Eq. (4.2.2) to Eq. (4.2.3), we use that the velocity at the contact points are parallel to the tangent direction of the substrate. That is,

$$
\mathbf{X}_t(p=0,t) \cdot \mathcal{N}(p=0,t) = \frac{d\tau_c^l}{dt}\mathcal{T}_{\mathrm{sub}}(\tau_c^l) \cdot \mathcal{N}(p=0,t) = -\frac{d\tau_c^l}{dt}\sin\theta_d^l.
$$

and the zero-curvature boundary condition.

Combine Eq. (4.2.1) and Eq. (4.2.3) , we can get the change rate of the total free energy in the strongly anisotropic case $W(t) + W_r(t)$ as

$$
\begin{aligned}
\frac{d(W + W_{\mathrm{w}})}{dt} &= \int_0^{L(t)} \Big(\kappa\big(\gamma(\theta) + \gamma''(\theta)\big) - \varepsilon^2(\kappa_{ss} + \frac{1}{2}\kappa^3) \Big) \mathbf{X}_t \cdot \mathcal{N} \, ds \\
&\quad + \frac{d\tau_c^r}{dt}\Big(\gamma(\theta_d^r)\cos\theta_d^r - \gamma'(\theta_d^r)\sin\theta_d^r + \gamma_{FS} - \gamma_{VS} - \varepsilon^2\kappa_s(\theta_d^r)\sin\theta_d^r \Big) \\
&\quad - \frac{d\tau_c^l}{dt}\Big(\gamma(\theta_d^l)\cos\theta_d^l - \gamma'(\theta_d^l)\sin\theta_d^l + \gamma_{FS} - \gamma_{VS} - \varepsilon^2\kappa_s(\theta_d^l)\sin\theta_d^l \Big) \\
&= \int_0^{L(t)} \mu\mu_{ss}\, ds - C\Big[\Big(\frac{d\tau_c^r}{dt}\Big)^2 + \Big(\frac{d\tau_c^l}{dt}\Big)^2 \Big] \\
&= -\int_0^{L(t)} \mu_s^2\, ds - C\Big[\Big(\frac{d\tau_c^r}{dt}\Big)^2 + \Big(\frac{d\tau_c^l}{dt}\Big)^2 \Big] < 0,
\end{aligned}
$$

where C is also a positive constant.

Hence, the total free energy of the system also decreases in the strongly anisotropic case. $\qquad \square$

4.3 The parametric finite element method (PFEM)

We still employ the parametric finite element method for solving the proposed models. The governing equations in the curved substrate case are the same as that in the flat substrate case, and only the boundary conditions change. So the weak formulations and the finite element approximations are the same as that in the flat substrate case, which are Eqs. (2.4.3, 2.4.11, 3.4.2, 3.4.3).

Here, we do not repeat writing these equations. We only want to point out that instead of updating x_c^l, x_c^r, we update τ_c^l and τ_c^r by discretizing Eq. (4.1.17) or Eq. (4.1.28). Then based on the information of the substrate, we can obtain the coordinates of the two contact points.

In addition, the spaces of the weak solution changes due to the new boundary conditions. The weak solution should be $\Gamma(t) = \mathbf{X}(I, t)$ with $\mathbf{X}(t) \in H_{l,r}^1 \times H_{ll,rr}^1$, where l, r, ll and rr stand for $x(\tau_c^l), x(\tau_c^r), y(\tau_c^l), y(\tau_c^r)$, respectively, instead of the space $H_{l,r}^1 \times H_0^1$ in the flat substrate case.

4.4 Island/film evolution simulation results

In this section, we report some simulation results under different (isotropic, weakly and strongly anisotropic) film/vapor energy densities for five kinds of substrates as shown in Fig. 4.2: (a) the convex circular substrate with radius R (curvature is a positive constant), (b) the concave circular substrate with radius R (curvature is a negative constant), (c) the sinusoidal substrate with expression $y_{\text{sub}} = A\sin(k\,x_{\text{sub}})$ (curvature is a continuous function of τ), (d) the sawtoothed substrate with slopes ± 1 and height (pit depth) H_{saw} (curvature is always 0 except for the corner points), (e) the inverted pyramidal substrate with pit depth H_{pyr} and mesa width L_{mesa}, the slopes are also ± 1 (curvature is similar to (d)). The numerical experiments on inverted pyramidal substrates were only performed for large islands as simulation of the templated solid-state dewetting shown in Fig. 1.2.

Note that the sawtoothed and the inverted pyramidal substates are not C^1
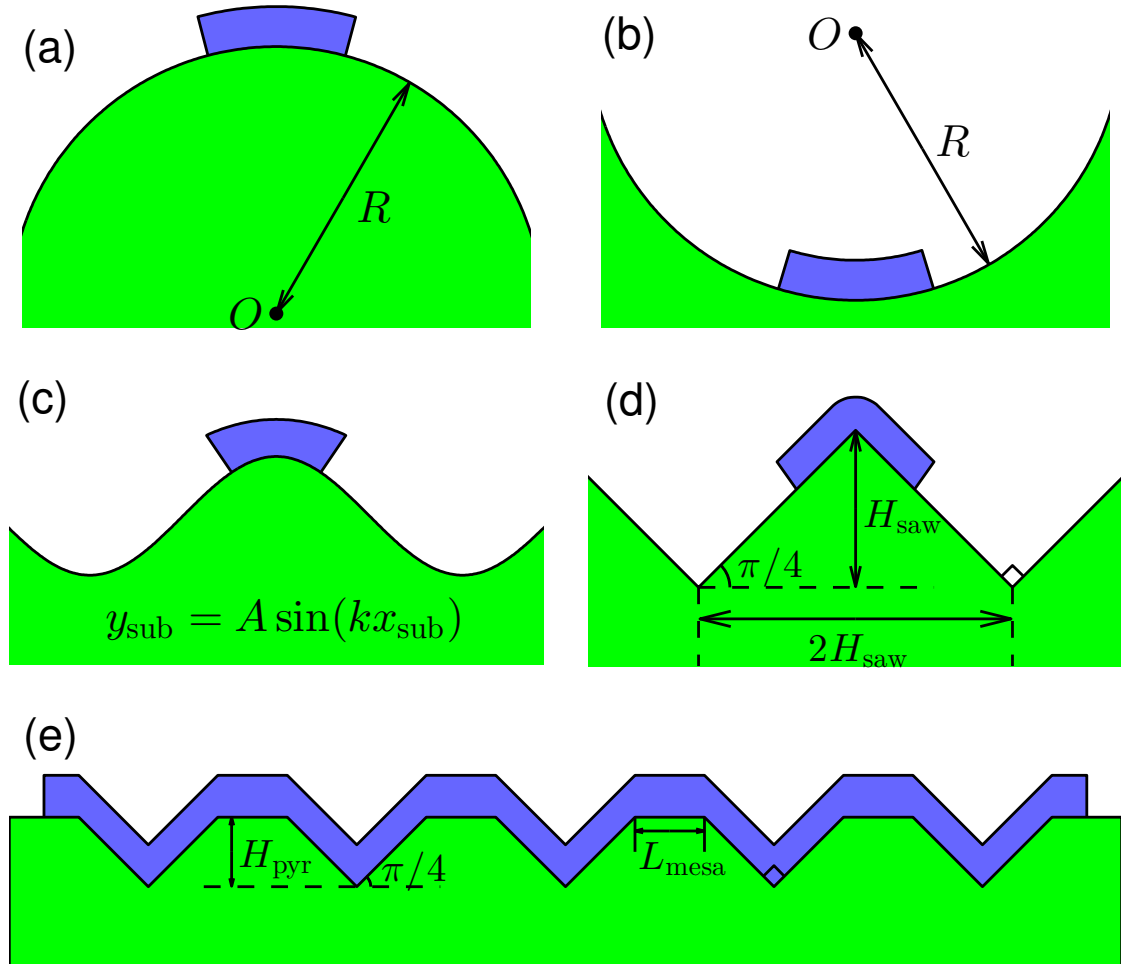
Figure 4.2: A schematic illustration of thin films lying on five types of curved substrates.

curves, regularization is needed according to our assumption (the contact points move along the tangent direction of the substrate). We regularize them by circle arcs at corners. In our simulations, the height of the film is measured along the normal direction of the substrate, and the length of the film/substrate interface is defined as the length of the film (shown in Fig. 4.3).

4.4.1 Small islands

1. Symmetric cases
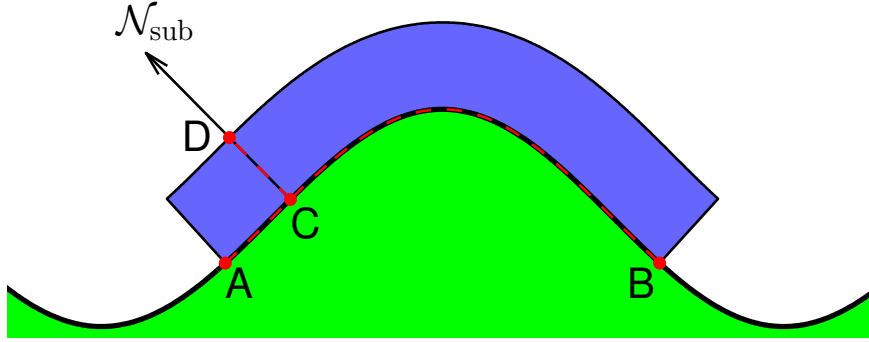
Figure 4.3: A thin film lying on a curved substrate. The height of the thin film is length of the straight line CD, and the length of it is the length of the curve AB.

We first examined the evolution of small islands that are placed symmetrically on different curved substrates. The length and height of the film are chosen to be 5 and 1(if not stated), respectively.

Fig. 4.4 shows the evolution of thin films with different energy densities on a convex circular substrate. The films are placed symmetrically on the top of the substrate. As can be seen that the morphology evolution is similar to that (shown in Fig. 2.7 and Fig. 3.23) in the flat substrate case: there exist only two thickened ridges and one valley in the isotropic and weakly anisotropic cases, while many ridges and valleys formed in the strongly anisotropic case; from (a4) to (c4), we can clearly see that the equilibrium changes from a circle-arc to anisotropic shapes. Moreover, as labeled in the caption that the isotropic contact angle in (a4) equals to the isotropic Young angle $\theta_i = 3\pi/4$, which is the same as the flat substrate case; while the anisotropic contact angles are different with that in the flat substrate case. These are all consistent with our analysis through the generalized Young equation.

Figs. 4.5, 4.6 and 4.7 show the equilibrium shapes of small island films with $\sigma = \pm 0.5$ on different substrates for the isotropic, weakly and strongly anisotropic cases, respectively. In the isotropic case, the contact angles of the equilibria all equal to the corresponding isotropic Young angles (either $2\pi/3$ or $\pi/3$). Moreover, comparing the equilibria in each column in Fig. 4.5, it can be seen that the equilibrium shapes
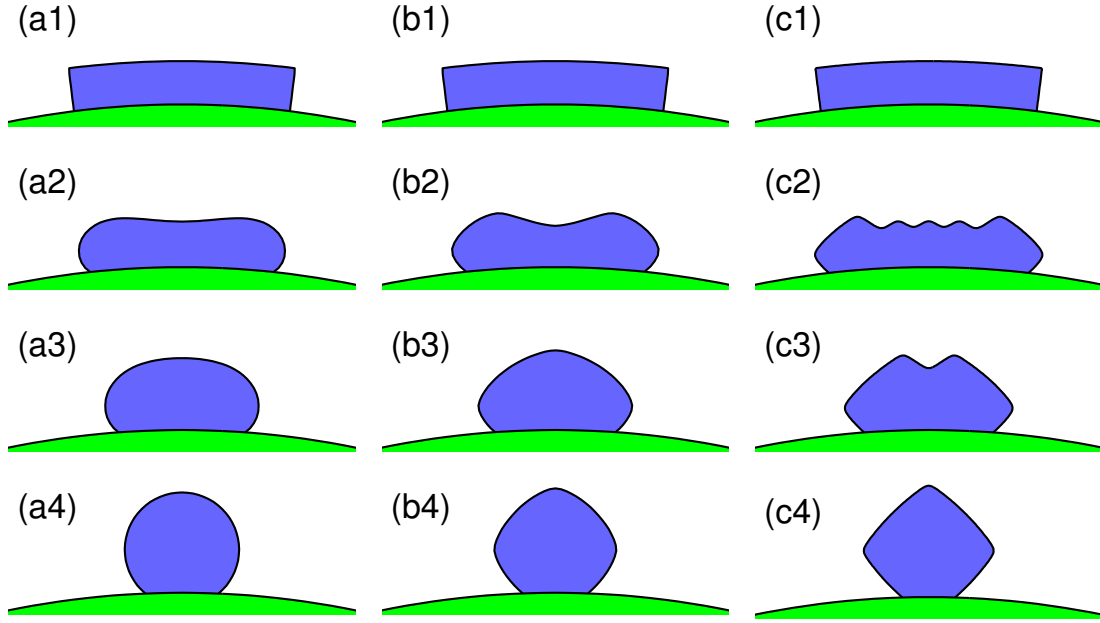
Figure 4.4: Evolution of thin films on a convex circular substrate with $R = 20$. (a1-a4) is the isotropic case, (b1-b4) is the weakly anisotropic case with $m = 4, \beta = 0.06$, and (c1-c4) is the strongly anisotropic case with $m = 4, \beta = 0.2$. $\sigma = -\sqrt{2}/2$ in all cases. The contact angles of the equilibria are (a) $2.356 \approx 3\pi/4$, (b) 2.369, (c) 2.376.

are different although they are of the same contact angle. In the anisotropic cases, there seems no obvious regularity of the contact angles for an arbitrary curved substrate. But for the sawtoothed substrate, i.e., (d1, d2) in Figs 4.6 and 4.7, we have $\theta_{\text{sub}} = \pm\pi/4$. Therefore, according to the relaxed contact angle boundary condition, the contact angles should satisfy the following generalized Young equation[1]:

$$\gamma(\theta \pm \frac{\pi}{4}) \cos(\theta) - \gamma'(\theta \pm \frac{\pi}{4}) \sin(\theta) - \sigma = 0. \tag{4.4.1}$$

It can be verified that the contact angles we obtained are exactly roots to this equation.

2. Asymmetric cases

---

[1]Note that similar to the flat substrate case, we cannot obtain the equation directly in the strongly anisotropic case, but we can obtain an equation which converges to it as $\varepsilon \to 0$.
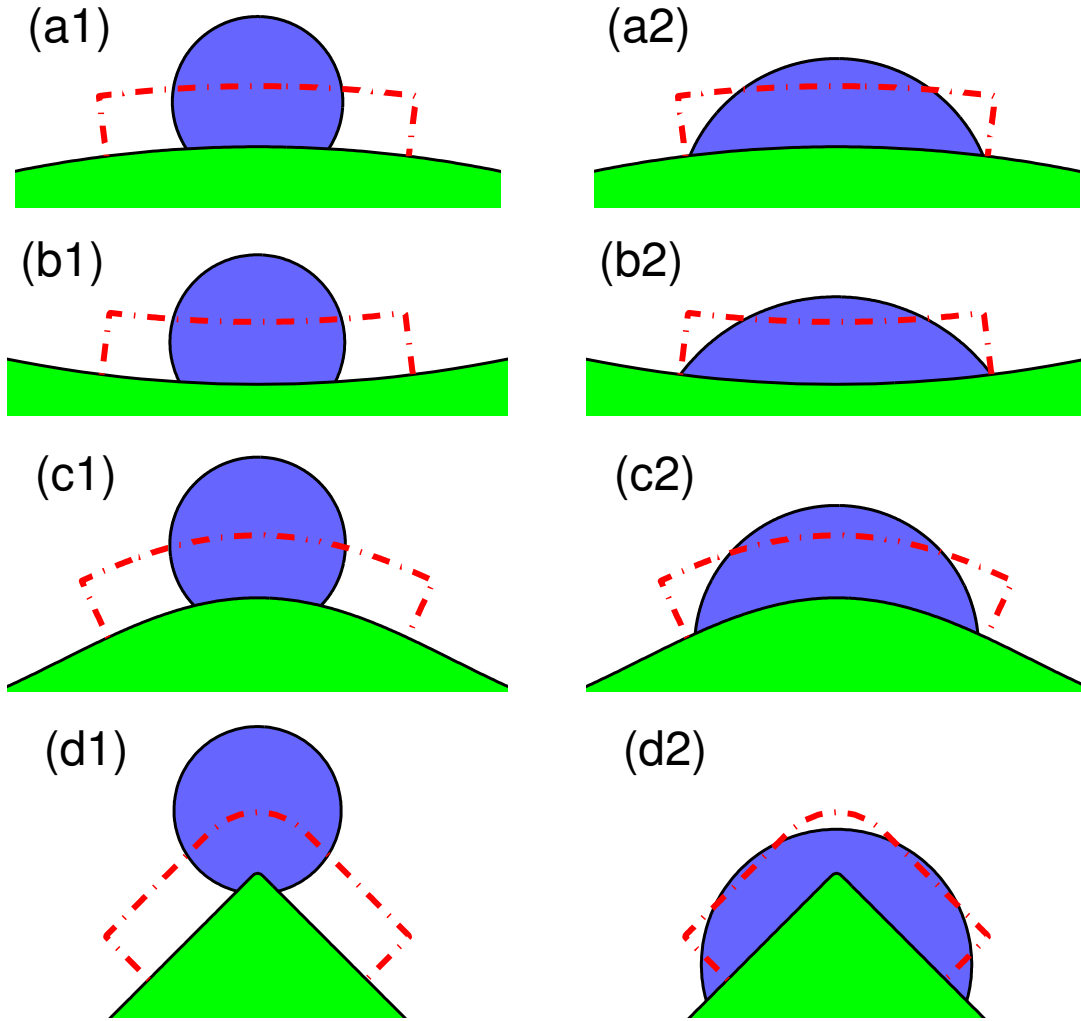
Figure 4.5: Equilibria of (isotropic) thin films on different curved substrates. The red dash-dot curve is the initial state. (a1, a2): the convex circular substrate with radius $R = 20$; (b1, b2): the concave circular substrate with radius $R = 20$; (c1, c2): the sinusoidal substrate with $A = 1, k = 1/2$; (d1, d2): the sawtoothed substrate $H_{\text{saw}} = 4$. Left column: $\sigma = -0.5$, contact angles are all around $2.094 \approx 2\pi/3$; Right column: $\sigma = 0.5$, contact angles are all around $1.047 \approx \pi/3$.

When a thin film is symmetrically placed on curved substrates, although it makes difference in the contact angles or the equilibrium shapes for different substrates, the geometric evolution is similar to that in the flat substrate case. In addition, since the thin film always evolves symmetrically, the two static contact angles must
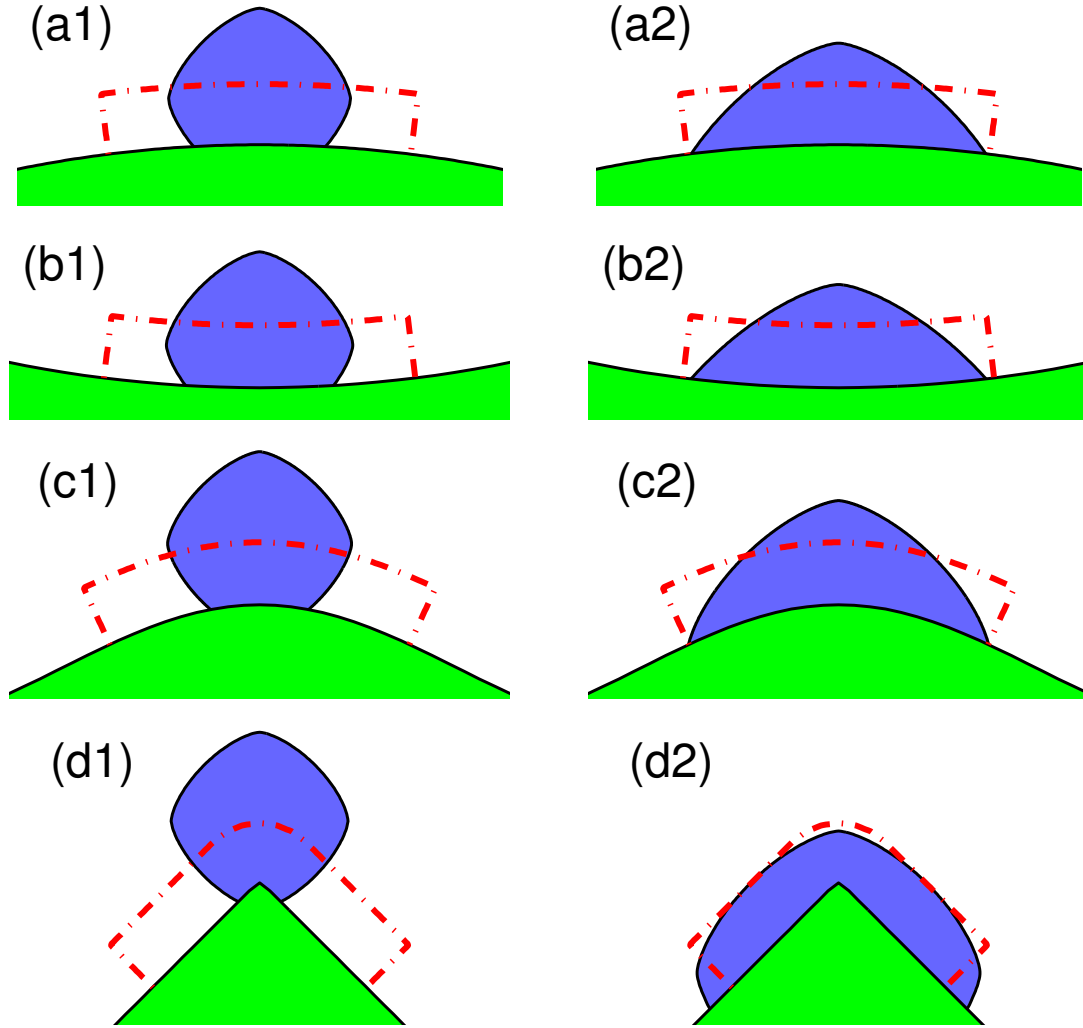
Figure 4.6: Equilibria of (weakly anisotropic with $m = 4, \beta = 0.06$) thin films on different curved substrates. The red dash-dot curve is the initial state. (a1, a2): the convex circular substrate with radius $R = 20$; (b1, b2): the concave circular substrate with radius $R = 20$; (c1, c2): the sinusoidal substrate with $A = 1, k = 1/2$; (d1, d2): the sawtoothed substrate $H_{\text{saw}} = 4$. Left column is for $\sigma = -0.5$, and right column is for $\sigma = 0.5$. Contact angles are (a1) 2.214, (a2) 0.857, (b1) 2.262, (b2) 0.958, (c1) 2.238, (c2) 0.904, (d1) 1.869, (d2) 1.273.

be of the same absolute value, and the value is unique in the weakly anisotropic case according to the generalized Young equation. However, when we place the films
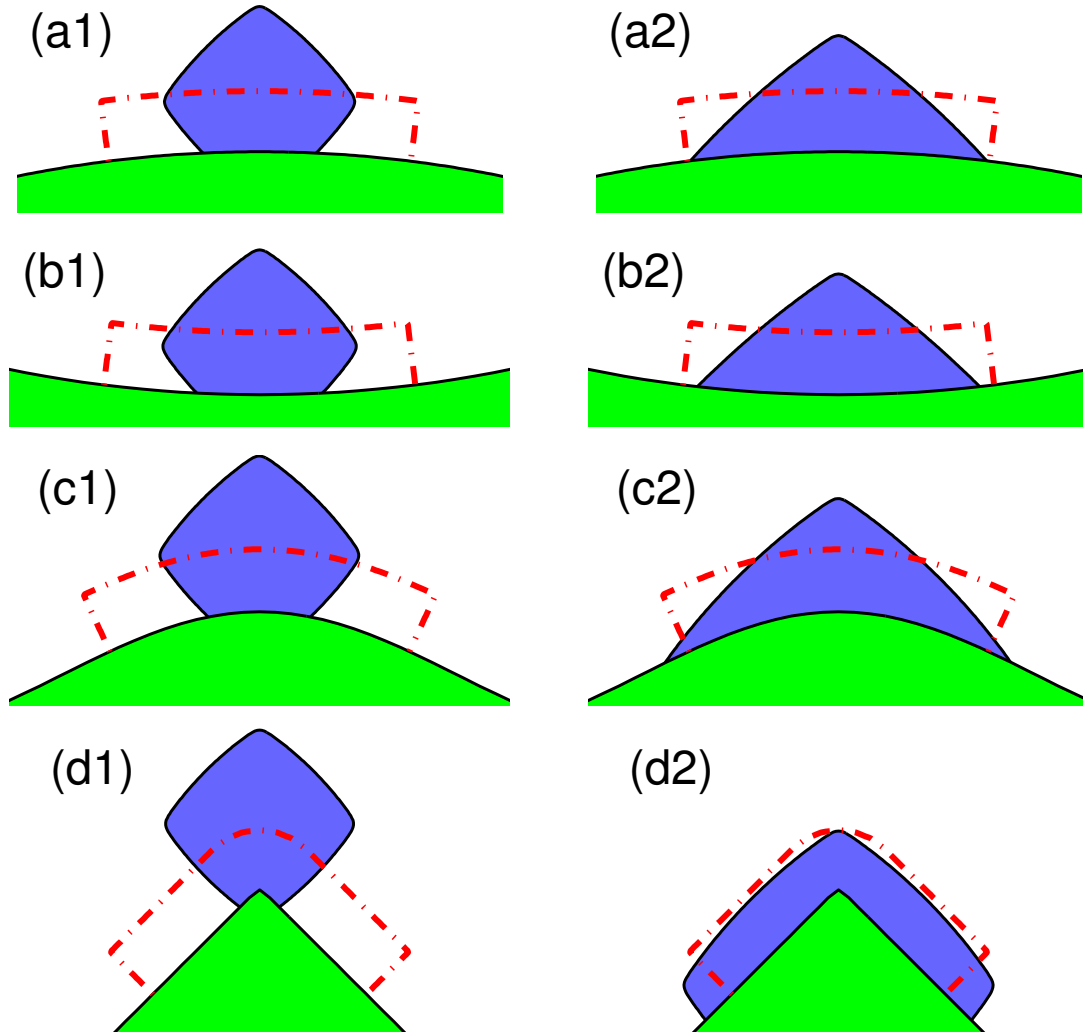
Figure 4.7: Equilibria of (strongly anisotropic with $m = 4, \beta = 0.2$) thin films on different curved substrates. The red dash-dot curve is the initial state. (a1, a2): the convex circular substrate with radius $R = 20$; (b1, b2): the concave circular substrate with radius $R = 20$; (c1, c2): the sinusoidal substrate with $A = 1, k = 1/2$; (d1, d2): the sawtoothed substrate $H_{\text{saw}} = 4$. Left column is for $\sigma = -0.5$, and right column is for $\sigma = 0.5$. Contact angles are (a1) 2.291, (a2) 0.712, (b1) 2.366, (b2) 0.896, (c1) 2.170, (c2) 0.495, (d1) 1.694, (d2) 1.437.

asymmetrically, not only the contact angle but also the geometric evolution change dramatically.

Fig. 4.8 shows the evolution of thin films with (a1-a4) isotropic and (b1-b4) weakly anisotropic surface energies on a convex circular substrate. It can be seen from (a1-a4) that the circular substrate does not affect the symmetric evolution of the film. This is easy to understand since both the substrate and the equilibrium are circle arcs which have infinite symmetries. While (b1-b4) shows that the film asymmetrically evolves to an anisotropic shape that seems to be the Wulff shape cutting by the substrate. It can be clearly seen that the two contact angles in (b4) are of different absolute values (also labeled in the caption). This is also reasonable according to the relaxed contact angle condition (4.1.17), which implies that both the tangent angle of the curved substrate and that of the film/vapor interface affect the contact angles.

Different with the evolution on circular substrates, Fig. 4.9 shows that the thin films migrate from the convex to concave sites, driven by energy reduction, when placed asymmetrically on the sinusoidal substrates in both the isotropic and weakly anisotropic cases. This kind of migration is consistent with both the experimental observations [1, 74] and the numerical simulations [1, 78].

Even different with the above two substrates, when a thin film is placed on a sawtoothed substate, the evolution of the film additionally depends on the initial position: When the film is placed away from the pit bottom, it initially moves towards the heavier side and then stays on the slope (shown in (a1-a4) of both Fig. 4.10 and Fig. 4.11); When the film is near the pit bottom initially, it will fall into the pit (shown in (b1-b4) of both Fig. 4.10 and Fig. 4.11).

According to all the above simulation results of small islands, we may draw some conclusions for the equilibrium configuration on curved substrates:

- on different substrates, the equilibria may be different even though they are of the same contact angle;

- on a fixed curved substrate, different initial positions of thin films may result in different equilibrium morphologies. Moreover, the equilibrium can be asymmetric with a surface energy that results in a symmetric equilibrium in the
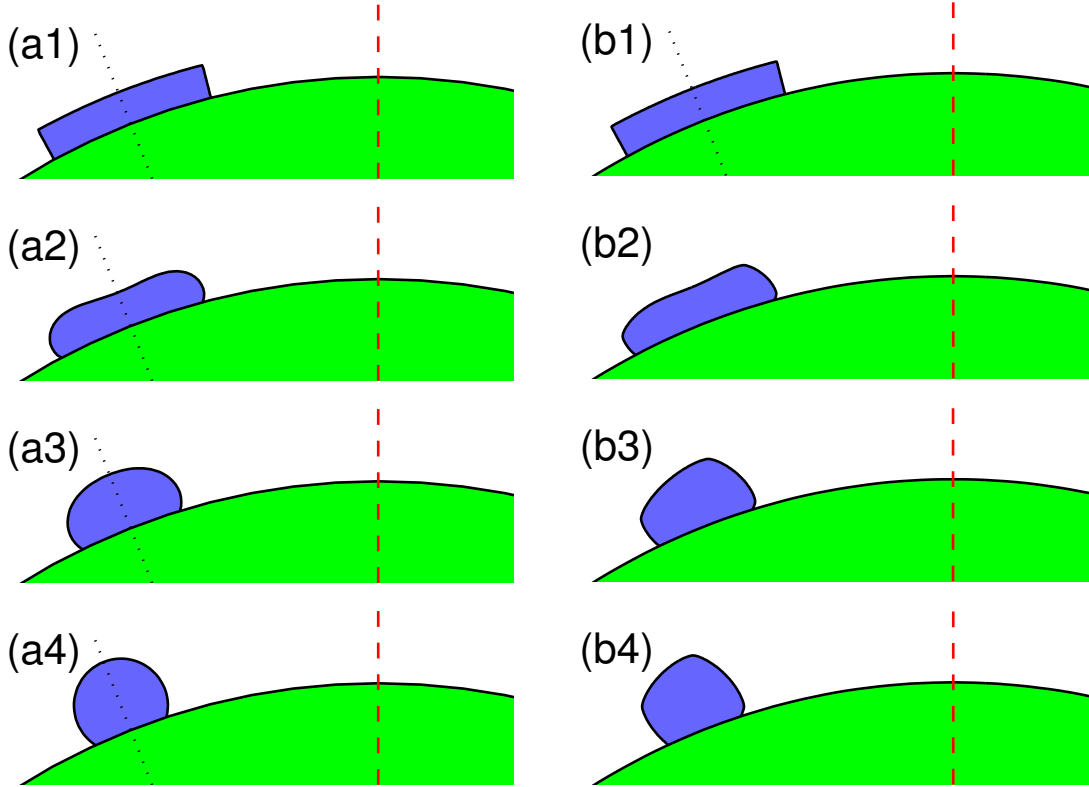
Figure 4.8: Evolution of thin films on a circular substrates ($R = 20$). (a1-a4) is the isotropic case, (b1-b4) is the weakly anisotropic case with $m = 4, \beta = 0.06$. The initial states (a1, b1) are the same: the distances from left contact point to the symmetry (red dash line, parallel to the (0, 1) direction) are both 10. $\sigma = -0.5$ in both cases. The contact angles in (b4) are (left) 2.025 and (right) -2.319.

flat substrate case;

- when the surface energy is isotropic, the contact angle is determined by the isotropic Young equation, that is, it equals to the isotropic Young angle;

- when the substrate has a fixed tangent angle, the contact angle is determined by a (simplified) generalized Young equation (4.1.20), and it must be unique inside the interval $[0, \pi]$ (left contact angle) or $[-\pi, 0]$ (right contact angle) when the surface energy is weakly anisotropic;
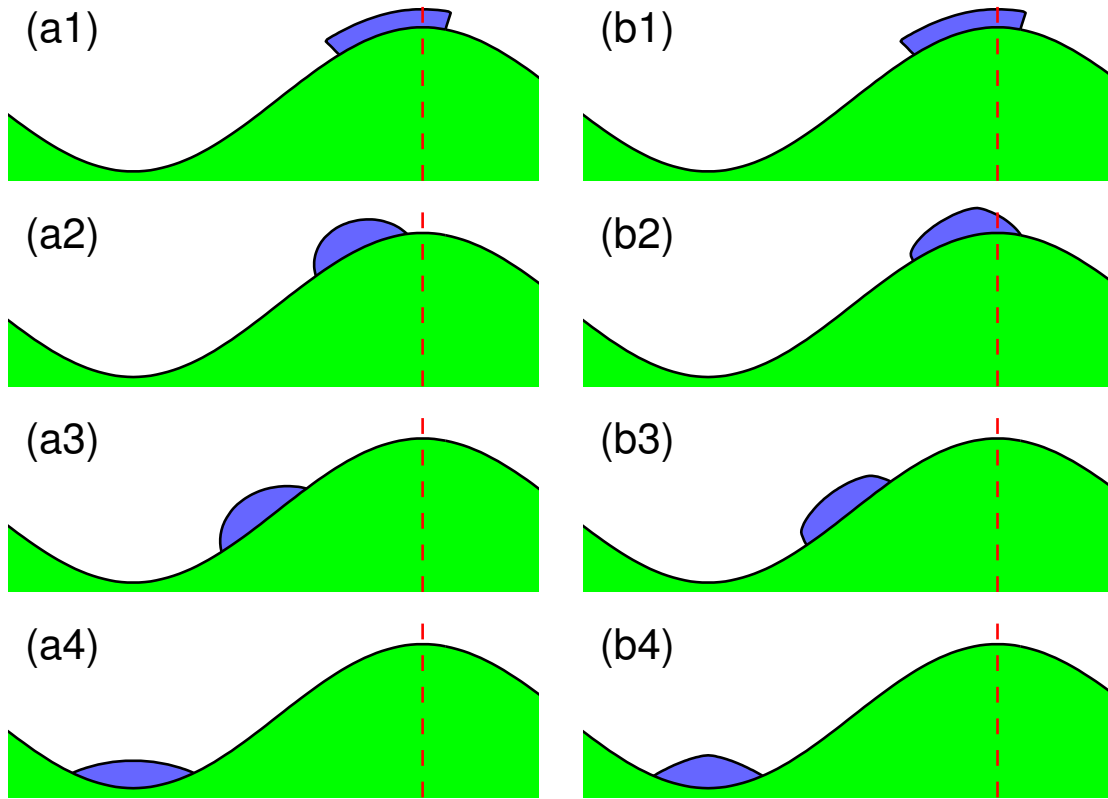
Figure 4.9: Evolution of thin films on sinusoidal substrates ($A = 4, k = 1/4$) with different initial positions. (a1-a4) is the isotropic case, (b1-b4) is the weakly anisotropic case with $m = 4, \beta = 0.06$. (a1) and (b1) are the same initial states: the distance from left contact point to the symmetry (red dash line) is 4. $\sigma = 0.5$ in both cases.

- when the substrate tangent continuously varies, the contact angle is not easy to be determined, but as a pair, the contact angle and the tangential angle of the thin film (or the substrate) at the contact point should satisfy the generalized Young equation (4.1.19).

4.4.2 Large islands and pinch-off

Similar to the flat substrate case, pinch-off occurs when the thin film is long enough. Fig. 4.12 and Fig. 4.13 show the pinch-off phenomena of long films with isotropic and weakly anisotropic surface energy densities, respectively. The evolution
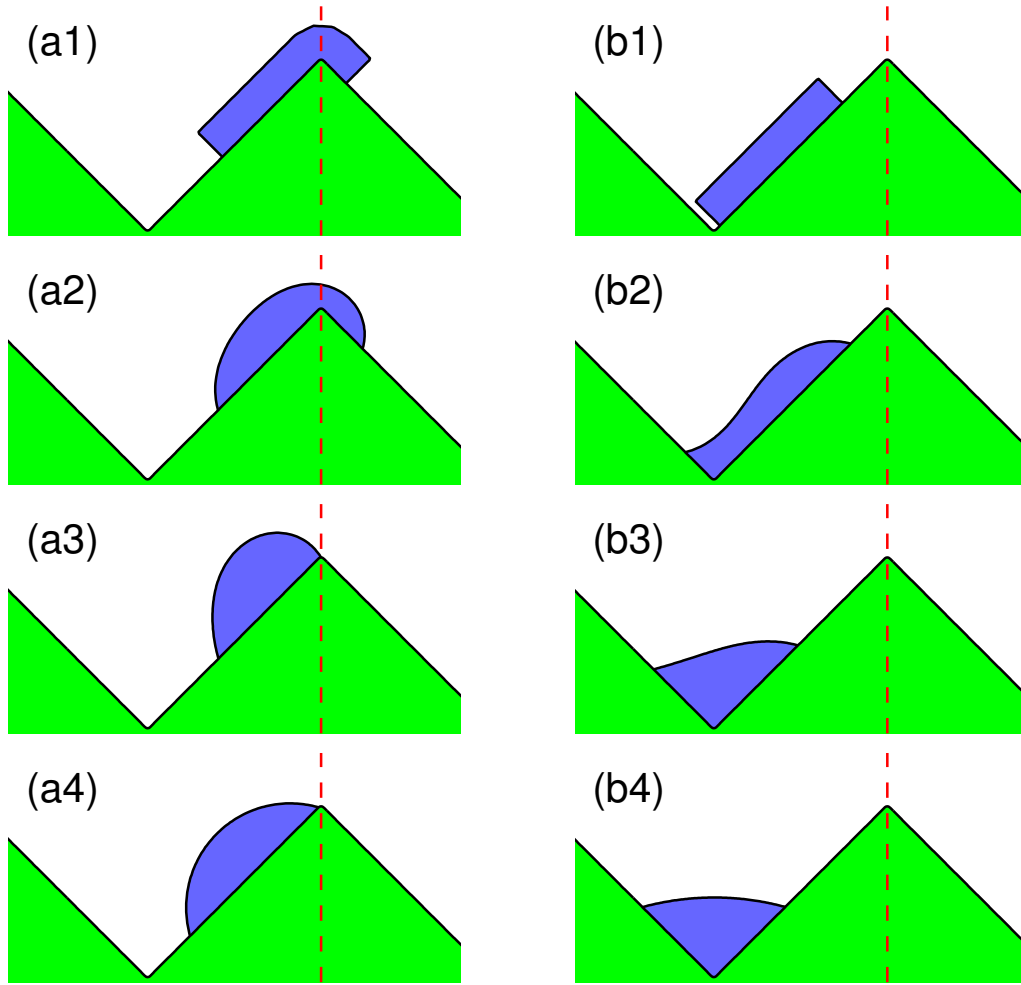
Figure 4.10: Evolution of (isotropic) thin films on sawtoothed substrates ($H_{\text{saw}} = 5$) with different initial positions. (a1) and (b1) are the two different initial states: the distances from left contact point to the symmetry (red dash line) are 4 in (a1) and 6.8 in (b1). $\sigma = 0.5$ in both cases.

of the film is quite similar to that in the flat substrate case: Initially, the edges retract to center, becoming (either rounded or anisotropic) thickened, followed by valleys; Then the two valleys merge in the center and the new valley deepens till touching the substrate; When the valley touches the substrate, pinch-off occurs and the two agglomerates form equilibria separately.

Apart from the geometric evolution, we found that the critical (initial) length
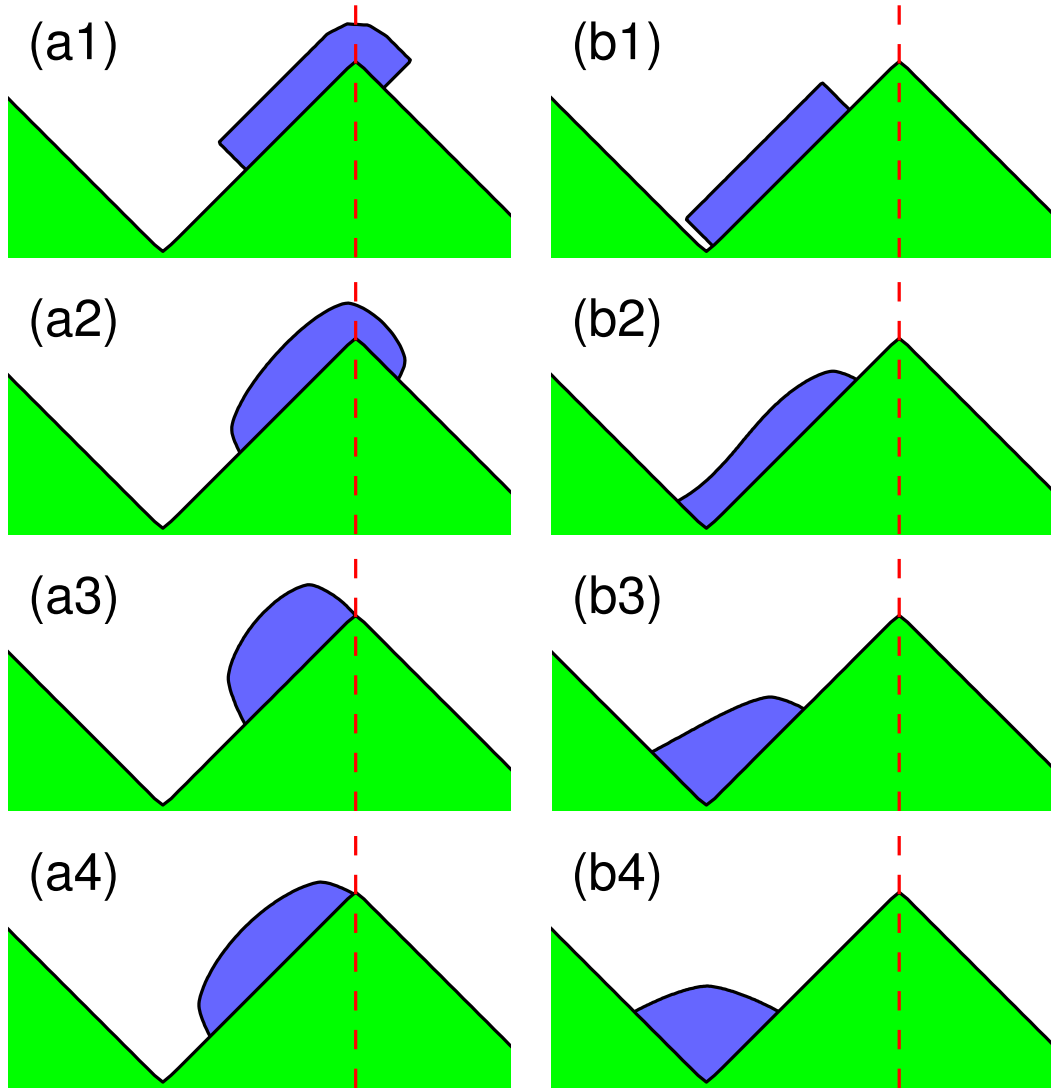
Figure 4.11: Evolution of (weakly anisotropic, $m = 4, \beta = 0.06$) thin films on sawtoothed substrates ($H_{\text{saw}} = 5$) with different initial positions. (a1) and (b1) are the two different initial states: the distances from left contact point to the symmetry (red dash line) are 4 in (a1) and 6.8 in (b1). $\sigma = 0.5$ in both cases.

causing pinch-off is also similar to that in the flat substrate case. We performed a series of experiments for the isotropic case. Fig. 4.14 shows the number of agglomerates formed during dewetting on a circular substrate with (a) $R = 30$ and (b) $R = 60$ for different θ_i and L. As shown in the figure, the critical length causing pinch-off
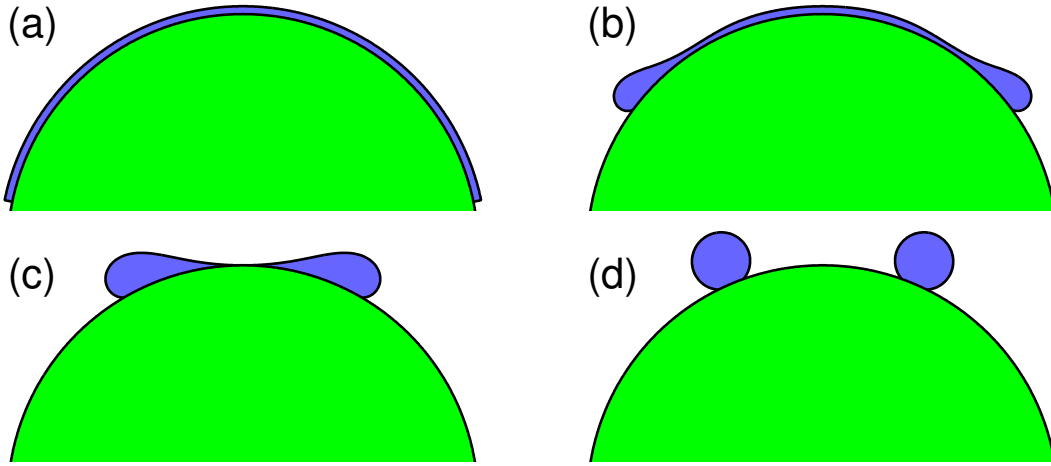
Figure 4.12: Evolution of a large island with isotropic surface energy on a circular substrate of radius $R = 30$. Film length $L = 82$, $\sigma = -\sqrt{3}/2$.
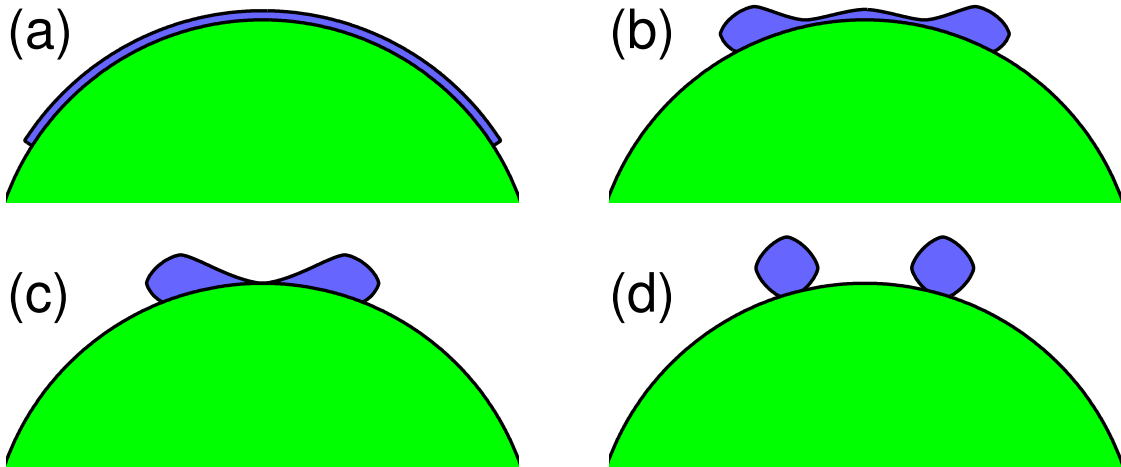
Figure 4.13: Evolution of a large island with weakly anisotropic surface energy on a (convex) circular substrate of radius $R = 30$. Film length $L = 60$, $m = 4, \beta = 0.06, \sigma = -\sqrt{3}/2$.

becomes larger as θ_i decreases, and the 1-2 islands boundary seems to be a straight line. The lines we used to fit the boundaries are (a) $L = 79.2/\sin(\theta_i/2) + 0.2$ for $R = 30$ and (b) $L = 85.0/\sin(\theta_i/2) + 0.3$ for $R = 60$, respectively. As clearly shown
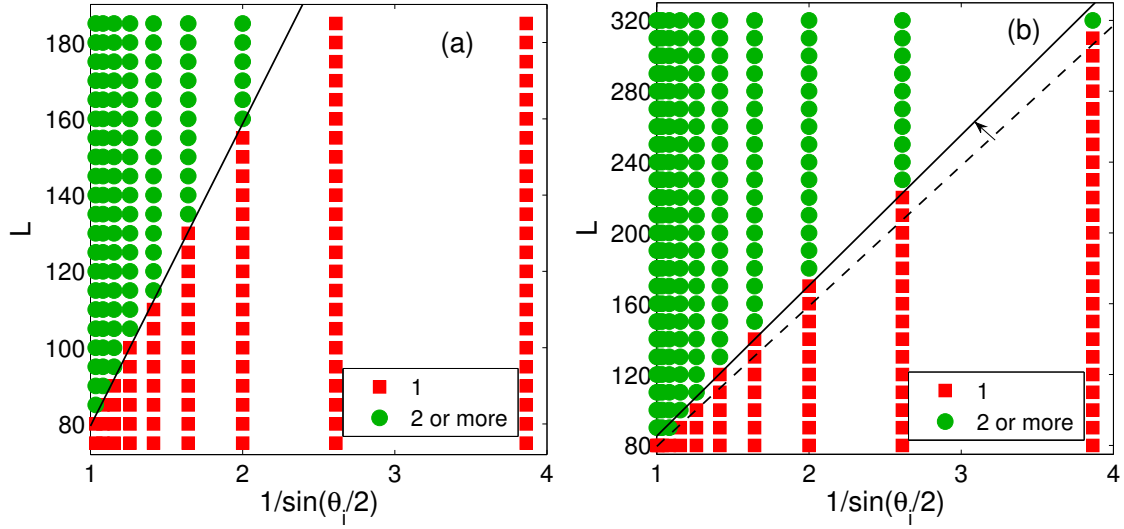
Figure 4.14: The number of islands formed from the retraction of a high aspect ratio island as a function of initial length L and θ_i ($h = 1$) on a circular substrate with (a) $R = 30$, (b) $R = 60$. The linear curve fittings (black solid lines) to the 1-2 islands boundary are (a) $L = 79.24/\sin(\theta_i/2) + 0.23$, (b) $L = 85/\sin(\theta_i/2) + 0.3$. The black dash line in (b) is the fitting (black solid) line in (a). Isotropic case.

in Fig. 4.14(b), the boundary line for $R = 60$ moves up compared to the line for $R = 30$. This implies that the flatten of the circular substrate delays the pinch-off. We performed similar simulations for this kind of substrate of other radiuses, and the critical lengths causing pinch-off for different R and θ_i are listed in Table. 4.1. The result for $R \to \infty$, which means the flat substrate case, is obtained by using the fitting given by Dornel *et. al.* in [41]. For each radius R, we fitted a function, similar to the functions for $R = 30$ and 60, for the critical pinch-off length L as

$$L = a(R)/\sin(\theta_i/2) + b(R).$$

And we find that $b(R)$ are around 0 for all the cases and $a(R)$ can be fitted by

$$a(R) = -320.2/R + 89.9.$$

Therefore, assuming isotropic surface energy, for given R and θ_i, we suggest that

	$R = 20$	$R = 30$	$R = 40$	$R = 50$	$R = 60$	$R \to \infty$
$\theta_i = \pi$	73.5	77.5	79.5	80.5	81.5	87.9
$\theta_i = \frac{11}{12}\pi$	74.5	78.5	80.5	81.5	82.5	88.8
$\theta_i = \frac{10}{12}\pi$	76.5	81.5	83.5	84.5	84.5	91.3
$\theta_i = \frac{9}{12}\pi$	80.5	85.5	87.5	88.5	89.5	95.9
$\theta_i = \frac{8}{12}\pi$	86.5	91.5	94.5	95.5	96.5	102.9
$\theta_i = \frac{7}{12}\pi$	94.5	100.5	103.5	105.5	106.5	113.1
$\theta_i = \frac{6}{12}\pi$	105.5	113.5	119.5	119.5	121.5	128.0
$\theta_i = \frac{5}{12}\pi$	120.5	131.5	137.5	140.5	142.5	150.0
$\theta_i = \frac{4}{12}\pi$	–	157.5	166.5	170.5	172.5	184.5
$\theta_i = \frac{3}{12}\pi$	–	–	210.5	219.5	224.5	243.8
$\theta_i = \frac{2}{12}\pi$	–	–	–	306.5	319.5	364.6

Table 4.1: Critical length of the first pinch-off for different σ and R(isotropic case) . "-" means no pinch-off. $R \to \infty$ is the flat substrate case according to the fitting given in [41].

the critical pinch-off length can be predicted according to the following relation

$$L = \frac{-320.2/R + 89.9}{\sin(\theta_i/2)}, \quad R \geq 10. \tag{4.4.2}$$

Here, the radius is restricted to be larger than 10 since pinch-off will not occur for small R.

In addition, pinch-off processes of thin films on sinusoidal and sawtoothed substrates are shown in Fig. 4.15 for the isotropic case and in Fig. 4.16 for the weakly anisotropic case. As shown in the figures, the anisotropy makes little difference in the morphology evolution, and the evolution of the films on these two kinds of substrates are similar: the edges of the film spread and the center of the film deepens; the film pinches off to two islands when the center of the film touches the substrate, and the two islands evolve to equilibria, staying in the bottom of the pits.
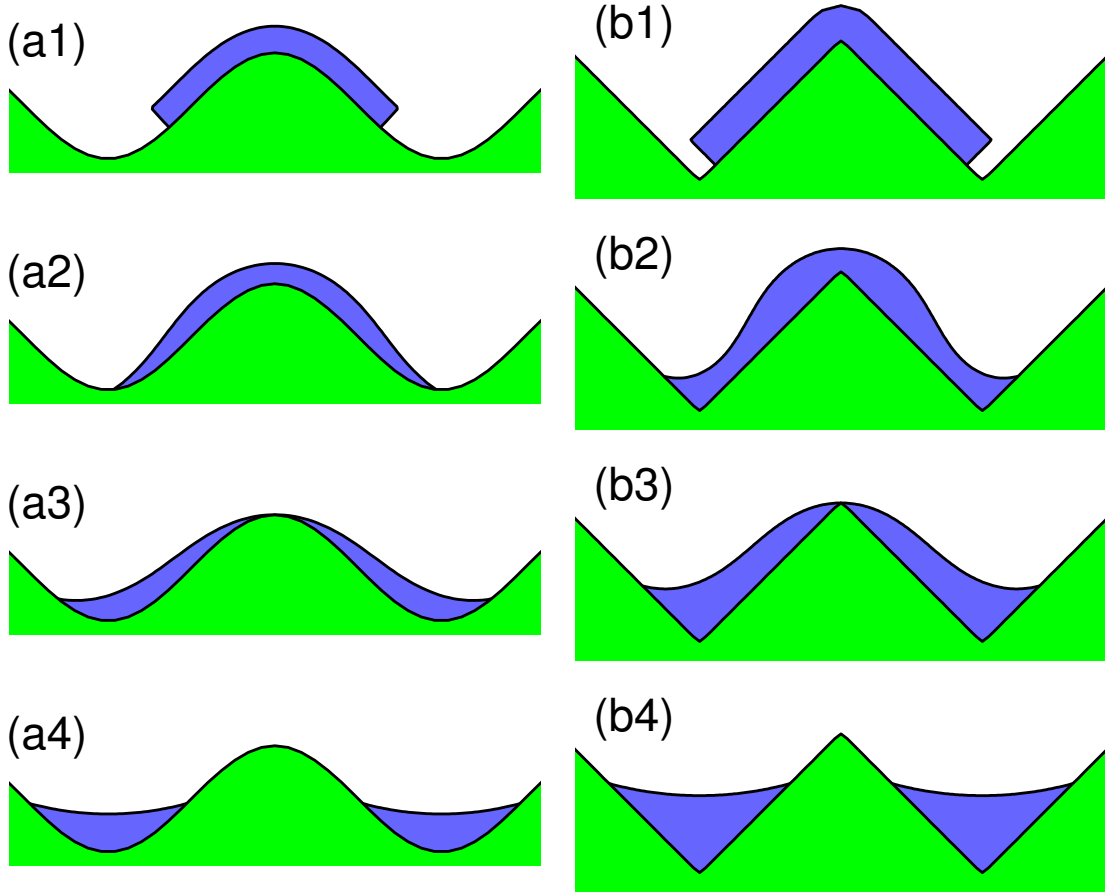
Figure 4.15: Evolution of (isotropic) large islands on different curved substrates. (a1 - a4): sinusoidal substrate with $A = 2, k = 1/2$; (b1 - b4): sawtoothed substrate $H_{\mathrm{saw}} = 4$. Isotropic case. Film length $L = 10$, $\sigma = \sqrt{3}/2$ in both cases.

4.4.3 Simulations for templated dewetting

At last, we performed some (isotropic) simulations for the inverted pyramidal substrate to capture the four observed categories of dewetting in the experimental results reported in [55]. The initial length of the initial film is chosen to cover 5 pits except for the one in Fig. 4.21. It can be seen that

- For the fixed pit depth $H_{\mathrm{pyr}} = 4$, Fig. 4.17 shows an ordered structure that there is no extra film on the mesa with one island per pit when $L_{\mathrm{mesa}} = 1$; When L_{mesa} increases to 3, there exist some small islands on the mesas with
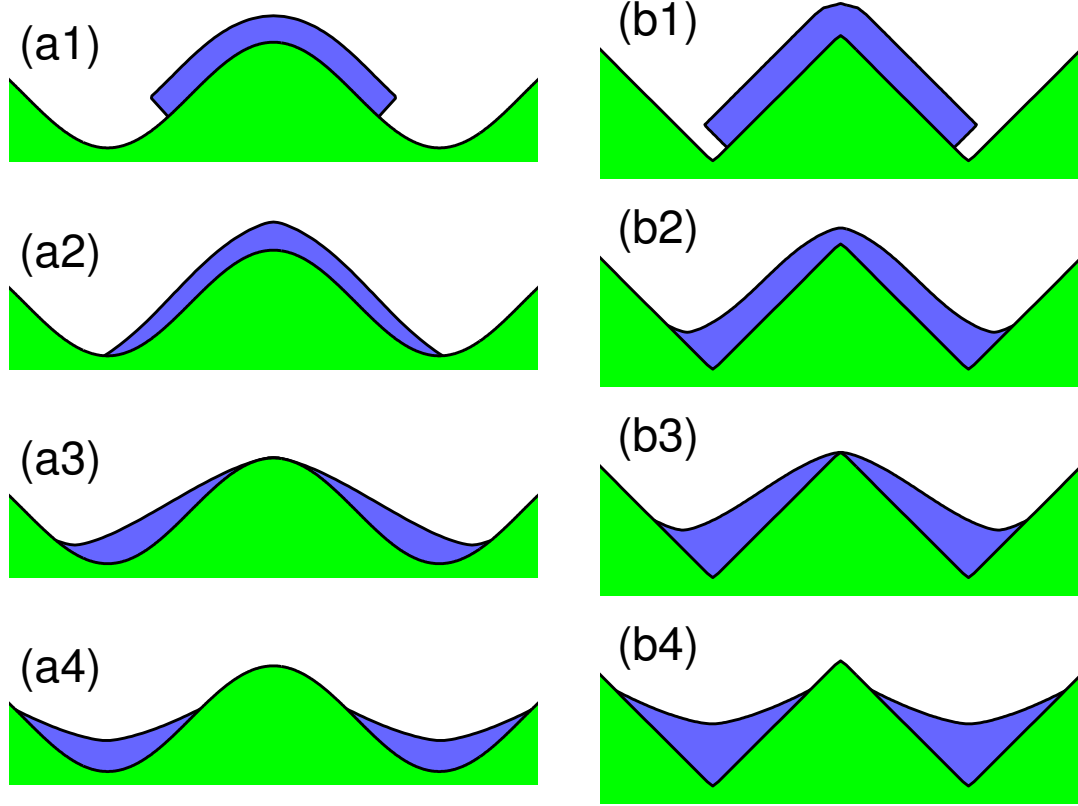
Figure 4.16: Evolution of (weakly anisotropic, $m = 4, \beta = 0.06$) large islands on different curved substrates. (a1 - a4): sinusoidal substrate with $A = 2, k = 1/2$; (b1 - b4): sawtoothed substrate $H_{\text{saw}} = 4$. Weakly anisotropic case. Film length $L = 10$, $m = 4, \beta = 0.06, \sigma = \sqrt{3}/2$ in both cases.

still one island per pit as shown in Fig. 4.18; These two figures show similar morphology as the experimental results shown in Fig.2(a) in [55]; When L_{mesa} increases to 6, Fig. 4.19 shows that the thin film pinches off to different sizes, covering the pits or the mesas, which corresponds to Fig. 2(b) in [55].

- For fixed $L_{\text{mesa}} = 6$, different with the $H_{\text{pyr}} = 4$ case, Fig. 4.20 shows that the film will not pinch-off when $H_{\text{pyr}} = 2$, which implies that the film does not interact with the substrate topography; This is also observed in Fig.2(d) in [55].

- When the pit is deep enough, Fig. 4.21 shows that the film will pinch off to several pieces even inside one pit. This captures the category shown in Fig.2(c) in [55].

As can be seen that, although our simulations are only for 2D, the numerical results can almost capture all the morphologies shown in experiments [55].
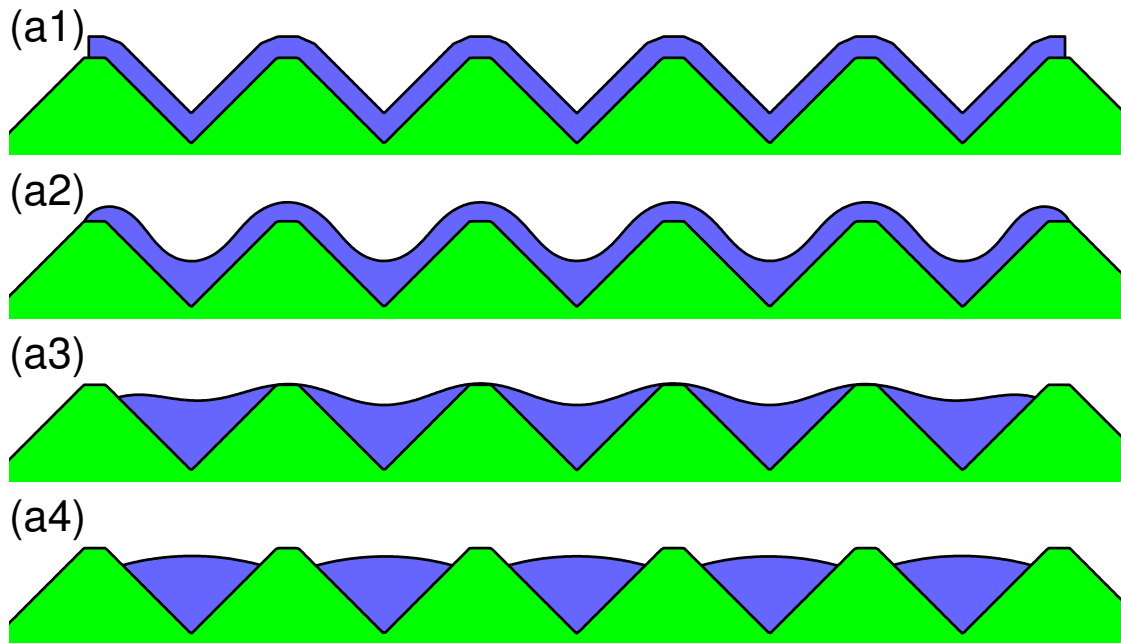
Figure 4.17: Evolution of an isotropic large island on an inverted pyramidal substrate.$H_{\mathrm{pyr}} = 4, L_{\mathrm{mesa}} = 1$, film length $L = 62$, $\sigma = 0.5$.
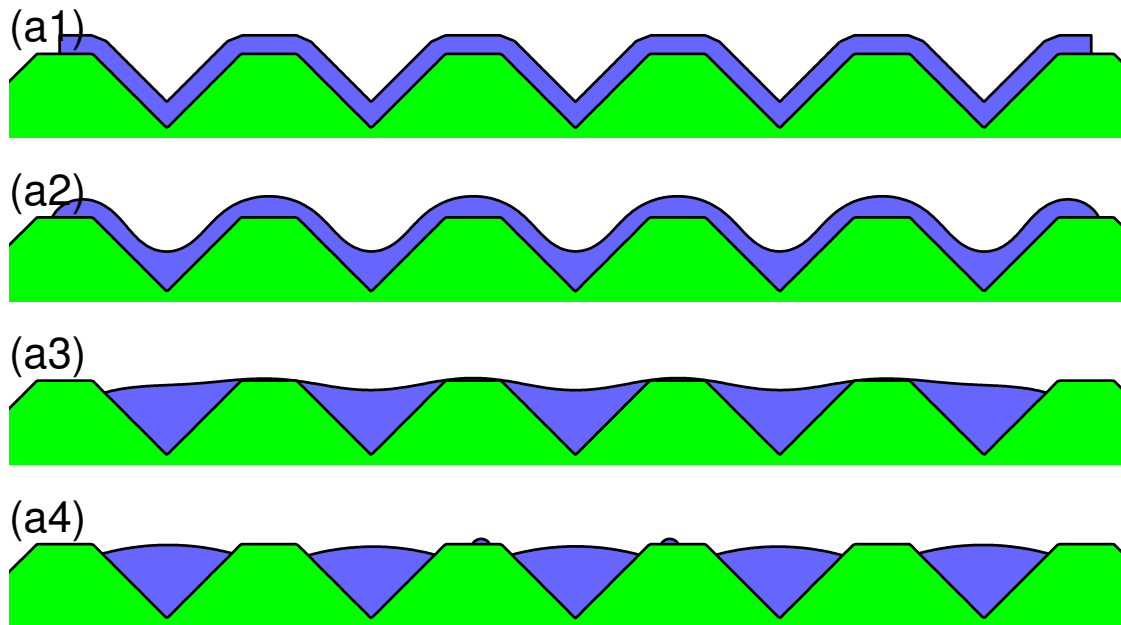
Figure 4.18: Evolution of an isotropic large island on an inverted pyramidal substrate.$H_{\mathrm{pyr}} = 4$, $L_{\mathrm{mesa}} = 3$, film length $L = 72$, $\sigma = 0.5$.
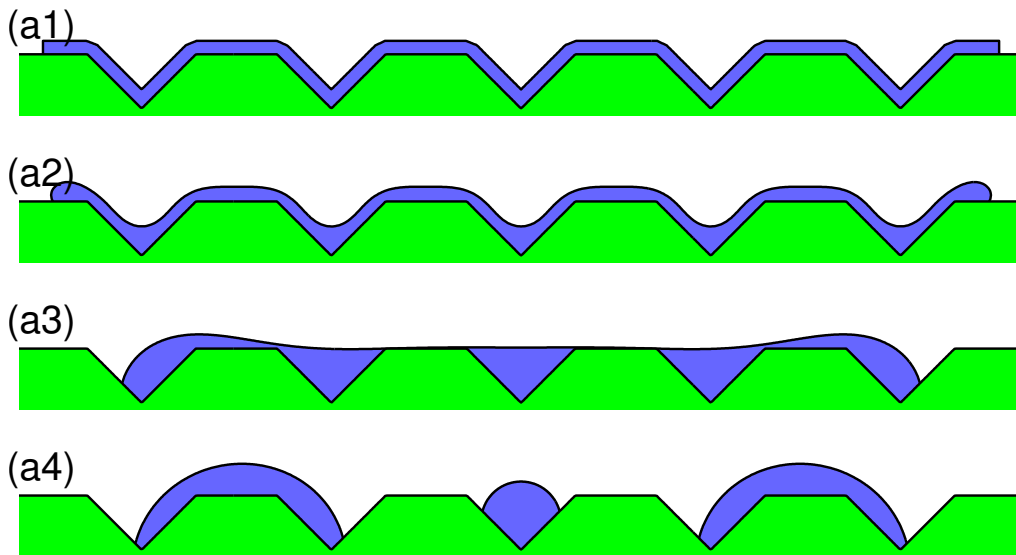
Figure 4.19: Evolution of an isotropic large island on an inverted pyramidal substrate.$H_{\mathrm{pyr}} = 4$, $L_{\mathrm{mesa}} = 6$, film length $L = 72$, $\sigma = -0.5$.
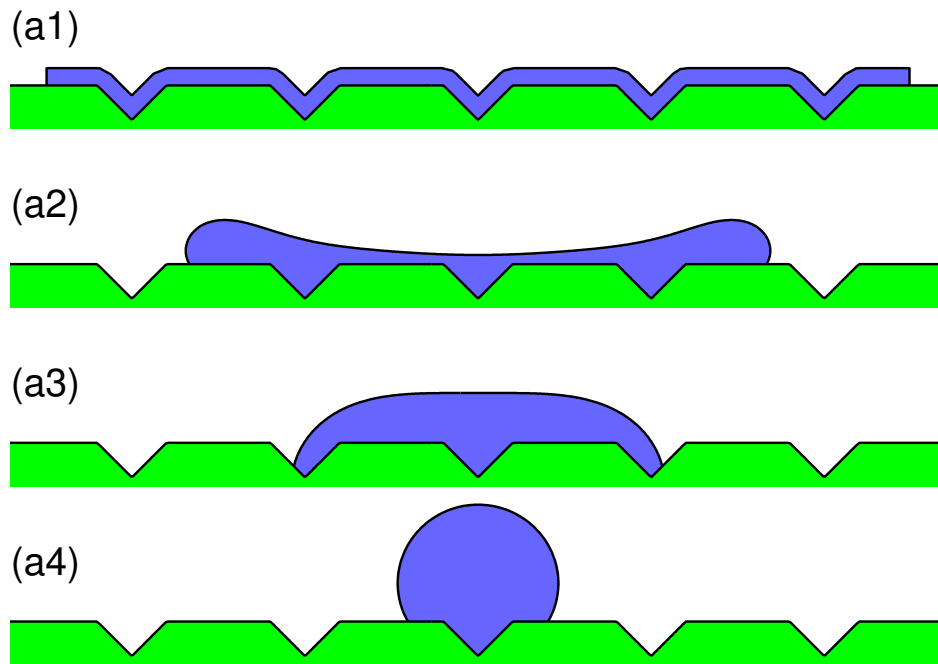
Figure 4.20: Evolution of an isotropic large island on an inverted pyramidal substrate. $H_{\mathrm{pyr}} = 2$, $L_{\mathrm{mesa}} = 6$, film length $L = 57$, $\sigma = -0.5$.
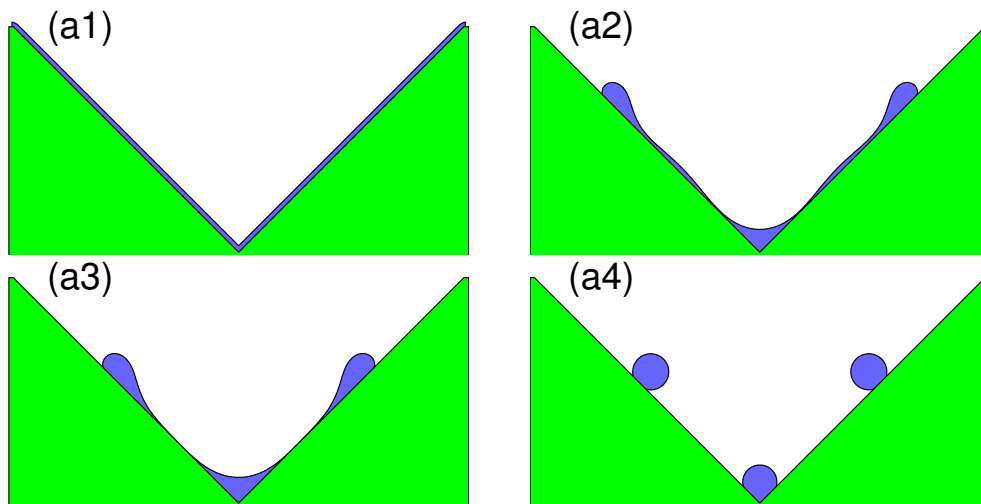
Figure 4.21: Evolution of an isotropic large island on an inverted pyramidal substrate. $H_{\mathrm{pyr}} = 50$, $L_{\mathrm{mesa}} = 1$, film length $L = 57$, $\sigma = -\sqrt{3}/2$.

Chapter 5

Conclusion and Future Work

This thesis focuses on the modeling and simulations for solid-state dewetting problems in 2D. The modeling, which is based on the thermodynamic variational approach, includes different kinds of surface energy anisotropies (both "smooth" and cusped cases) and different substrates (flat and curved substrates). For simulation, we propose a revised "marker particle" method (MPM) (explicit and easy to be implemented) and a parametric finite element method (PFEM) (semi-implicit and efficient). The simulation results can both capture the complex geometric evolution shown in solid-state dewetting experiments and predict some interesting phenomena.

In Chapter 2, we described a sharp interface model for simulating solid-state dewetting of thin films with weakly anisotropic surface energy, as well as the mass conservation and energy dissipation properties. The evolution of the films is governed by surface diffusion and contact line migration. The derivation of the sharp interface model is based on an energy variational approach. Unlike other sharp interface models, we included a finite contact line mobility during the contact line migration. This gives rise to dynamic contact angles that may be different from the equilibrium contact angles from the Young equation. Many observations have been made of dynamic triple junction angles in grain boundary migration and contact line angles in liquid wetting of substrates that differ markedly from static equilibrium contact angles. We proposed two numerical approach for solving the sharp interface

model. One is based upon an explicit finite difference scheme combined with the cubic spline interpolation for evolving marker points. The other is a semi-implicit parametric finite element method. Numerical results for solid-state dewetting in two dimensions demonstrate the excellent performance of the methods, including stability, convergence and numerical efficiency, especially for the PFEM.

With the validated mathematical and numerical approaches, we simulated the evolution of thin film islands, semi-infinite films, and films with holes as a function of film dimensions, isotropic Young angle θ_i, anisotropy strength and symmetry, and film crystal orientation relative to the substrate normal. Like others, we found that contact point retraction rate can be well described by a power-law, $l \sim t^n$. Our results demonstrate that the exponent n is sensitive to the isotropic Young angle θ_i (and insensitive to anisotropy). We have also observed that in addition to classical wetting (where holes in a film heal) and dewetting (where holes in a film grow), another possibility is where the holes heal leaving a continuous film but with a void at the FS interface which can of finite or infinite extent. Surface energy anisotropy was also shown to (i) increase or decrease the instability that leads to island break-up into multiple islands, (ii) enhance hole healing, and (iii) lead to finite island size even under some conditions where the isotropic Young angle θ_i suggests that the film wets the substrate. The numerical results presented in Chapter 2 capture many of the complexities associated with solid-state dewetting experiments [75,125,136–139].

In Chapter 3, by adopting a regularization approach [27,48,126], the governing equation in Chapter 2 is revised and becomes well-posed for the strongly anisotropic surface energy. In order to make the model problem complete, we introduced a "zero-curvature" condition, which comes from the variation of the total energy functional, for the moving contact line. A similar dynamical (relaxed) contact angle condition, giving a equation that converges to the anisotropic Young equation introduced in Chapter 2, was adopted for the moving contact line. However, different with the weakly anisotropic case, strong anisotropy may result in multiple roots to the anisotropic Young equation. By taking $m = 2, 3, 4, 6$ in the smooth surface energy

density (Eq. 1.2.2) as example, we have shown the phase diagrams of the number of (stable) roots to the anisotropic Young equation.

The proposed model is mainly used to investigate the strong anisotropic effects on thin solid film dewetting including contact line dynamics. We have shown that multiple equilibrium shapes may appear for sufficiently strong surface energy anisotropy, among which some can not be described by the widely employed Winterbottom construction, i.e., the generalized Wulff construction for an island on a substrate. Therefore, we proposed a generalized Winterbottom construction, including multiple equilibrium shapes, for the equilibrium configuration under anisotropic surface energy and re-classified the six types of wetting/dewetting. By employing our evolution model, we demonstrate that all the equilibria predicted by the proposed generalized Winterbottom construction are dynamically accessible.

Chapter 4 is the extension of previous two chapters to curved substrates. The models and boundary conditions are derived similarly in an energy variational way. However, different with that in the flat substrate case, the relaxed contact angle boundary condition depends on two variables (both the dynamic contact angle and the film or substrate tangential angle at the contact point) instead of only the dynamic contact angle. Due to this difference in the boundary condition for the moving contact line, the geometric evolutions of thin films change dramatically when placed on different substrates or at different initial positions on the same substrate, which demonstrates that the evolution strongly depends on the initial position, as well as the substrate topography. In addition, we performed experiments on inverted pyramidal substrates, which are simulations of the templated solid-state dewetting shown in Fig. 1.2, the simulation results can capture the four major categories of dewetting reported in [55].

Some future works:

Our future studies on solid-state dewetting are fruitful and mainly focused on three dimensional problems. For example,

- We will extend sharp interface models to three dimensions using the thermo-dynamic variational method. Before we fight for the real 3D problems, we will first extend the modeling and numerical methods to a cylindrically symmetric case, which is in fact a quasi-3D problem and straight forward.

- The computation results in [13] have demonstrated the good performance of the PFEM for solving the motion by surface diffusion of a closed hypersurface in $\mathbb{R}^3$. Therefore, we will develop a PFEM for solving 3D solid-state dewetting problems.

- Following validation of the mathematical and numerical approaches, we will perform numerical simulations to compare with the real experiments, studying the edge retraction [41, 138], fingering instabilities [37, 68] and so on.

- In [84], the authors derived the (isotropic) equilibrium shape conditions for a particle lying on a spherically foreign curved substrate. Besides this, there is little research on the equilibrium configuration on curved substrates, especially including anisotropy. Based on the proposed models and the simulation results, we expect some progress in this area in the future. We will also extend the models on curved substrates to 3D cases.

- In addition to the sharp interface model, we plan to study the phase field model for the solid-state dewetting problems, such as including film/vapor interfacial anisotropy in the model and analyzing its sharp interface limits.

Bibliography

[1] T.M. Ahn, J.K. Tien and P. Wynblatt, Coarsening kinetics of platinum particles on curved oxide substrates, J. Catal., 66 (1980), 335–346.

[2] T.L. Alford, L.H. Chen and K.S. Gadre, Stability of silver thin films on various underlying layers at elevated temperatures, Thin Solid Films, 429 (2003), 248–254.

[3] S. Angenent and M. Gurtin, Multiphase thermomechanics with interfacial structure 2. Evolution of an isothermal interface, Arch. Rational Mech. Anal., 108 (1989), 323–391.

[4] L. Armelao, D. Barreca, G. Bottaro, A. Gasparotto, S. Gross, C. Maragnob and E. Tondello, Recent trends on nanocomposites based on Cu, Ag and Au clusters: a closer look, Coord. Chem. Rev., 250 (2006), 1294–1314.

[5] R.W. Balluffi, S.M. Allen, and W.C. Careter, Kinetics of Materials, Wiley-Interscience, John Wiley, 2005.

[6] E. Bänsch, P. Morin and R.H. Nochetto, A finite element method for surface diffusion: the parametric case, J. Comput. Phys., 203 (2005), 321–343.

[7] K. Bao, Y. Shi, S. Sun and X.P. Wang, A finite element method for the numerical solution of the coupled Cahn–Hilliard and Navier–Stokes system for moving contact line problems, J. Comput. Phys., 231 (2012), 8083–8099.

[8] W. Bao, W. Jiang, Y. Wang and Q. Zhao, A parametric finite element method for solid-state dewetting problems with anisotropic surface energies, arXiv: 1601.05877 (2016).

[9] W. Bao, W. Jiang and Y. Wang, Thermodynamic variation and stable equilibrium shapes for solid-state dewetting of thin films, in preparation.

[10] J.W. Barrett, R. Nürnberg and V. Styles, Finite element approximation of a phase field model for void electromigration, SIAM J. Numer. Anal., 42 (2004), 738–772.

[11] J.W. Barrett, H. Garcke and R. Nürnberg, A parametric finite element method for fourth order geometric evolution equations, J. Comput. Phys., 222 (2007), 441–467.

[12] J.W. Barrett, H. Garcke and R. Nürnberg, On the variational approximation of combined second and fourth order geometric evolution equations, SIAM J. Sci. Comput., 29 (2007), 1006–1041.

[13] J.W. Barrett, H. Garcke and R. Nürnberg, On the parametric finite element approximation of evolving hypersurfaces in $\mathbb{R}^3$, J. Comput. Phys., 227 (2008), 4281–4307.

[14] J.W. Barrett, H. Garcke and R. Nürnberg, Numerical approximation of anisotropic geometric evolution equations in the plane, IMA J. Numer. Anal., 28 (2008), 292–330.

[15] J.W. Barrett, H. Garcke and R. Nürnberg, Finite element approximation of coupled surface and grain boundary motion with applications to thermal grooving and sintering, European J. Appl. Math., 21 (2010), 519–556.

[16] J.W. Barrett, H. Garcke and R. Nürnberg, The approximation of planar curve evolutions by stable fully implicit finite element schemes that equidistribute, Numer. Methods Partial Differ. Equ., 27 (2011), 1–30.

[17] J.W. Barrett, H. Garcke and R. Nürnberg, Parametric approximation of isotropic and anisotropic elastic flow for closed and open curves, Numer. Math. 120 (2012), 489–542.

[18] J. Basu, C.B. Carter, R. Divakar, B. Mukherjee and N. Ravishankar, Nanopatterning by solid-state dewetting on reconstructed ceramic surfaces, Appl. Phys. Lett., 94 (2009), article 171114.

[19] E. Bauer, Phänomenologische theorie der kristallabscheidung an oberflächen. I, Zeitschrift f. Krystall. Mineral., 110 (1958), 372–394.

[20] N. Baumann, E. Mutoro, J. Janek, Porous model type electrodes by induced dewetting of thin Pt films on YSZ substrates, J. Solid State Ionics, 181 (2010), 7–15.

[21] K.A. Brakke, The surface evolver, Exp. Math., 1 (1992), 141–165.

[22] K.A. Brakke, The surface evolver, http://www.susqu.edu/facstaff/b/brakke/evolver, 2003.

[23] R.G.W. Brown, Thin Films for Optical Systems, ed. F.R. Flory, Marcel Dekker, New York, 1995.

[24] W.K. Burton, N. Cabrera and F.C. Frank, The growth of crystals and the equilibrium structure of their surfaces, Phil. Trans. R. Soc. Lond. A, 243 (1951), 299–358.

[25] J.W. Cahn and J.E. Taylor, Surface motion by surface diffusion, Acta Metall. Mater., 42 (1994), 1045–1063.

[26] J.W. Cahn and W.C. Carter, Crystal shapes and phase equilibria: A common mathematical basis, Metall. Mater. Trans. A, 27 (1996), 1431–1440.

[27] A. Carlo, M. Gurtin, and P. Podio-Guidugli, A regularized equation for anisotropic motion-by-curvature, SIAM J. Appl. Math., 52 (1992), 1111–1119.

[28] W.C. Carter, A.R. Roosen, J.W. Cahn and J.E. Taylor, Shape evolution by surface diffusion and surface attachment limited kinetics on completely faceted surfaces, Acta Metall. Mater., 43 (1995), 4309–4323.

[29] H.Y. Chen, D. Jasnow and J. Vinals, Interface and contact line motion in a two phase fluid under shear flow, Phys. Rev. Lett., 85 (2000), 1686–1689.

[30] J.H. Chen, T.F. Lei, D. Landheer, X. Wu, J. Liu and T.S. Chaod, Si nanocrystal memory devices self-assembled by in situ rapid thermal annealing of ultra-thin a-Si on SiO_2, Electrochem. Solid State Lett., 10 (2007), H302–H304.

[31] M. Chhowalla, K.B.K. Teo, C. Ducati, N.L. Rupesinghe, G.A.J. Amaratunga, A.C. Ferrari, D. Roy, J. Robertson and W.I. Milne, Growth process conditions of vertically aligned carbon nanotubes using plasma enhanced chemical vapor deposition, J. Appl. Phys., 90 (2001), 5308–5317.

[32] W.K. Choi, T.H. Liew, H.G. Chew, F. Zheng, C.V. Thompson, Y. Wang, M.H. Hong, X.D. Wang, L. Li and J. Yun, A combined top-down and bottom-up approach for precise placement of metal nanoparticles on silicon, Small, 4 (2008), 330–333.

[33] D.L. Chopp and J.A. Sethian, Motion by intrinsic Laplacian of curvature, Interfaces Free Bound, 1 (1999), 107–123.

[34] A. Colli, A. Fasoli, P. Beecher, P. Servati, S. Pisana, Y. Fu, A.J. Flewitt, W.I. Milne, J. Robertson, C. Ducati, S. De Franceschi, S. Hofmann and A.C. Ferrari, Thermal and chemical vapor deposition of Si nanowires: shape control, dispersion and electrical properties, J. Appl. Phys., 102 (2007), article 034302.

[35] M. Czubanowski, C. Tegenkamp, W. Ernst, and H. Pfnür, Roughness and stability of silicon on insulator surfaces, Appl. Phys. Lett., 84 (2004), 350–352.

[36] U. Czubayko, V.G. Sursaeva, G. Gottstein, and L.S. Shvindlerman, Influence of triple junctions on grain boundary motion, Acta Mater., 46 (1998), 5863–5871.

[37] D.T. Danielson, D.K. Sparacin, J. Michel and L.C. Kimerling, Surface-energy-driven dewetting theory of silicon-on-insulator agglomeration, J. Appl. Phys., 100 (2006), article 083057.

[38] F. Davi and M.E. Gurtin, On the motion of a phase interface by surface diffusion, Z. Angew. Math. Phys., 41 (1990), 782–811.

[39] P.G. de Gennes, Wetting: statics and dynamics, Rev. Mod. Phys., 57 (1985), 827–863.

[40] A. Dinghas, Uber einen geometrischen Satz von Wulff für die Gleichgewichts-form von Kristallen, Zeitschrift f. Krystall. Mineral., 105 (1944), 304–314.

[41] E. Dornel, J.C. Barbe, F. Crecy, G. Lacolle, and J. Eymery, Surface diffusion dewetting of thin solid films: Numerical method and application to Si/SiO_2, Phys. Rev. B, 73 (2006), article 115427.

[42] M. Droske and M. Rumpf, A level set formulation for Willmore flow, Interfaces Free Bound, 6 (2004), 361–378.

[43] P. Du, M. Khenner and H. Wong, A tangent-plane marker-particle method for the computation of three-dimensional solid surfaces evolving by surface diffusion on a substrate, J. Comput. Phys., 229 (2010), 813–827.

[44] M. Dufay and O. Pierre-Louis, Anisotropy and coarsening in the instability of solid dewetting fronts, Phys. Rev. Lett., 106 (2011), article 105506.

[45] E.B. Dussan, On the spreading of liquids on solid surfaces: static and dynamic contact lines, Ann. Rev. Fluid Mech., 11 (1979), 371–400.

[46] G. Dziuk, E. Kuwert and R. Schätzle, Evolution of elastic curves in $\mathbb{R}^n$: existence and computation, SIAM J. Math. Anal, 33 (2002), 1228–1245.

[47] M. Dziwnik, A. Munch and B. Wagner, A phase-field model for solid-state dewetting and its sharp interface limit, preprint.

[48] J.J. Eggleston, G.B. McFadden and P.W. Voorhees, A phase-field model for highly anisotropic interfacial energy, Phys. D, 150 (2001), 91–103.

[49] C.M. Elliott and H. Garcke, Existence results for diffusive surface motion laws, Adv. Math. Sci. Appl., 7 (1997), 465–488.

[50] J. Escher, U.F. Mayer and G. Simonett, The surface diffusion flow for immersed hypersurfaces, SIAM J. Math. Anal., 29 (1998), 1419–1433.

[51] J. Escher, H. Garcke and K. Ito, Exponential stability for a mirror-symmetric three phase boundary motion by surface diffusion, Math. Nachr., 257 (2003), 3–15.

[52] I. Fonseca, The Wulff theorem reivisited, Proc. R. Soc. A, 432 (1991), 125–145.

[53] F.C. Frank, The geometrical thermodynamics of surfaces, Am. Soc. Metals, (1963), 1–15.

[54] M. Gao and X.P. Wang, A gradient stable scheme for a phase field model for the moving contact line problem, J. Comput. Phys., 231 (2012), 1372–1386.

[55] A.L. Giermann and C.V. Thompson, Solid-state dewetting for ordered arrays of crystallographically oriented metal particles, Appl. Phys. Lett., 86 (2005), article 121903.

[56] A.L. Giermann and C.V. Thompson, Requirements for graphoepitaxial alignment through solid-state dewetting of Au films, J. Appl. Phys., 109 (2011), article 083520.

[57] C. Herring, Effect of change of scale on sintering phenomena, J. Appl. Phys., 21 (1950), 301–303.

[58] C. Herring, Physics of Powder Metallurgy, ed. W.E. Kingston, McGraw-Hill, 1951.

[59] C. Herring, Some theorems on the free energies of crystal surfaces, Phys. Rev., 82 (1951), 87–93.

[60] D.W. Hoffman and J.W. Cahn, A vector thermodynamics for anisotropic surfaces. I. Fundamentals and application to plane surface junctions, Surf. Sci., 31 (1972), 368–388.

[61] D.W. Hoffman and J.W. Cahn, A vector thermodynamics for anisotropic surfaces-II. Curved and faceted surfaces, Acta Metall. Mater., 22 (1974), 1205–1214.

[62] T. Y. Hou, J. S. Lowengrub and M. J. Shelley, Removing the stiffness from interfacial flows with surface tension, J. Comput. Phys., 114 (1994), 312–338.

[63] C. Huh and S.G. Mason, The steady movement of a liquid meniscus in a capillary tube, J. Fluid Mech., 81 (1977) 401–419.

[64] Y. Ishikawa, Y. Imai, H. Ikeda and M. Tabe, Pattern-induced alignment of silicon islands on buried oxide layer of silicon-on-insulator structure, Appl. Phys. Lett., 83 (2003), 3162–3164.

[65] C. Jahan, O. Faynot, L. Tosti and J.M. Hartmann, Agglomeration control during the selective epitaxial growth of Si raised sources and drains on ultra-thin silicon-on-insulator substrates, J. Cryst. Growth, 280 (2005), 530–538.

[66] W. Jiang, W. Bao, C.V. Thompson and D.J. Srolovitz, Phase field approach for simulating solid-state dewetting problems, Acta Mater., 60 (2012), 5578–5592.

[67] W. Jiang, Y. Wang, Q. Zhao, D.J. Srolovitz and W. Bao, Solid-state dewetting and island morphologies in strongly anisotropic materials, Script. Mater., 115 (2016), 123–127.

[68] E. Jiran and C.V. Thompson, Capillarity instabilities in thin films, J. Elect. Mater., 19 (1990), 1153–1160.

[69] E. Jiran and C.V. Thompson, Capillary instabilities in thin, continuous films, Thin Solid Films, 208 (1992), 23–28.

[70] W. Jost, Diffusion in Solids, Liquids, Gases, Academic Press, 1952.

[71] R. Kaischew, Equilibrium shape and work of formation of crystalline nuclei on a foreign substrate (in Bulgarian), Commun. Bulg. Acad. Sci., 1 (1950), 100.

[72] R. Kaischew, Arbeitstagung Festkörper Physik, Dresden, 1952.

[73] M. Khenner, A. Averbuch, M. Israeli and M. Nathan, Numerical simulation of grain-boundary grooving by level set method, J. Comput. Phys., 170 (2001), 764–784.

[74] K.T. Kim and S.K. Ihm, Sintering behavior of nickel particles supported on alumina model catalyst in hydrogen atmosphere, J. Catal., 96 (1985), 12–22.

[75] G.H. Kim, R.V. Zucker, J. Ye, W.C. Carter and C.V. Thompson, Quantitative analysis of anisotropic edge retraction by solid-state dewetting of thin single crystal films, J. Appl. Phys., 113 (2013), article 043512.

[76] L. Klinger, D. Amram and E. Rabkin, Kinetics of a retracting solid film edge: the case of high surface anisotropy, Scripta Mater., 64 (2011), 962–965.

[77] L. Klinger and E. Rabkin, Shape evolution by surface and interface diffusion with rigid body rotations, Acta Mater., 59 (2011), 6691–6699.

[78] L. Klinger and E. Rabkin, Capillary-driven motion of nanoparticles attached to curved rigid substrates, Acta Mater., 60 (2012), 6065–6075.

[79] J. Koplik, J. R. Banavar and J. F. Willemsen, Molecular dynamics of Poiseuille flow and moving contact lines, Phys. Rev. Lett., 60 (1988), 1282–1285.

[80] J. Koplik, J. R. Banavar and J. F. Willemsen, Molecular dynamics of fluid flow at solid surfaces, Phys. Fluids A, 1 (1989), 781–794.

[81] M.D. Korzec, M. Roczen, M. Schade, B. Wagner and B. Rech, Equilibrium shapes of polycrystalline silicon nanodots, J. Appl. Phys., 115 (2014), article 074304.

[82] A. Kosinova, L. Klinger, O. Kovalenko and E. Rabkin, The role of grain boundary sliding in solid-state dewetting of thin polycrystalline films, Scripta Mater., 82 (2014), 33–36.

[83] M.V. Laue, Der Wulffsche Satz für die Gleichgewichtsform von Kristallen, Zeitschrift f. Krystall. Mineral., 105 (1943), 124–133

[84] J.K. Lee, J.H. Choy and Y. Choi, Equilibrium shape and heterogeneous nucleation barrier at spherical interfaces, Surface Science, 256 (1991), 147–158.

[85] F. Leroy, F. Cheynis, T. Passanante and P. Muller, Dynamics, anisotropy, and stability of silicon-on-insulator dewetting fronts, Phys. Rev. B, 85 (2012), article 195414.

[86] H. Liebmann, Der Curie-Wulff'sche Satz über Combinationsformen von Krystallen, Zeitschrift f. Krystall. Mineral., 53 (1914), 171–177.

[87] D.H. Min and H. Wong, The effect of strong surface energy anisotropy on migrating grain-boundary grooves, J. Appl. Phys., 100 (2006), article 053523.

[88] J. Mizsei, Activating technology of SnO_2 layers by metal particles from ultra-thin metal films, Sens. Actuators B, 16 (1993), 328–333.

[89] C.E. Morosanu, Thin Films by Chemical Vapour Deposition, Elsevier, New York, 1990.

[90] W.W. Mullins, Theory of thermal grooving, J. Appl. Phys., 28 (1957), 333–339.

[91] W.W. Mullins, Flattening of a nearly plane solid surface due to capillarity, J. Appl. Phys., 30 (1959), 77–83.

[92] W.W. Mullins, Proof that the two dimensional shape of minimum surface free energy is convex, J. Appl. Phys., 3 (1962), 754–759.

[93] G.D. Nessim, A.J. Hart, J.S. Kim, D. Acquaviva, J. Oh, C.D. Morgan, M. Seita, J.S. Leib and C.V. Thompson, Tuning of vertically-aligned carbon nanotube diameter and areal density through catalyst pre-treatment, Nano Lett., 8 (2006), 3587–3593.

[94] R. Nuryadi, Y. Ishikawa and M. Tabe, Formation and ordering of self-assembled Si islands by ultrahigh vacuum annealing of ultrathin bonded silicon-on-insulator structure, Appl. Surf. Sci., 159 (2000), 121–126.

[95] R. Nuryadi, Y. Ishikawa,Y. Ono and M. Tabe, Thermal agglomeration of single-crystalline Si layer on buried SiO2 in ultrahigh vacuum. J. Vac. Sci. Technol. B, 20 (2002), 167-172.

[96] C. Ograin and J. Lowengrub, Geometric evolution law for modeling strongly anisotropic thin-film morphology, Phys. Rev. E, 84 (2011), article 061606.

[97] Y. Ono, M. Nagase, M. Tabe, and Y. Takahashi, Thermal agglomeration of thin single crystal Si on SiO2 in vacuum, Jpn. J. Appl. Phys., Part 1, 34 (1995), 1728–1735.

[98] D. Peng, S. Osher, B. Merriman and H. Zhao, The geometry of Wulff crystal shapes and its relations with Riemann problems, Contemp. Math., 238 (1999), 251–303.

[99] O. Pierre-Louis and Y. Saito, Wetting of solid adsorbate islands on nanogroove surfaces, Europhys. Lett., 86 (2009), article 46004.

[100] O. Pierre-Louis, A. Chame and Y. Saito, Dewetting of ultrathin solid films, Phys. Rev. Lett., 103 (2009), article 195501.

[101] T. Qian, X.P. Wang and P. Sheng, Generalized Navier boundary condition for the moving contact line, Comm. Math. Sci., 1 (2003), 333–341.

[102] T. Qian, X.P. Wang and P. Sheng, Molecular hydrodynamics of the moving contact line in two phase immiscible flows, Commun. Comput. Phys., 1 (2006), 1–52.

[103] T. Qian, X.P. Wang, and P. Sheng, A variational approach to moving contact line hydrodynamics, J. Fluid Mech., 564 (2006), 333–360.

[104] E. Rabkin, D. Amram and E. Alster, Solid state dewetting and stress relaxation in a thin single crystalline Ni film on sapphire, Acta Mater., 74 (2014), 30–38.

[105] J. Ralston, M. Popescu and R. Seder, Dynamics of wetting from an experimental point of view, Annu. Rev. Mater. Res., 38 (2008), 23–43.

[106] S.J. Randolph, J.D. Fowlkes, A.V. Melechko, K.L. Klein, H.M.III Meyer , M.L. Simpson and P.D. Rack, Controlling thin film structure for the dewetting of catalyst nanoparticle arrays for subsequent carbon nanofiber growth, Nanotechnology, 18 (2007), article 465304.

[107] S. Rath, M. Heilig, H. Port and J. Wrachtrup, Periodic organic nanodot patterns for optical memory, Nano Lett., 7 (2007), 3845–3848.

[108] W. Ren and W. E, Boundary conditions for the moving contact line problem, Phys. Fluid, 19 (2007), article 022101.

[109] W. Ren, D. Hu, and W. E, Continuum models for the contact line problem, Phys. Fluid, 22 (2010), article 102103.

[110] W. Ren and W. E, Contact line dynamics on heterogeneous surfaces, Phys. Fluid, 23 (2011), article 072103.

[111] A.R. Roosen and J.E. Taylor, Modeling crystal growth in a diffusion field using fully faceted interfaces, J. Comput. Phys., 114 (1994), 113–128.

[112] A.R. Roosen, R.P. McCormack and W.C. Carter, Wulffman: A tool for the calculation and display of crystal shapes, Comp. Mat. Sci., 11 (1998), 16–26.

[113] V. Schmidt, J.V. Wittemann, S. Senz and U. Gosele, Silicon nanowires: a review on aspects of their growth and their electrical properties, Adv. Mater., 21 (2009), 2681–2702.

[114] E.J. Siem and W.C. Carter, Orientation-dependent surface tension functions for surface energy minimizing calculations, J. Mater. Sci., 40 (2005), 3107–3113.

[115] P. Smereka, Semi-implicit level set methods for curvature and surface diffusion motion, J. Sci. Comput., 19 (2003), 439–455.

[116] K.A. Smith, F.J. Solis and D.L. Chopp, A projection method for motion of triple junctions by level sets, Interfaces Free Bound, 4 (2002), 263–276.

[117] D.J. Srolovitz and S.A. Safran, Capillarity instabilities in thin films. I, Energetics, J. Appl. Phys., 60 (1986), 247–254.

[118] D.J. Srolovitz and S.A. Safran, Capillarity instabilities in thin films. II. Kinetics, J. Appl. Phys., 60 (1986), 255–260.

[119] A.P. Sutton and R.W. Balluffi, Interfaces in Crystalline Materials, Clarendon, Oxford University, 1996.

[120] T. Tasdizen, R. Whitaker, P. Burchard and S. Osher, Geometric surface processing via normal maps, ACM Transactions on Graphics (TOG), 22 (2003), 1012–1033.

[121] J.E. Taylor, Existence and structure of solutions to a class of non-elliptic variational problems, Symposia Mathematca, 14 (1974), 499–508.

[122] J.E. Taylor, II-Mean curvature and weighted mean curvature, Acta Metall. Mater., 40 (1992), 1475–1485.

[123] J.E. Taylor, Crystalline variational methods, Proc. natl. Acad. Sci., USA, 99 (2002), 15277–15280.

[124] P.A. Thompson and M.O. Robbins, Simulations of contact-line motion: slip and the dynamic contact angle, Phys. Rev. Lett., 63 (1989), 766–769.

[125] C.V. Thompson, Solid-state dewetting of thin films, Annu. Rev. Mater. Res., 42 (2012), 399–434.

[126] S. Torabi, J. Lowengrub, A. Voigt and S. Wise, A new phase-field model for strongly anisotropic systems, Proc. R. Soc. A, 465 (2009), 1337–1359.

[127] M. Upmanyu, D.J. Srolovitz, L.S. Shvindlerman and G. Gottstein, Molecular dynamics simulation of triple junction migration, Acta Mater., 50 (2002), 1405–1420.

[128] D. Wang, R. Ji and P. Schaaf, Formation of precise 2D Au particle arrays via thermally induced dewetting on pre-patterned substrates, Beilstein J. Nanotechnol., 2 (2011), 318–326.

[129] X.P. Wang, T. Qian and P. Sheng, Moving contact line on chemically patterned surfaces, J. Fluid Mech., 605 (2008), 59–78.

[130] Y. Wang, W. Jiang, W. Bao and D.J. Srolovitz, Sharp interface model for solid-state dewetting problems with weakly anisotropic surface energies, Phys. Rev. B, 91 (2015), article 045303.

[131] Y. Wang, W. Jiang, Q. Zhao, D.J. Srolovitz and W. Bao, Solid-state dewetting of thin films on rigid curved substrates, in preparation.

[132] A.A. Wheeler, Cahn-Hoffmann ξ-vector and its relation to diffuse interface models of phase transitions, J. Stat. Phys., 95 (1999), 1245–1280.

[133] W.L. Winterbottom, Equilibrium shape of a small particle in contact with a foreign substrate, Acta Metall., 15 (1967), 303–310.

[134] H. Wong, P.W. Voorhees, M.J. Miksis, and S.H. Davis, Periodic mass shedding of a retracting solid film step, Acta Mater., 48 (2000), 1719–1728.

[135] G. Wulff, Zur frage der geschwindigkeit des wachstums und der auflösung der krystallflächen, Zeitschrift f. Krystall. Mineral., 34 (1901), 449–530.

[136] J. Ye and C.V. Thompson, Mechanisms of complex morphological evolution during solid-state dewetting of single-crystal nickel thin films, Appl. Phys. Lett., 97 (2010), article 071904.

[137] J. Ye and C.V. Thompson, Regular pattern formation through the retraction and pinch-off of edges during solid-state dewetting of patterned single crystal films, Phys. Rev. B, 82 (2010), article 193408.

[138] J. Ye and C.V. Thompson, Anisotropic edge retraction and hole growth during solid-state dewetting of single crystal nickel thin films, Acta Mater., 59 (2011), 582–589.

[139] J. Ye and C.V. Thompson, Templated solid-state dewetting to controllably produce complex Patterns, Adv. Mater., 23 (2011), 1567–1571.

[140] T. Young, An essay on the cohesion of fluids, Philos. Trans. R. Soc. London, 95 (1805), 65–87.

[141] J. Yun, R. Wang, W.K. Choi, J.T.L. Thong, C.V. Thompson, M. Zhu, Y.L. Foo and M.H. Hong, Field emission from a large area of vertically-aligned carbon nanofibers with nanoscales tips and controlled spatial geometry, Carbon, 48 (2010), 1362–1368.

[142] C.G. Zimmermann, K. Nordlund, M. Yeadon, J.M. Gibson, R.S. Averback, U. Herr and K. Samwer, Burrowing of nanoparticles on clean metal substrates: Surface smoothing on a nanoscale, Phys. Rev. B, 64 (2001), article 085419.

[143] R.V. Zucker, D. Chatain, U. Dahmen, S. Hagége and W.C. Craig, New software tools for the calculation and display of isolated and attached interfacial-energy minimizing particle shapes, J. Mater. Sci., 47 (2012), 8290–8302.

[144] R.V. Zucker, J.H. Kim, W.C. Carter and C.V. Thompson, A model for solid-state dewetting of a fully-faceted thin film, C. R. Phys., 14 (2013), 564–577.